RÉPUBLIQUE FRANÇAISE
Liberté Égalité Fraternité

Université de Toulouse

Doctorat de l'Université de Toulouse

préparé à l'ISAE-SUPAERO

Investigation des propriétés globales des matériaux granulaires dans le contexte de l'instrument WheelCams à bord du rover MMX.

Thèse présentée et soutenue, le 24 avril 2026 par

Colas ROBIN

École doctorale
SDU2E - Sciences de l'Univers, de l'Environnement et de l'Espace

Spécialité
Astrophysique, Sciences de l'Espace, Planétologie

Unité de recherche
ISAE-ONERA PSI Physique Spatiale et Instrumentation

Thèse dirigée par
Naomi MURDOCH et David MIMOUN

Composition du jury
M. Yves GOURINAT, Président, ISAE-SUPAERO
M. Pierre DELAGE, Rapporteur, École Nationale des Ponts et Chaussées
M. Daniel HESTROFFER, Rapporteur, Observatoire de Paris - Université PSL
M. Stephan ULAMEC, Examinateur, Deutsches Zentrum für Luft- und Raumfahrt
Mme Naomi MURDOCH, Directrice de thèse, ISAE-SUPAERO
M. David MIMOUN, Co-directeur de thèse, ISAE-SUPAERO

Membres invités
M. Simon TARDIVEL, CNES

Résumé

Les petits corps, vestiges des blocs à l'origine du Système solaire, contiennent des informations clés sur la formation et l'évolution de ses planètes. Ils sont récemment devenus les cibles d'un nombre croissant de missions d'exploration spatiale, impliquant souvent des interactions directes avec leur surface. Ainsi, comprendre le comportement mécanique de la surface de ces corps est essentiel au succès de ces missions. Les surfaces des astéroïdes visités par ces missions sont couvertes de régolithe, un matériau granulaire meuble dont les propriétés sont gouvernées par les interactions entre ses particules, leurs morphologies, ainsi que par les conditions externes telles que la faible gravité. Cependant, il n'est pas évident de déterminer dans quelles mesures les hypothèses de la mécanique des milieux granulaires sur Terre restent valables en faible gravité. Nous souhaitons donc étudier les propriétés mécaniques des matériaux granulaires en faible gravité, avec un intérêt pour les lunes martiennes Phobos et Deimos, dans le contexte de la mission Martian Moons eXploration (MMX) de l'agence spatiale japonaise. En particulier, ce travail se concentre sur le rover Idefix de la mission MMX, développé par l'agence spatiale allemande (DLR) en collaboration avec l'agence spatiale française (CNES). Cette thèse vise à contribuer à l'atteinte des objectifs scientifiques des WheelCams, des caméras installées sous le rover et orientées vers ses roues. Pour ce faire, différentes techniques d'analyse ont été utilisées, incluant l'analyse morphologique de particules à partir d'images et des simulations numériques basées sur la méthode des éléments discrets (DEM) à sphères déformables, afin d'étudier les propriétés mécaniques macroscopiques des matériaux granulaires en faible gravité.

Dans un premier temps, une étude d'analyse morphologique de matériaux granulaires est proposée. Une chaîne de traitement d'images a été développée et validée afin d'extraire des descripteurs morphologiques quantitatifs à partir des images des WheelCams. Cette chaîne a été appliquée à des images issues du banc d'essai des WheelCams ainsi qu'à une étude approfondie de blocs rocheux présents à la surface de différents astéroïdes de type « rubble-pile ». Les morphologies observées ont pu être mises en relation avec les propriétés mécaniques de ces blocs et montrer qu'ils proviendraient de la disruption d'un corps parent.

Dans un second temps, cette thèse s'intéresse aux propriétés mécaniques macroscopiques de matériaux granulaires simulés, qui ont été utilisés dans la thèse de Cecily Sunday, publiée en 2022. À l'aide du logiciel *Project Chrono* et de son code DEM à sphères déformables, une boîte de cisaillement direct a été conçue afin de reproduire numériquement des essais géotechniques de laboratoire. Cet outil permet d'extraire les propriétés macroscopiques de ces matériaux, telles que l'angle de frottement interne et la cohésion macroscopique. Les résultats de ces tests ont permis d'étudier l'influence des propriétés inter-particulaires, de la pression de confinement et de la gravité sur les propriétés macroscopiques de ces matériaux. Ces résultats mettent en évidence un lien entre la diminution de la gravité, de la pression de confinement ou de la charge normale sous un certain seuil avec une baisse importante de la cohésion apparente du matériau. Ils ont ensuite été interprétés dans le cadre de la terramécanique afin d'en tirer des informations pour la mobilité des rovers et les interactions avec le régolithe en faible gravité.

Dans l'ensemble, cette thèse propose de nouveaux outils ainsi que des éléments de compréhension supplémentaires afin de caractériser les matériaux granulaires et leur comportement à la surface des petits corps. Ces résultats sont particulièrement pertinents pour l'interprétation scientifique et les opérations de la mission MMX, et d'autres missions dédiées aux petits corps.

Abstract

Small bodies, as the leftovers of the building blocks of the Solar System contain key informations on the formation and evolution of the planets of the Solar System. These small-bodies have thus become the targets of a increasing number of space exploration missions, often involving direct interactions with their surface. Understanding the mechanical behaviours of the surfaces of these bodies is thus essential for the success of these missions. The surfaces of the asteroids that have been visited by space missions to date are covered by regolith, a loose granular material whose properties are governed by complex inter-particle interactions, grain morphology, and environmental conditions such as low gravity. Predicting regolith behaviour in such conditions is a challenge as it is not clear how terrestrial assumptions on granular material scale in low gravity. This thesis aims to investigates the mechanical properties of granular materials in low gravity, with a focus on the Martian moon Phobos in the context of the future Japanese space agency's Martian Moon eXploration mission. Notably, this study focuses on the MMX Rover Idefix provided by the German space agency, and the French space agency. More specifically, this thesis aims to contribute to the scientific objectives of the WheelCams, cameras placed under the rover pointing towards its wheels. To do so, we combined different analysis techniques such as morphological analysis of particles from images and numerical simulations using a soft-sphere Discrete Element Method (DEM) code, in order to investigate the bulk mechanical properties of granular material in low gravity.

First, we propose a morphological analysis study of granular material. An image analysis pipeline has been developed and validated, with the aim to extract quantitative morphological descriptors from the WheelCams images. We used this pipeline on images from the WheelCams testbed and in a comprehensive study of boulders at the surfaces of different rubble-pile asteroids, including the last image captured of Dimorphos by the DART spacecraft that aimed to change its orbit in the context of planetary defense. We were notably able to link the observed morphologies with bulk properties of the boulders at the surface of these asteroids and make further interpretations regarding their formations, showing that these boulders originated from the disruption of a parent body.

Then, this thesis focuses on the bulk mechanical properties of simulated granular materials that were studied in a precedent thesis published by Cecily Sunday in 2022. Using *Project Chrono* and its soft-sphere DEM framework, a digital direct shear box has been designed to reproduce laboratory geotechnical tests in a numerical environment. This digital shear box aims to extract the mechanical bulk properties of simulated granular materials, as these materials are defined by their inter-particle properties. Finally, using the results of the direct shear tests, we investigated the influence of inter-particle properties, confining pressure and gravity on the macroscopic properties of granular materials. Most notably our results highlight the fact that decreasing gravity, confining pressure or normal load under a certain threshold will drastically decrease the bulk cohesion of granular materials. These results have been then interpreted in the framework of terramechanics, to draw further interpretations relevant to rover mobility and surface interactions in low gravity.

Overall, this thesis aims to provides new tools as well as further insights to characterize granular materials and granular behaviours at the surface of small bodies. These results are notably of importance for the interpretation and operations of MMX and other current or future small body exploration missions.

Contents

Résumé **2**

Abstract **4**

Acknowledgements **14**

Introduction - Version Française **17**

Introduction **21**

1 The study of small bodies and the JAXA MMX Mission **25**

1.1 Small Bodies of the Solar System 25

1.1.1 Observing small bodies 26

1.1.2 Getting close to small bodies 27

1.1.3 The era of surface interaction with small bodies 29

1.2 Surfaces of small bodies in the Solar System 34

1.2.1 The diversity of surfaces in the Solar System 34

1.2.2 Regolith and granular materials 36

1.2.3 Investigating granular behaviours in low gravity 41

1.3 Phobos, Deimos and the Martian Moon eXploration Mission (MMX) 45

1.3.1 Exploration of the moons of Mars 45

1.3.2 Phobos and Deimos, the moons of Mars 46

1.3.3 The JAXA MMX Mission 51

1.4 Thesis objectives and outline 57

2 Morphologies of grains related to mechanicals properties of granular materials **59**

2.1 Grain morphology: formation mechanisms and effects on mechanical behaviour in terrestrial and extraterrestrial environments 59

2.2 Morphological descriptors . . . 62
2.3 Development and validation of an image analysis pipeline for the MMX WheelCams . . . 65
2.3.1 Presentation of the pipeline and motivation for its development . . . 65
2.3.2 Influence of resolution on the results of the pipeline . . . 67
2.4 Test of the pipeline on images of the WheelCams testbed . . . 71
2.5 Mechanical properties of rubble pile asteroids through surface boulder morphological analysis (Robin et al., 2024). . . . 75
2.5.1 Morphological analysis of boulders at the DART impact site . . . 76
2.5.2 Implications for Dimorphos' mechanical properties and boulder formation mechanisms . . . 78
2.5.3 Image selection of other rubble pile asteroids surfaces . . . 79
2.5.4 Comparative morphological analysis of boulders on rubble pile asteroids 80
2.5.5 Discussion of the results . . . 83
2.5.6 Application and use of the results in other studies . . . 87
2.6 New studies of boulder morphology since 2022 . . . 88
2.7 Conclusion . . . 89

3 From simulated micro-parameters to bulk properties 91
3.1 Simulation of granular materials . . . 91
3.2 *Project Chrono* and its SSDEM . . . 94
3.2.1 Description of the adopted physical models . . . 97
3.2.2 Motivation and objectives using *Project Chrono* . . . 103
3.3 The physics of box objects in *Project Chrono* . . . 104
3.3.1 Fixed wall - particles interactions . . . 104
3.3.2 Moving particles with box objects . . . 108
3.4 Laboratory Geotechnical Tests: which is most suitable for simulations? . . . 118
3.4.1 Direct Shear Test . . . 118
3.4.2 Triaxial Test . . . 119
3.5 Digital direct shear tests in the literature . . . 122
3.6 Constructing a Digital Shear Box . . . 123
3.7 A direct shear test simulation . . . 125
3.8 Conclusion . . . 129

4 Digital Shear Box Simulations for Macroscopic Characterization 132
4.1 C. Sunday's thesis results and tested materials. . . . 132
4.2 Parameters influencing the material bulk density . . . 134

4.3 Loading parameters 141
4.4 Results of the Direct Shear Test 142
4.4.1 From Direct Shear Test to maximum shear stresses 142
4.4.2 Estimation of the measurement variability 142
4.4.3 From maximum shear stresses to bulk properties 143
4.4.4 Influence of inter-particle properties on bulk properties of granular material 145
4.4.5 Influence of normal stress on bulk properties of granular materials . . 148
4.5 Implication of the results of the shear tests for terramechanics 152
4.5.1 An introduction to terramechanics 152
4.5.2 Linking the shear tests results with terramechanics parameters 154
4.6 Conclusions, future works and implications for the MMX rover Idefix and other small-body missions 158

Conclusion and perspectives **161**

Conclusion et perspectives **165**

Bibliography **170**

List of Figures

1 Mars, Phobos et Deimos 18
2 Les WheelCams sur le rover MMX. 18
3 Mars, Phobos and Deimos 22
4 The WheelCams on the MMX rover Idefix. 22

1.1 Orbital semi-major axis as a function of eccentricity for objects classified as asteroids and comets for semi-major axis smaller than 10 AU. 26
1.2 First image of asteroid (951) Gaspra and first full picture of asteroid (243) Ida 28
1.3 Images of the Philae lander taken by the Rosetta spacecraft 30
1.4 Series of images captured by the Hayabusa2 spacecraft during the sampling operations at the surface of asteroid (162173) Ryugu 32
1.5 Images of the OSIRIS-Rex sampling site at the surface of Bennu, the Hokioi crater 33
1.6 Images of low-albedo surfaces in the Solar System 35
1.7 Images of high-albedo surfaces in the Solar System 35
1.8 Images of granular materials in avalanche 37
1.9 Images of Phobos captured by the Viking 1 orbiter and the Mars Reconnaissance Orbiter 46
1.10 Shape models of Phobos and Deimos 47
1.11 Schematic representation of the three main formation hypotheses for Phobos and Deimos 50
1.12 Design of the MMX spacecraft 51
1.13 Schematic illustration and simulation impression of the MMX rover self uprighting strategy 53
1.14 Different views of the MMX Rover Idefix 55
1.15 The single-wheel MMX WheelCam testbed 56

2.1 A two-dimensional particle with its different associated variables used to compute the morphological parameters 64

2.2 Overview diagram of the morphological image analysis pipeline developed for the MMX rover WheelCams . . . 68
2.3 Krumbein's diagram for estimating particle roundness . . . 69
2.4 Roundness chart used to validate and seek for the limits of the pipeline . . . 70
2.5 Residuals of different morphological parameters measured for different equivalent diameters on the charts at different resolutions . . . 71
2.6 Analysed images from the WheelCam testbed . . . 74
2.7 Kernel density estimates of morphological parameters of images from the WheelCam testbed . . . 75
2.8 Rubble pile asteroids visited by space missions: asteroids (65803) Didymos | Dimorphos, (25143) Itokawa, (162173) Ryugu and (101955) Bennu . . . 77
2.9 Examples of one of the High-resolution images for each asteroid surfaces studied 81
2.10 Distribution and kernel density estimates of the roundness of the boulders at the surface of Dimorphos, Itokawa, Ryugu and Bennu . . . 82
2.11 Distribution and kernel density estimates of the ellipsoidal ratios of the boulders at the surface of Dimorphos, Itokawa, Ryugu and Bennu . . . 83
2.12 Boxplots of the internal friction angles values from the boulders larger than 30 pixels analyzed on the images of Dimorphos, Itokawa, Ryugu and Bennu . 85

3.1 Illustration of a spatially binned 3D environment and of the Axis Aligned Bounding Box (AABB) of a cylinder . . . 97
3.2 Schematic of the interaction between two particles in *Project Chrono* . . . 99
3.3 Schematic of the free-fall validation test . . . 105
3.4 Force acting on a particle and on the ground for a particle free-falling on the ground as a function of time . . . 106
3.5 Schematic of the different steps of the cohesion test . . . 107
3.6 Contact force during the cohesive force tests with schematics representing the corresponding test . . . 109
3.7 Average velocity of the particles and velocity of the ground during the elevator test . . . 110
3.8 Schematic of the horizontal particle displacement test . . . 111
3.9 Velocity of the individual particles and average velocity of the particles in a box during the horizontal displacement test . . . 112
3.10 Visualisation of the displacement of particles inside of a container made of teleported box objects . . . 112
3.11 Position in x of the particles and the ground during the friction test . . . 113

3.12 Schematic of the sliding test . . . 113
3.13 Velocity of the individual particles and average velocity of the particles in the box during the horizontal displacement test with teleported fixed particles . 114
3.14 Visualisation of the displacement of particles inside of a container made of teleported box objects and a first layer of teleported fixed particles 115
3.15 Velocity of the individual particles and average velocity of the particles in the box during the motorised horizontal displacement test . . . 116
3.16 Visualisation of the displacement of particles inside of a container made of motorised box objects . . . 116
3.17 Simplified experimental configuration of a shear box and a real direct shear test system . . . 119
3.18 Simplified experimental configuration of a triaxial shear test and real tri-axial shear test system . . . 121
3.19 Snapshots of numerical direct shear tests from the literature . . . 123
3.20 Schematic of the shear box setup in *Project Chrono* . . . 124
3.21 ParaView visualisation of a sample of ≈ 12000 glass beads before and after a 20 mm displacement of the lower frame of the shear box . . . 126
3.22 Inter-particle contact forces network in the simulated direct shear box test . 127
3.23 Average stress in the slices of the shear box during the shear test . . . 127
3.24 Shear stress as a function of the displacement of the lower walls of the shear box . . . 128

4.1 Density of a granular sample during the settling of the "set box" simulation with different drop heights . . . 137
4.2 Density of a granular sample during the settling of the "set box" simulation with different number of particles . . . 137
4.3 Visualisation of the pressure on each particles of the system after a set box simulation . . . 138
4.4 Density of a granular sample during the settling of the "set box" simulation with different Young's moduli . . . 139
4.5 Coefficient of friction as a function of sand density . . . 140
4.6 Bulk densities obtained for the studied simulated granular cases during the settling of the particle samples . . . 140
4.7 Shear stress as a function of the displacement of the lower frame of the shear box during the shearing of a sample of simulated low frictional glass particles 143

4.8 Shear stress as a function of the displacement of the lower frame of the shear box during the direct shear test of a sample of simulated low frictional glass beads from three different "set box" simulations 144
4.9 Shear stress as a function of normal stress for a sample of simulated low frictional glass beads 145
4.10 Shear stress as a function of displacement of the lower frame of the shear box and shear stress as a function of normal stress for samples of simulated frictional particles with and without inter-particle cohesion 146
4.11 Shear stress as a function of displacement of the lower frame of the shear box and shear stress as a function of normal stress for a simulated sample of a low frictional material without twisting or rolling friction 147
4.12 Mohr-Coulomb curves obtained from laboratory direct shear test experiments 149
4.13 Shear stress as a function of displacement of the lower frame of the shear box and shear stress as a function of normal stress for a simulated sample of a low frictional glass beads under Phobos gravity 150
4.14 Bulk cohesion as a function of angle of internal friction of different granular materials measured at different at different gravity levels 152
4.15 Sinkage modulus as a function of sinkage exponent estimated from different studies 156
4.16 Bulk cohesion as a function on angle of internal friction of different materials 157

Acknowledgements

Ces prochains paragraphes sont dédiés à toutes les personnes que j'ai rencontré, de près ou de loin et que j'aimerais remercier, sans qui je n'aurais pas réalisé cette thèse.

En premier lieu, j'aimerais bien sûr remercier ma directrice de thèse Naomi Murdoch, qui m'a épaulé et supporté dans tous les sens du terme pendant un peu plus de 3 ans et demi, sans qui je ne serais sûrement pas allé jusqu'au bout. Tes conseils, que je n'ai pas toujours suivi, était toujours éclairé et je conseillerais moi-même à tous tes autres étudiants de les suivre. Je te remercie aussi pour ta bienveillance, ta compréhension et ta patience (avec moi notamment). Je voulais aussi te remercier de m'avoir toujours pousser que ce soit à publier, à aller en conférence ou à rencontrer et parler à d'autres personnes, ce qui a clairement été les parties préférées de ma thèse ! Merci de m'avoir permis de m'émanciper et aussi d'avoir mon propre avis sur les choses.
Je souhaites aussi remercier David Mimoun, mon co-directeur de thèse, merci d'avoir cru en moi mais aussi d'avoir su me recadrer les idées, surtout vers la fin de la thèse. Merci pour tes précieux conseils, ta bienveillance et ta franchise, cette dernière m'ayant beaucoup aidé à me poser les bonnes questions.
Merci aussi à mon jury de thèse : Daniel Hestroffer, Pierre Delage, Stephan Ulamec, Yves Gourinat et Simon Tardivel.

Un grand merci à tous mes collègues de bureau, en particulier Baptiste et Solène dès la première année avec qui je me suis beaucoup amélioré en géographie. Un grand merci aussi à Alexia avec qui j'ai partagé beaucoup de moments en France et à l'étranger et avec qui j'ai collaboré. Merci ensuite à tous mes autres collègues du bureau 07.185, Arnau, Jeanne, Martin mais aussi tous les autres qui y sont passés, en stage ou en visite. Un grand merci à Cecily sans qui cette thèse n'aurait sûrement pas vu le jour non plus et qui m'a beaucoup aidé au début et à la fin de ma thèse. Thank you, Alexander, for being there for me emotionally on so many occasions and also thanks Joe for always beeing so cheerful. Merci aussi à Raphael, Anthony, Alexandre, Arnaud, Alice, Pauline, Hai et Mélanie de l'équipe

SSPA. Merci à toute l'équipe du DEOS, mais aussi l'équipe rover MMX du CNES à Toulouse.

Un grand merci aussi à mon comité de suivi de thèse: Miguel Charlotte, Jérémie Lassue et SImon Tardivel, vos conseils étaient toujours bienveillants et éclairés et m'ont beaucoup aidé de la première année à la fin de ma thèse.

Thanks to all the DART team, without whom I would not have published my first paper, and thanks to the JAXA MMX team, especially the SSG-SST team.

Merci à toutes les personnes qui m'ont fait confiance avant ma thèse durant mes études, depuis mon premier stage d'observation en L1 avec Alexandre Gelabert, puis mon stage de L3 avec Laurent Pagani, mon stage de M1 avec Ehouarn Millour et bien sûr mon stage de M2, avec Alice Le Gall et Emmanuel Lellouch. Tous ces stages m'ont donné le goût de la recherche et m'ont passionés.

J'aimerais aussi particulièrement remercier Fabrice Minoletti et Aymeric Spiga, qui ont encadré les 2 masters que j'ai fait durant mes études, et qui m'ont aiguillé avant mes débuts dans la recherche.

J'aimerais remercier tous mes amis, celles et ceux que j'ai rencontré avant Toulouse, et à Toulouse et ailleurs pendant et après ma thèse. Un énorme merci à toute la team Altissimo Montaudran, où j'ai passé beaucoup (beaucoup) de temps, pour grimper, pour les jeudis magie et tout le reste. Un grand merci aussi à mes amis de Paris, pour quand j'étais à Toulouse et pour après. Et un merci spécial à Inki de m'avoir supporter dans mon travail tardif et pour le reste ...

Enfin, j'aimerais remercier toute ma famille (Bert et Robin !) mais particulièrement mes parents, Gisèle et Thierry, mes frères Antoine et Benoît et ma soeur Léa, pour votre soutien et votre amour. Et merci aussi aussi à mes neveux et nièces même si je ne travaille pas (au moins physiquement) sur Mars.

Merci pour tout.

Introduction - Version Française

En septembre 2026, l'agence spatiale japonaise (JAXA, Japanese Aerospace Exploration Agency) lancera la mission Martian Moon eXploration (MMX) à destination de Phobos. L'un des principaux objectifs de cette mission est de percer les mystères entourant l'origine des lunes de Mars, Phobos et Deimos (voir Figure 1). En effet, plusieurs théories existent quant à l'origine des lunes martiennes. Elles pourraient soit s'être formées dans la ceinture d'astéroïdes puis avoir été capturées gravitationnellement par Mars, soit résulter d'un impact géant entre Mars et un impacteur, ou encore s'être formées in situ en même temps que Mars. Cependant, des analyses supplémentaires sont nécessaires afin de parvenir à plus de conlusions. Ainsi, la mission MMX propose de rapporter sur Terre un échantillon prélevé à la surface de Phobos afin de l'analyser. La sonde MMX sera donc équipée de nombreux instruments scientifiques destinés à soutenir les opérations de retour d'échantillons, mais également à mener diverses études scientifiques de Phobos, Deimos et Mars. En particulier, le vaisseau MMX embarquera un rover, Idefix, alimenté par énergie solaire conçu pour effectuer des mesures in situ à la surface de Phobos. Ce rover a été développé dans le cadre d'une collaboration entre l'agence spatiale allemande, le Deutsches Zentrum für Luft- und Raumfahrt (DLR), et l'agence spatiale française, le Centre National d'Études Spatiales (CNES). Le rover MMX jouera notamment le rôle de démonstrateur technologique des capacités de déplacement dans un environnement de très faible gravité, la gravité à la surface de Phobos étant de 0,006 m/s^2. Afin de comprendre le comportement du rover dans un tel environnement, Idefix est équipé de deux caméras pointées vers deux roues différentes du rover : l'instrument WheelCams (voir Figure 2).

Cette thèse vise ainsi à préparer l'analyse des images issues des WheelCams et constitue également la continuité de la thèse de Cecily Sunday, qui a étudié le comportement d'enfoncement et de déplacement des roues du rover MMX en faible gravité à l'aide de simulations numériques. Dans ce contexte, cette thèse s'intéresse aux petits corps de manière générale, leurs surfaces étant caractérisées par des conditions de faible gravité, et Phobos leur étant similaire en de nombreux points.

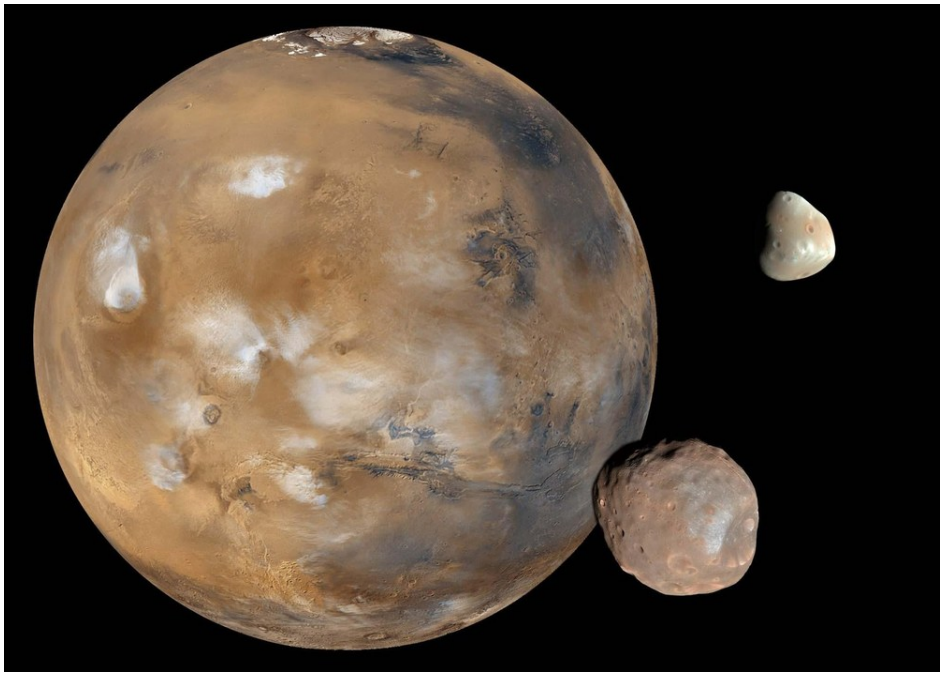

Figure 1: Mars et ses lunes, Phobos (en bas) et Deimos (en haut). Crédit : DLR

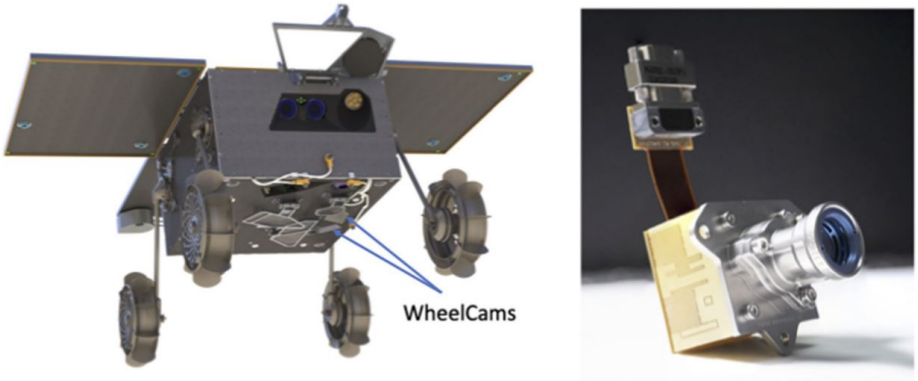

Figure 2: Les WheelCams sur le rover MMX Idefix. (Gauche) Idefix et l'emplacement des deux WheelCams. (Droite) Le modèle de vol d'une WheelCam. Crédit : CNES, d'après Murdoch et al. (2025).

Le terme petits corps désigne les objets orbitant autour du Soleil dans le Système solaire. Ces corps, tels que les astéroïdes ou les comètes, sont des témoins de la formation et de l'évolution planétaires dans le Système solaire. Ils sont observés depuis la Terre dès 1059 av. J.-C., cependant, une des premières mission à avoir rencontré un astéroïde fut la mission Pioneer 2 de la NASA en 1972, et le premier survol d'un petit corps fut celui d'une comète par la sonde International Cometary Explorer (ICE) de la NASA en 1985. À la suite de ces deux missions, et au cours des cinquante dernières années, les missions vers les petits corps sont devenues de plus en plus nombreuses. En particulier, les astéroïdes de type "rubble-pile" (25143) Itokawa, (162173) Ryugu, (101955) Bennu, ainsi que l'astéroïde binaire (65803) Didymos, ont fait l'objet de quatre missions spatiales distinctes. Ces missions ont, entre autre, mis en évidence l'influence majeure de la faible gravité lors des interactions avec la surface de ces petits corps, que ce soit avec des objets artificiels ou naturels. Cet environnement de faible gravité est particulièrement déterminant car ces corps, dont Phobos, sont recouverts d'un matériau granulaire meuble appelé régolithe. Le régolithe est la couche meuble recouvrant les surfaces planétaires et se présente sous une grande diversité de compositions, de distributions de taille et de contextes géologiques.

En tant que matériau granulaire, le régolithe est constitué de particules solides, de formes et de tailles variées, interagissant entre elles par collisions, emboîtement et friction. Le comportement d'un matériau granulaire est donc de nature complexe, puisqu'il peut se comporter comme un solide, un liquide, voire un gaz, selon les forces externes qui s'exercent sur lui et ses propres propriétés. L'étude de ces matériaux en faible gravité est encore plus complexe, et plusieurs approches existent pour analyser leur comportement dans ces conditions, notamment les expériences, les observations in situ et les simulations numériques, ces dernières qui seront abordées dans cette thèse. Comme indiqué précédemment, C. Sunday a étudié le comportement d'enfoncement et de déplacement des roues du rover MMX dans un environnement numérique sous faible gravité. Ces tests ont été réalisés à l'aide de matériaux granulaires, toutefois, ces matériaux numériques sont définis par leurs propriétés inter-particulaires, alors que les propriétés des matériaux granulaires mesurées in situ ou en laboratoire correspondent généralement à des propriétés macroscopiques (ou "bulk"). En l'absence des propriétés macroscopiques des matériaux testés dans la thèse de C. Sunday, la comparaison entre les résultats numériques et les données expérimentales ou in situ sont plus difficile.

Cette thèse se concentrera donc sur l'étude des propriétés macroscopiques des matériaux

granulaires dans le contexte des missions d'exploration spatiale des petits corps, et plus particulièrement pour la mission MMX, afin de soutenir les objectifs scientifiques des WheelCams embarquées sur le rover MMX Idefix. Pour commencer, le premier chaptire de cette thèse propose une revue bibliographique des thèmes abordés dans cette thèse et présente la mission MMX de manière plus détaillée, ainsi que les objectifs de cette thèse, en lien avec l'instrument WheelCams.

Introduction

In September 2026, the Japan Aerospace Exploration Agency (JAXA) will launch the Martian Moon eXploration (MMX) mission to Phobos. One of the main objective of this mission is to unravel the mysteries around the origins of the moons of Mars, Phobos and Deimos (see Figure 3). Indeed, several theories exist concerning the origins of the Martian moons. It is thought that they could have been either formed in the asteroid belt, then gravitationally captured by Mars, or formed after a giant impact between Mars and an impactor or they may have been formed in situ at the same time as Mars. However, to draw further conclusions, more analysis are needed, and the MMX mission propose to return a sample from the surface of Phobos to Earth in order to analyse it. The MMX spacecraft will therefore be equipped with several scientific instruments to help with the sample return operations but also to perform other different scientific studies of Phobos, Deimos or Mars. Notably, the MMX spacecraft will carry a rover, Idefix, a solar-powered rover designed to perform in situ measurements at the surface of Phobos. This rover has been provided by a collaboration between the German space agency: the Deutsches Zentrum für Luft und Raumfahrt (DLR), and the French space agency : the Centre National d'Etudes Spatiales (CNES). The MMX rover will most notably act as a technical demonstration of roving capabilities in a low-gravity environment, as gravity at the surface of Phobos is 0,006 m/s^2. In order to understand the behaviours of the rover in such an environment, Idefix is equipped with two cameras pointing at two different wheels of the rover: the WheelCams instrument (see Figure 4).

This thesis thus aims to prepare for the analysis of the WheelCams images and, is also the continuation of Cecily Sunday's thesis, which notably studied the sinking and roving behaviour of the MMX wheels in low gravity through numerical simulations. In this regard, this thesis will be concerned with small bodies in general, since their surfaces are characterised by low-gravity conditions, and considering that Phobos is similar in many ways with small bodies.

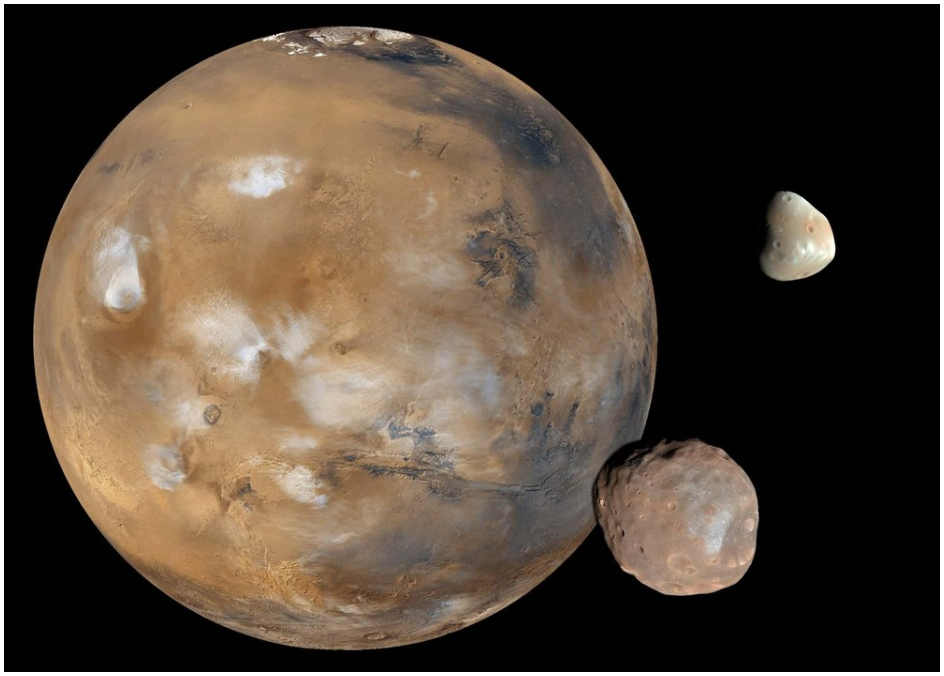

Figure 3: Mars and its moons, Phobos (bottom) and Deimos (top). Credit: DLR

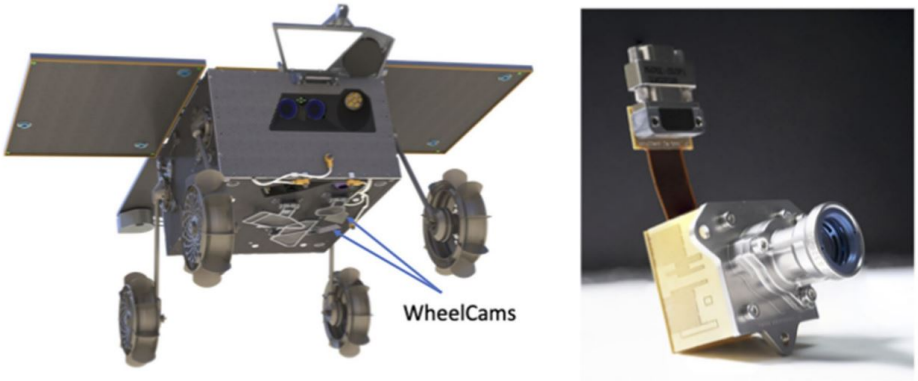

Figure 4: The WheelCams on the MMX rover Idefix. (Left) Idefix and the location of the two WheelCams. (Right) The flight model of a Wheelcam. Credit : CNES, from Murdoch et al. (2025).

The term small bodies refers to the rocky objects orbiting the sun in the Solar System. These bodies, such as asteroids or comets are fundamental witnesses of planetary formation and evolution in the Solar System. These bodies have been observed from Earth as early as 1059 B.C., however, the first mission that encountered an asteroid was the NASA Pioneer 2 mission in 1972 and the first flyby of a small body was that of a comet by the NASA International Cometary Explorer (ICE) spacecraft in 1985. After these two missions and over the last 50 years, missions to small bodies became more and more popular. Most notably, the rubble-pile asteroids (25143) Itokawa, (162173) Ryugu, (101955) Bennu and the (65803) Didymos binary asteroid were the subject of four different space missions. These four missions notably highlighted the influence of low gravity when interacting with the surface of these small bodies, either with human-made objects or natural objects. This low gravity environment is particularly influent because these bodies, including Phobos, are covered with a loose granular material, called regolith. Regolith is the loose covering of planetary surfaces and exists in many different compositions, size distributions and locations.

As a granular material, regolith is made of solid particles with different shapes and sizes, interacting between each other through collisions, interlocking and friction. The behaviour of a granular material is thus of complex nature as it can behave as a solid, a liquid or even a gas depending on the external forces acting on it and its own properties. Studying these materials in low gravity can be even more complex and several different ways exist to investigate their behaviours in these conditions, such as experiments, in situ and numerical simulations, the latter of which will be studied in this thesis. As previously stated, C. Sunday studied the sinking and roving behaviour of the MMX wheels in a numerical environment under low gravity. These tests have been performed with granular materials, however, these numerical materials are defined by their inter-particle properties whereas granular material properties measured in situ or in laboratory are usually the bulk properties of the material. Without the bulk properties of the materials tested in C. Sunday's thesis, it is more difficult to compare numerical results with experimental or in situ data.

This thesis will therefore study the bulk properties of granular materials in the context of space exploration missions to small bodies, and in particular for the MMX mission to support the scientific objectives of the WheelCams, on board the MMX rover Idefix. To begin, the following chapter provides a bibliographic overview of the topics studied in this thesis and presents the MMX mission in more detail, as well as the objectives of this thesis, related to the WheelCams.

Chapter 1

The study of small bodies and the JAXA MMX Mission

1.1 Small Bodies of the Solar System

Small bodies orbiting around the Sun, such as asteroids and comets, are the leftovers of the building blocks of the planets, dwarf planets, and satellites of the Solar System (Chapman, 1975). Considering this, studying their formation and evolution is crucial for understanding processes from the formation of the Solar System to the emergence of water on Earth, that could come from asteroids (Marty and Yokochi, 2006; Matsumoto et al., 2024; Glavin et al., 2025; Zega et al., 2025) or even asteroids impact hazard (Hills and Goda, 1993; Collins et al., 2005).

They orbit the Sun in different regions of the Solar System, from the proximity of Earth to the hypothetical Oort cloud, at the very limit of the Solar System. The names of such bodies differ from their region of orbit:

- The near-Earth objects (NEOs), with Earth-like orbits around the Sun
- The Main Belt Asteroid (MBAs), orbiting the Sun between Mars and Jupiter
- The Trojan Asteroids, sharing Jupiter's orbit
- The trans-Neptunian objects (TNOs), orbiting the Sun beyond the orbit of Neptune

In addition, comets and asteroids can be differentiated by their orbit: comet orbits generally have higher eccentricity and semimajor axis than those of asteroids (Figure 1.1), meaning comets have more elliptical orbits, further from the Sun. Indeed, most of the asteroids are situated in the main belt between two and three Astronomical Units (AU) (Figure 1.1, 1

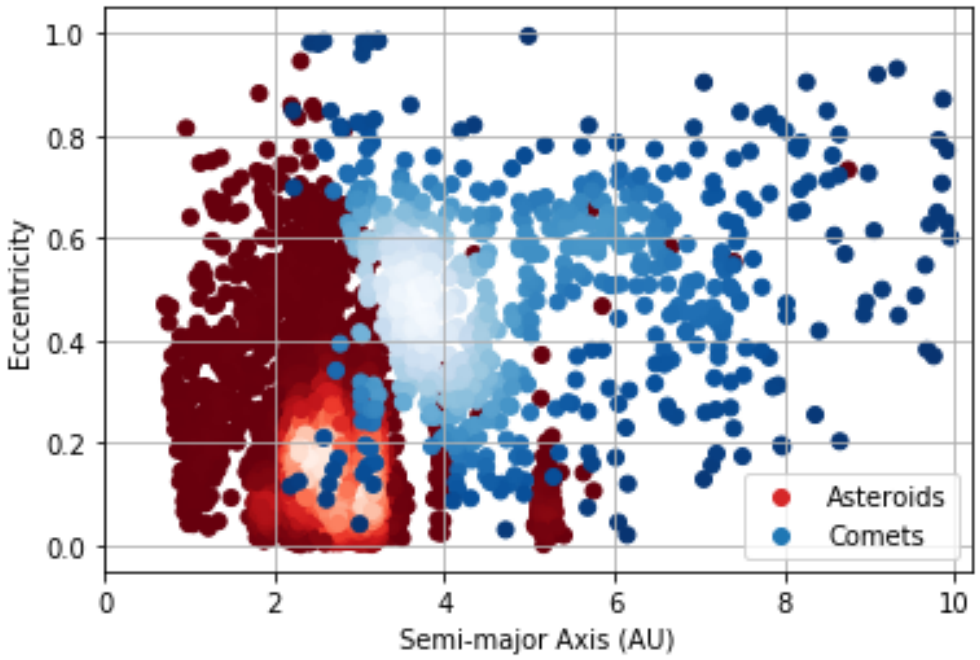

Figure 1.1: Orbital semi-major axis as a function of eccentricity for objects classified as asteroids (red) and comets (blue) for semi-major axis smaller than 10 AU. The brighter the colour, the higher the point density. Data are from the Small Body Database Query. There are 724 comets and only a random sample of 20000 asteroids is displayed for more clarity.

AU is the average distance between the sun ans Earth). Another parameter that helps to distinguish comets and asteroids orbits is the Tisserand parameter: a number calculated from the semi-major axis, orbital eccentricity, and inclination of the orbits of a small-bodies as it gravitationally interacts with a larger body like a planet (Radau, 1896). The Tisserand parameter T with respect to a given planet, is such as:

$$T = \frac{a_p}{a} + 2\cos i \sqrt{\frac{a}{a_p}\left(1 - e^2\right)} \tag{1.1}$$

with a the semi-major axis of the small-body, a_p the semi-major axis of the planet, e the orbital eccentricity of the small-body and i its orbital inclination. For example, the Tisserand parameter T_J of an asteroid interacting with Jupiter is smaller than 3 ($T_J > 3$) and that of comets is between two and three ($2 < T_J < 3$).

1.1.1 Observing small bodies

The first written records of the observation of small bodies were observations in 1059 BC. The first named comet is 1P/Halley, rediscovered in 1758 by Johann Georg Palitzsh, who

observed the return of the comet, predicted by Edmond Halley in 1705. In fact, traces of its observation can be found throughout human history from 611 BC (Tsu, 1934) in China, and its last close approach from Earth was in 1986 (Broughton, 1979). Comets are easily observable to the naked eye because of their high water ice content: when a comet crosses the ice limit when approaching the Sun, its water ice sublimates, making it very bright in the sky with sometimes two characteristic tails, one curved dust tail and one straight ion tail, the latter pointing away from the sun (McFadden and Britt, 2003).

In comparison, the first observed asteroid in history is (1) Ceres[1], the largest asteroid of the main asteroid belt, with a mean radius of 476.2 km (Thomas et al., 2005). It was discovered in 1801 by Giuseppe Piazzi, using the Palermo Circle. Then, 3 other asteroids of the main belt, (2) Pallas, (3) Juno and (4) Vesta have been discovered between 1802 and 1807 (Sawyer Hogg, 1948). In 1868, the 100th asteroid was discovered, in 1921 the 1000th, in 1969 the 10000th and as of 07/01/2026, 1494207 asteroid orbits are available on the the Small Body Database Query along with 4041 comets.

However, the vast majority of these small bodies are observed from Earth with telescopes. In order to study the surfaces of these asteroids in detail, their composition, or the behaviour of these surfaces during interactions with human-made objects for sample return or landing missions, or even planetary defense missions, we need to get closer.

1.1.2 Getting close to small bodies

The first encounter of a space probe with an asteroid was in 1972 by the NASA Pioneer 2 mission on its way to Jupiter. The spacecraft had to travel through the main asteroid belt and was thus the first to do so. Actually, the spacecraft's closest approach to an asteroid, (307) Nike, was in 1972, 8.8 millions km away and no data has been recovered (Fimmel et al., 1980).

The first small body flyby was the flyby of a comet, performed by the NASA International Cometary Explorer (ICE) spacecraft after its launched in 1978. The spacecraft flew past the 21P/Giacobini–Zinner comet in 1985 at a distance of 7800 km from the comet's nucleus.

The same year, in 1985, the Japan Aerospace Exploration Agency (JAXA) launched its first spacecraft, Sakigake, that flew past comet 1P/Halley at 6.99 millions km in 1986. JAXA then attempted to change the spacecraft's orbit to flyby 21P/Giacobini–Zinner but the idea

[1]Today, Ceres is classified as a dwarf planet.

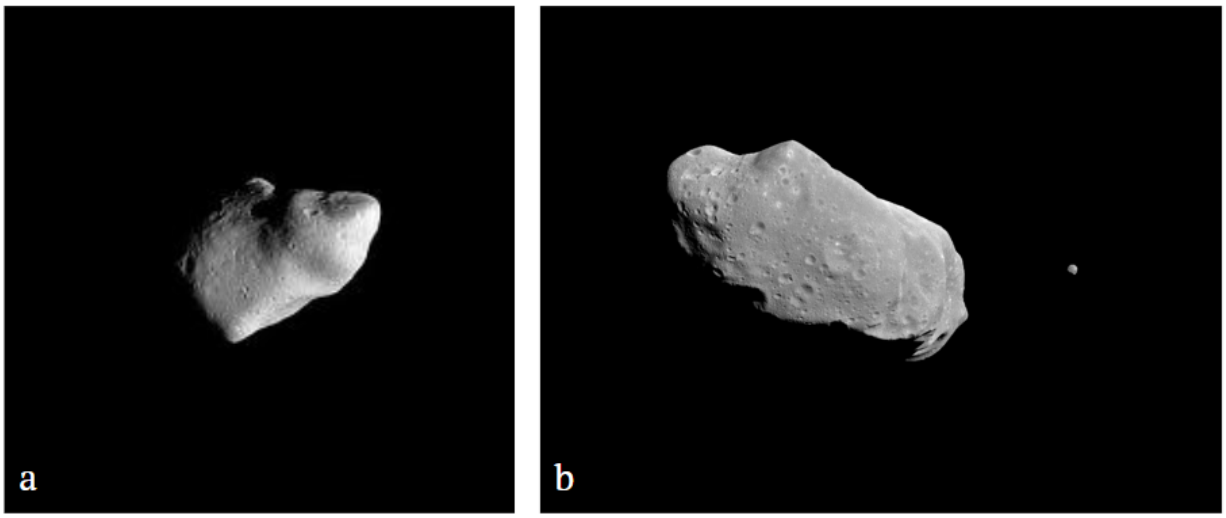

Figure 1.2: a) First image of asteroid (951) Gaspra taken by the Galileo spacecraft in 1991, from a distance of 16200 km. The asteroid is 16 by 12 km. b) First full picture showing asteroid (243) Ida and its moon to the right, taken by the Galileo spacecraft in 1993. The asteroid is approximately 56 km long. Photo credit: NASA/JPL

was abandoned, the probe having almost run out of fuel (Hirao and Itoh, 1988; Farquhar et al., 1988).

The first asteroid flybys were performed by the NASA Galileo mission in 1991 and 1993, also while traveling through the main asteroid belt on its way to Jupiter (D'Amario et al., 1992). These flybys of (951) Gaspra and (243) Ida allowed the first close images of asteroids to be captured (Figure 1.2) and also provide the first evidence that a natural satellite can orbit an asteroid.
In 1994, NASA launched the Clementine mission, that was supposed to study the Moon and the NEO (1620) Geographos. However, the spacecraft failed to leave the geocentric orbit after exploring the Moon and never visit the asteroid.

In 1997, the Near Earth Asteroid Rendezvous (NEAR) Shoemaker spacecraft, part of the Discovery program, performed a flyby of the asteroid (253) Mathilde and then a flyby of (433) Eros in 1998. In 2000, the NEAR shoemaker spacecraft was able to enter into orbit around (433) Eros. In 2001, 2 days before the end of the mission, it was decided to try to land the spacecraft on the surface of the asteroid. The spacecraft survived the landing and was able to continue operations for a few days. This was the first time in human history that a spacecraft has orbited and landed on an asteroid (Cheng, 1997, 2002), which likely marked a turning point for asteroid missions by proving the feasibility of asteroid missions,

showing that spacecrafts could not only reach but also orbit and interact with small bodies in the Solar System.

1.1.3 The era of surface interaction with small bodies

Two years after the success of the NASA NEAR Shoemaker mission in 2001, the JAXA launched its first mission Hayabusa to an asteroid, with the ambitious aim of returning a sample from asteroid (25143) Itokawa. The asteroid was reached in 2005 (Fujiwara et al., 2006) and, after a first failed attempt of touchdown, the sampling operations did not happened as planned. Indeed, on the second attempt, the sampling system was supposed to fire a small projectile to lift fragments of the surface to sample them. However, due to a malfunction, the projectile has not been fired, but Hayabusa was still able to successfully bring back thousands of small grains from Itokawa, and thus performed the first successful sample return from an asteroid (Yoshikawa et al., 2021). These samples allowed to give insight on the water and organic content of Itokawa (Chan et al., 2021).

Another relevant mission in the scope of interaction with small bodies is the European Space Agency (ESA) Rosetta mission. Launched in 2004, the mission aimed for the 67P/Churyumov-Gerasimenko comet to study its behaviour when approaching the sun (Glassmeier et al., 2007). Notably, the mission included a lander, Philae, that was supposed to land on the surface of the comet. Although Philae did land, it actually landed several times as it bounced on the surface of the comet (see Figure 1.3). It was originally planned to activate a cold gas system, to push the lander to the surface, and to fire two anchoring harpoons to fix it to the ground. Unfortunately, the operations did not go as planned, as the the anchor harpoons did not fire and the cold gas system did not work either, leading to the bouncing of the lander. Even if this part of the mission did not go as planned, it allowed to recover engineering data that provided informations on the mechanical properties of the surface of the comet. Notably, it has been estimated that the surface where the first bounce occurred was a granular soft surface with a compressive strength (i.e. a resistance to deformation) of 1 kPa and a thickness of approximately 20 cm, on top of a more rigid layer. The final landing site, on the other hand, was estimated to be a hard surface (Biele et al., 2015).

A year after the launch of the ESA Rosetta mission, the NASA launched the Deep Impact mission to perform a flyby of the 9P/Tempel comet and an impactor experiment, in order to analyse the matter thus ejected from orbit (Blume, 2005). Richardson and Jay Melosh (2013) showed that the 400 kg impactor, created a shallow crater of approximately 50 m

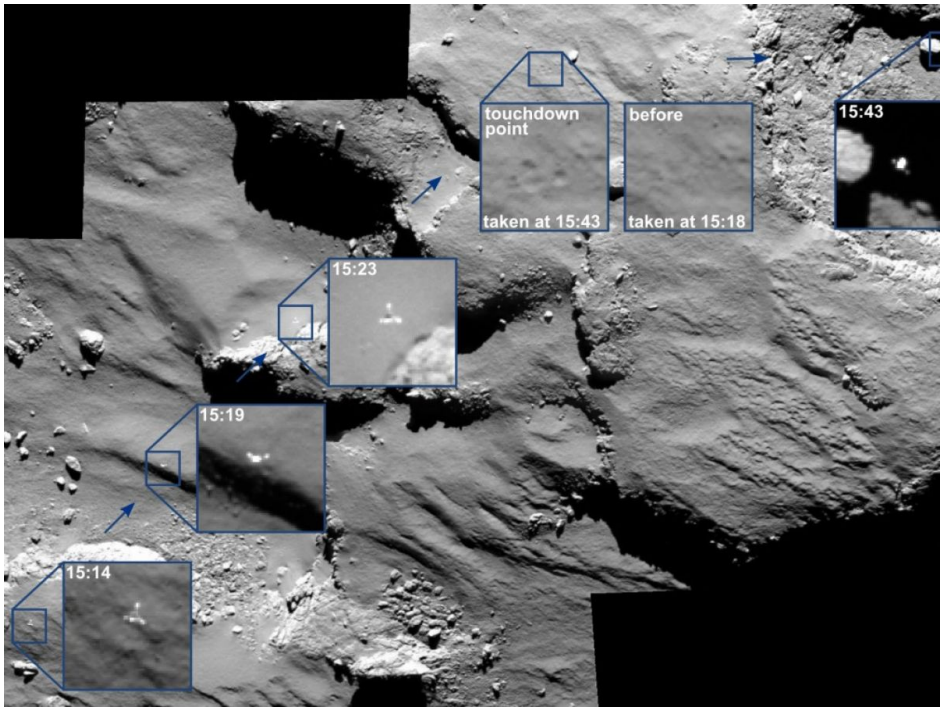

Figure 1.3: Images of the Philae lander taken by the Rosetta spacecraft. The lander is descending towards the comet before bouncing off several times at it surface. (Credits: ESA/Rosetta/MPS for OSIRIS team.)

in diameter with an ejecta blanket of 85-120 m in diameter, as well as an important dust cloud, which was unexpected. This study then showed that the comet was actually covered by a fine dust layer and if this crater estimation is correct, the mechanical properties of this material is roughly similar to lightly-packed "dry" mountain snow.

In 2014, the sequel of Hayabusa was launched: the JAXA Hayabusa2 mission. The spacecraft visited the (162173) Ryugu asteroid between June 2018 and November 2019 (Watanabe et al., 2017, 2019) and performed a sample return from the asteroid of 5.4 g, recovered on Earth, in 2020 (Tsuda et al. (2020); Oba et al. (2023), see the sampling operations in Figure 1.4). The mission included a lander: Mascot, provided by DLR and CNES (Ho et al., 2017). Mascot also bounced several times after hitting a boulder on its first descent, before finally landing (Scholten et al., 2019). Hayabusa2 also included two mini "hopping" rovers, MINERVA-II-1A and MINERVA-II-1B for technology demonstration, and were able to collect hundreds of close-up images from the surface of Ryugu (Lange et al., 2020; Yoshikawa et al., 2022). Hayabusa2 spacecraft also conducted an in-situ impact experiment, that created a 10 m large crater (Arakawa et al., 2020). Thanks to this experiment and simulations, Jutzi et al. (2022) showed that the cohesion between grains at the surface of asteroids, even

in a very small amount, may strongly influence the formation of such craters thus influencing the cratering scaling-laws used to estimate the ages of surfaces in the Solar System. Moreover, they explain that cohesion could therefore explain the different ages estimated of the different geological units across the surface of Ryugu. Preliminary analysis of the returned samples showed that the carboneous composition of the sample was representative of asteroid Ryugu (Yada et al., 2022). Another study showed that these samples are similar to CI chondrites (meteorites with a chemical composition similar to the Sun) but more chemically pristine, with a chemical composition the closest to the Sun's photosphere for a natural sample studied in laboratory, mostly highlighting the effect of the terrestrial atmosphere on CI chondrites (Yokoyama et al., 2022). It has also been possible to estimate that the parent body of Ryugu, from which its boulders were formed, has been formed at large heliocentric distance (beyond 5 AU) because of the absence of a remnant magnetization of the samples that could be present near the center of the Solar nebula during the formation of the Solar System (Maurel et al., 2024). The diversity of these results shows that the value of these sample returns is not limited to the sampled body.

The most recent sample return mission was the NASA OSIRIS-Rex mission, launched in 2016, to study the (101955) Bennu asteroid (Lauretta et al., 2017). OSIRIS-Rex studied the asteroid between 2018 and 2021, and sampled the surface in 2020. The spacecraft returned a sample of approximately 120 g of Bennu's surface (Lauretta et al., 2019, 2022, 2024), see the sampling operations in Figure 1.5). Prior to the mission, it was estimated that the Touch-and-Go Sample Acquisition Mechanism (TAGSAM) sampling instrument would mobilize regolith particles on asteroid Bennu (Bierhaus et al., 2021), but the sampling operations even created a 9-meter long elliptical crater at the sampling site, as the surface of Bennu behaved as a viscous fluid, with minimal resistance to the penetration of the spacecraft into the regolith (Lauretta et al., 2021, 2022). Indeed, the forces measured by the spacecraft during this interaction with the surface of the asteroid are close to simulations of this interaction in a granular bed with close to zero cohesion. Moreover, the low gravity at the surface of the asteroid weakens the near surface as the upper layers are not compacted by their own weight, also minimizing the influence of inter-particle cohesion (Walsh et al., 2022).

Finally, the latest mission that interacted with a small body was the NASA DART mission, launched in 2021 and aimed for the (65803) Didymos binary asteroid in order to perform a kinetic impact test on Dimorphos, the smallest of the binary system (Rivkin et al., 2021). The mission was a success, after the DART spacecraft intentionally crashed into Dimorphos, changed its orbit and demonstrate that kinetic impact is a viable technique to defend Earth

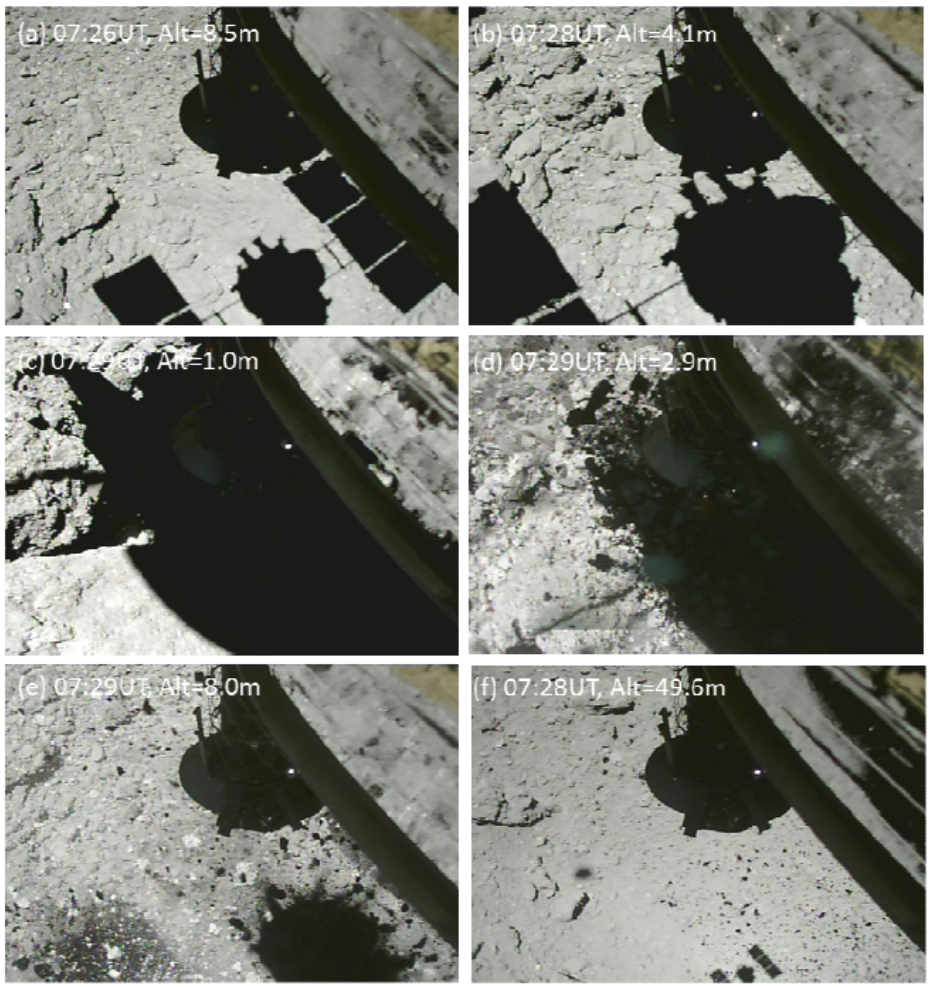

Figure 1.4: Series of images captured by the Hayabusa2 spacecraft during the sampling operations at the surface of asteroid Ryugu. Images a, b, c are before the touchdown and images d, e, f are after. Figure from Tsuda et al. (2020).

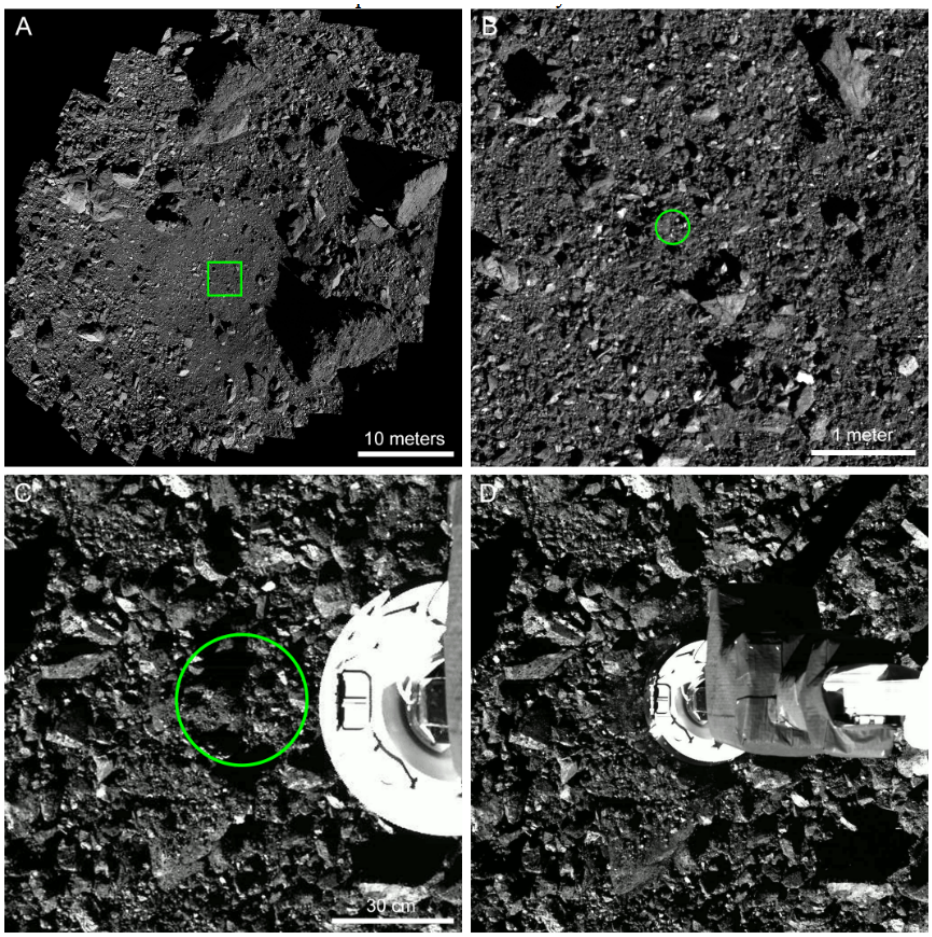

Figure 1.5: Images of the OSIRIS-Rex sampling site at the surface of Bennu, the Hokioi crater. A) Mosaic of images taken by the OCAMS PolyCam imager (Rizk et al., 2018), the green box indicates the area shown in B. B) & C) Closer images of the Hokioi crater, the green circle with a 32cm diameter is the size of the TAGSAM instrument. D) Image of TAGSAM in contact with Bennu. Figure from Lauretta et al. (2022).

from hazardous asteroids if necessary (Daly et al., 2023; Cheng et al., 2023). The expected change of orbital period was of 7 minutes if all the momentum of the spacecraft was transferred to the asteroid (Cheng et al., 2018). However, Thomas et al. (2023) reported a change of orbital period of 33 minutes, estimated from radar and light-curves observations from Earth. In addition, they reveal that this result means that the consequences of the DART impact have been enhanced by the formation of an ejecta, changing the momentum of the asteroid and its orbital period drastically.

1.2 Surfaces of small bodies in the Solar System

The bodies in the Solar System apart from the 4 gas giants, Jupiter, Saturn, Uranus and Neptune, have a solid surface. These planetary surfaces vary widely throughout the Solar System, highlighting various compositions and processes on the surfaces of these bodies, which will be addressed in this section. It is a subject of great importance for planetary exploration nowadays, as *in situ* and sample return missions are becoming increasingly popular, both for their scientific interest and their technological challenges as previously seen in this manuscript. It is thus important to expand our knowledge on the characteristics and behaviour of these surfaces when interacting with natural objects and human-made objects for space missions.

1.2.1 The diversity of surfaces in the Solar System

Planetary surfaces provide valuable insights into the history and physical properties of celestial bodies, even when considered just through their visual characteristics. At first sight, surface reflectivity varies significantly from one surface to another (de Pater and Lissauer, 2015). For example, carbonaceous asteroids, comet nuclei, or maria on the Moon have a very low Bond albedo, a measure of the reflectiveness of celestial bodies (lower than 0.1, see Figure 1.6), which means that these surfaces absorb light a lot.

On the other hand, icy moons tend to be highly reflective. For example, with a Bond albedo up to 0.9, Enceladus is the most reflective body in the Solar System (Howett et al., 2010) (See Figure 1.7a). However, bodies sometimes have completely different albedos even on the same surface, such as Saturn's icy moon Iapetus (See Figure 1.7c): Its leading face is almost ten times less optically bright than its trailing face (Spencer and Denk, 2010). The source of the dark material is the dust ring surrounding Phoebe (another moon of Saturn) which spreads and settles on the surface of Iapetus (Verbiscer et al., 2009).

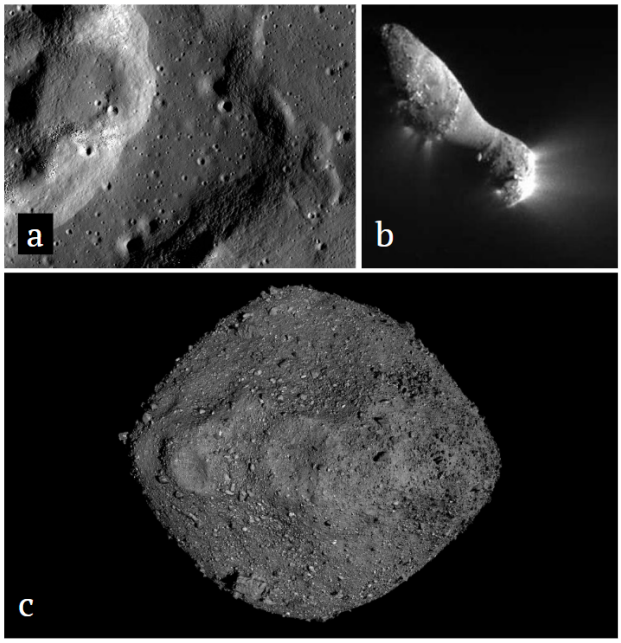

Figure 1.6: Images of low-albedo surfaces in the Solar System. a) Close-up image of the Mare Crisium on the Moon by the Lunar Reconnaissance Orbiter. (Credits: NASA/GSFC/ASU) b) Image of the 103P/Hartley comet captured by the Deep Impact spacecraft during a flyby. The bright rays are the jets streaming out of the nucleus. (Credits: NASA/JPL) c) Mosaic of Bennu created using observations made by the OSIRIS-Rex spacecraft. (Credits: NASA/Goddard/University of Arizona)

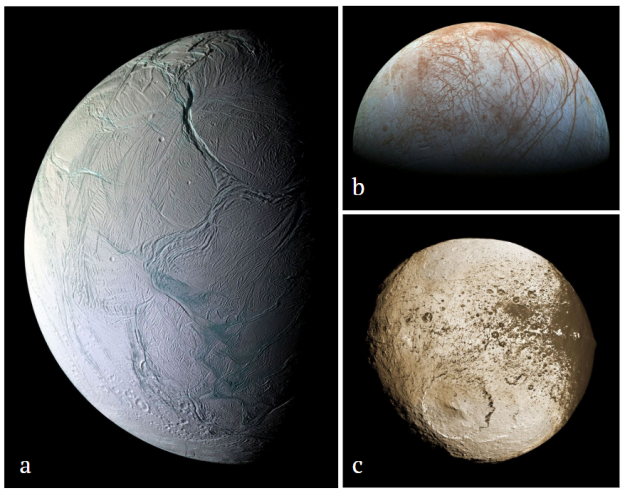

Figure 1.7: Images of high-albedo surfaces in the Solar System. a) Mosaic of Saturn's moon Enceladus, created with images taken by the Cassini spacecraft. (Credits: NASA/JPL/Space Science Institute). b) Image of the Jupiter's moon Europa captured by the Juno spacecraft. (Credits: NASA/JPL-Caltech/SwRI/MSSS) c) Global image of Iapetus showing the albedo dichotomy of this icy moon of Saturn. (Credits: NASA/JPL/Space Science Institute).

In addition to albedo variations, revealing differences in surface composition or texture, the presence (or not) and distribution of impact craters offer valuable clues about the age and geological history of planetary surfaces. Although some planetary surfaces are sometimes densely covered with impact craters such as the Moon (Figure 1.6a) or Saturn's moon Mimas, others show minimal evidence of cratering like Io, Europa (Figure 1.7b) or the Earth, indicating active or recent resurfacing processes (de Pater and Lissauer, 2015). In particular, the crater counting method, as mentioned earlier for Ryugu, based on the analysis of crater distribution and spatial density, enables estimation of the age of a planetary surface (Neukum et al., 2001; Hartmann and Neukum, 2001).

Most rocky bodies also presents linear features like faults, ridges or scarps, suggesting active phenomena distorting the surfaces of these objects. Europa presents for example large faults (Figure 1.7b) caused by ice tectonic events driven by large tidal stress due to the proximity of Jupiter (Hoppa et al., 1999). These different linear features are also quite common at different scales at the surface of smaller bodies like asteroids, with chains of craters, elongated depressions or ridges, or even faults (Murdoch et al., 2015). The nature of these surfaces, particularly those of large satellites or those coupled with an atmosphere, is highly diverse, even on the same body (de Pater and Lissauer, 2015). However, for dry-airless bodies similar to the small bodies visited by the missions presented above in Sect. 1.1, the surface is often covered with a loose unconsolidated granular matter called regolith (Robinson et al., 2002), made from rocks of various sizes, formed by different processes. The grain-size distribution of regolith ranges from dust to boulders (meter-scale rocks). Regolith will be one of our main topics of discussion throughout this thesis.

1.2.2 Regolith and granular materials

The first definition of regolith appeared in 1897 by George Perkins Merrill, based on the combination of two Greek words: *regos* and *lithos*, respectively meaning blanket and stone. George Merrill defined it as a geological term to describe unconsolidated particulate matter above the bedrock on the Earth's surface, formed by various natural processes (Merrill, 1897). It was then in 1967 that Eugene Merle Shoemaker described the surface of the moon as a "surface debris layer or regolith" (Shoemaker et al., 1967). Today, regolith commonly refers to the loose covering of planetary surfaces and exists in many different compositions, size distributions, and locations (Murdoch et al., 2015). However, regardless of these differences, the grains making up the regolith follow the same physical laws that govern granular materials on Earth (Hestroffer et al., 2019). A granular material is a set of solid particles

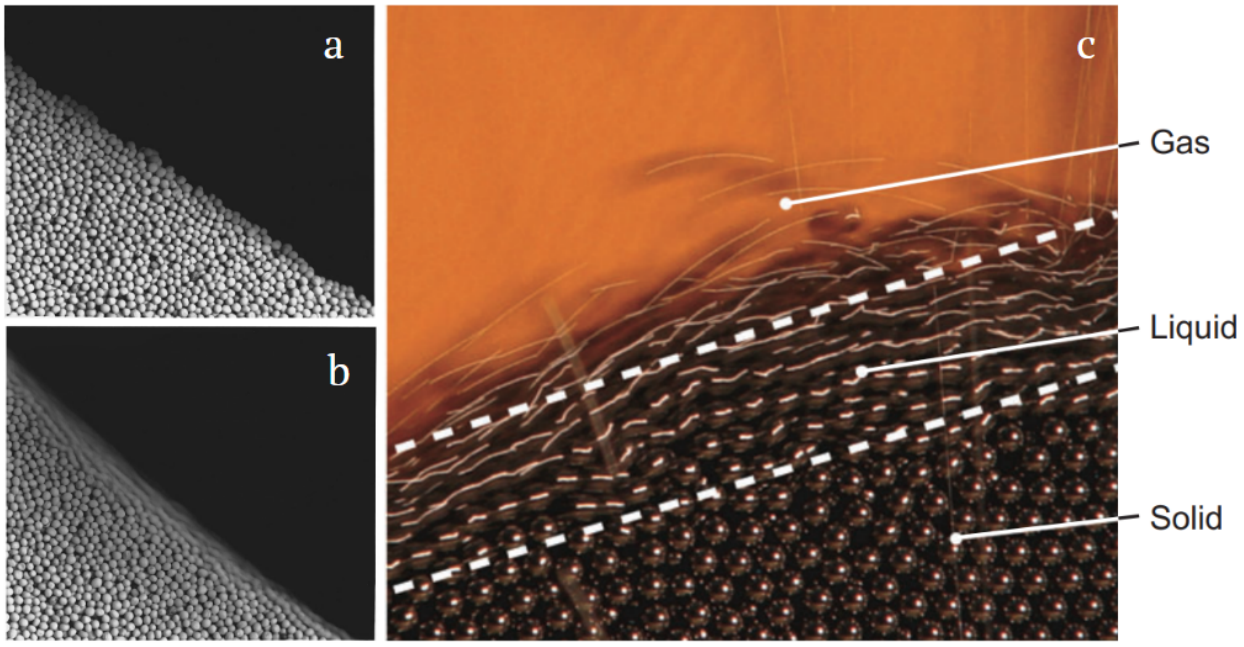

Figure 1.8: a) A pile of mustard seeds tilted below the angle of repose. b) The same pile tilted beyond the angle of repose, triggering an avalanche of grains from the top. c) Image of steel beads poured onto a pile, illustrating the co-existence of solid, liquid and gas flow regimes within a granular material. Figures a) and b) from Jaeger et al. (1996) and Figure c) from Forterre and Pouliquen (2008).

that interact through mechanisms such as interlocking, friction, and collisions, all of which lead to the dissipation of energy.

In 1996, Heinrich Jaeger, Sidney Nagel and Robert Behringer described granular materials as unusual solids, liquids and gases (Jaeger et al., 1996). Remarkably, a single granular sample may simultaneously exhibit characteristics of all three states as seen on Figure 1.8 and in Forterre and Pouliquen (2008). In a static equilibrium, like a sand pile or sand confined within a box, a granular material behaves like a solid (see Figure 1.8a). However, upon a disturbance by an external force, it may transition to a fluid-like state if the grains remain in contact, or to a gas-like state if interactions between grains become rare. In Figure 1.8b, gravity acts as the external force, overcoming the contact and attractive forces between grains and causing a defined surface layer to flow, while the rest of the pile remains undisturbed. This example shows the complexity of granular material and the different interactions at micro-scales (at the particles level) and at macro-scales (considering the whole granular sample). The following paragraphs will present and describe different properties of granular materials, at both micro- and macro-scales.

Inter-particle properties

Contact forces are the forces in action during the contacts between two bodies. For granular materials, these forces are normal forces, tangential friction forces and cohesive forces. The first ideas of contact forces in a granular material was brought by Charles Coulomb in 1773 with the idea of static friction (Coulomb, 1773). It is the exact phenomenon witnessed in Figure 1.8b: Coulomb conducted experiments on the collapse of sand piles and empirically identified two critical angles: the maximum stable angle or dynamic angle of repose, θ_m, and the static angle of repose, θ_r. When the slope of the sand pile reaches θ_m, the surface grains begin to slide, initiating an avalanche. This flow continues until the slope decreases to θ_r, at which point the pile stabilizes and motion stops. The existence of these different angles in granular material is due to the force chains in granular materials. Indeed, rather than being shared uniformly, forces are conducted along networks of grains in contact (Travers et al., 1987; Radjai et al., 1999; Majmudar and Behringer, 2005; Peters et al., 2005; Zuriguel et al., 2007). The structure of these networks depend on the spatial arrangement, packing and shapes of each individual grains in the granular material.

Although some granular materials are composed of dry grains only interacting through frictional contact, granular systems are often more complex. They involve cohesive interactions or even viscous forces. Cohesion may result from van der Waals forces, which originate from the forces between the molecules that constitute the particles of the granular material (Castellanos, 2005; Li, 2006), electrostatic interactions if the particles are charged, geometric cohesion caused by interlocking or the presence of a wet medium forming capillary bridges between grains (Bocquet et al., 2002). Cohesion will highly modify the flow property of granular materials. Cohesion is also closely linked to shear resistance in granular flows: for small cohesion, the friction between grains is enhanced leading to fewer sliding contacts because particles are more likely to stick with cohesion, without forming clumps (Rognon et al., 2008). As cohesion grows, grain agglomeration causes greater heterogeneity (more voids between grain clumps), which enhances shear resistance. Finally, at very high cohesion, the granular material breaks apart because strong clumps of particles are formed, and even if cohesion is strong enough to form these clumps, it is not strong enough to keep different clumps as a granular material as the material is flowing (Rognon et al., 2008).

In regolith, the largest contributor to cohesion is the van des Waals force F_c. It can be expressed as:

$$F_c = \frac{A}{48(t+d)^2} r_{eff} \tag{1.2}$$

with A the Hamaker constant, a physical constant defined for van der Waals interaction between two bodies, t the minimum distance between the particles surfaces, d the actual distance between the particles surfaces and r_{eff} the effective radius of the two particles (Perko et al., 2001). This equation is simplified for planetary application(Perko et al., 2001; Scheeres et al., 2010) :

$$F_c = \frac{AS^2}{48\Omega^2} r_{eff} \tag{1.3}$$

with the introduction of the cleanliness factor S, a parameter to quantitatively describe the variations of adsorption thicknesses of soil particles and Ω the diameter of an oxygen ion.

Cohesive forces can also be electrostatic forces if the particles are charged. In contrast with van der Walls forces, electrostatic forces can be effective at longer distance, however regolith needs to be charged by solar winds or other electrostatic phenomena, making the impact of these forces location dependant (Scheeres et al., 2010; Wang et al., 2016; Hartzell and Carter, 2017).

At first glance, cohesive forces, such as the van der Waals forces described in equations 1.2 and 1.3, appear to be independent of gravity. However the ratio between attractive forces and gravitational forces (i.e. particle weight) actually has a crucial role. When gravity is reduced, cohesive forces become increasingly dominant in the system as the weight of the material is reduced. This relationship is emphasized by the granular Bond number (Nase et al., 2001), the ratio between the inter-particle cohesive force F_c and the weight of the particle W:

$$B_o = \frac{F_c}{W} \tag{1.4}$$

The granular Bond number will thus indicate whether the granular system if gravity dominated ($B_o < 1$) or cohesion-dominated ($B_o > 1$).

The shape of particles plays also a crucial role in the mechanical and flow properties of a granular material. Granular materials such as sand, regolith, or even pharmaceutical powders consist of irregular, angular, or elongated particles. These non-spherical shapes influence how particles interlock, pack, and transmit forces, affecting properties like friction,

density, or flowability. Notably, the morphology of regolith particles is closely linked to the processes that shape planetary surfaces, leaving morphological marks at scales from nm to km (Viles, 2001). Such processes include impacts (Hörz, 1977; Housen et al., 1979; Ballouz et al., 2020), thermal processing (Dombard et al., 2010; Delbo et al., 2014, 2022; Lucchetti et al., 2024), or weathering and erosion in the presence of an atmosphere and hydrological processes (Ehlmann et al., 2008). The shapes of particles also gave insights into the history and physical properties of planetary surfaces such as comet 67P/Churyumov-Gerasimenko (Cambianica et al., 2019) or asteroid (101955) Bennu (DellaGiustina et al., 2019) and the shapes of boulders at the surface of Mars was consistent with the known history of its surface (Yingst et al., 2007). Sometimes, the shape can even give insights into the history and physical properties of the whole body, for example with asteroids, for which it's possible to make hypotheses on their formations through the shapes of the boulders constituting them (Michikami et al., 2008, 2010, 2019; Michikami and Hagermann, 2021; Robin et al., 2024).

These different parameters change the inter-particle behaviours, but these changes impact the granular material as a whole.

Bulk properties

As explained earlier with the study of Rognon et al. (2008), granular materials are able to resist shear thanks to friction and cohesion between individual particles (Terzaghi and Peck, 1954). The resistance to shear or shear strength of a granular material is thus strongly linked to the shape, size, size distribution, friction, spatial arrangement and confining pressure of the grains in the system. For example, the shape of particles has been shown to influence the shear strength of granular materials, with rounder particles generally leading to weaker materials (Santamarina and Cho, 2004; Cho et al., 2006; Yang and Wei, 2012; Yang and Luo, 2015; Suh et al., 2017; Kim et al., 2019), and as explained earlier, inter-particle cohesion can also change how the friction between particles occurs (Rognon et al., 2008).

Quantitatively, the overall strength of a granular material is given by the Mohr-Coulomb failure criterion (Coulomb, 1776):

$$\tau = \sigma \tan\theta + c \tag{1.5}$$

linking the shear strength with the the internal friction angle θ and the bulk cohesion c of the material. In this equation (1.5), τ is the maximum shear stress that the material can endure before failing under a given normal stress σ. The internal friction angle θ is linked with the coefficient of friction μ such that $\mu = \tan\theta$. Thus, the main bulk parameters used

to describe granular materials are the angle of internal friction and the bulk cohesion.

In environments where gravity is weak, such as the surfaces of small bodies, cohesive interactions become increasingly important and can dominate as we saw with the Bond number (Eq. 1.4. Indeed, at the surfaces of small-bodies, cohesive forces, originating from Van der Walls forces (Scheeres et al., 2010), may increases the strength of the regolith, and even the overall asteroid strength preventing disruption from rotation-induced centrifugal forces (Holsapple, 2007). These forces also enable finer particles to remain coupled with the surface of these bodies (Wang et al., 2016; DellaGiustina et al., 2019), and also enable smaller particles to act as a cement between larger particles (Scheeres et al., 2010).

Cohesion is thus a key factor in understanding the behaviour of regolith and granular materials in general, even if recent small bodies missions suggest that some asteroids may be nearly cohesionless (cohesion < 1 Pa), like asteroids Ryugu, Bennu or Dimorphos (Barnouin et al., 2019; Arakawa et al., 2020; Raducan et al., 2024).

1.2.3 Investigating granular behaviours in low gravity

Studying granular materials in low gravity involves a combination of experimental, computational, and in-situ approaches. Laboratory experiments on parabolic flights, drop towers, suborbital rockets, or on the International Space Station (ISS) provide brief periods to continuous microgravity to directly observe granular behaviour under reduced gravitational forces. Numerical simulations, such as discrete element methods (DEM), allow researchers to model grain interactions and system dynamics over longer timescales and varied conditions, offering insights not easily accessible through physical experiments. Finally, in-situ investigations conducted aboard space missions or planetary explorations enable studies in microgravity or low-gravity environments, supplying valuable data on granular mechanics in extraterrestrial settings. Together, these methods lead to a comprehensive understanding of how granular materials behave beyond Earth.

Laboratory experiments

To investigate granular behaviour under low gravity, a variety of experimental platforms are employed, each offering different durations and conditions of microgravity. Classical drop towers, consisting of a free-falling capsule, allow reduced gravity for a few seconds, useful for simple and short interactions such as low-velocity impacts (Brisset et al., 2020; Guo et al., 2024) enabling to improve our understanding on interactions between various objects, either

natural or human-made, and regolith. While these type of drop towers allow a few tests per day, active drop towers allow more repeatability, in smaller towers with a continuously accelerated capsule (Könemann et al., 2015; Gierse et al., 2017; Gautier et al., 2020). Low velocity impacts experiments were also performed in the space shuttle (Colwell and Taylor, 1999), parabolic flights (Colwell et al., 2008; Kobayashi et al., 2009; Colwell et al., 2017; Moore et al., 2022) or with magnetic-induced gravity (Mo et al., 2019).

Granular material experiments have also been made in the ISS, notably the ARISE experiment, a vibrating container filled with glass beads (Steinpilz et al., 2019), and an experimental study investigated granular flow under long-duration artificial gravity using a centrifuge (Ozaki et al., 2023).

Rover driving experiences have also been performed, however it is more difficult to study driving in a reduced-gravity environment as the time scales needed are longer. A first approach, without actually reducing gravity, has been to build a single wheel test rig in Earth gravity with low loading tests to simulate the reduced gravitational conditions (Ding et al., 2013; Takehana et al., 2025). However, only the weight of the wheel is reduced, and the granular material remains at earth gravity which has been shown to be misleading thanks to a numerical study (Hu et al., 2025).

Numerical simulations

Complementing experiments, numerical simulations provide a powerful tool to explore granular dynamics with high control and repeatability. Notably, thanks to powerful computing, it's possible to simulate complete granular material, particle by particle using DEM simulations. All the experiments that can be done in laboratory such as piling and rotating drum tests in reduced gravity can be simulated (e.g. Richard and Taberlet, 2008; Sunday et al., 2020; Zhu et al., 2023; Kumar et al., 2024). Notably, wheel simulations have been carried out in 2D (Nakashima et al., 2010) and 3D (e.g. Schäfer et al., 2010; Knuth et al., 2012; Taheri et al., 2015; Zhang et al., 2020; Sunday, 2022; Zhang et al., 2025) to investigate wheel-regolith interactions in reduced gravity environments. In the same manner, simulations of wheel driving on an inclined bed have been made to scale other dimensionless numbers, taking into account gravity, slope and other characteristic lengths (Zhang et al., 2020; Hu et al., 2024). DEM simulations also make it possible to simulate a whole rubble-pile asteroid and, for example, test its resistance to rotational failure (Zhang et al., 2018; Sánchez and Scheeres, 2020). Finally, low-speed impacts have also been investigated through DEM simulations under microgravity conditions (e.g. Çelik et al., 2022).

In-situ study

Direct observations from space missions offer valuable data by studying granular materials in an in-situ low-gravity environment. In the following paragraph, I will focus on small-body missions as it is the main topic of this thesis.
As previously stated in Sect.1.1.3, several interactions with small-bodies during space exploration missions allowed to learn more about regolith in low-gravity environments, during missions such as the Hayabusa mission (Fujiwara et al., 2006), the Rosetta mission with the Philae lander (Glassmeier et al., 2007), the Deep Impact mission (Blume, 2005), the Hayabusa2 mission with the Mascot lander and the MINERVA-II-1A and -1B hopping rovers (Watanabe et al., 2017, 2019), the OSIRIS-Rex mission (Lauretta et al., 2017) and most recently the DART mission (Rivkin et al., 2021; Daly et al., 2023).

Findings from low-gravity studies on granular materials

After reviewing the various existing tools available for studying granular materials under low-gravity conditions, the following section will focus on experimental, numerical and in-situ observations of bulk behaviours of granular materials. The subjects of interest of this section are related to this thesis and will focus on bulk properties and strength of granular materials and their relationship with gravity, wheel-regolith interactions in reduced gravity or more generally granular behaviours in the scope of space exploration missions.

As stated in Sect. 1.2.2, the inter-particle properties of a granular material will affect the bulk properties of this material. Notably, if gravity is reduced, naturally, the normal forces between the particles will be reduced as their weight is reduced resulting in looser packing as well as lower friction forces between the particles. For example, several studies investigated the influence of gravity on the angle of repose and internal friction. Some reduced-gravity experiments conducted in parabolic flights have observed variations in the angle of repose of granular materials with gravity (Klein and White, 1990; Kleinhans et al., 2011). However, in Klein and White (1990), the dynamic angle of repose (θ_m) is studied, and it is found to increase as gravity decrease. On the other hand, Kleinhans et al. (2011) observed that the static angle of repose (θ_r) increases about 5° whereas the dynamic angle of repose (θ_m) decreases with about 10° as gravity decreases. Kleinhans et al. (2011) also described the parabolic flights experiments by Klein and White (1990) as "poorly controlled". However, more recent experimental and simulation studies have found that reduced gravity has minimal or no impact on the angle of repose (Marshall et al., 2018; Chen et al., 2019; Karapiperis et al., 2020). Moreover, it has been observed that the angle of internal friction may slightly

increase as gravity decreases (Marshall et al., 2018; Karapiperis et al., 2020). The actual effect of gravity on the different angles characterising granular materials is thus still poorly understood and under debate as gravity affects numerous inter-particle parameters.

However, low-velocity impact experiments have shown that, under low-gravity conditions, the reduced quasi-static regime of granular materials leads to lower strength, resulting in decreased resistance to penetration and increased penetration depths (Murdoch et al., 2017, 2021). Loading tests have also revealed that, for some surfaces, gravity strongly influences the bearing capacity (Kobayashi et al., 2009), and that penetration resistance increases with gravity in the case of cohesionless materials (Mo et al., 2019). It means that for space exploration missions or interactions of objects with regolith, penetration will be enhanced compared to expectation, or unexpected, as it has often been the case with missions that performed surface interactions (see Sect. 1.1.3).

Supported by DEM simulations, hourglass granular flow experiments aboard the ISS have shown consistency between different gravity conditions and revealed that the mass flow rate decreases with gravity due to reduced bulk density: this highlights the need to adjust bulk density in low-gravity simulations to improve the accuracy of lander and rover design (Ozaki et al., 2023). Similarly, simulated rotating drum tests have demonstrated that comparable flow patterns occur at Earth and reduced-gravity levels when the drum rotation speed and gravity level are scaled according to the same Froude number (Sunday et al., 2020), a dimensionless number defined as the ratio between the flow inertia and the gravity.

Finally, mobility studies have provided further insight into the mechanical response of granular materials. A single-wheel experiment performed during parabolic flight revealed that reduced gravity increases wheel slippage but does not significantly influence wheel sinkage. This behaviour arises because lower gravity reduces wheel loads and enhances regolith flowability, whereas the opposite occurs under higher gravity, cancelling out these effects (Kobayashi et al., 2010). Consistently, simulated sinking and driving experiments have shown that both a projectile's penetration depth and collision duration, as well as a wheel's driving performance, are independent of gravity when equivalent Froude numbers are considered (Sunday, 2022). Regarding rover of wheel laboratory experiments, only the weight of the wheel is reduce. However, it is important to note that in low-gravity environments, the effect of cohesion compared to gravity is amplified, and at the same time, the regolith is more likely to fluidize under wheel movement, similar to low-velocity granular impacts where fluidisation is enhanced under low-gravity (Murdoch et al., 2017).

1.3 Phobos, Deimos and the Martian Moon eXploration Mission (MMX)

Now that I have introduced regolith and some of its interesting behaviour, I will focus on Phobos and Deimos, the moons of Mars. Indeed, the objectives of this thesis that will be presented at the end of this introduction are centred on the Japan Aerospace Exploration Agency (JAXA) Martian Moon eXploration Mission (MMX) that will be launched in 2026, with the aim of returning a sample from Phobos. This mission as well as how this thesis align with the science objectives of the mission will also be presented in this section.

1.3.1 Exploration of the moons of Mars

Three natural satellites orbit a terrestrial planet in the Solar System: the Moon, Phobos and Deimos, the latter two orbiting Mars. Phobos and Deimos are small, airless bodies that share many similarities with larger asteroids as I will discuss below.

Phobos and Deimos were both discovered in 1877 by astronomer Asaph Hall. It is not until 1971, nearly 100 years later, that the NASA Mariner 9 spacecraft took the first pictures of Phobos at a distance of 5500 km as well as the first pictures of Deimos. Then NASA Viking 1, in 1977, which was more dedicated to the study of Phobos, made a flyby of it at a distance of 90 km. Thanks to these high-quality images of Phobos (Figure 1.9a), the satellite was found to be smaller than estimated after the Mariner 9 mission (5200 km^3 against 5700 km^3) (Carr et al., 1980). The Viking 2 mission then approached several times Deimos in 1977, up to a distance of 22 km. Phobos and Deimos were then partly studied by different exploration missions focused on Mars, such as the NASA Mars Global Surveyor mission launched in 1996 (Albee et al., 1998), the ESA Mars Express mission launched in 2003 (Oberst et al., 2006) and most recently by the NASA Mars Reconnaissance Orbiter mission launched in 2005 (Thomas et al., 2011), which took high resolution images of Phobos and Deimos (see Phobos on Figure 1.9b).

The first Phobos-dedicated space program was the Phobos program in 1988, led by the Soviet Union, with the Phobos 1 and Phobos 2 missions. However, the first spacecraft, Phobos 1 was lost on its way to Mars when the end-of-mission order was sent to the spacecraft after a computer malfunction. The second spacecraft, Phobos 2, launched a few days after Phobos 1, was able to travel to Mars and captured 37 images of Phobos with a resolution of up to 40 m/px between February and March 1989. Unfortunately, in March 1989, communications with the spacecraft were lost when it was 50 m above Phobos' surface and released 2 landers, whose fate is unknown.

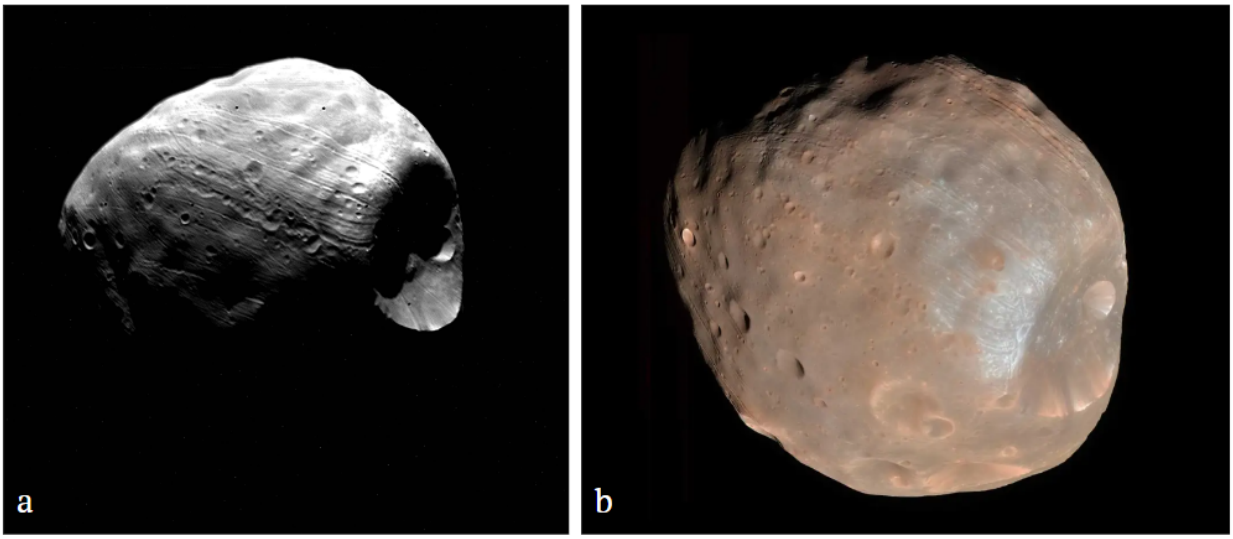

Figure 1.9: a) One of the first high resolution image of the Martian satellite Phobos captured by the Viking 1 Orbiter. b) Recent picture of Phobos captured by NASA's High Resolution Imaging Science Experiment (HiRISE) camera on the Mars Reconnaissance Orbiter. Phobos is around 20 km across in these images. Photo credits: NASA/JPL

The last launched mission to study Phobos was the Roscosmos (The Russian Space Agency) Phobos-Grunt mission, in collaboration with the Centre National d'Etudes Spatiales (CNES). It was supposed to perform a sample return from Phobos (Marov et al., 2004). However, after its launch in 2011, the spacecraft was never able to leave Earth's orbit and was recovered a few months later in the pacific ocean.

It is only in 2020, almost 10 years after the failure of the Phobos-Grunt mission, that the JAXA Martian Moon eXploration (MMX) mission entered its development phase, in collaboration with CNES and others, with a first launch scheduled in 2024. Today, the launch is now expected in November 2026.

1.3.2 Phobos and Deimos, the moons of Mars

The data of Phobos and Deimos collected through the numerous observations made by the missions previously cited helped to build shape models and maps (see Figure 1.10), as well as estimates of their size, density, gravity, and orbital characteristics (see Table 1.1) amongst many other parameters.

Observations of Phobos have also made it possible to begin determining the nature of its

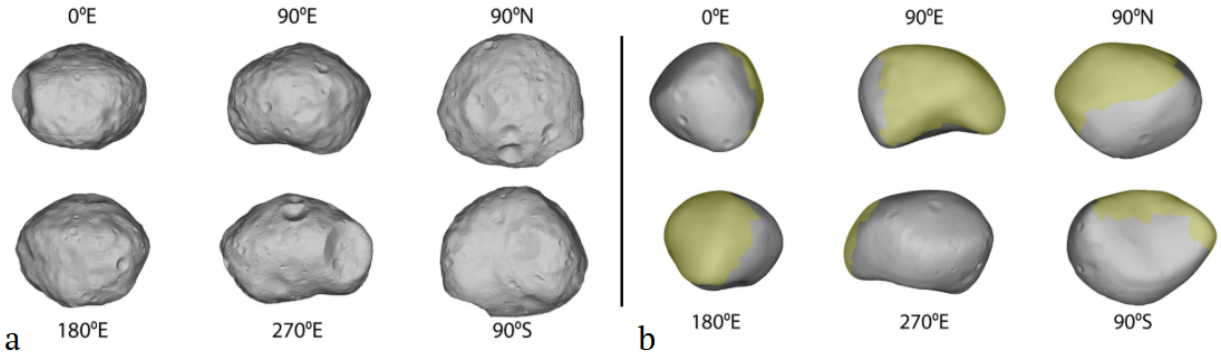

Figure 1.10: Shape models of Phobos and Deimos. a) Shape model of Phobos seen along the axes, rendered without albedo. b) Shape model of Deimos seen along the axes, rendered without albedo. The yellow areas are the poorly constrained zones. Positions at 0E correspond to the sub-Mars points of the moons. Figures and shapes models from Ernst et al. (2023).

Parameter	Phobos	Deimos	Reference
Size (km)	$26.06 \times 22.80 \times 18.28$	$15.0 \times 12.2 \times 10.4$	[1, 2]
Average Radius (km)	11.08 ± 0.04	6.27 ± 0.07	[3]
Bulk Density ($kg.m^{-3}$)	1861 ± 11	1465 ± 51	[3]
Surface gravity ($m.s^{-2}$)	$3 - 7 \times 10^{-3}$	2×10^{-3}	[4]
Geometric Albedo	0.071 ± 0.012	0.068 ± 0.007	[5,6]
Orbital period (h)	7.66	30.3	[7]
Orbital semimajor axis (Mars radius)	2.76	6.92	[8]
Orbital eccentricity	0.0151	0.0003	[8]
Orbital inclination (deg)	1.093	0.93	[8]

References: [1] Willner et al. (2014), [2] Thomas (1993), [3] Ernst et al. (2023), [4] Jacobson (2010), [5] Simonelli et al. (1998), [6] Thomas et al. (1996), [7] Murchie et al. (2015), [8] JPL database of Solar System Dynamics (SSD), https: ssd.jpl.nasa.gov/sats/

Table 1.1: Main properties estimations of Phobos and Deimos. Adapted from Sunday (2022).

regolith, however, it is still poorly constrained. Notably, the grain size was initially estimated to average the range of 50-100 μm based on thermal inertia measurements (Lunine et al., 1982) but a later analysis using a new method with the same data, suggested an average size up to 2 mm (Gundlach and Blum, 2013). However, this result does not exclude the presence of smaller particles at the surface of Phobos. Given its close proximity to Mars and the potential for material redistribution from micrometeoritic impacts, Phobos may be covered by a fine dust layer, or small grains, greater than 300 μm in size (Ramsley and Head, 2013; Miyamoto et al., 2021). This fine dust layer may be composed of Mars ejecta, with a bulk concentration of $\approx$ 250ppm of Mars ejecta fragments in the upper $0.4 - 1.0$m of Phobos' regolith (Ramsley and Head, 2013). Indeed, a shortage of particles smaller than 300 μm on the surface of Phobos has been suggested, as these particles are especially sensitive to changes in orbital eccentricity: if they do not re-impact Phobos shortly after ejection, they are lost to interplanetary space or drift into the Martian atmosphere (Ramsley and Head, 2013; Basilevsky et al., 2014). In conclusion, the regolith of Phobos is thought to contain particles in the $300\mu m - 2mm$ range, with a small concentration of Mars ejecta in its upper-layer.

Numerous spectral data of both Phobos and Deimos has also been collected through the numerous missions that observed these bodies. These spectral data highlighted the mystery around the debated origin of Phobos and Deimos. First, to understand this debate, a quick introduction to asteroid spectral classes is needed: this taxonomic system has been implemented in 1975 for asteroids based on their colour, albedo and spectral shape. The categories were C-types for dark carbonaceous asteroids, S-types for siliceous asteroids and U-types for others that did not fit in C- or S-types asteroids (Chapman et al., 1975). Today, 3 main taxonomies are used. The Tholen classification (Tholen, 1984), covering observations of asteroids in the 0.3-1 μm range with albedo measurements. Then, the taxonomy from DeMeo et al. (2009), does not take in account albedo but covers a wider wavelength range, from 0.45 to 2.45 μm. Finally, the most recent asteroid taxonomy was proposed in Mahlke et al. (2022), taking in account different wavelength coverage, in the visible and near-infrared, and the albedo. With these new classifications, other subtypes were identified such as the D-type asteroids, corresponding to dark objects observed from the outer rim of the main belt to the Trojans of Jupiter (Tholen, 1984). T-types asteroids are also dark objects but mostly found in the inner parts of the main belt(Tholen, 1984). M-type asteroids are metal rich asteroids mostly found in the main belt, just like P-type asteroids, but with more albedo (Tholen, 1984). Finally, another relevant subtype for Phobos spectroscopy is the Z-type, also corresponding to dark objects but likely formed far from the sun (**?**).

Phobos is thus a relatively small body that was thought to have a carbonaceous chondritic [2] composition from its low albedo and spectral data from the Mariner 9 and both Viking missions. Phobos is presenting a red and a blue unit, respectively similar to class D- and T-type asteroids (Pang et al., 1978; Pollack et al., 1978). D-types asteroids are characterised by a low albedo and relatively featureless spectrum and a very steep red slope and T-types asteroids are also characterised by a low albedo but a moderately reddish shortward of 0.75 μm and flat afterward (Cellino et al., 2002). More recently, the red unit spectrum is similar to a D- or Z-type asteroid, whereas the blue unit is similar to the spectra of an M- or P-type asteroid (Fraeman et al., 2012; Pajola et al., 2012).

After the flyby by the Viking 1 spacecraft, it was theorized that Phobos was formed in the outer part of the asteroid belt (Tolson et al., 1978) and, later on, was gravitationally captured by Mars in the early stages of the Solar System (Hunten, 1979). Thus, Phobos was considered to be like an asteroid. For example, features such as its grooves (visible on Figure 1.9a) were predicted to be common on the surface of small bodies (Thomas and Veverka, 1979).

However, the lack of detectable amounts of hydrated minerals was inconsistent with an origin for Phobos and Deimos in the outer asteroid belt (Rivkin et al., 2002). Moreover, Phobos' near-equatorial orbit and Deimos' near-circular orbit challenge the gravitational capture scenario (Rosenblatt, 2011). But these theories do not yet completely invalidate the captured asteroids theory as recent spectral analysis of Deimos showed similarities between the two moons of Mars, highlighting that Phobos and Deimos may have rather originated from one or two captured asteroids from the inner main belt (Wargnier et al., 2025).

More recently, the hypothesis that Phobos and Deimos originated from a giant impact event is gaining popularity, where both Phobos and Deimos were created from the disruption of a parent body during a giant impact (Burns, 1992; Craddock, 2011; Bagheri et al., 2021).

The last alternative theory for the formation of Phobos and Deimos is an in situ formation, at the same time as Mars, by co-accretion around the planet (Rosenblatt, 2011). However, a precise chemical evaluation of these moons, and particularly of returned samples, is necessary to draw further conclusions. For example, Pignatale et al. (2018) conducted a study using thermodynamic equilibrium and investigate the composition of dust and solids that could

[2] Chondrites are thought to represent the original material from which the planets of the Solar System were formed

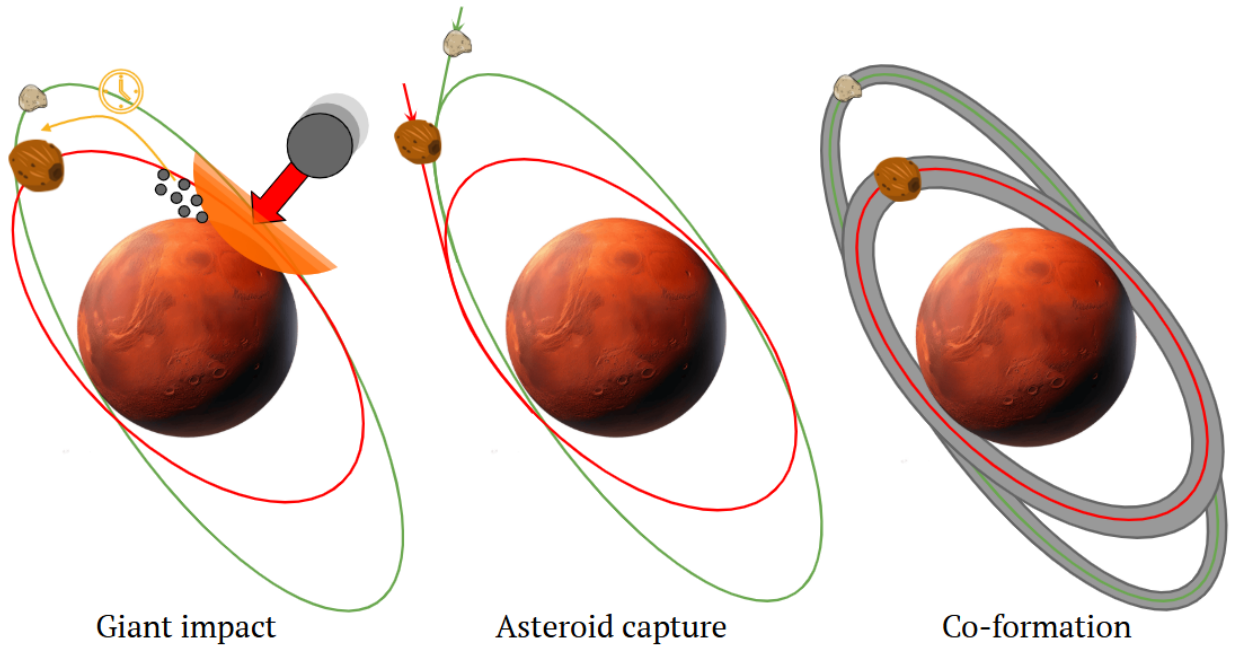

Figure 1.11: Schematic representation of the three main formation hypotheses for Phobos and Deimos: giant impact with re-accretion after disruption, gravitational capture of two asteroids migrating across the Solar System, and Phobos-Deimos-Mars co-formation. Not to scale.

result from different Mars impactors. Their calculations showed distinct results between the different chemical compositions of solid and dust depending on the impactor and if the chemical composition of the moons of Mars could fit their model, it could favour the giant impact theory.

A schematic summary of these 3 scenarios is provided in Figure 1.11.

Unravelling the origin of the Martian moons is of high scientific value, as each formation scenario offers insights into material transport in our Solar System. On the one hand, if the captured asteroid hypothesis is correct, the moons' surface compositions should include chondrites, interplanetary dust particles, or material indicative of either the inner or outer Solar System, depending on their provenance (Usui et al., 2020). On the other hand, if the moons formed as a result of a giant impact on Mars, their surfaces should exhibit signatures of high-temperature impact processes and include material similar to that found on Mars itself (Usui et al., 2020). Finally, if Phobos and Deimos would have been formed in-situ by co-accretion with Mars, the moons would exhibit a bulk chemistry similar to the chondritic bulk Mars (Usui et al., 2020).

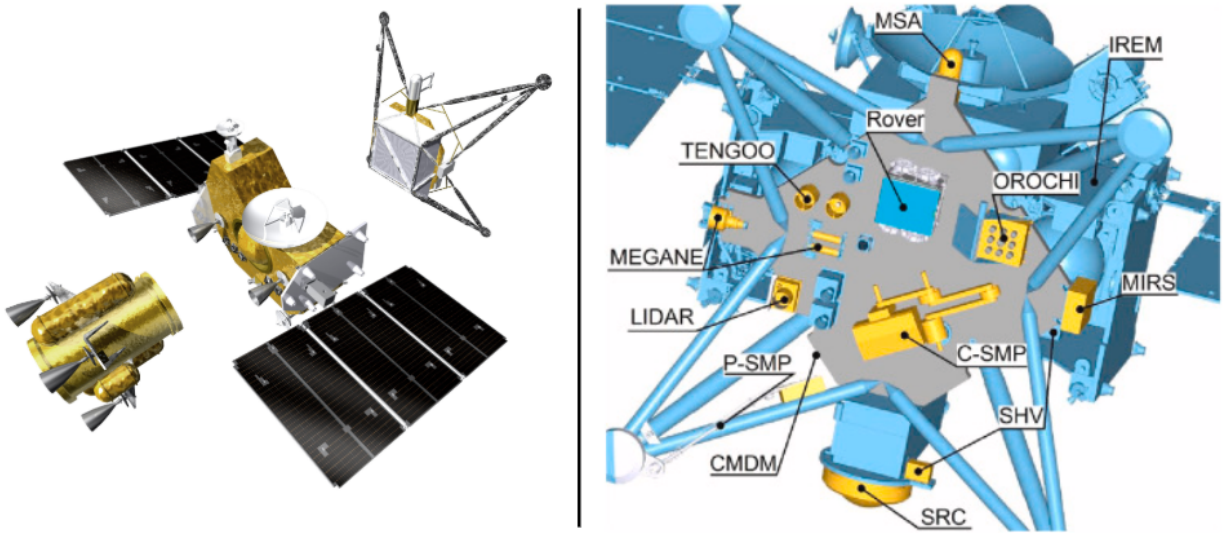

Figure 1.12: Design of the MMX spacecraft. Left: from left to right: the propulsion module, the return module and the exploration module. Figure provided by JAXA for Kuramoto et al. (2022). Right: Mission instruments installation aboard the exploration module. Figure from Kawakatsu et al. (2023).

To test these hypotheses and answer these questions, close observations, *in situ* exploration and sample return from the surface of Phobos would enable precise chemical analysis and many other insights on Mars' moons. These are the primary objectives of the JAXA MMX mission (Kuramoto et al., 2022).

1.3.3 The JAXA MMX Mission

The Japan Aerospace Exploration Agency (JAXA) will launch the Martian Moon eXploration (MMX) spacecraft in 2026, with the goal of returning a sample from the martian moon Phobos. Phobos was selected over Deimos because of its greater spectral diversity, its presumed content of Martian ejecta at its surface, and the availability of more images provided by previous missions. These factors make Phobos both the most scientifically interesting and the least challenging of Mars' moons to explore. The primary science objectives of the mission are to explore and understand the origins of Phobos and Deimos, in order to constrain the processes of planetary formation and material transport in the Solar System. One of the other objectives is also to deepen our understanding of Mars' history and the mechanisms behind the evolution of Mars and its moons (Kuramoto et al., 2022).

In order to answer these questions, the MMX spacecraft (Figure 1.12) will study Phobos and

Deimos with a package of scientific instruments, which will also help to select and characterize a sampling site in terms of safety for landing, geologic context, and representativeness with respect to Phobos. These instruments and their roles are as follows (from Kuramoto et al., 2022):

LIDAR (Light Detection And Ranging), a laser altimeter designed to characterize the geologic structures on the surface of Phobos and Deimos, provided by the Planetary Exploration Research Center (PERC) in Chiba, Japan (Senshu et al., 2021).

TENGOO (TElescopic Nadir imager for GeOmOrphology), a telescopic camera designed for the same purposes as the LIDAR and to perform observations of H_2O and dust circulation in the Martian climate, provided by the Institute of Space and Astronomical Science (ISAS)/JAXA in Tokyo, Japan (Kameda et al., 2021).

OROCHI (Optical RadiOmeter composed of CHromatic Imagers), a wide-angle multiband camera designed to determine the global surface composition of Phobos, and also to participate in the observations of the Martian climate, provided by the Institute of Space and Astronomical Science (ISAS)/JAXA in Tokyo, Japan (Kameda et al., 2021).

MIRS (MMX InfraRed Spectrometer), an infrared spectrometer designed to determine the global surface composition of Phobos and Deimos, and observe the Martian climate, provided by the Laboratoire d'Instrumentation et de Recherche en Astrophysique (LIRA) in Meudon, France (Barucci et al., 2021, 2025).

MEGANE (Mars-moon Exploration with GAmma rays and NEutrons), a gamma spectrometer designed to determine the global surface composition of Phobos and Deimos, provided by the Johns Hopkins University Applied Physics Laboratory (APL), in Laurel, Md, USA (Lawrence et al., 2019; Lawrence, 2025).

MSA (Mass Spectrum Analyzer), a mass spectrometer designed to determine the global surface composition of Phobos and Deimos, and to search for gas torus and escaping Martian atmosphere, provided by Osaka University, in Osaka, Japan (Yokota et al., 2021, 2025).

CMDM (Circum-Martian Dust Monitor dust counter), a dust counter designed to detect dust flux and ring to reveal the weathering process on Phobos' and Deimos' surface by micro-meteoroid bombardments, provided by the PERC in Chiba, Japan (Kobayashi et al., 2018, 2024).

Idefix (MMX Rover), a solar-powered rover designed to perform in situ measurements of mineralogy and physical properties on the surface of Phobos, while also serving as a

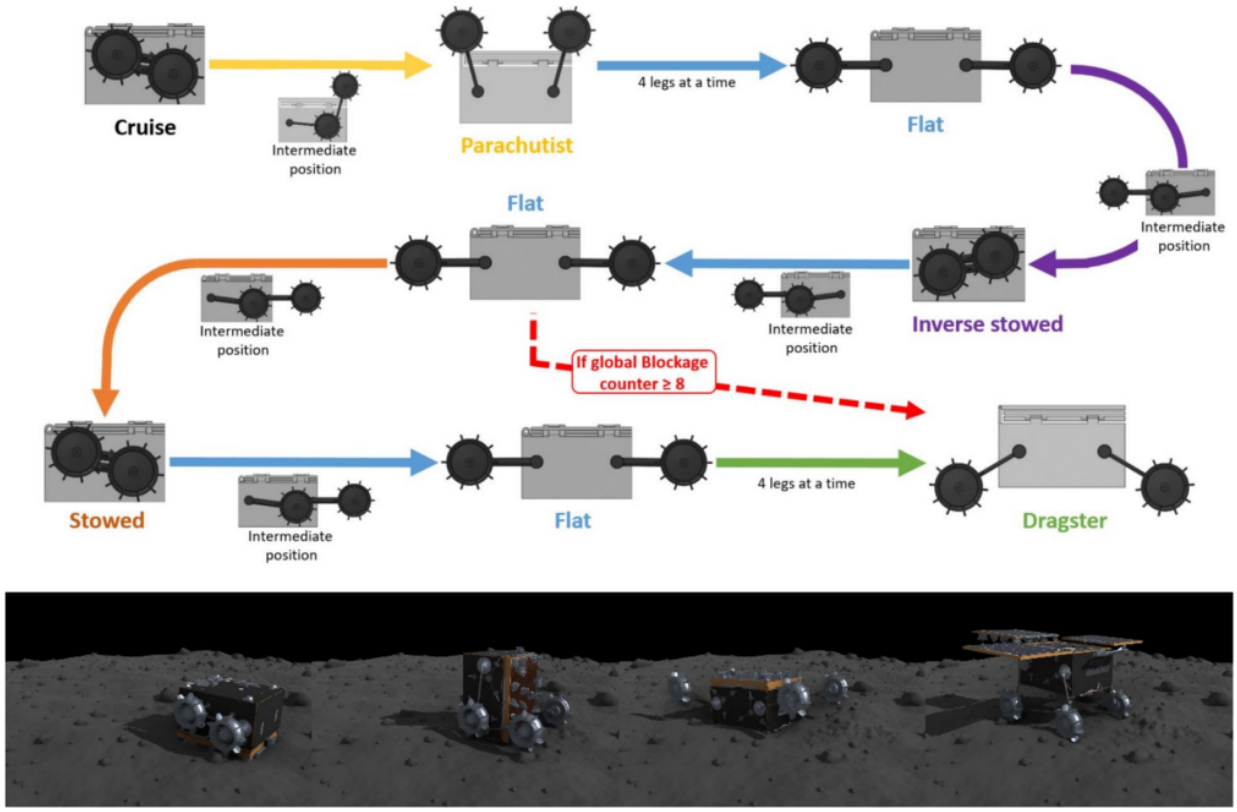

Figure 1.13: (Top) Schematic illustrating the sequences of the MMX rover self up-righting strategy (Bottom) Impression of the rover in a simulated environment. From Ulamec et al. (2025).

technical demonstration of roving capabilities in a low-gravity environment, provided by CNES in France and DLR in Germany (Michel et al., 2022b; Ulamec et al., 2025).

Within the scope of this thesis, the primary instrument of interest is the MMX rover Idefix, developed and manufactured by the Centre National d'Études Spatiales (CNES) and the German Aerospace Center (DLR). As previously stated, it is intended to conduct *in situ* experiments on the surface of Phobos as a technical demonstrator and to serve as a scout for the landing and sampling site selection during the MMX mission.

The MMX rover: Idefix and the WheelCAMs

The rover is scheduled to be deployed onto the surface of Phobos during a landing rehearsal of the spacecraft. Separation of the rover will occur when the spacecraft reaches a nominal altitude of 40 meters above the surface. Following release, the rover will free fall, bounce and finally unfold itself. (Ulamec et al. (2025), see Figure 1.13.)

The MMX rover Idefix is tasked to provide data on the regolith properties thanks to scientific instruments that will deliver high-resolution images, measurements of the thermal properties, and Raman spectroscopy (Michel et al., 2022b). Figure 1.14 provides different views of the rover and the positions of the instruments. The instruments are the following:

NavCams NavCams are a stereo pair of navigation cameras with the aim to study to the origin of the colour dichotomy, the nature of space weathering processes, and the dust transport and exogenous contamination at the surface of Phobos. The instrument is a contribution from CNES and the scientific leadership is provided by the Laboratoire d'Astrophysique de Marseille, France (Vernazza et al., 2025).

WheelCams WheelCams are 2 cameras placed inside the rover, each looking at a different wheel of the rover. They aim to study the surface properties of Phobos, as well as the regolith behaviour on small-bodies and rover mobility in low-gravity. The WheelCams are a contribution from CNES and the scientific leadership is provided by ISAE-Supaero, in Toulouse, France (Murdoch et al., 2025).

Rax Rax is a Raman spectrometer to determine the minerals on the surface of Phobos. The scientific aim is to address the question of Phobos' origin, heterogeneity, and the material transport around Mars. The instrument was developed by DLR, the Instituto Nacional de Técnica Aeroespacial (INTA), the University of Valladolid, Spain (UVa) and The University of Tokyo, JAXA, and Rikkyo University, Japan (Cho et al., 2021)

miniRAD miniRAD is a multispectral instrument measuring the infrared radiative flux in 6 different wavelengths. Its main objective is to determine Phobos' surface brightness temperature during nighttime in order to derive the thermal inertia of the surface. MiniRAD is a contribution of DLR and the scientific leadership is provided by DLR, Berlin, Germany (Knollenberg et al., 2025).

As stated earlier, the rover is a technical demonstrator and aims to validate the capability of roving on the surface of small bodies, where the gravity is very low. Unlike previous *in situ* missions to small-bodies, which only involved touch-and-go interactions, static landers or hopping rovers (see Sect. 1.1.3), this will be the first demonstration of wheeled roving in a low-gravity environment. It is, therefore, very important to characterize and understand the behaviour of the regolith in interaction with the wheels of the MMX rover Idefix, a task specifically intended for the WheelCams instrument.

This instrument consists of 2 cameras, aiming towards the wheels to provide high-resolution images of the interactions between the wheels and the regolith. The front WheelCam points

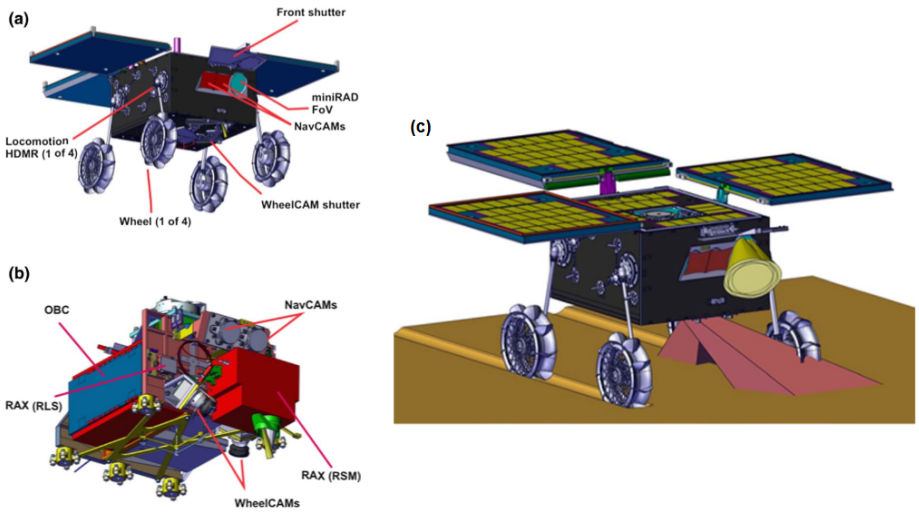

Figure 1.14: Different views of the MMX Rover Idefix. **a)** Rover in deployed configuration with the indicated positions of miniRAD, NavCams and the rear WheelCam. **b)** Internal compartment with indicated positions RAX, NavCams and WheelCams. RLS stands for Raman Laser Spectrometer and RSM for RAX Spectrometer Module. **c)** Idefix in the on-surface configuration. Field of views of miniRAD and WheelCAMs are displayed in yellow and red respectively. Figures provided by CNES originally for Michel et al. (2022b).

at the front left wheel as it drives through the pristine regolith, while the rear WheelCam monitors the rear left wheel as it follows the track left by the front wheel (FOVs in Figure 1.14c). The cameras are also equipped with LEDs: white LEDs, but also three different coloured LEDs, at 590, 720 and 880 nm to allow to perform relative reflectance and albedo analyses to help constrain the surface mineralogy of Phobos (Murdoch et al., 2025). Images of the WheelCams testbed and images generated from the testbed are provided in Figure 1.15, simulating what will be observed at the surface of Phobos by the WheelCams. The testbed is described in more detail in Section 2.4.
The scientific objectives of the WheelCams are defined as the following (from Murdoch et al., 2025):

1. **Determine the physical properties of the regolith particles.** The physical properties of the regolith particles will mainly be retrieved through the size and shape distribution of the regolith particles thanks to images retrieve at the surface of Phobos with the WheelCams. It will also be possible to detect and characterise regolith clumps to determine the inter-particle cohesion of the particles. Regolith stuck to the wheel or to the shutter of the cameras may also provide informations on the adhesion properties of these particles.

2. **Determine the bulk mechanical properties of the regolith.** Thanks to the

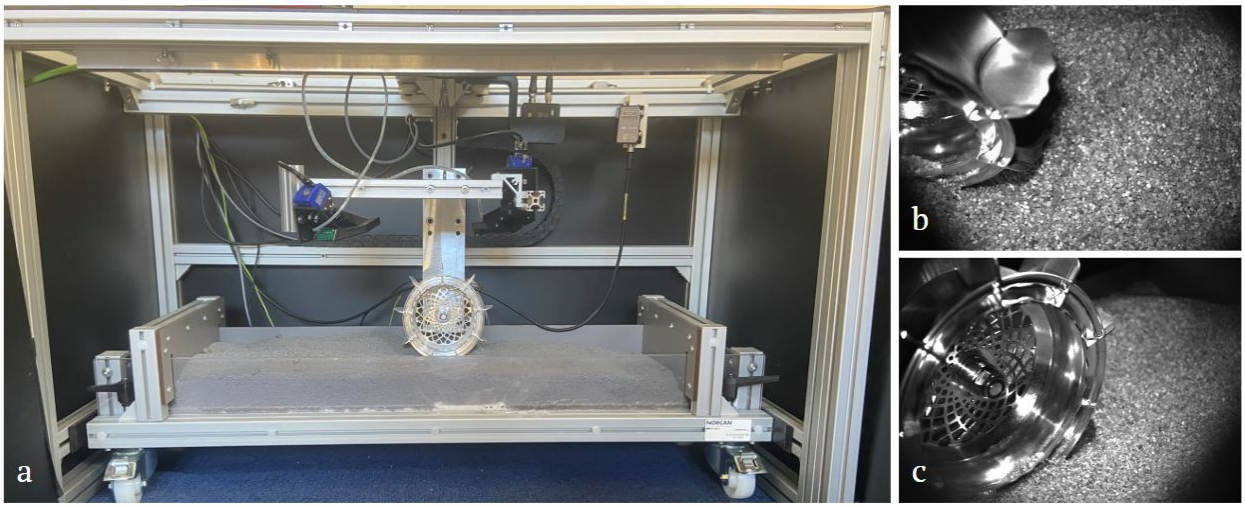

Figure 1.15: The single-wheel MMX WheelCam testbed. a) The WheelCam testbed. Image b) corresponds to the rear WheelCam perspective from the testbed and image c) corresponds to the front WheelCam perpective (Murdoch et al., 2025).

average particle angularity, a shape parameter, it is possible to infer the angle of friction of the regolith. It will also be possible to retrieve the bearing capacity of the regolith at the surface of Phobos from the wheel sinkage or from the trench depth made by the wheel. It will also be possible to retrieve the mechanical properties of the regolith, notably the angle of friction and the bulk cohesion, from the sinkage and slippage of the wheel while driving at the surface of Phobos, but also from the trench morphology left by the rover.

3. **Determine the dynamical behaviour of the regolith.** In addition to mechanical properties, determining wheel slip during driving will help to understand granular behaviour when set in motion. The wheels may also lift material, and the WheelCam images can be used to determine the motion of these particles. The design of the wheels also makes it possible that regolith may avalanche inside the wheel, that could analysed similarly to a rotating drum experiment.

4. **Observe possible layering in the shallow sub-surface.** The trench made by the wheels may reveal differences in textures, relative reflectance or albedo, both inside and outside of the trench, that could analysed by the WheelCams and its LEDs.

5. **Constrain the mineralogical composition of the surface material.** Relative reflectance and albedo analyses thanks to the images of the surface of Phobos under different illumination conditions made by the LEDs will help to constrain the mineralogical composition of Phobos' regolith.

6. **Assess space weathering.** Relative reflectance and albedo differences between the inside and the outside of the trenches formed by the wheels may indicate the effect of space weathering on the material at the surface of Phobos.

7. **Determine regolith geological classes.** Thanks to all the retrieved data and interpretations made, it will be possible to classify the different observed lithologies.

8. **Constrain the absolute local gravitational acceleration.** If particles of Phobos' regolith get ejected while driving, it would be possible to track their motion and determine their acceleration.

1.4 Thesis objectives and outline

The objective of this thesis is to support the scientific objectives **1.** and **2.** of the WheelCams: determining the physical properties of the regolith particles and the bulk mechanical properties of the regolith at the surface of Phobos.

In order to help achieve these objectives, I will first focus on objective **1.** of the WheelCams, I will present an image analysis pipeline developed during my thesis to analyse the shapes and size distribution of the individual particles and make further interpretations from these at the surface of Phobos thanks to the WheelCams images. This pipeline has notably been tested on images of several rubble-pile asteroids including the last image captured by the DART spacecraft before it intentionally impacted Dimorphos to change its orbit.

Next, in order to determine the bulk mechanical properties from wheel-surface interactions, we start from the work of Cecily Sunday (Sunday, 2022), who performed single wheel rolling simulations in DEM. However, the bulk properties are unknown in DEM. I will present how it is possible to go from simulated micro-parameters to bulk properties, that are measured in the laboratory or in-situ, thanks to shear tests simulations.

Finally, I will discuss the influence of inter-particle parameters on the bulk properties of granular material and the implication of these results regarding further interpretation regarding the surface of Phobos and the work that has been done by Cecily Sunday during her thesis.

Chapter 2

Morphologies of grains related to mechanicals properties of granular materials

In this first chapter, I will present the morphological analysis pipeline that was developed to be used on the images that will be captured by the WheelCams at the surface of Phobos. The pipeline first semi-automatically segments the observed boulders or particles, then extracts a range of morphological parameters from which physical properties or history of the regolith can be inferred. Notably, this pipeline has been used on the last image captured by the NASA Double Asteroid Redirection Test (DART) mission before slamming into the secondary asteroid of (65803) Didymos, hereby referred to as Dimorphos (Daly et al., 2023), and on images captured on other visited rubble-pile asteroids. These results are presented in this chapter and have been published in Robin et al. (2024).

2.1 Grain morphology: formation mechanisms and effects on mechanical behaviour in terrestrial and extraterrestrial environments

Morphology of particles and boulders is well known for recording the effects of sorting or abrasion, whether due to the environment or to formation mechanisms (Krumbein and Sloss, 1963; Pettijohn, 1975). Studying the morphology of particles is a standard analysis technique for investigating terrestrial sites (Wadell, 1932, 1933; Zingg, 1935; W. C. Krumbein, 1941; Sneed and Folk, 1958; Folk, 1980). Sphericity of grains can for example be related to the distance travelled and the abrasive properties inherent to the rock type (Sneed and Folk, 1958). For example, the more a rock travels, the rounder it becomes, which is a well-known behaviour of pebbles going downstream in rivers, studied since the ancient Greeks (Krynine,

1960) and still today (Domokos et al., 2014).

On terrestrial sites, these morphological analyses are often coupled with field studies (Ehlmann et al., 2008), or laboratory experiments (Cho et al., 2006; Yang and Luo, 2015; Suh et al., 2017; Domokos et al., 2014; Bareither et al., 2008). This approach makes it possible to link the shapes of the particles constituting the granular material to mechanical properties such as the angle of internal friction (Cho et al., 2006; Yang and Luo, 2015; Suh et al., 2017; Kim et al., 2019).

In extraterrestrial environments, the size and morphology of the particles of the regolith are also influenced by the processes that shape planetary surfaces. These processes include impacts, principally breaking the rocks apart but also eroding them (Hörz, 1977; Housen et al., 1979; Ballouz et al., 2020). Thermal processes can also reshape boulders or particles by creating and breaking fractures (Dombard et al., 2010; Delbo et al., 2014; Attree et al., 2018; Lucchetti et al., 2024). Finally, weathering and erosion are able to modify boulders or particles at different scales, from their texture to their size or general shape (Yingst et al., 2007; Ehlmann et al., 2008).

The detailed morphology of boulders has been studied at the surface of different planetary bodies such as rocks at the pathfinder landing site on Mars (Yingst et al., 2007). By analysing the boulders' roundness, it was possible to highlight the impact processing and catastrophic flooding the boulders went through, matching predictions from other analyses. On comet 67P/Churyumov-Gerasimenko, isolated boulder fields have been studied, revealing that boulders exhibit similar shapes across the surface (Cambianica et al., 2019). However, variations are expected in regions receiving the most solar insolation, particularly when the comet approaches perihelion, the point of the comet orbit the closest to the sun, as a result of gravitational events caused by sublimation and thermal erosion (Pajola et al., 2015). At the beginning of this thesis in 2022, detailed investigation of morphological parameters of boulders at the surface of asteroids such as roundness or sphericity had not yet been performed. Mostly the size-frequency distributions of boulders at the surface of asteroid have been studied. For example on Eros (Thomas et al., 2001), the size-frequency distribution obtained from images combined with ejecta-emplacement models, allowed to suggest that most large ejecta boulders on Eros originate from a relatively young 7.6-km-diameter crater. On Itokawa, combined with a model based on cratering experiments, the boulder size frequency distribution indicated that the boulders on the surface of Itokawa cannot exclusively be the product of cratering and that the boulders rather originated from the disruption of the larger

parent body of Itokawa (Michikami et al., 2008). It is consistent with the measurements of the axial ratios, that have been studied for large boulders (>5m) on Itokawa (Michikami et al., 2010), but also Ryugu (Michikami et al., 2019), and Eros (Michikami and Hagermann, 2021). These studies primarily highlighted that the boulders of these asteroids originated from the catastrophic disruption of a parent body, as their average axial ratios are similar to those of fragments produced in laboratory impact experiments (Michikami et al., 2016). A catastrophic disruption event in this context, is an impact event between two objects that reduce the target mass to less than half of its original mass (Holsapple and Housen, 2019). As a result, this event notably forms a new body.

Moreover for Itokawa, Tancredi et al. (2015) observed size segregations effects of the boulders through their size-distribution at the surface of the asteroid. This size segregation has been correlated with the gravity field of the asteroid: large objects were gathering in high potential regions while smaller objects were gathering low potential ones. They also observed a shape segregation, with the more rounded boulders in the high potential regions and the more elongated ones in the low potential regions. Similarly to Itokawa, the particle size-frequency distribution at the surface of asteroid (4179) Toutatis suggest that the asteroid has been formed by catastrophic disruption of a parent body and that most boulders cannot only be the products of cratering (Jiang et al., 2015). The same goes for Bennu, the size-frequency distribution of boulders at its surface suggests that the largest boulders of the asteroid have been formed by catastrophic disruption of a parent body and micro-scale particles are recent in-situ production (DellaGiustina et al., 2019). The particle size-frequency distribution at the surface of Bennu has also been used to assess the viability of the candidate sites for the sample collection of the OSIRIS-Rex mission (Burke et al., 2021). At the surface of Ryugu, the size-frequency distribution of the boulders lacks large boulders, implying that some boulders may be buried in a regolith layer made of finer particles (Michikami et al., 2019). Particle size-frequency distributions have also been studied on other planetary surfaces, such as the Moon (Carrier et al., 1991; Li et al., 2017), or Mars (Golombek et al., 2021; Verdier et al., 2023).

In the following sections, we focus on morphological descriptors that had not yet been studied on asteroid surfaces, following approaches previously applied to the surfaces of Mars (Yingst et al., 2007) and comet 67P (Cambianica et al., 2019). These descriptors are first introduced and we then describe their implementation within a semi-automated processing pipeline. The pipeline is then tested on images from the WheelCam test bed (Murdoch et al., 2025) before being used for a comparative analysis of several asteroids, including Dimorphos, which

had just been encountered by the DART spacecraft in September 2022.

2.2 Morphological descriptors

Morphological analysis of granular materials such as sands or crushed sands is an analysis technique to investigate terrestrial sites from images (Wadell, 1932, 1933; Zingg, 1935; W. C. Krumbein, 1941; Sneed and Folk, 1958; Folk, 1980). Most morphological parameters are dimensionless quantities commonly used in image analysis to describe shapes regardless of their sizes. The morphological parameters we chose to study are the following:
As a size parameter metric, we used the **equivalent diameter** (Wadell, 1933), D_c, the diameter of the circle with the same projected area as the particle or boulder analysed.

$$D_c = 2 \times \sqrt{A/\pi} \tag{2.1}$$

with A the projected area of the particle.

The **circularity** (Cox, 1927), C, or compactness of a particle describe how closely the particle shape of a particle matches a circle of the same area. It is a measure of the large-scale roughness of a particle: a circularity of 1 indicates that the particle is a circle.

$$C = \frac{4\pi A}{P_S^2} \tag{2.2}$$

with P_S the perimeter of the particle.

The **solidity** or convexity ratio (Mora and Kwan, 2000) is the ratio between the area of the particle and the area of its own convex hull. It is a measure of the small-scale roughness of a particle or a boulder: a solidity of 1 indicates that the shape of a particle is its convex hull.

$$Solidity = \frac{A}{H} \tag{2.3}$$

with H the area of the convex hull of the particle.

The 2D axial ratio can be expressed in two forms: the **ellipsoidal ratio** and the **bounding box ratio**. The ellipsoidal ratio is computed with the major and minor axis of the fitted ellipse of the particle :

$$Ellipsoidal\ ratio = \frac{b}{a} \tag{2.4}$$

with a and b the major and minor axis of the ellipse, respectively. The bounding box ratio is computed using the width and length of the minimal bounding box of the particle, a rectangle minimizing its area, including all the particle:

$$Bounding\ box\ ratio = \frac{d_2}{d_1} \tag{2.5}$$

with d_1 and d_2, the bounding box length and width, respectively. Both these parameters can be used to measure the apparent axial ratio of a particle: an apparent axial ratio of 1 indicates that the particle is equidimensional.

Sphericity, S, or circle ratio sphericity (Riley, 1941) is a three dimensional parameter to measure the ratio between the the shape of the particle to a sphere. Sphericity can also be studied in two dimension as the ratio of the shape of the particle to a circle. A 2D sphericity equal to 1 indicates that the particle is a circle.

$$s = \frac{D_{ins}}{D_{cir}} \tag{2.6}$$

D_{cir} is the diameter of the minimum circumscribing circle and D_{ins} the diameter of the largest inscribing circle.

Finally, **roundness**, R, is a measurement of the relative curvature of the projected shape of the particle quantifying the sharpness of its corner and edges (Wadell, 1932, 1933, 1935). It is defined by Wadell as the ratio of the average radius curvature of the corners of the particle to the radius of the maximum inscribed circle. Higher roundness indicates that the particle is less angular and lower roundness indicates that the particle is more angular.

$$R = \frac{\Sigma_{i=1}^{N} r_i}{N \times R_{ins}} \tag{2.7}$$

with N the number of corners, r_i the radius of each corner circle, and R_{ins} the radius of the largest inscribed circle. A shape classification has been proposed based on Wadell's definition of roundness (Powers, 1953). See Table 2.1.
A schematic of a particle with the different variables used to calculate all those parameters is available in Figure 2.1.

Description	Roundness
Very angular	≤ 0.17
Angular	$0.17 - 0.25$
Sub-angular	$0.25 - 0.35$
Sub-rounded	$0.35 - 0.49$
Rounded	$0.49 - 0.70$
Well-rounded	> 0.70

Table 2.1: Classification of grain shapes based on roundness values. From Powers (1953).

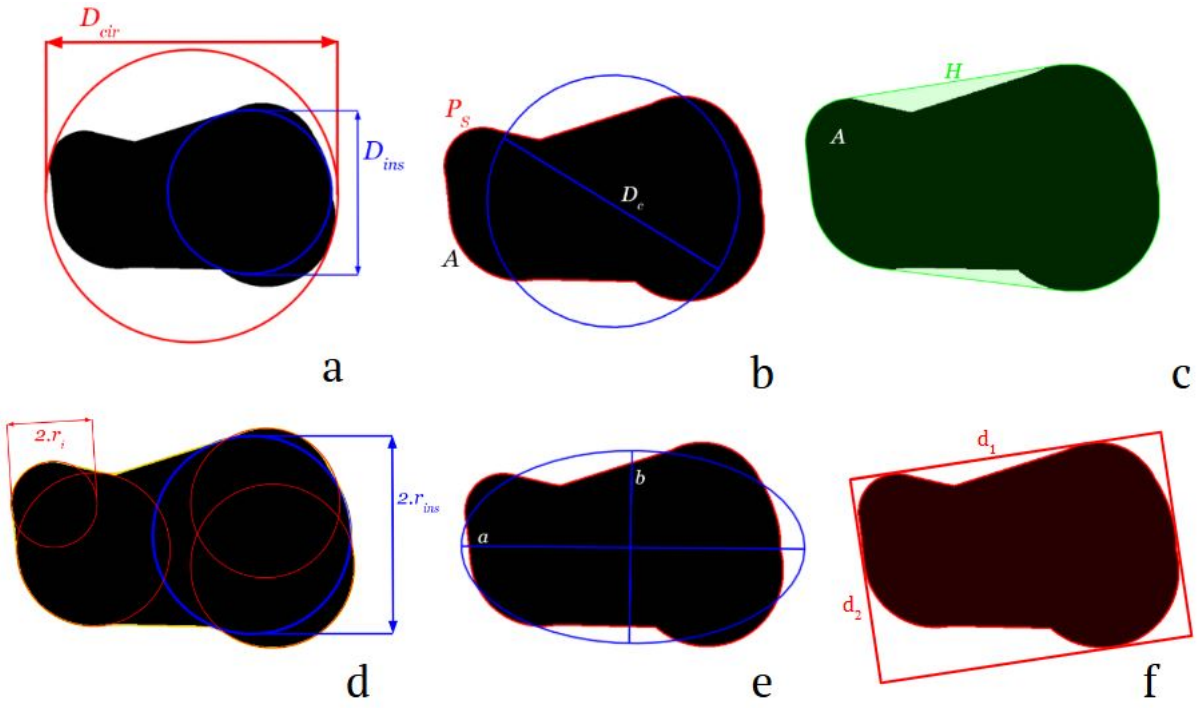

Figure 2.1: A two-dimensional particle with its different associated variables used to compute the morphological parameters. a) D_{cir} is the diameter of the minimum circumscribed circle, and D_{ins} is the diameter of the maximum inscribed circle of the particle, used to compute the sphericity. b) D_c is the diameter of the blue circle, with the same projected area A as the particle. P_s is the perimeter of the particle, used in the calculation of the circularity of the particle. c) H is the area of the convex hull of the particle of area A. These variables are used in the computation of the solidity. d) r_i is the radius of the corner circle i and r_{ins} is the radius of the maximum inscribed circle of the particle, used in the calculation of the roundness. e) a is the major axis and b is the minor axis of the fitted blue ellipse of the particle, used in the calculation of the ellipsoidal ratio. f) d_1 is the length and d_2 is the width of the minimal bounding box of the particle, used to calculate the bounding box ratio of the particle.

2.3 Development and validation of an image analysis pipeline for the MMX WheelCams

Previous studies have provided valuable insights into boulder morphology linked with their origin and mechanical properties through in-situ and remote observations at the surface of Mars (Yingst et al., 2007) and comet 67P (Cambianica et al., 2019). To support this similar goal in the context of the Martian Moons eXploration (MMX) mission, we developed and validated a dedicated image analysis pipeline for the MMX WheelCams, aboard the MMX rover Idefix.

2.3.1 Presentation of the pipeline and motivation for its development

The image-processing pipeline developed at ISAE-SUPAERO for the MMX WheelCams is a MATLAB code originally developed by Alexia Duchêne during her master's project in 2021 and automatized by Gabriella Cuervo as part of her internship. At the time, the code was computing the sphericity and roundness of binary images of particles, following the methodology of Zheng and Hryciw (2015).

The first improvement made was to add the computation of the equivalent diameter, solidity, circularity, ellipsoidal ratio and bounding box ratio. Parameters needed to compute these metrics such as the area of the particle, its perimeter, convex hull, and major and minor axis are computed using the MATLAB *regionprops* function. The bounding box rectangle, used to compute the bounding box ratio, is calculated using the 2D minimal bounding box function (Diener, 2025).

For sphericity, the diameter of the minimum inscribed circle is computed using the methodology of Zheng and Hryciw (2015): the concave points around the contour of the particle are used to define a first circle of a diameter corresponding to the largest distance between two points. If all points of the contour are inside the circle, the minimum circumscribed circle has been found. Otherwise the procedure is repeated by including the outside point the furthest away from the previous circle to fit a new circle from 3 points. The computation of the diameter of the maximum inscribed circle, however, has been improved, by A. Duchêne, as part of her internship in 2023. The new method calculates the Euclidean distance transform of the particle (Maurer et al., 2003) with the *bwdist* function of the Image Processing MATLAB ToolBox. This function computes the minimum distance to the contour from each

pixel inside the particle: the maximum value of the distance transform map corresponds to the most enclosed point of the particle that is the furthest away from the contours. The maximum inscribed circle has a radius equal to the maximum value of the distance transform. A. Duchêne also improved the computation of the roundness. The roundness calculation require to find the corners of the particle and their associated radius. To do so, the discrete curvature of the smoothed contour of the particle is computed. The contour of the particle is smoothed in order to remove any angular or square shape contour from the pixels, following a LOESS (Cleveland and Devlin, 1988) (LOcally Estimated Scatterplot Smoothing) method of 5%. The curvature γ of a 2D closed line is the second derivative of the contour coordinates: if $\gamma = 0$, the line is straight, if $\gamma < 0$ and $\gamma > 0$, the curvatures are respectively concave and convex at the computed point. Thus, the associated radius r_p of a curvature at one given point of the curvature γ_p is its inverse such as $r_p = \frac{1}{\gamma_p}$. In the definition of Wadell's roundness (Wadell, 1935), the radii of the corner circles cannot be larger than the radius of the maximum inscribed circle (i.e. $r_i < r_{ins}$). Following this definition, we define a corner of a particle as successive concave points of a curvature higher or equal to $\frac{1}{r_{ins}}$. In this manner, the local maximum of the curvature of each corner is identified, corresponding to the largest circle that can fit in the corner. For more details on this methodology see Duchêne et al. (2025).

With these improvements, it was already possible to perform detailed analysis of the morphology of boulders from images of space missions. However, we had to manually select the contours of the particles which was laborious and not exempt from human error. As we wanted to remove human subjectivity as far as possible, and automatize the pipeline as much as possible to analyse more images and boulders, we chose a semi-automatic image segmentation method. The method was implemented by A. Duchêne as a two-step process using the *segmenteverygrain* Python package (Sylvester, 2024). This package uses a machine learning model to detect and obtain precise and accurate outlines of grain-like objects. It also comes with functionalities to let the user decide if he wants to keep an object, or even add objects that were not segmented at first, by clicking the grain.

An overview diagram of the whole pipeline is provided in Figure 2.2.

The motivation for developing this pipeline is to apply image analysis techniques to help space missions infer the mechanical properties of materials constituting asteroids and other bodies covered with regolith or boulders. Mechanical properties of rare asteroid samples from Itokawa (Tanbakouei et al., 2019), Ryugu (Nakamura et al., 2022; Nakato et al., 2023;

Onodera et al., 2025) or Bennu (Lauretta et al., 2024) have been analysed on Earth, along with recent missions that performed direct interaction with the surfaces of small-bodies (see Sect. 1.1.3). However, before retrieving any sample from Phobos, this image analysis pipeline aims to support the science objectives of the MMX Idefix rover WheelCams to determine both the physical properties of the regolith particles and also the bulk mechanical properties of the regolith (Murdoch et al., 2025). Notably, the angle of internal friction θ can be inferred from the roundness R, based on an empirical relationship derived in laboratory experiments (Suh et al., 2017):

$$\theta = 25.02 \times (1 - R) + 20 \tag{2.8}$$

This study by Suh et al. (2017) analysed several types of sands, crushed sands and glass beads. The roundness of the particles was computed from binarized 2D images with a MATLAB code from Zheng and Hryciw (2015). The internal friction angles (θ) of these different soils were measured using a triaxial shear test. The experiment measures under which shear stress a material fails for a given normal stress. The internal angle of friction (along with the material cohesion) is then determined from the Mohr-Coulomb law (Lade, 2016). Note that there are also three other equations linking roundness and the bulk internal friction angle following the same experimental approach, but the method for calculating roundness is different from that of this thesis: one is measuring roundness by comparing a sample of grains with the Sloss & Krumbein roundness chart (W. C. Krumbein, 1941; Cho et al., 2006), another one is using the combined roundness (Yang and Wei, 2012), taking in account mixed materials (Yang and Luo, 2015) and the last one taking in account the coefficient of uniformity of the material (Kim et al., 2019).

2.3.2 Influence of resolution on the results of the pipeline

Theoretically, large scale morphological descriptors such as sphericity, solidity and axial-ratios are little to not resolution dependant, considering the variables needed to compute them. These variables are, for example the major or minor axis length of the fitted ellipse of the particle, the radii of the circumscribed or inscribed circle of the particles or the area of the particle or of the convex hull of the particle. However, smaller scale descriptors such as roundness (Zheng and Hryciw, 2015) and circularity (Nagaashi et al., 2021) are highly resolution dependant, and the size in pixel of a particle affects the results of these morphological parameters, as the variables needed to compute them such as the perimeter or the curvature of the corners of a particle depends on the number of pixels defining the outline of the particle.

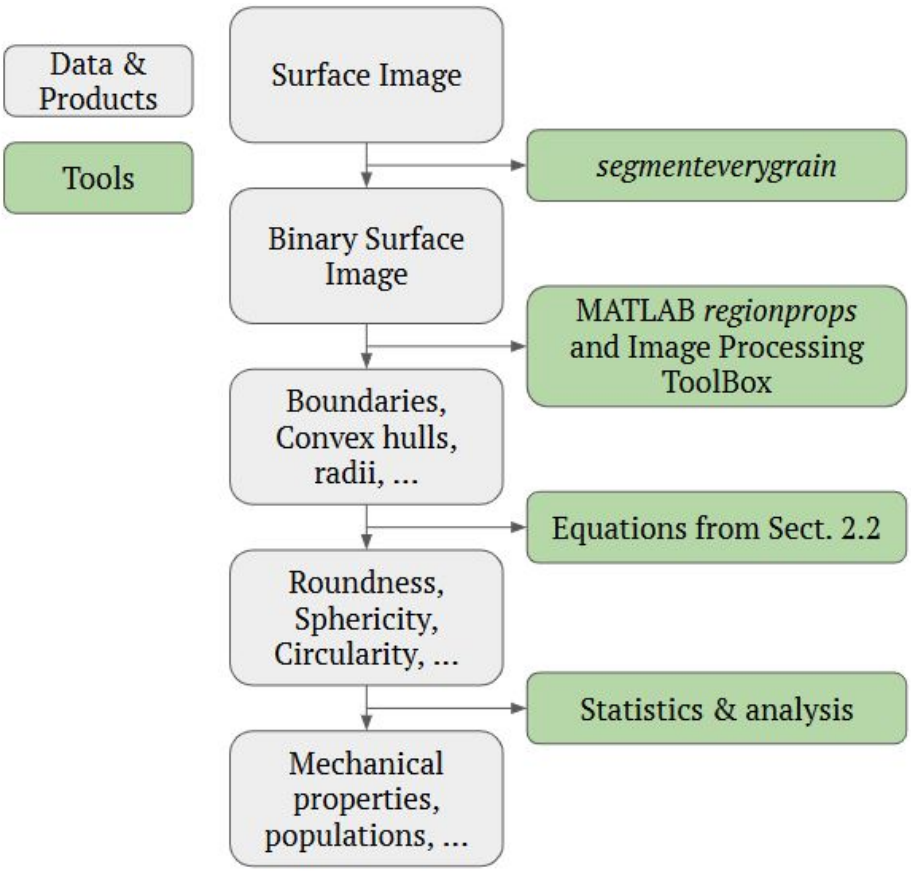

Figure 2.2: Overview diagram of the morphological image analysis pipeline developed for the MMX rover WheelCams. Original data and subsequent products are shown in gray and tools for moving from one stage to the next are shown in green.

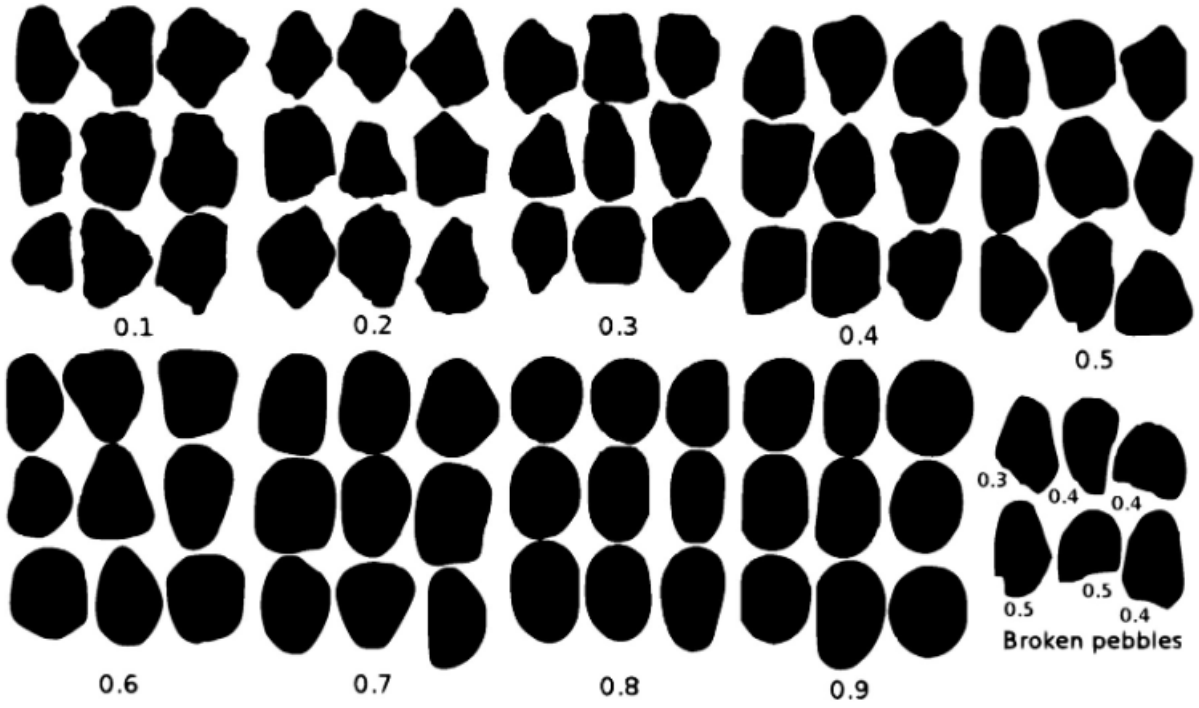

Figure 2.3: Krumbein's diagram for estimating particle roundness. The roundness are indicated under the particles. From (From W. C. Krumbein, 1941).

In order to verify these assertions, test the accuracy of the pipeline, and quantify these errors on the values obtained for the morphological parameters, especially for roundness, we created a roundness chart similar to the Krumbein's chart (W. C. Krumbein, 1941, see Figure 2.3). However, the Krumbein's chart is used to visually identify the roundness by comparing particles with the chart. For this reason, we recreated a chart with particles of known roundness, following Eq. 2.7. For example, to create a particle with $R = 0.1$, we draw a particle with 4 corners for which the sum of the radii $\Sigma_{i=1}^{N} r_i$ is equal to 40 pixels and the radius of the maximum inscribed circle is 100 pixels, giving a roundness $R = \frac{\Sigma_{i=1}^{N} r_i}{N \times R_{ins}} = \frac{40}{4*100} = 0.1$. We created 4 particles for each roundness of 0.1, 0.3, 0.5, 0.7 and 0.9 for a chart with a total of 20 particles (See Figure 2.4).
Finally, in order to verify the influence of the size in pixels of the particle on the morphological parameters we declined this roundness chart (Figure 2.4) in 9 different versions of 9 different resolutions. The smallest resolution is 10 pixels per particle (PPP) on average, meaning that the particles are on average 10 pixels large. The other resolutions are 20, 30, 60, 125, 250, 500, 1000 and the largest is 2000 PPP.

In order to estimate the influence of resolution on the morphological parameters, we looked

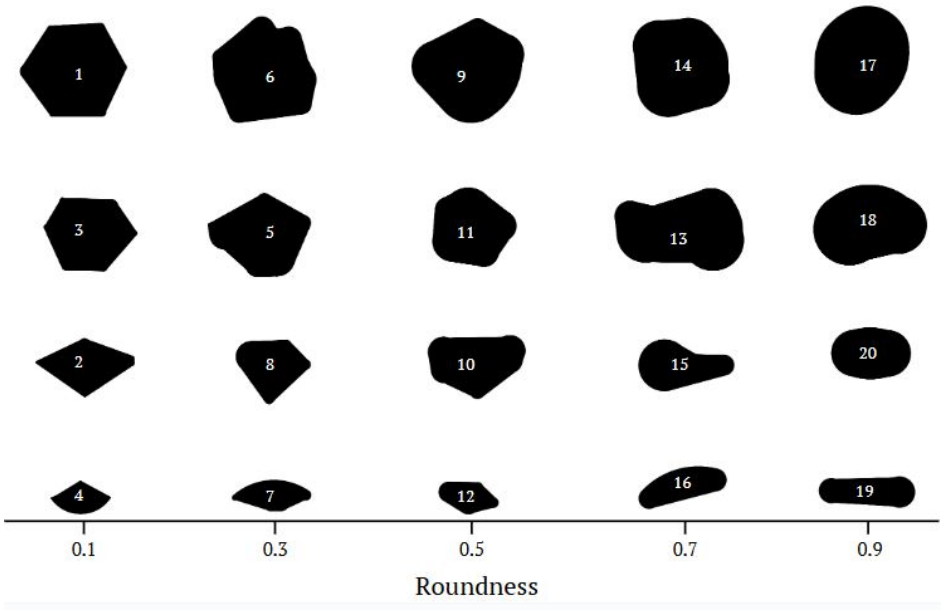

Figure 2.4: Roundness chart used to validate and seek for the limits of the pipeline. The ID number of each particle is given by the pipeline, according to the order in which it has analysed the particles.

at the residuals r between the measured parameters at different particle sizes in pixels y and the same measured parameters from the image with the best resolution $\hat{y}$ (See Figure 2.5). The residuals r is thus defined as:

$$r = y - \hat{y} \tag{2.9}$$

with y the measured value and $\hat{y}$ the expected value. First, we can see a clear influence of the resolution on roundness and circularity. When the size of the particle decreases, roundness tends to be underestimated and the pipeline can't measure any roundness for particles with a smaller equivalent diameter of 20 pixels. An underestimated roundness means that the particles are more angular than in reality, which is the case when resolution is decreasing: pixels create rougher particle boundaries and smaller corner circles resulting in smaller computed roundness. For circularity, the values are overestimated for the same reason: the particle boundaries are pixelated resulting in underestimated perimeters of the particles.

We can also see the influence of the resolution on sphericity, elongation ratio as well as on solidity but it varies within a more acceptable range compared to roundness and circularity.

To conclude, resolution noticeably affects the computation of morphological parameters but we consider that we can trust a morphological analysis for residuals in the range of ± 0.15 a

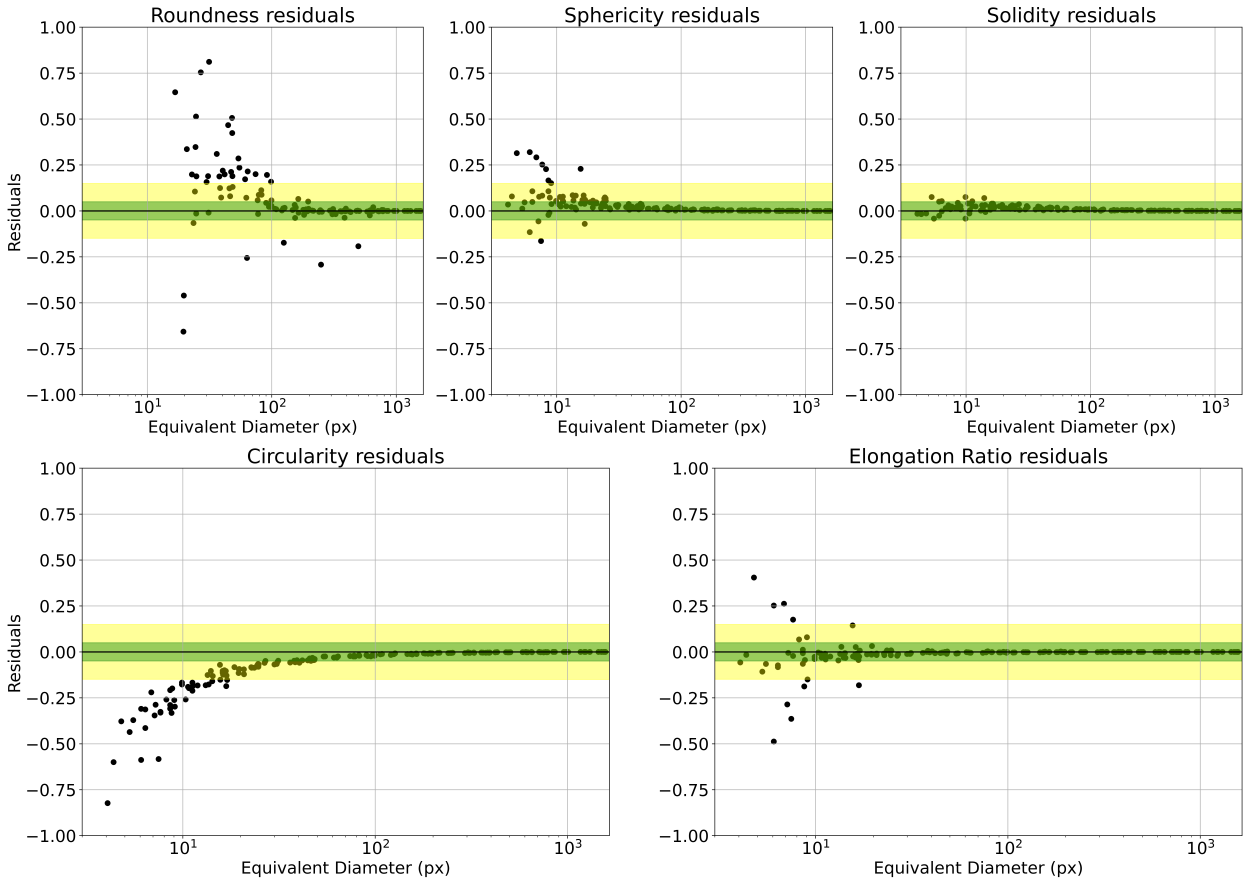

Figure 2.5: Residuals of different morphological parameters measured for different equivalent diameters on the charts at different resolutions (Figure 2.4). The reference value are the value computed by the pipeline from the chart at the highest resolution. Roundness values under an equivalent diameter of 20 pixels are NaNs. The yellow and green shaded areas respectively correspond to ±0.05 and ±0.15 residuals.

morphological analysis and we would be able to differentiate populations. The influence of resolution, however, has to be taken in account, especially for roundness and circularity, and we recommend to avoid analysing individual particles with a smaller equivalent diameter than 100 pixels and 10 pixels for other parameters, if possible. If the average roundness or circularity values of a population are studied, it should be considered that the roundness value will be underestimated and the circularity value overestimated and these values should be respectively considered as lower and upper limits.

2.4 Test of the pipeline on images of the WheelCams testbed

In order to test the morphological analysis pipeline on images that may be more similar to those that will be retrieved at the surface of Phobos by the MMX WheelCams, we used the

pipeline on images from the MMX WheelCams testbed.

The MMX WheelCams testbed is a single-wheel test bed developed during the thesis of C. Sunday (Sunday, 2022) and then improved throughout the years by several students, in order to generate images similar to the WheelCams (Murdoch et al., 2025). On the testbed, the two cameras point towards the same wheel whereas the actual MMX WheelCams point towards two different wheels. The testbed is 1340 mm long by 650 mm wide by 665 mm high. The wheel is the same as that of the MMX rover, and is attached to a horizontal slider, allowing the wheel to move freely in the lateral direction as the wheel rotates thanks to a motor. The wheel sits in a material container of 1140 mm long by 290 mm wide by 95 mm high. The testbed cameras are not replica of the WheelCams but they produce grey-scale images similarly to the WheelCams and have a resolution of 1936 x 1216 pixels (Matrix Vision mvBlueFOX3-2-2024 cameras with Matrix Vision MV-01620-5M-TA lenses). The cameras are mounted on flight-equivalent 3D printed camera baffles and equipped with flight-equivalent LEDs. The testbed can also be covered with blackout panels in order for the LEDs to be the principal light source for the images. Images of the testbed and from the cameras of the testbed are shown in Figure 1.15.
Thanks to the testbed, several materials have been tested in order to prepare for the image analysis of the WheelCams at the surface of Phobos. Here, we analysed some of theses images to test the morphological analysis pipeline. The images we tested are images of the wheel in a low sinkage configuration and in a high sinkage configuration for a Phobos simulant (from a mixture recipe provided by DLR), an image of the wheel in gravel, an image of the wheel in a JAXA optical simulant of Phobos (Miyamoto et al., 2021) and an image of the wheel in a lunar simulant provided by CNES (see Figure 2.6).

For the Phobos simulant mixture, two different wheel sinkages have been tested in order to test if we would observe differences between both images as the distance from the granular material is different as well as the configuration of the particles. The high sinkage configuration has been set up by manually adding material around the wheel. As both configurations are with the same material, we expect similar results between them.

Results of the analysis are displayed on Figure 2.7, as kernel density estimates. Kernel density estimation (KDE) (Rosenblatt, 1956) or the Parzen's window (Parzen, 1962) is an approach to estimate the underlying probability function of a data set Chen (2017). In this study, it allows us to smooths the histograms of our data to compare them more effectively and easily. This smoothing is also the reason why values can exceed 1 on the figures even if

no value exceeds 1 in the dataset. The KDE is computed using the seaborn Python library (Waskom, 2021) with the *kdeplot* function.

Here, we analysed all the semi-automatically segmented particles by *segmenteverygrain*. The average equivalent diameter of images a, b, c, d and e from Figure 2.6 are respectively 22.7, 23.3, 53.2, 41.3 and 18.8 pixels and for particles for which roundness has been calculated the average equivalent diameters are respectively 24.6, 27.0, 56.5, 44.0 and 24.3 pixels. Thus, we should note that values of roundness are underestimated and the values of circularity are overestimated as explained in Sect. 2.3.2. Thanks to the roundness values, we can estimate the upper limits of the angles of internal friction of the observed materials: a) $37.7 \pm 6.0°$ for the Phobos simulant mixture in a low sinkage configuration, b) $38.5 \pm 5.2°$ for the Phobos simulant in a high sinkage configuration, c) $36.6 \pm 4.1°$ for gravel, d) $37.9 \pm 2.9°$ for the JAXA optical simulant of Phobos and e) $36.7 \pm 6.6°$ for the Moon simulant. Those values are consistent with the values of dry soils in the mm size range (Keaton, 2017). We also note that the distributions of the morphological parameters of the images of the wheel in low and high sinkage in the Phobos simulant mixture show comparable distributions, as well as similar angles of internal friction with a less than 1° difference.

After this preliminary test on images of the MMX WheelCams test bed, showing that we are able to measure the morphological properties of particles with our image analysis pipeline, we propose a complete and detailed study of the morphological parameters of boulders at the surface of different asteroids, mainly focus on asteroid Dimorphos, published in Robin et al. (2024). Thanks to this pipeline, this study aims to provide important constraints on the mechanical properties of rubble pile asteroids, while also providing insights into rubble pile and binary asteroid formation mechanisms.

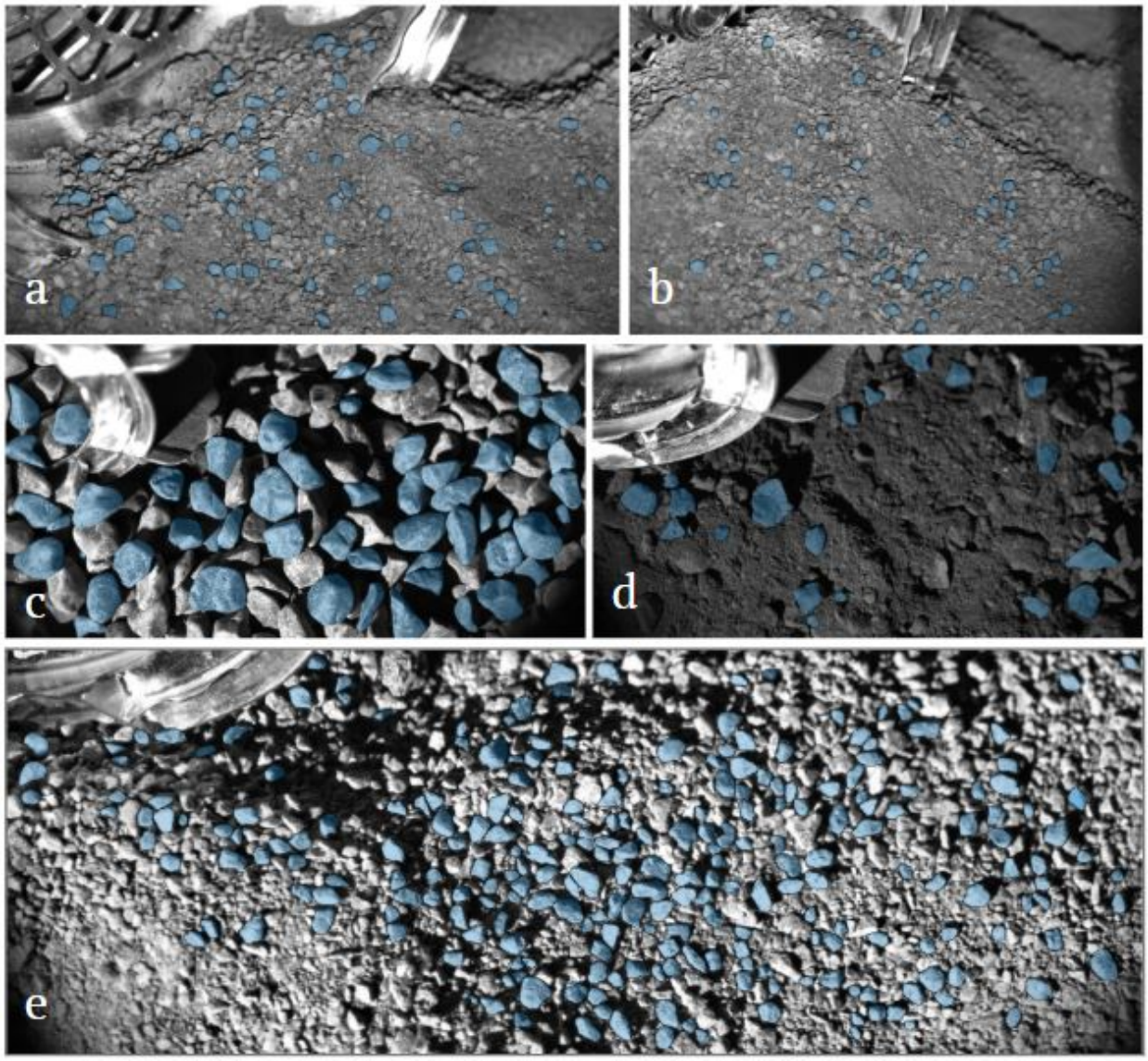

Figure 2.6: Analysed images from the WheelCam testbed. The images has been cropped around zones where particles are not out of focus. a) Image of the front WheelCam in a low sinkage configuration in a Phobos simulant mixture. b) Image of the front WheelCam in a high sinkage configuration in a Phobos simulant mixture. c) Image of the rear WheelCam in gravel. d) Image of the rear WheelCam in the JAXA optical simulant of Phobos. e) Image of the rear WheelCam in a Moon simulant.

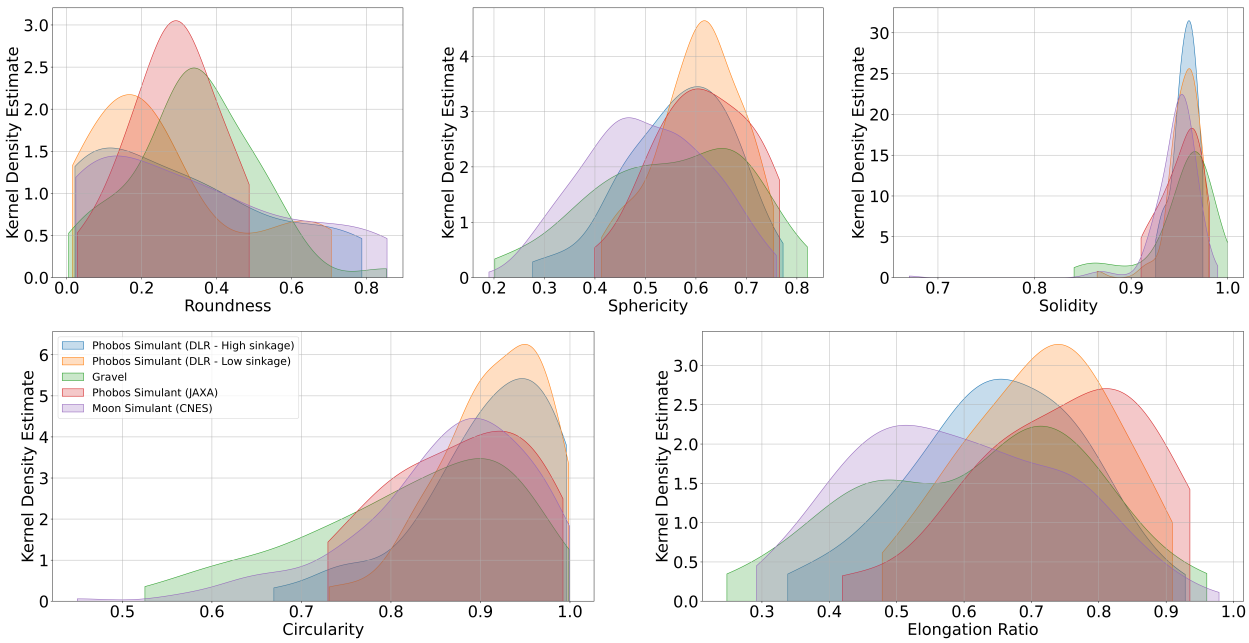

Figure 2.7: Kernel density estimates of the roundness, the sphericity, the solidity, the circularity and the elongation ratio of images from the WheelCam testbed. Here, the KDEs have been cut at the data limits.

2.5 Mechanical properties of rubble pile asteroids through surface boulder morphological analysis (Robin et al., 2024).

On September 26 2022, the NASA Double Asteroid Redirection Test (DART) mission, deliberately slammed into the natural satellite of the S-type asteroid Dimorphos and modified its orbit as a planetary defense test (Rivkin et al., 2021; Daly et al., 2023). The DART impact produced at least an estimated $\approx 6 \times 10^6 kg$ of ejecta (Moreno et al., 2023; Li et al., 2023; Jewitt et al., 2023), changed Dimorphos' orbital period of 33 minutes (Thomas et al., 2023) and enhanced the momentum factor of between 2.2 and 4.9, depending on the (currently unknown) mass of Dimorphos (Cheng et al., 2023).

Given the primary objective of the mission: impact Dimorphos with the DART spacecraft, the latter was only equipped with the Didymos Reconnaissance and Asteroid Camera for Optical navigation (DRACO) (Fletcher et al., 2022). It was the perfect occasion to test and validate the image analysis pipeline developed for the WheelCams as images were the primary data source of the mission. We used the last complete image retrieved from DRACO and computed the detailed morphological characteristics of boulders on the surface of Dimorphos around the DART impact site. Additionally, we analysed boulders on the surfaces of three other visited rubble-pile asteroids; Itokawa, a 0.32 km diameter large S-type asteroid with

estimated 40% porosity (Fujiwara et al., 2006; Abe et al., 2006), Ryugu, a 0.90 km diameter large C-type asteroid with estimated 50% porosity (Watanabe et al., 2019), and Bennu, a 0.49 km diameter large C-type asteroid with estimated 50% porosity (Lauretta et al., 2019). The studied asteroids are shown in Figure 2.8. The analysis that will be presented, allowed to constrain the angle of internal friction of Dimorphos, and to compare the results obtained for other rubble-pile asteroids with already known results. I will also present how we were able to investigate the mechanism by which the boulders may have formed and how the Didymos-Dimorphos system may have evolved since its creation.

2.5.1 Morphological analysis of boulders at the DART impact site

We conduct an in-depth examination of the last complete image captured by DRACO 2.78 s before the DART impact (Figures 2.8a and 2.9a) to retrieve the boulder dimensions and several dimensionless morphological parameters: roundness, sphericity, circularity, solidity, and two different axial ratios : ellipsoidal ratio and bounding box ratio. The image covers an approximate area of $880m^2$ on the surface of Dimorphos with a resolution of 0.055 m/pixel (Daly et al., 2023).

For this study, we analysed all the boulders with the large-scale descriptors (sphericity, solidity, and axial ratios) and, in order to avoid computational errors and increase the reliability of our results, we selected boulders with diameters larger than 30 pixels to compute the roundness and circularity (See Sect. 2.3.2). In this study, the 30 pixels threshold size was defined for our analysis, in order to have a large enough sample size for each body studied ($>$ 30 boulders Zheng and Hryciw (2016); Edil et al. (1975)) to have reliable statistics. Dimorphos was the limiting case, where only one image was analysed: to have a sample size of at least 30 boulders to compute the smaller scale descriptors, all boulders with a resolution above 30 pixels were included. Even if we don't recommand analysing the roundness of circularity of individual particles with a diameter under 30 pixels, here we only study populations. Moreover, we can see on figure 2.5 that the residuals for circularity for 30 pixels large particles are still in the ± 0.15 shaded area. For these reasons, and considering that the average values that we will compute are overestimated for circularity and underestimated for roundness, we consider the diameter size of 30 pixels acceptable for this study.

Our analysis therefore focuses on 53 selected boulders situated around the impact site of DART with 34 boulders larger than 30 pixels in diameter. The average values and the standard deviations of all of the computed morphological characteristics are displayed in

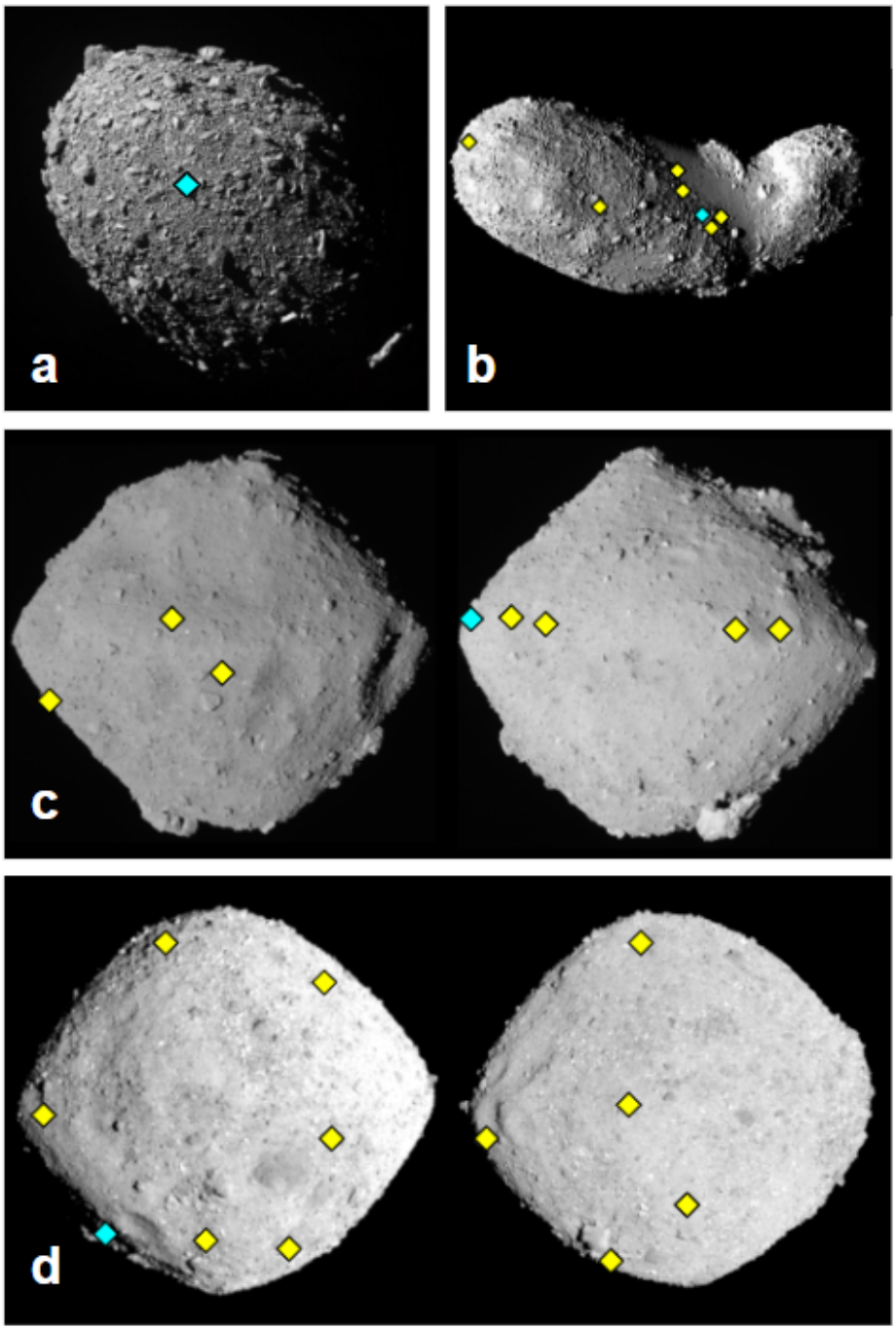

Figure 2.8: Rubble pile asteroids visited by space missions. a) Dimorphos (208 × 160 × 133 m), the secondary of the (65803) binary system Didymos visited by the NASA DART mission (Daly et al., 2023), b) Asteroid (25143) Itokawa (607 × 287 × 264 m) visited by the JAXA Hayabusa mission (Fujiwara et al., 2006), c) Asteroid (162173) Ryugu (1040 × 1020 × 880 m) visited by the JAXA Hayabusa-2 mission (Watanabe et al., 2019), d) Asteroid (101955) Bennu (565 × 535 × 508 m) visited by the NASA OSIRIS-REx mission (Lauretta et al., 2019). The diamonds indicates the approximate geographical locations of the images that we used of these asteroids and the blue ones are the images displayed in Figure 2.9 Images are not to scale.

Table 2.3. The Dimorphos boulders selected close to the DART impact site have an average equivalent diameter of 2.15 ± 0.94 m, are slightly elongated (sphericity of 0.61 ± 0.12) and sub-rounded in shape (roundness of 0.49 ± 0.10), as defined by Powers (1953). The roundness value of 0.49 should be considered as an upper limit (See Sect. 2.3.2). The Dimorphos boulders do not exhibit a large degree of small-scale or large-scale roughness (solidity of 0.95 ± 0.02 and circularity of 0.84 ± 0.09).

2.5.2 Implications for Dimorphos' mechanical properties and boulder formation mechanisms

The mechanical properties such as the internal angle of friction are critical parameters with direct implications for the modelling and comprehension of the DART impact event (Stickle et al., 2022; Kumamoto et al., 2022; Raducan et al., 2024), notably on the behaviour and responses exhibited by the asteroid (Stickle et al., 2022). We use our calculated roundness of individual boulders to deduce the regolith's internal friction angle θ, based on the empirical relationship presented in Sect. 2.8.

The average roundness of the boulders at the DART impact site is 0.49 ± 0.10 (Figure 2.10). This leads to a mean internal friction angle of at least $32.7 \pm 2.5°$, estimated from a sample of the boulders with diameter larger than 30 pixels at the surface of Dimorphos.

Fragments formed during laboratory impact experiments typically have an average axial ratio (b/a) of 0.70-0.74. Moreover, fragments formed by catastrophic disruptions (See 2.1) are more oblate ($c/a \approx 0.5$) while fragments formed by impact cratering are flatter ($c/a \approx 0.2$) (Michikami et al., 2016). Previous work has relied on such experiments to conclude that most boulders of diameters ranging from 5 to 85 m on Itokawa and Ryugu (Michikami et al., 2010, 2019; Michikami and Hagermann, 2021), have likely been formed by catastrophic disruption based on the observed axial ratios of the surface boulders and boulders on Eros were formed by impact cratering (Michikami and Hagermann, 2021). In these studies, the axial ratios, obtained by fitting ellipses on the boulders observed at Ryugu and Itokawa surfaces, were found to be slightly smaller than in the laboratory experiments (0.68 and 0.63 respectively) whereas boulders at the surface of Eros were less elongated (ratio of 0.72) (Michikami and Hagermann, 2021). However, the observed discrepancy between the ellipsoidal ratios and the laboratory impact ratio is attributed to the inclination of boulders on asteroid surfaces. Indeed, for Itokawa and Ryugu, where gravity is lower, gravity does not force most boulders to lie on their c axes perpendicular to the asteroid surface (Michikami and Hagermann,

2021). The resulting inclination influences the apparent axial ratio contrary to what has been deduced for Eros where gravity is relatively high. Indeed, at the surface of Eros, the c axes of the boulders is most likely to be perpendicular to the surface and thus the apparent axial ratio is closer to the actual axial ratio (Michikami and Hagermann, 2021).

The apparent axial ratio has been computed in two ways in this study: with the minor and major axis of a fitted ellipse on a boulder (the ellipsoidal ratio) or with the width and length of the minimum bounding box of the boulder (the bounding box ratio). The ellipsoidal ratio tends to be smaller than the bounding box ratio (Table 2.3), due to the differences in the axis selection in both methodologies. For Dimorphos, the upper range of the ellipsoid ratio and the bounding box ratio (0.66 ± 0.15 and 0.70 ± 0.17, Table 2.3) also fall within the axial ratio acquired from the laboratory impact fragmentation experiments (Michikami et al., 2016). Figure 2.11 shows the histogram and the kernel density estimate for the apparent axial ratio. Following the same logic as previous interpretations (Michikami et al., 2010), we can therefore conclude that the boulders on the surface of Dimorphos were likely formed by catastrophic disruption.

2.5.3 Image selection of other rubble pile asteroids surfaces

We selected the most suitable images available for our study of the surfaces of Itokawa, Ryugu and Bennu (Figures 2.8 and 2.9) in order to produce the most reliable morphological analyses possible. These asteroids were selected based on their rubble pile nature (Fujiwara et al., 2006; Watanabe et al., 2019; Lauretta et al., 2019) and the high resolution images we have of their surfaces (Nakamura et al., 2001; Kameda et al., 2017; Rizk et al., 2018). The selection of images was based on several criteria: the pixel resolution must be under 0.1 m/px; if available, the phase angle should be under 20° to minimize boulder shadowing effects; and finally if available, we tried to select images from varied locations on the surface of the asteroids. Based on our image selection criteria, the detailed boulder analysis of these asteroids were determined from different images at different locations if available for Itokawa, Ryugu and Bennu. For Itokawa, we selected 7 images with a total of 277 boulders detected, located at 2 different areas. For Ryugu we selected 8 images with a total of 318 boulders detected, based on the distance of the spacecraft with the asteroid (i.e. resolution) but the phase angles were not available. Finally, for Bennu, we randomly selected 12 images at 12 different locations because images retrieved by the OSIRIS-REx missions offered an almost global coverage of very high resolution images, for a total of 955 boulders. The detailed data of each images are detailed in Table 2.2.

Body	File name	Resolution (m/px)	Phase Angle (°)	Emission Angle (°)	Latitude	Longitude
Dimorphos	dart_0401930049_43695_02_iof	0.055	59.73	0.58–74.59	-9.3	262.6
Itokawa	st_2530297837_v	0.065	17.93	36.62	-4.5	179.1
Itokawa	st_2532629277_v	0.075	10.66	51.5	-20.9	84.4
Itokawa	st_2539429953_v	0.022	16.71	47.82	-6.1	89.4
Itokawa	st_2539437177_v	0.058	17.44	47.24	9.7	53.5
Itokawa	st_2539444467_v	0.062	16.05	24.24	9.1	49.8
Itokawa	st_2539451609_v	0.065	15.29	19.28	10.5	50.4
Itokawa	st_2539467169_v	0.050	16.56	68.78	9.8	153.2
Ryugu	hyb2_onc_20180921_034938_tvf	0.063	-	-	11.3	141.8
Ryugu	hyb2_onc_20180921_040634_tvf	0.055	-	-	14.7	127.5
Ryugu	hyb2_onc_20180921_041826_tvf	0.081	-	-	13.8	115.5
Ryugu	hyb2_onc_20181003_003121_tnf	0.095	-	-	-12.6	27.1
Ryugu	hyb2_onc_20181003_021156_tvf	0.076	-	-	-23.7	312.3
Ryugu	hyb2_onc_20181015_130841_tuf	0.074	-	-	4.3	235.4
Ryugu	hyb2_onc_20181015_133137_tpf	0.060	-	-	5.1	217.6
Ryugu	hyb2_onc_20190710_232532_tvf	0.096	-	-	-0.1	5.4
Bennu	20210407T070929S250_pol_iofL2pan	0.050	10.43	65.93	-59.9	345.2
Bennu	20210407T033629S004_pol_iofL2pan	0.050	8.42	48.4	-50.5	285.6
Bennu	20210407T044726S838_pol_iofL2pan	0.049	7.98	51.21	-47.3	188.1
Bennu	20210407T053451S162_pol_iofL2pan	0.049	8.30	63.85	-61.9	124.5
Bennu	20210407T063137S357_pol_iofL2pan	0.050	9.41	63.27	-59.4	42.0
Bennu	20210407T062633S202_pol_iofL2pan	0.048	8.89	15.92	-13.7	45.9
Bennu	20210407T054353S664_pol_iofL2pan	0.048	8.60	5.30	-6.7	104.9
Bennu	20210407T033605S787_pol_iofL2pan	0.049	10.05	4.61	-4.0	282.1
Bennu	20210407T092153S748_pol_iofL2pan	0.048	12.61	4.51	-2.3	161.4
Bennu	20210407T060703S295_pol_iofL2pan	0.050	9.58	69.96	60.3	60.6
Bennu	20210407T044147S537_pol_iofL2pan	0.051	11.07	88.02	76.0	161.2
Bennu	20210407T072730S766_pol_iofL2pan	0.050	9.29	64.61	57.8	317.8

Table 2.2: Available observation data used for image selection on Dimorphos, Itokawa, Ryugu and Bennu from PDS. Some information is not yet publicly available for Ryugu.

The images of Itokawa were taken by the AMICA (Nakamura et al., 2001) instrument on board the Hayabusa spacecraft, the images of Ryugu were taken by the ONC-T camera (Kameda et al., 2017) instrument onboard the Hayabusa-2 spacecraft, and the images of Bennu were taken by OCAMS (Rizk et al., 2018) onboard the OSIRIS-REx spacecraft.

2.5.4 Comparative morphological analysis of boulders on rubble pile asteroids

The contours of boulders were detected and retrieved semi-automatically (see Figure 2.9). The subsequent morphological analysis was performed using the same analysis pipeline as for the image of Dimorphos. The average values and the standard deviations of calculated morphological parameters are displayed in Table 2.3 for all studied asteroids.

The boulders analysed on the surface of the four rubble pile asteroids are all between 0.33 m to 12.15 m in equivalent diameter. These four rubble pile asteroids exhibit striking similarities in the distributions and average parameters of boulder shapes (Table 2.3). The mean roundness values span from 0.49 to 0.56, circularity ranges between 0.84 and 0.90 and solidity varies from 0.95 to 0.96. The ellipsoidal axial ratio extends from 0.66 to 0.71 and the bounding box axial ratio extends from 0.70 to 0.75 (Figure 2.11). Both of these axial ratios

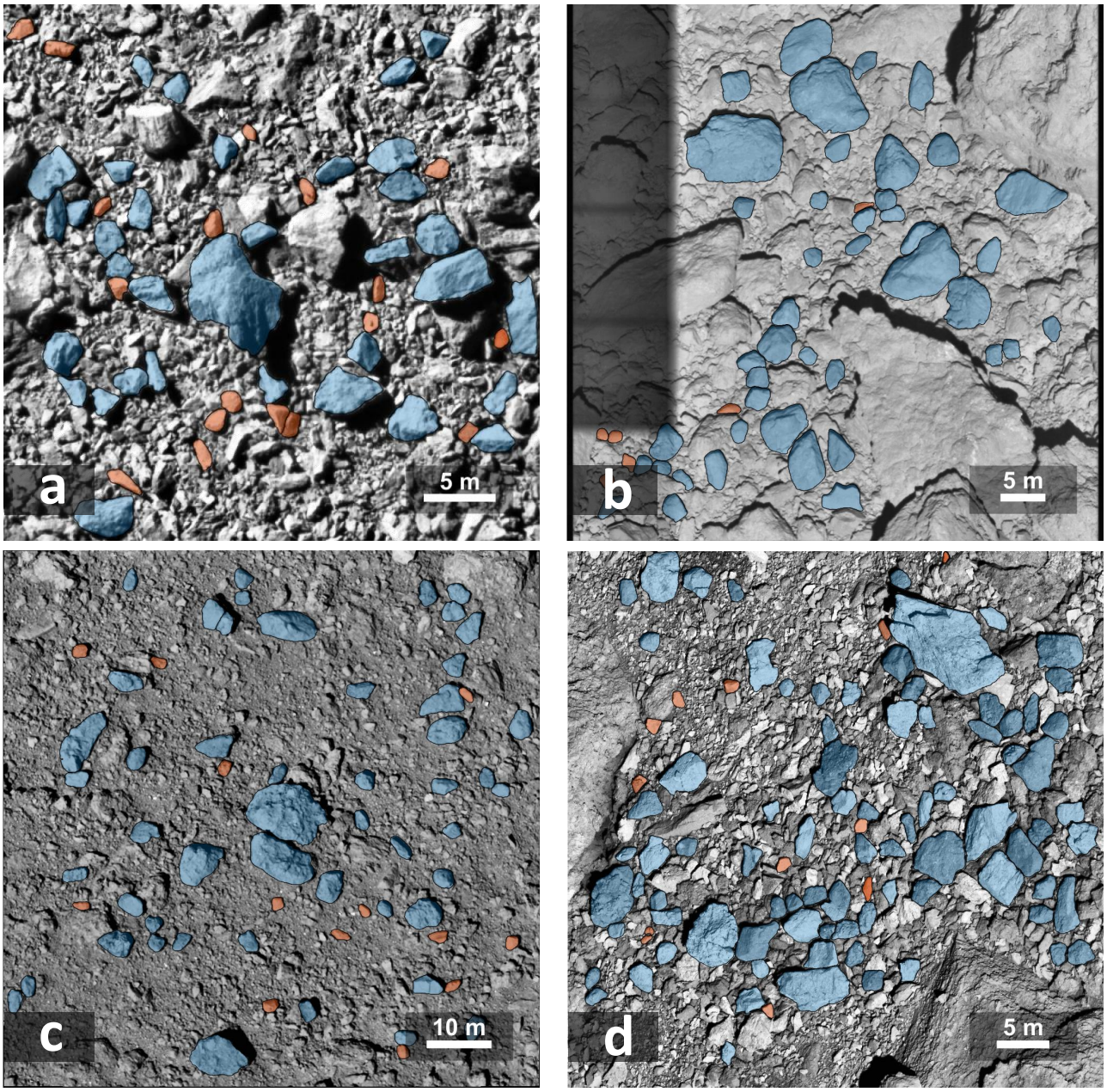

Figure 2.9: Examples of one of the High-resolution images for each asteroid surfaces studied. The images contrast have been enhanced with a CLAHE filtering for visualisation purposes only (Zuiderveld, 1994). a) Dimorphos of the (65803) binary system Didymos taken by DRACO (Fletcher et al., 2022) (`dart_0401930049_43695_02_iof`) (the only image analysed for this body), b) Asteroid (25143) Itokawa taken by AMICA (Nakamura et al., 2001) (`st_2539437177_v`)) (1 of the 7 images analysed), c) Asteroid (162173) Ryugu taken by ONC-T (Kameda et al., 2017) (`hyb2_onc_20180921_041826_tvf`) (1 of 8 images analysed), d) Asteroid (101955) Bennu taken by OCAMS (Rizk et al., 2018) (`20210407T033629S004_pol_iofL2pan`) (1 of the 12 images analysed). All other images analysed can be find in the supplementary information. Boulders selected and analysed are coloured in blue and red. The red boulders indicate the smaller resolved boulders (<30px), which haven't been included in the analysis of the resolution dependant morphological parameters.

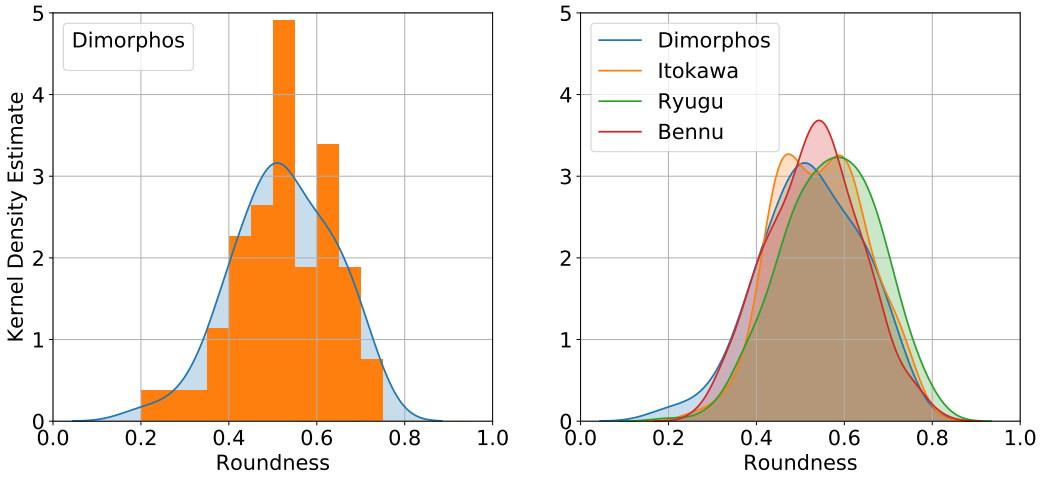

Figure 2.10: (Left) Distribution of the roundness of the boulders with a diameter larger than 30 px at the surface of Dimorphos. The orange histogram shows the distribution and the blue shaded region represents the kernel density estimate of the internal friction angle for Dimorphos. (Right) Kernel density estimates of the roundness of surface boulders with a diameter larger than 30 px on Dimorphos (blue with 34 boulders), Itokawa (orange with 230 boulders), Ryugu (green 267 boulders) and Bennu (red with 703 boulders).

are consistent with previous measurements made for boulders larger than 5 m on Itokawa (Michikami and Hagermann, 2021) and Ryugu (Michikami et al., 2019); 0.62 ± 0.19 and 0.70, respectively.

As for Dimorphos, the roundness values of the surface boulders analysed here can also be used to estimate the angle of internal friction of the surface material of each of these asteroids (Figure 5) giving values of $32.2 \pm 2.5°$, $31.6 \pm 2.5°$ and $31.1 \pm 2.7°$ for asteroids Itokawa, Ryugu and Bennu, respectively. These values are consistent with numerical simulations suggesting a friction angle $\lesssim 35°$ for Bennu (Zhang et al., 2022), and the surface slopes on Bennu at the site of the sample collection, which were $\leq 40°$ (Lauretta et al., 2022; Barnouin et al., 2019). This gives an average internal friction value for all of the boulders on the four rubble pile asteroids of $31.8 \pm 5.1°$. Similarly to the analyses of Dimorphos, we only selected boulders with a diameter larger than 30 pixels. We note that these are estimates for the bulk internal friction angle for a material constituted only from the boulders. This provides a reasonable approximation of the bulk internal friction angle for bodies that seem to be dominated by such boulders. However, any finer material present will also influence the bulk material properties (Sánchez et al., 2025), so this value should only be interpreted as the internal friction angle of the boulder-material.

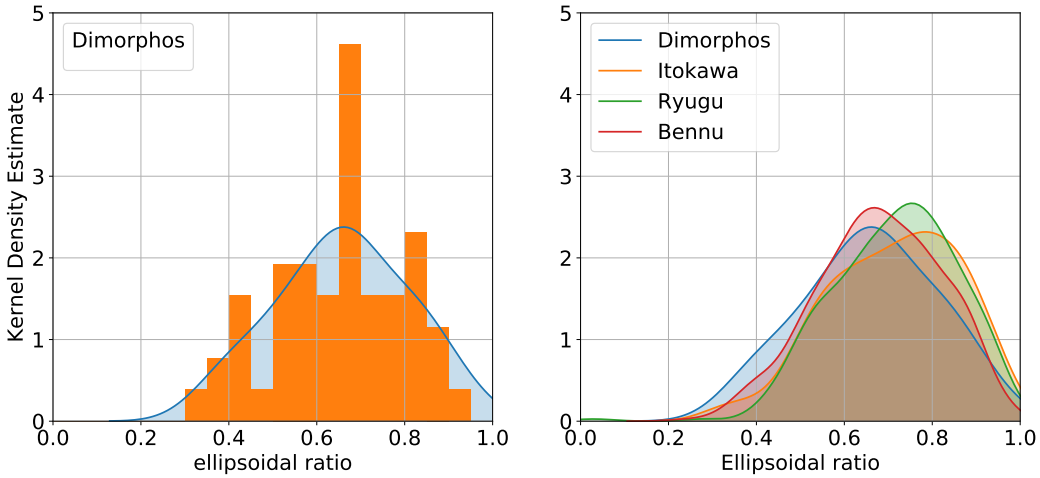

Figure 2.11: (Left) Distribution of the ellipsoidal ratio of the boulders at the surface of Dimorphos. The orange histogram shows the distribution and the blue shaded region represents the kernel density estimate of the internal friction angle for Dimorphos. (Right) Kernel density estimates of the ellipsoidal ratio of surface boulders on Dimorphos (blue with 53 boulders), Itokawa (orange with 277 boulers), Ryugu (green with 318 boulders) and Bennu (red with 955 boulders).

Despite the diverse global morphologies and varying spectral classes (indicative of different lithologies) of these four rubble pile asteroids, the shared resemblance of boulder morphology strongly suggests a common formation mechanism as well as a common response to this mechanism, responsible for shaping the boulders across their surfaces. By comparison with laboratory impact experiments (Michikami et al., 2016), the measured axial ratio for boulders on all four asteroids supports the catastrophic disruption hypothesis (Chapman, 1978), as previously suggested for Itokawa and Ryugu (Michikami and Hagermann, 2021) and suggested above for Dimorphos.

2.5.5 Discussion of the results

In the absence of direct measurements of mechanical properties, we showed that images can be used to constrain the angle of internal friction of asteroid material through a detailed morphological analysis of the surface boulders. We show that the boulders on the surfaces of four different small (<1 km) rubble pile asteroids show strikingly similar morphologies suggesting a common boulder formation mechanism as well as a common response to this mechanism. In general, many factors can influence the observed shapes of boulders on

Asteroid	(65803) Dimorphos		(25143) Itokawa	
	All	>30 px	All	>30 px
Number of boulders analyzed	53	34	277	230
Average boulder diameter (m)	2.15 ± 0.94	2.55 ± 0.96	2.36 ± 1.71	2.60 ± 1.76
Boulder diameter (min/max/median) (m)	1.07/6.64/1.89	1.67/6.64/2.26	0.33/10.70/2.12	0.66/10.70/2.33
Roundness *	0.49 ± 0.10		0.54 ± 0.10	
Circularity *	0.84 ± 0.09		0.90 ± 0.08	
Solidity	0.95 ± 0.02		0.96 ± 0.02	
Sphericity	0.61 ± 0.12		0.67 ± 0.12	
Axial ratio: Bounding box	0.70 ± 0.17		0.74 ± 0.16	
Axial ratio: Ellipsoidal	0.66 ± 0.15		0.71 ± 0.15	

Asteroid	(162173) Ryugu		(101955) Bennu	
	All	>30 px	All	>30 px
Number of boulders analyzed	318	267	955	703
Average boulder diameter (m)	3.52 ± 1.67	3.77 ± 1.70	2.04 ± 0.98	2.35 ± 0.96
Boulder diameter (min/max/median) (m)	1.22/10.39/3.04	1.65/10.39/3.29	0.51/12.15/1.85	1.45/12.15/2.10
Roundness *	0.56 ± 0.11		0.51 ± 0.10	
Circularity *	0.90 ± 0.09		0.86 ± 0.09	
Solidity	0.96 ± 0.03		0.95 ± 0.02	
Sphericity	0.67 ± 0.11		0.63 ± 0.11	
Axial ratio: Bounding box	0.75 ± 0.16		0.72 ± 0.16	
Axial ratio: Ellipsoidal	0.71 ± 0.14		0.68 ± 0.14	

Table 2.3: **Mean values of the morphological characteristics of the studied boulders** Mean and standard deviation values of the morphological characteristics of boulders at the surface of different rubble pile bodies. The boulder diameters reported here are the equivalent diameters. Morphological characteristics with * are resolution-dependant and are computed only using boulders with diameter >30 px, and these should be considered as higher limits.

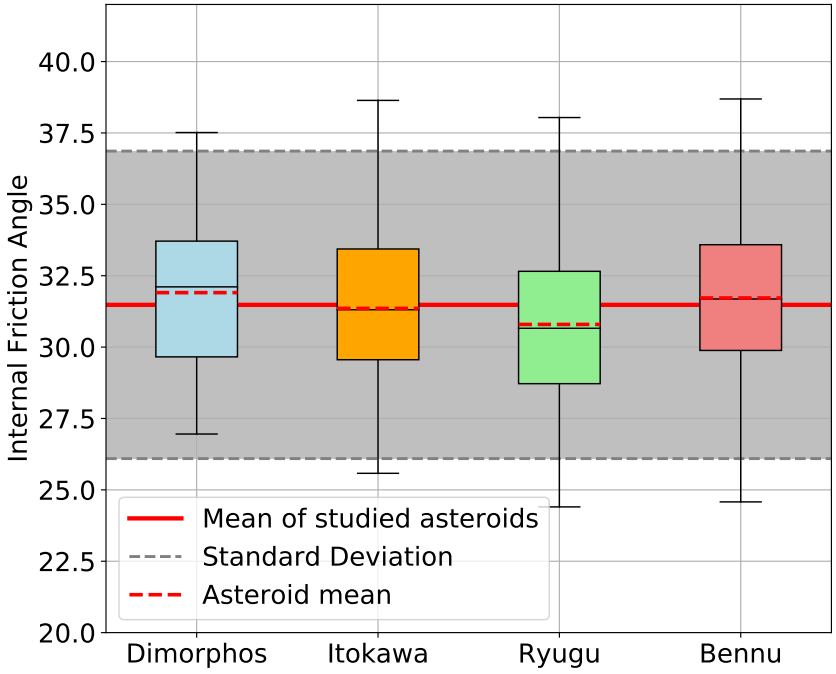

Figure 2.12: Boxplots of the internal friction angles values from the boulders larger than 30 pixels analyzed on the images of Dimorphos 34 boulders), Itokawa (230 boulders), Ryugu (267 boulders) and Bennu (703 boulders), see Figure 2. The red dotted line is the mean internal friction angle of boulders on each asteroid, the black line is the median, the limit of the boxes are the lower and upper quartiles of the distribution and the limits outside the boxes are the lower and upper extremes. The red line in the background is the average of the 4 asteroids and the shaded area lies between the propagated standard deviation between all 4 asteroids.

planetary surfaces such as their original shapes, their lithology or the nature, violence and duration of the alteration process that the boulders went through (Krumbein and Pettijohn, 1966). Usually, it is difficult to attribute the observed morphology to one factor such as the formation mechanism. However, in the case of the dry- and atmosphere-less asteroid surface, alteration and erosion processes are likely to be minimal; the material is transported around asteroid surfaces (Miyamoto et al., 2007; Murdoch et al., 2015) but due to the low gravity environment, any motion will occur at low speed, and the small normal force will reduce friction interactions (Murdoch et al., 2013, 2021). This decreases the influence of erosion, except for episodic events such as impacts (Ballouz et al., 2020). In the case of impact disruption, it was found that the original target shape does not strongly affect the final fragment shape but are strongly influenced by the kinetic energy of the projectile (Michikami et al., 2016). Furthermore, although the lithologies of the studied asteroids are different, we still find similar boulder morphologies. Consequently, a shared formation process can explain the similarities in boulder shape amongst the four asteroids.

The measured boulder axial ratios support the catastrophic disruption formation hypothesis for small rubble pile asteroids (Chapman, 1978), as previously suggested for Itokawa, Ryugu and Eros (Michikami and Hagermann, 2021). Following the same logic as previous work, our results suggest that the boulders on Dimorphos were also formed through catastrophic disruption, later followed by rotation-driven mass transfer between the two satellites in the binary system. This implies either that catastrophic disruption was involved in the binary asteroid formation, or more likely that the process forming the secondary did not significantly modify the boulder morphology, since we are still witnessing morphological markers indicating catastrophic disruption. Also note that Dimorphos' boulders have the smallest value of mean axial ratios probably because the image was taken with a higher phase angle than the other images of asteroids (See Table 2.2), which can influence the shape distribution (Michikami et al., 2010).

Other processes could shape boulders at the surface of asteroids such as thermal fatigue (Dombard et al., 2010; Delbo et al., 2014; Molaro et al., 2020). Indeed, cracks that may have been formed by such a process have been identified at the surface of Dimorphos and it is predicted that 10-100 Myr are needed to break the boulders (Lucchetti et al., 2024). However, Dimorphos' surface is relatively young ($\leq$ 0.3 Myr) (Barnouin et al., 2023). It is, therefore, unlikely that thermal processing has had sufficient time to reshape boulders after the formation of the binary asteroid (Pajola et al., 2024).

On the other hand, from our measurements of the angularity of individual boulders, we constrained what should be considered an upper limit of the mean bulk angle of internal friction of the surface boulders of these rubble pile asteroids. This average value amongst Itokawa, Ryugu, Bennu and Dimorphos is 31.8 ± 5.1°. Regarding Dimorphos, the bulk angle of internal friction of the ensemble of boulders at the DART impact site is found to be 32.7 ± 2.5°, indicating that Dimorphos boulders are typical rubble pile boulders, and that the angle of internal friction of a rubble pile would be independent of spectral type and, by extension, composition.

In the future, it would be interesting to include more images of Dimorphos' surfaces in these analyses. The European Space Agency Hera mission (Michel et al., 2022a, 2025) will provide global images of the surfaces of both Dimorphos and Didymos allowing more detailed analyses to be made of the DART target, and allowing for a comparison of the boulder morphology on the surfaces of the primary and secondary asteroids. However, it will not be possible to perform a better analysis of the area we studied, as the area does not exist anymore after the DART impact.

2.5.6 Application and use of the results in other studies

As previously stated, mechanical properties, such as the internal angle of friction, are key parameters that significantly influence the modelling and understanding of the DART impact event, because it changes the behaviours and response of the asteroid in such studies (Stickle et al., 2022). The results of the study I led have notably been used to model the DART impact, taking as input parameter the angle of internal friction (Raducan et al., 2024). The simulation that best matched the observations of the impact indicates that Dimorphos has a cohesive strength of less than a few Pascals, similar to other rubble-pile asteroids like Ryugu or Bennu.

The image analysis technique was also complementary to the analysis of the shape model of Dimorphos (Barnouin et al., 2023). Combined with other image analysis and a shape model of Dimorphos, it was observed that no rock or boulder sits on any slope exceeding 35°. If there is no cohesion between the boulders or rocks, this 35° angle is equal to the angle of internal friction between two rocks or boulders at the surface of Dimorphos, which is in accordance with our study as an upper estimate. Additionally, Barnouin et al. (2023) propose a crater-size frequency analysis indicating that the surface age of Didymos is 40-130 times older than Dimorphos, with respective ages of $\approx$ 12.5 Myr and $<$ 0.3 Myr.

Therefore, our findings are useful for the continued interpretation of the DART impact, for planetary defense efforts that rely on estimates of asteroid mechanical properties in order to estimate the potential damage an asteroid may cause if it were to impact the Earth (Hills and Goda, 1993; Collins et al., 2005; Mathias et al., 2017; Rumpf et al., 2020), and to evaluate the effectiveness of key asteroid deflection techniques (Council, 2010).

2.6 New studies of boulder morphology since 2022

In parallel of our study or after it has been published other publications also studied morphologies of boulders at the surface of Dimorphos or other asteroids. For example, as we were finishing this study, Jawin et al. (2023) was published, where boulders around the sampling site of OSIRIS-REx have been analysed through their albedo, morphology and surface roughness. This study highlighted four morphological groups within the observed boulders and using documented contacts between those different groups, they conclude that boulders on Bennu originated from a single parent body that was disrupted. They also highlighted that these boulders bear striking resemblance with boulders at the surface of Ryugu, as we have also shown.

In the same set of publications as our study, Pajola et al. (2024) showed that Dimorphos' boulder size frequency distribution suggests that Dimorphos inherited boulders coming from Didymos, the larger asteroid of the binary system, and that the boulders were formed by multi-phase fragmentation.

More recently, Shimizu et al. (2025) mapped the majority of boulders at the surface of Ryugu and Bennu to study their size-frequency distributions and axial ratios and notably observed a latitudinal particle size sorting on both asteroids. However, where Bennu displays features of material movements towards its equator, Ryugu's features indicate material movements towards its poles. This study explain this difference by their different rotation periods and demonstrate that variations of a few hours in rotation period, can drastically change the gravitational field on an asteroid, sometimes even reversing local gravity direction as it is the case here.

Finally, one of the most recent publication has been Tusberti et al. (2025). In this study, the authors propose a lithologic study of Dimorphos' surface, based on a morphological analysis of its boulders. They were notably able to identify two main morphological classes: 178 angular and rough boulders, interpreted as igneous or metamorphised rocks, originating from

deep regions of the parent body and 210 more round and friable looking boulders interpreted as a breccia lithology, that would be characteristic of the outer layers of the parent body.

All these different studies show the variety of results and interpretations that can be made from the morphological analysis of boulders at the surface of asteroids.

2.7 Conclusion

In this chapter, we presented the morphological analysis pipeline, originally developed to be used for the WheelCams images. We took the opportunity to test and validate the pipeline on real space mission data, and participated in the effort of the understanding of the DART impact, as well as the formation of the Didymos binary system and help constrain the properties of Dimorphos. However, we saw that the pipeline is actually limited by the resolution of the images studied. The WheelCams have a pixel resolution of 100 μm at 30 cm distance (Murdoch et al., 2025), and particles at the surface of Phobos are thought to be in the 300 μm to 2 mm size range (see Sect. 1.3.2). Following the same approach of our study of Dimorphos, it will be possible to analyse the detailed morphology of the regolith of Phobos from its largest grains: at 30 cm, a particle of 2 mm large will be 20 pixels large, which is the limit to compute roundness values, even if they will be underestimated. In order to verify this idea, we tested the morphological analysis pipeline on images of the MMX WheelCam testbed and we were able to retrieve morphological parameters from these as well as what should be considered as upper limits of the internal friction angles of the observed materials.

Chapter 3

From simulated micro-parameters to bulk properties

In this chapter, we will explore how it is possible to measure the bulk properties of simulated granular materials, in order to characterize the materials that have been used in C. Sunday's thesis (Sunday, 2022). Indeed, the Discrete Element Method (DEM), that has been chosen to investigate the wheel-surface interactions in the scope of the Idefix rover, defines the mechanical properties of granular materials with their inter-particle properties. To measure the bulk properties of a simulated material, we first investigate methods for replicating direct shear experiments with the discrete element method. Then, these simulations will be used to measure the angle of friction and bulk cohesion of simulated granular materials.

3.1 Simulation of granular materials

Regolith, as a granular material, can be modelled with different approaches: with an Eulerian or Lagrangian methods, or even hybrid methods. All these methods have their advantages and disadvantages, depending on the type of simulated granular system and the problem studied.

Regolith, as a granular material, can be modelled using numerical methods that adopt either an Eulerian or Lagrangian point of view, or hybrid formulations that combine both. Each method offers different advantages depending on the density regime, the degree of flow or deformation, and the physical processes of interest.

From an Eulerian perspective, the granular medium is described on a fixed spatial grid, and the evolution of the physical parameters such as stresses, strains, and flow fields are

solved at fixed locations. Various constitutive relationships, often based on macroscopic laboratory experiments, govern how the granular material deforms or flows under external loading (Mühlhaus et al., 2001). For example, dense granular surfaces can be represented as a viscoplastic continuum whose deformation is controlled by local state variables such as pressure, packing fraction, or shear rate (da Cruz et al., 2005; Jop et al., 2006; Dunatunga and Kamrin, 2015). Eulerian methods are well suited to model scenarios dominated by bulk deformation or high strain rates, where grain-scale details can be homogenized across the granular medium. However, because Eulerian approaches rely on averaged parameters, it is difficult to capture transitions where the granular medium switches between solid-, liquid-, and gas-like behaviours.

In contrast, a Lagrangian perspective tracks the motion of each material element or grain as it moves, making it particularly well suited to capture grain-scale rearrangements, contact forces, or the transitions between the different material states. In this regard, the Discrete Element Method (DEM), explicitly follows individual particles and their interactions. Depending on how collisions and contacts are treated, various DEM schemes exist: Hard-Sphere DEM (HSDEM), Soft-Sphere DEM (SSDEM), Contact Dynamics (CD) or Molecular Dynamics (MD).

In HSDEM, grains are considered as rigid, and at each time step, the collisions are predicted based of the distance between two objects, and the outcomes of the collisions are found by resolving a set of impulse and constraint equations (Jean, 1999). Thus, HSDEM computation is fast as the relations after collisions are analytic, however resulting in the simplification of many physical phenomena (Kosinski et al., 2020).

In SSDEM, grains are treated as deformable bodies: bodies are permitted to overlap upon collision, and the overlapping is used to compute the resulting forces and torques acting on each body. Then, at each time step the equations of motion are integrated to update the positions of the grains (Cundall and Strack, 1979). SSDEM requires smaller time steps but adapts well to parallel computing techniques, as SSDEM uses time-stepping integration: all contacts can be resolved together in a matrix, where in HSDEM the simulation advance from one collision event to another (Stratton and Wensrich, 2010). It performs well for dense systems, slow flows, and problems where persistent contacts matter.

Both HSDEM and SSDEM reproduce macroscopic penetration and loading behaviour by resolving particle-scale dynamics (Pazouki et al., 2017). However, HSDEM cannot reproduce

phenomena such as shock propagation and requires artificial thresholds for stability (Pazouki et al., 2017).

Although DEM, and particularly SSDEM, provides high physical fidelity, it is computationally expensive, typically running at Real Time Factor (RTF) values of 3000–15000 (Hu et al., 2025) with the RTF defined as the amount of time a computer works to simulate 1 second of the system. An RTF of 1 signifies real-time performances, RTF > 1 indicates the computer is slower than real time and RTF < 1 means the computer is faster than real time (Unjhawala et al., 2025).

The CD method also uses a fully Lagrangian point of view, resolving non-smooth contacts, impenetrability, and Coulomb friction without penalization parameters (without artificial parameters such as stiffness or damping) (Moreau, 1988, 1997; Radjai et al., 1999; Radjai and Vincent, 2009). It is especially suited for stiff, densely packed granular systems where explicit soft-sphere methods are slower. On the other hand, MD is very versatile. Indeed, it can be used to study both dense and dilute granular flows (Dippel and Wolf, 1999). MD can also consists of simulations of small samples of granular materials that are then used to derive macroscopic relations to describe the material as a continuum (Luding, 2004). MD has also been used to model 2D granular materials with grains composed of triangles forming convex and concave shapes (Poeschel and Buchholtz, 2002). It is also widely used for understanding the physical behaviour of biological macromolecules. For example, proteins are studied as dynamic models and the simulations predict the movements of the atoms constituting the protein. The interactions between these atoms are based on interatomic physics (Karplus and McCammon, 2002; Hollingsworth and Dror, 2018).

Finally, hybrid Eulerian–Lagrangian approaches have been developed to improve computational efficiency (Chen et al., 2015, 2021). Common implementations include finite-volume or finite-difference solvers as well as the Material Point Method (MPM), a hybrid Eulerian–Lagrangian scheme in which material points carry state variables while computations occur on a background grid (Dunatunga and Kamrin, 2015, 2017). Current models typically run at RTF of 30–150 (Hu et al., 2025). An example is the simulation framework used for the VIPER rover, where a DEM model ran on a Central Processing Unit (CPU) for the rover while an Eulerian continuum terrain model ran on a Graphical Processing Unit (GPU), exchanging coupling parameters to advance in time efficiently (Hu et al., 2025). Another partially Eulerian method is Resistive Force Theory (RFT), which estimates local stresses on an intruding body by decomposing it into segments and approximating the granular resistance

each segment experiences (Maladen et al., 2009). Initially developed for sand-swimming organisms, RFT has been used to model wheel–soil interactions in terramechanics (Li et al., 2013). As a semi-empirical method, it relies on experiments to characterize granular response.

Given the scientific goals of studying grain-scale processes and the behaviour of regolith under low gravity—where transitions between static, flowing, and ballistic regimes are essential, C. Sunday selected a SSDEM approach for simulations relevant to the MMX rover on Phobos (Sunday, 2022). SSDEM is widely used in planetary science for simulating low-gravity granular processes (Wada et al., 2006; Tancredi et al., 2012; Matsumura et al., 2014) and is a standard tool for modelling spacecraft and rover interactions with planetary surfaces (Johnson et al., 2015; Thuillet et al., 2018; Zhang et al., 2020; Ballouz et al., 2021).

3.2 *Project Chrono* and its SSDEM

A variety of software packages have been developed to model granular materials using the Soft-Sphere Discrete Element Method (SSDEM), Sunday (2022) notably identified different SSDEM frameworks including YADE (Kozicki and Donzé, 2009), LIGGGHTS/LAMMPS (Kloss and Goniva, 2011), *pkdgrav* (Schwartz et al., 2012), and ESyS-Particle (Tancredi et al., 2012). On the other hand, Dosta et al. (2024) compared different open-source DEM frameworks such as Blaze-DEM (Govender et al., 2016), granOO (André et al., 2015), Kratos Multiphysics (Dadvand et al., 2010), the open source version of LIGGGHTS, LIGGGHTS-public (Kloss et al., 2012), MercuryDPM (Weinhart et al., 2020), MUSEN (Dosta and Skorych, 2020) and a more recent version of Yade (Smilauer et al., 2021). For all the different softwares, several case studies have been run to test their basic functionalities. Dosta et al. (2024) shown that by simulating a similar initial setup leads to similar results for most cases and the deviations or differences obtained have been attributed to the differences in the implementation of contact models. This study also showed that running DEM codes on the GPU can reduce computational time by an order of magnitude compared to the fastest multithread CPU simulations.

To investigate wheel–regolith interactions, C. Sunday employed *Project Chrono* (or *Chrono*), which was reviewed by Naomi Murdoch alongside some of the previously cited and other DEM codes (Murdoch, 2018).

Chrono has been selected in this thesis in order to continue the work of Sunday (2022), who investigated how the low-gravity environment on Phobos could influence the landing, sinking

and roving behaviour of the Idefix rover, if Phobos is covered by regolith. The SSDEM of *Chrono* has notably been improved and validated by C. Sunday during her thesis, allowing to show that sinkage is independent of gravity in the quasi-static regime and that driving behaviours can be predicted when the driving speed is scaled with gravity.

Chrono is an open-source C++ multi-physics simulation engine developed and maintained by the University of Wisconsin–Madison and the University of Parma (Tasora et al., 1998, 2016, 2018). The platform supports both soft- and hard-body dynamics through a wide range of modules that implement various methods such as SSDEM, HSDEM, and continuum-based models. One of *Chrono*'s main advantages is its ability to simulate complex geometries, including detailed wheel designs, full rover assemblies, and non-spherical particles, using predefined triangular meshes or custom shapes created with a *SolidWorks* plug-in, a 3D computer-aided design (CAD) software own by Dassault Systèmes. In this study, only spherical particles were used and all other geometries are referred to as box objects throughout the manuscript.

Another strength of *Chrono* is its ability to simulate motion through built-in motor models, which can apply forces or torques to set objects in motion, which is very convenient to model wheel-regolith interactions, or other experiments. It is also possible to "fix" objects, that will remain immobile under any perturbation while still providing an accurate physical response to the bodies in contact.

In *Chrono*, the soft sphere discrete element method is integrated into three different modules of the code:

Chrono::Engine This module runs a simple SSDEM algorithm running on a single CPU.

Chrono::Multicore Also known as the Chrono::Parallel module in *Chrono* 4.0.0 and earlier, it runs a more complex SSDEM algorithm using OpenMP, an application programming interface (API) made for shared-memory parallel computing with CPUs.

DEM-Engine (DEME) This module runs in the Compute Unified Device Architecture (CUDA, developed by NVIDIA®) language to allow parallel computing with GPUs and allows to simulate poly-disperse granular materials and can handle complex shapes generated from assemblies of spheres, called clumps (Zhang et al., 2024).

For simulations with more than a few thousands particles, it is more efficient and often necessary to use parallel computing (Mazhar et al., 2011), which is the case to simulate

the most realistic regoliths. Simulations ran in C. Sunday's thesis between 2019 and 2022 have been conducted with the Chrono::Multicore module since the Chrono::Granular module was still under development. The simulations in this thesis have also been run with the Chrono::Multicore module as it has been validated (Sunday et al., 2020) and to ensure the continuity and extend the work that has already been done with it.

In Chrono::Multicore, the soft-sphere discrete element method algorithm can be divided into three fundamental steps. First, all contact points, i.e. the position where 2 bodies overlap, in the system are identified, including both particle-to-particle and particle-to-wall contact pairs. Next, forces and torques are computed for each contact pair, as a function of the overlap and accumulated on the corresponding bodies, and then used to update their positions and velocities. Finally, the system state is refreshed and the particles are advanced in preparation for the next iteration. These three stages are referred to as collision detection, system advance, and system update and a further detailed below.

Collision detection The collision detection is performed in two different phases: the "Broad-phase" and the "Narrow-phase" (Mazhar et al., 2013). First, during the "Broad-Phase", the system is spatially binned (see Figure 3.1a) and all the bodies are approximated by their Axis Aligned Bounding Boxes (AABBs). The AABB of an object is a rectangular box defined by the minimum and maximum coordinates along each axis enclosing the object (see Figure 3.1b). The Broad-Phase aims to determine if any contact is possible: if two AABBs of two different objects are in the same bin, a contact can potentially occur.

Once these potential contacts has been identified, the second phase is the "Narrow-Phase", that determines if the contact actually occurs or not, with the real shapes of the objects: if there is an overlap, there is a contact. The Narrow-Phase also determines the magnitude of the overlap i.e. the depth of penetration between two objects depending on the geometries of the bodies and the geometry of the contact. For example, the Narrow-Phase algorithm in *Chrono* takes into account if the particle encounters a face, an edge or a corner of a wall.

System Advance The Chrono::Multicore module advances its system using a custom first-order semi-implicit Euler integration integrator. This notably means that the system is sensitive to the time step of the system: if it is too large, the system will be unstable but small time steps recquire more computing time. The integration step computes the resulting forces and torques from collisions using a user-defined contact force model, available in the *function_CalcContactForces* function of the Chrono::Multicore module. When setting-up

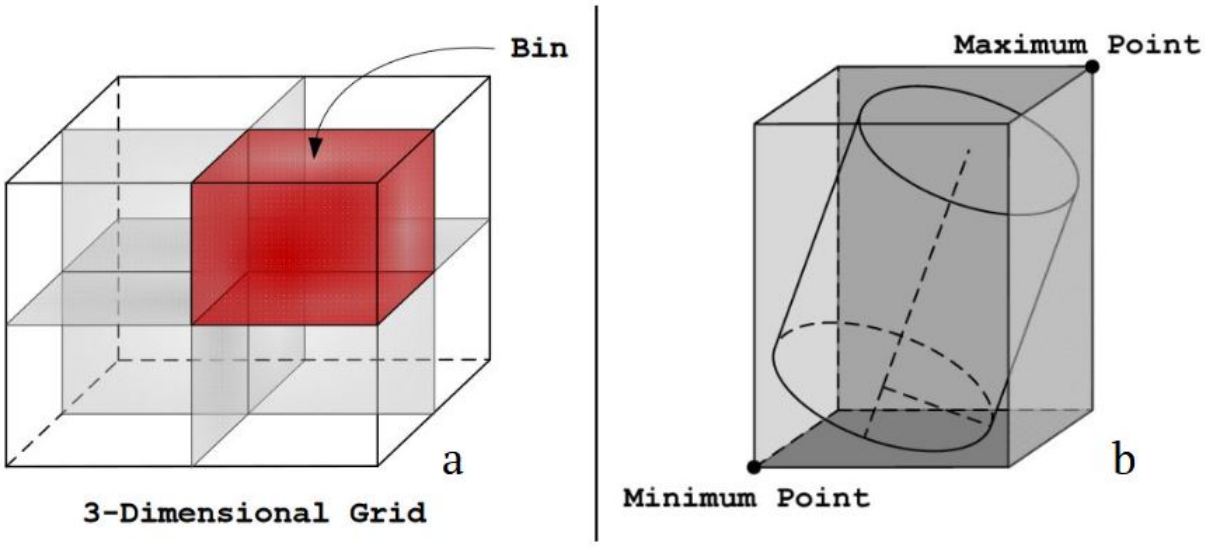

Figure 3.1: a) Example of a spatially binned 3D environment. b) Example of the Axis Aligned Bounding Box (AABB) of a cylinder. From Mazhar et al. (2013).

a simulation the user can choose between 3 different contact models for normal forces: a Hookean contact model (Tsuji et al., 1992), a Hertzian contact model or the Flores model (Flores et al., 2011). Tangential contact forces can either be computed independently at each time step or updated based on the stored displacement history from previous steps (Fleischmann et al., 2015). The module also includes rolling and twisting friction models as well as 3 different cohesion models acting as attractive forces between bodies. One of these can be added to the system, using either a constant force model, the Derjaguin-Muller-Toporov (DMT) model, or the Perko model (Perko et al., 2001). Many other models exist such as wet granule cohesive models. For example, the Johnson Kendall-Roberts (JKR) model and its simplified version (SJKR) (Carr et al., 2023; Ajmal et al., 2020) is largely used, however, it is not clear which model accurately describe the nature of cohesive contacts between particles (Huynh et al., 2025).

System update Finally, all the informations about the system is gathered for the current time step and integrated to update the positions, velocities and torques of all the bodies for the next time step.

3.2.1 Description of the adopted physical models

In this section, I will describe the chosen physical models allowing to perform contact physics from the depth of overlaps to new positions of the bodies in the system, that have been used

Variable	**Symbol**	units
Adhesion factor	C	J/m^2
Coefficient of restitution	e	-
Coefficient rolling friction	μ_r	-
Coefficient spinning friction	μ_t	-
Coefficient of static friction	μ_s	-
Cohesive force	$\vec{F_c}$	N
Contact normal unit vector	$\hat{n}$	
Effective mass	$\bar{M}$	kg
Effective radius	$\bar{R}$	m
Effective Shear modulus	$\bar{G}$	Pa
Effective Young's modulus	$\bar{E}$	Pa
Gravitational acceleration	$\vec{g}$	m/s^2
Mass of a particle	m	kg
Normal damping	g_n	N.s/m
Normal force	$\vec{F_n}$	N
Normal overlap	δ_n	m
Normal relative velocity	$\vec{v_n}$	m/s
Normal stiffness	k_n	N/m
Poisson's ratio	ν	-
Radius of a particle	r	m
Radius of the overlap	r_c	m
Relative rotational velocity	$\vec{v_{rot}}$	rad/s
Rolling friction moment	$\vec{M_r}$	N.m
Rotational velocity	$\vec{\omega}$	rad/s
Spinning friction moment	$\vec{M_t}$	N.m
Tangential damping	g_t	N.s/m
Tangential force	$\vec{F_t}$	N
Tangential relative velocity	$\vec{v_t}$	m/s
Tangential stiffness	k_t	N/m
Torque	$\vec{T}$	N.m
Translational velocity	$\vec{v}$	m/s
Young's modulus	E	Pa

Table 3.1: Symbols of the variables and parameters used in *Project Chrono* to compute the forces and torques. The "effective" values are the effective values for a contacting pair.

to conduct all the simulations during this PhD thesis. All the parameters and variables can be found in Table 3.1.

First and foremost, positions and velocities of the bodies in the system are updated at the end of each time step by resolving all forces and torques in the n-body systems following these two equations:

$$m_i \frac{d\vec{v}_i}{dt} = m_i \vec{g} + \sum_{j=1}^{n} (\vec{F_n} + \vec{F_c} + \vec{F_t}) \tag{3.1}$$

$$I_i \frac{d\vec{\omega}_i}{dt} = \sum_{j=1}^{n} (\vec{T} - \vec{M_{r,i}} - \vec{M_{r,j}}) \tag{3.2}$$

with m, I, $\vec{v}$ and $\vec{\omega}$ respectively the particle mass, rotational inertia, translational velocity, and rotational velocity. $\vec{F_n}$, $\vec{F_c}$ and $\vec{F_t}$ are the normal, cohesive and tangential force vectors, $\vec{g}$ is the gravitational acceleration, and $\vec{T}$ is the torque such as $\vec{T} = r_i \vec{F_t} \times \hat{n}$, where r_i is the particle radius and $\hat{n}$ is the unit vector normal to the contact. $\vec{M_{r,i}}$ and $\vec{M_{t,i}}$ are respectively the moments generated by rolling and twisting friction. The following paragraphs describe how the forces $\vec{F_n}$, $\vec{F_c}$ and $\vec{F_t}$ and moments $\vec{M_{r,i}}$ and $\vec{M_{t,i}}$ are computed in *Project Chrono*. Figure 3.2 represents an interaction between two particles with the forces involved in Eq. 3.1..

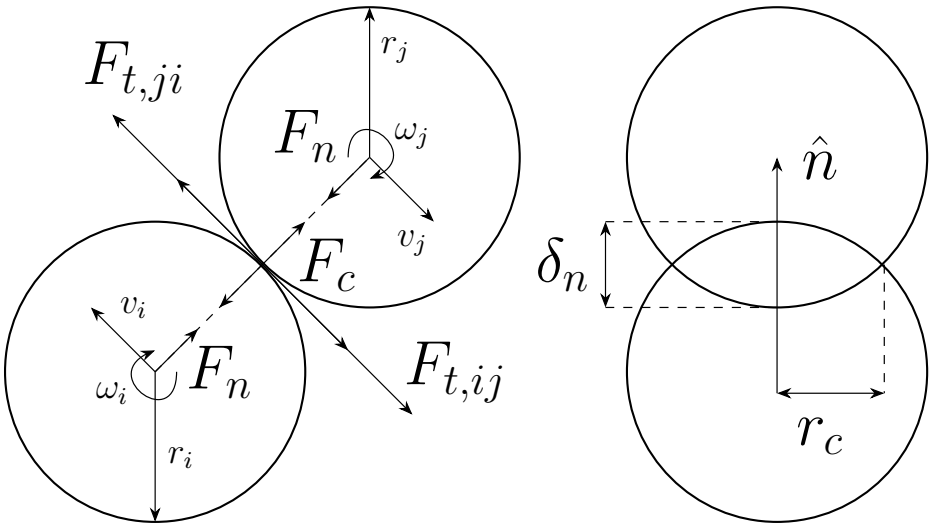

Figure 3.2: Schematic of the interaction between particles 'i' and 'j'. F_n, F_c and F_t are the normal, cohesive and tangential forces acting on the bodies, $r_{i,j}$ is the particle radius, $v_{i,j}$ is the translational velocity, $\omega_{i,j}$ is the rotational velocity, δ_n is the particle overlap, r_c is the radius of the overlap between the particles and $\hat{n}$ unit vector, normal to the contact. Friction moments are not represented. Adapted from Sunday et al. (2020).

First, the contact force model chosen is the Hertzian model (Tsuji et al., 1992), which has been the overall most accurate model compared to laboratory experiments and other numerical works for sphere-sphere contacts and for piling and tumbler tests (Sunday et al., 2020).

Normal force $\vec{F_n}$

This Hertzian visco-elastic model calculates the normal force $\vec{F_n}$ as follows:

$$\vec{F_n} = k_n \delta_n^{3/2} \hat{n} - g_n \delta_n^{1/4} \vec{v_n} \tag{3.3}$$

with k_n is normal stiffness, g_n is normal damping, and $\vec{v_n}$ is the normal component of the relative velocity $\vec{v}$ at the point of contact:

$$\vec{v} = \vec{v_j} - \vec{v_i} + r_j(\hat{n} \times \vec{\omega_j}) - r_i(\hat{n} \times \vec{\omega_i}) \tag{3.4}$$

$\vec{v_i}$ and $\vec{v_j}$ are the translational velocities and $\vec{\omega_i}$ and $\vec{\omega_j}$ are the rotational velocities of particles i and j. k_n and g_n are calculated directly in the code depending on user-supplied body properties as follows:

$$k_n = \frac{4}{3}\bar{E}\sqrt{R} \tag{3.5}$$

$$g_n = \frac{-2\ln(e)}{\sqrt{\ln^2(e) + \pi^2}}\sqrt{\frac{5}{6}}\sqrt{\frac{3}{2}Mk_n} \tag{3.6}$$

with $\bar{E}$ the effective Young's modulus, $\bar{M}$ the effective mass and $\bar{R}$ the effective radius of the contacting pair of particles i and j such as $\bar{E} = \left(\frac{1-\nu_i^2}{E_i} + \frac{1-\nu_j^2}{E_j}\right)^{-1}$, $M = \left(\frac{1}{m_i} + \frac{1}{m_j}\right)^{-1}$ and $\bar{R} = \frac{r_i r_j}{(r_i + r_j)}$ for a sphere-sphere interaction. For an interaction between a sphere and a flat surface for example, $\bar{R} = r$, the radius of the sphere. $\nu_{i,j}$, $E_{i,j}$, $m_{i,j}$ and $r_{i,j}$ are respectively the Poisson's ratios, the Young's moduli, the masses and the radii of the individual particles i and j of the colliding pair. Those parameters are defined by the user.

Tangential force $\vec{F_t}$

The tangential force $\vec{F_t}$, is limited by the Coulomb friction condition, enabling a maximum force $\vec{F_{t,max}}$ such as:

$$|\vec{F_{t,max}}| = \mu_s|\vec{F_n} + \vec{F_c}| \tag{3.7}$$

with $\vec{F_c}$, the cohesive force between the contacting pair and the user-supplied coefficient of static friction μ_s, on which the condition between tangential slipping or sticking is based. Below the slipping threshold, $\vec{F_t}$ is defined in the Hertzian model such as:

$$\vec{F_t'} = -k_t\delta_n^{\frac{1}{2}}\vec{\delta_t} - g_t\delta_n^{\frac{1}{4}}\vec{v_t} \tag{3.8}$$

with k_t, the tangential stiffness, $g_n t$ the tangential damping, and $\vec{v_t}$, the tangential component of the relative velocity $\vec{v}$ at the point of contact. k_t and g_n are computed similarly to their normal counterparts, depending on user-supplied material properties such as:

$$k_t = 8\bar{G}\sqrt{R} \tag{3.9}$$

$$g_t = \frac{-2\ln(e)}{\sqrt{\ln^2(e)+\pi^2}}\sqrt{\frac{5}{6}}\sqrt{Mk_t} \tag{3.10}$$

with $\bar{G}$ the effective shear modulus of the contacting pair of particles i and j such as $\bar{G} = \left(\frac{2(2+\nu_i)(1-\nu_i)}{E_i} + \frac{2(2+\nu_j)(1-\nu_j)}{E_j}\right)^{-1}$.
If $|\vec{F_t'}| \geq |\vec{F_{t,max}}|$, then $|\vec{F_t}| = |\vec{F_{t,max}}|$. The condition for calculating the tangential force can be summarized as follows:

$$\vec{F_t} = min\left[\mu_s|\vec{F_n} + \vec{F_c}|\frac{\vec{\delta_t}}{|\delta_t|}, \vec{F_t'}\right] \tag{3.11}$$

Cohesive force $\vec{F_c}$

The cohesive force model used is based on the work of Perko et al. (2001). It has been selected and added to *Chrono* as part of C. Sunday's thesis (Sunday, 2022), due to its frequent use in the planetary science field (Scheeres et al., 2010). This model gives the van der Waals force between two bodies (see Eq. 1.2), as a function of the cleanliness factor S, a parameter to quantitatively describe soil particles surfaces with different adsorbate thicknesses (i.e. thickness of a layer of gas or liquid molecules), the Hamaker constant A, depending on the composition of the regolith and its dielectric properties, the effective radius $\bar{R}$ and an inter-particle distance Ω. The cohesive force $\vec{F_c}$ is applied along the contact normal direction $\hat{n}$ as a function of an adhesion factor C as follows:

$$\vec{F_c} = -C\bar{R}\hat{n} \tag{3.12}$$

$$C = \frac{AS^2}{48\Omega^2} \tag{3.13}$$

Scheeres et al. (2010) uses the constants for lunar regolith: $A = 4.3 \times 10^{-20} J$ and $\Omega = 1.5 \times 10^{-10}$ giving:

$$\vec{F_c} = -3.6 \times 10^{-2} S^2 R\hat{n} \tag{3.14}$$

These values are thus valid for Moon-like conditions and are a conservative estimate for asteroid and small body surfaces though a little bit under-estimated as they are computed for the surface of the Moon where there is still some remnant atmosphere contributing to surface contamination (Scheeres et al., 2010). A "clean" surface, like the lunar regolith on the sun side can tend to $S = 1$ while in terrestrial sites, the presence of the atmosphere and

water vapour gives $S \approx 0.1$ (Perko et al., 2001).

Note that the cohesive force in the Perko model is a function of the effective radius of the contacting pair: as explained earlier (see Sect. 3.2.1) for a particle-particle interaction, the effective radius $\bar{R}$ is $\bar{R} = \frac{r_i r_j}{(r_i + r_j)}$ and if $r_i = r_j = r$, $\bar{R} = r/2$. For a particle-wall interaction, the effective radius in *Chrono* used for contact physics is r, the radius of the sphere in contact with the wall. This is important to note, because it means that for a simulation with cohesion, this force will be on average twice stronger for particle-wall interactions.

Rolling friction $\vec{M}_r$

Chrono follows the approach of Schwartz et al. (2012) for the rolling friction, acting as a rolling resistance, added to *Project Chrono* along with the spinning friction during C. Sunday's thesis (Sunday, 2022). The torque of the rolling friction $\vec{M}_{r,i}$ is calculated when two particles in contact exhibit a relative rotational motion with a velocity $\vec{v_{rot}}$. These calculations are as follows:

$$\vec{M}_{r,i} = \mu_r r_i \frac{(\vec{F}_n \times \vec{v_{rot}})}{|\vec{v_{rot}}|} \tag{3.15}$$

$$\vec{v_{rot}} \equiv r_i(\omega_i \vec{\times} \hat{n}) - r_j(\vec{\omega_j} \times \hat{n}) \tag{3.16}$$

with the user-supplied μ_r rolling coefficient, r_i the particle radius, $\vec{F}_n$ the normal force, $\hat{n}$ the orientation of the contact and $\vec{\omega_{i,j}}$ the respective rotational velocities of particles i and j.

Spinning friction $\vec{M}_t$

Similarly to rolling friction, spinning friction or twisting resistance follows the approach of Schwartz et al. (2012). This resistance occurs when two bodies in contact experience relatives spinning velocities around their contact normal axis $\hat{n}$. The spinning friction is calculated as follows:

$$\vec{M}_{t,i} = \mu_t r_c \left[\frac{(\omega_j \vec{-} \omega_i) \cdot \hat{n}}{|\vec{\omega_j} - \vec{\omega_i}|} \right] \vec{F}_n \tag{3.17}$$

where r_c is the radius of the overlap between two bodies, defined as the scalar distance from the contact point out to the circumference of the circle that describes the intersection of the two particles' surfaces (see Figure 3.2), μ_t the spinning friction coefficient and $\omega_{i,j}$ the respective rotational velocities of bodies i and j.

Therefore, following all these calculations, the values of the forces $\vec{F_n}$, $\vec{F_c}$ and $\vec{F_t}$ are used in Eq. 3.1 and the values of the moments of rolling and spinning frictions $\vec{M_n}$ and $\vec{M_t}$ are used in Eq. 3.2. These steps are repeated for each contact, at each time step of a simulation. The other contact and cohesion models available in *Chrono* are described in Sunday et al. (2020).

3.2.2 Motivation and objectives using *Project Chrono*

Thanks to this whole physical model we are able to simulate precise granular material behaviour. However, we can see in Table 3.1 that all these parameters are grain-scale parameters and these are really difficult to infer from space missions. In the context of the MMX mission, we want to interpret the Idefix behaviour from the WheelCams observations thanks to simulations run with *Project Chrono*. To do so, we need to be able to know or measure the bulk properties of the simulated granular materials such as the angle of internal friction and bulk cohesion of the material, mentioned in Sect. 1.2.2.

On Earth, these parameters can be obtained with laboratory experiments, like shear testing. Shear testing is a method used to determine the strength of a material, whose parameters are the internal friction angle and the bulk cohesion of the material obtained thanks to the Mohr-Coulomb failure criterion (Taylor, 1948) (Sect. 1.2.2 and Eq. 1.5). The principle of the test is to shear a sample of a material under different normal stresses, and when the material fails or after a certain displacement, the shear stress is measured. It is then possible to perform a linear regression of the measured points at the different normal stresses and deduce the unknown values $tan(\theta)$ and c, the macroscopic shear strength properties of the material.

Therefore, we want to replicate a shear test experiment with *Chrono* to infer the bulk strength parameters of the simulated granular material. However, we first need to make sure that *Chrono* is suitable for such experiments. Indeed, the particle-particle interactions have been validated (Sunday et al., 2020), however, it is not the case for interactions with box objects. It was not critical when focusing on the grain behaviours, but to perform shear test, we need to make sure that we understand how the box objects register the forces and if they record them correctly, or if they interact correctly with particles, especially for moving box objects.

Notably, in Sunday et al. (2020), the contact arrays were sized with the assumption that one body can hold a maximum of 20 contacts in *Chrono 5.0.0* and contact information can

be lost, especially on a plate where hundreds to tens of thousands of contacts can occur for one object (Sunday, 2022). During this thesis, we used *Chrono 7.0.0*, where the previous behaviour has been fixed.

In the next section, the tests conducted to physically validate and understand how the box objects behave, will be presented.

3.3 The physics of box objects in *Project Chrono*

In *Project Chrono*, box objects are usually used as walls, grounds or roofs, to form objects acting as containers for granular materials for example. Each of them can act as a sensor, as we have access to various variables at each time step such as its position, velocity, acceleration and the total forces and torques acting on this object. Notably, we want to use box objects to perform shear tests of simulated granular materials, in order to characterise them.

3.3.1 Fixed wall - particles interactions

First, we tested the behaviours of "fixed" box objects. A fixed object in *Chrono*, is an object that doesn't move with respect to the absolute reference of the system, despite constraints, forces or anything else that could put it in motion (even motors).

Sliding, rolling and spinning frictions

First, sliding, rolling and spinning frictions with fixed box-shaped bodies has been verified with tests 5, 6 and 7 in Sunday et al. (2020), respectively corresponding to a sliding test between two box objects, a rolling test of a particle on a box object and a spinning test of a particle on top of a box-shaped. While box objects are largely used with *Chrono* (Kwarta and Negrut, 2017; Sunday et al., 2020, 2021, 2022; Sunday, 2022; Hu et al., 2025; Zhang et al., 2025), collisions and their ability to record forces to act as sensors have not been validated with simple tests similar to the tests conducted by C. Sunday for particle-particle interactions.

First, we will test that the normal forces are correctly registered by the box objects for any number of particles in contact with it. Then, we will test that the cohesion between a box object and a particle is correctly computed. At the beginning of each subsection, a summary outlining the test, our expectations, and the motive for the test is provided.

Parameter	Symbol	Value	unit
Young's modulus	E	7×10^7	Pa
Poissons's ratio	ν	0.24	-
Coefficient of static friction, grain-to-grain	$\mu_{s,pp}$	0.16	-
Coefficient of static friction, grain-to-wall	$\mu_{s,pw}$	0.45	-
Coefficient of rolling friction	μ_r	0.09	-
Coefficient of spinning friction	μ_t	0	-
Coefficient of restitution, grain-to-grain	e_{pp}	0.9	-
Coefficient of restitution, grain-to-wall	e_{pw}	0.5	-
Adhesion factor	C	0	J/m^2
Particles radius	r	3.75	mm
Particles density	ρ	2480	kg/m^3
Gravity	g	-9.81	m/s^{-2}
Time step	Δt	100	μs
Force model	-	Hertz	-
Cohesion model	-	Perko	-

Table 3.2: DEM parameters for validation tests. Values from Sunday (2022).

Normal force

Test Free-falling particles on a box object.
Expectation The weight of all particles is registered by the box object.
Motive Make sure that box objects record forces correctly for any number of particles and thus can act as force sensors.

The first test we conducted was a free-fall test of particles on a fixed ground (see Figure 3.3) with different numbers of particle. The user-set parameters for the particles are the parameters for non-frictional glass beads available in Table 3.2.

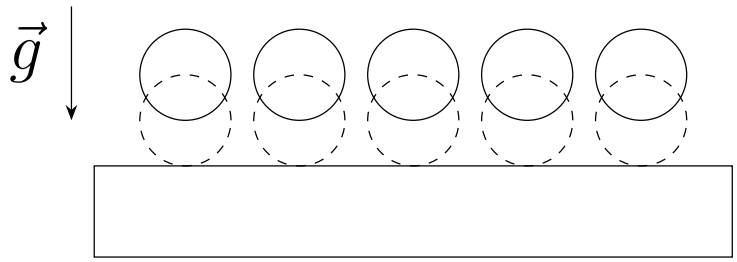

Figure 3.3: Schematic of the free-fall validation test. $\vec{g}$ is the gravitational acceleration.

This test is considered successful if the force registered by the ground is the sum of the weights of the particles. If the force is less than expected, not all contacts are detected or registered. For one particle, with a 3.75 mm radius, and a 2480 kg/m^3 density, under a 9.81 m/s^{-2} gravity, the expected force is its weight $P = mg = \rho \cdot \frac{4}{3}\pi r^3 \cdot g = 5.37$ mN.

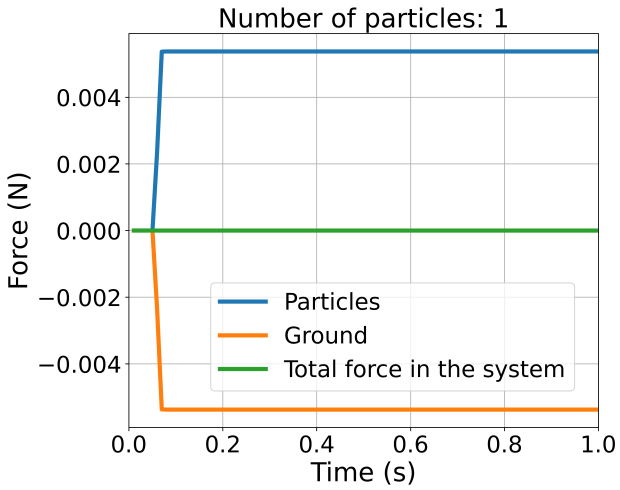

Figure 3.4: Force acting on a particle and on the ground for a particle free-falling on the ground as a function of time. The observed behaviours are the same for 3, 12, 75, 330 and 8925 particles.

Number n of particles	Weight of n particles (mN)	Last registered force value (mN)	Last registered force value divided by n (mN)
1	5.37	−5.37	−5.37
3	16.12	−16.12	−5.37
12	64.49	−64.49	−5.37
75	403.06	−403.06	−5.37
330	1773.44	−1773.44	−5.37
8925	47963.55	−47963.55	−5.37

Table 3.3: Expectation and results of the free-fall test with different numbers of particles.

The test conducted with one particle gives at equilibrium a force of −5.37 mN registered by the box object and an equivalent force of 5.37 mN registered by the particle (see Figure 3.4, the z axis is pointing upward). The results of this test are in Table 3.3. We can see that all collisions are detected and registered and that the values are those expected. The box objects can therefore correctly register simultaneous collisions from a large number of particles.

Cohesive force

Test Separation of bodies stuck together by cohesion using gravity.
Expectation If the weight of the body (mass × gravity) is higher or equal to the cohesive force, the bodies separate.
Motive Make sure that box objects apply cohesive force as expected.

Now that we verified that contacts between particles and box objects are correctly registered with a large number of particles in *Chrono*, we want to know how particles interact with box

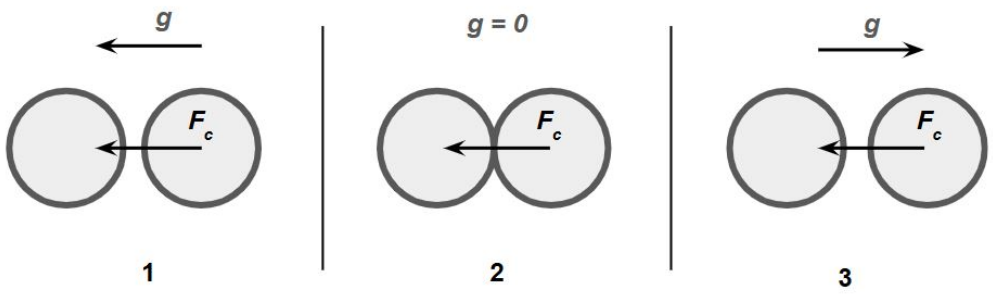

Figure 3.5: Schematic of the different steps of the cohesion test. The fixed particle is on the left.

objects when we add cohesion to the system. For this purpose, we ran similar simulations to those in Sunday et al. (2020) to test the cohesive force: in our case, we stuck two bodies together, one of them is fixed and the other is falling on top with gravity. Gravity is then removed in order for the cohesive force to be the only force in the system, sticking the bodies together. Finally, we reverse the gravity, in opposition to the cohesive force, in attempt to separate the unfixed body from the fixed one (see Figure 3.5). We performed this test in 3 different setups, one with the gravitational force smaller than the cohesive force ($mg < F_c$), another with the gravitational force equal to the cohesive force ($mg = F_c$) and finally one with the gravitational force larger than the cohesive force ($mg > F_c$). In order to compare particle-particle interactions and particle-box objects interactions, we performed these three tests with two particles and with one particle and one box object, with two different thicknesses of box objects, for a total of 9 tests. We tested different thicknesses of box objects to make sure that the thickness of box objects has no influence on the cohesion between box shape objects and particles, as it does for the sizes of particles when two of them are in contact.

The parameters used for these tests are shown in Table 3.4. As explained earlier (Sect. 3.2.1), for a contact to experience the same cohesive force between two particles and between a particle and the flat surface of a box object, the adhesion factor, which is the user-defined parameter for cohesion, has to be two times smaller than for a particle-particle contact (see row *Adhesion factor* in Table 3.4). For the other parameters, we used similar particle properties that were used in Sunday et al. (2020) in these tests.

These tests are considered successful if the bodies remain in contact when $mg < F_c$ and separate when $mg \geq F_c$ (i.e. no contact force).
For the same cohesive forces, but different adhesion factors, Figure 3.6 shows that the be-

Parameter	Symbol	Test 1	Test 2	Test 3	Test 4	Test 5	Test 6	Test 7	Test 8	Test 9	unit
Young's modulus	E	5×10^6	-	-	-	-	-	-	-	-	Pa
Poissons's ratio	ν	0.3	-	-	-	-	-	-	-	-	ø
Coefficient of static friction, grain-to-grain	$\mu_{s,pp}$	0.3	-	-	-	-	-	-	-	-	ø
Coefficient of static friction, grain-to-wall	$\mu_{s,pw}$	0.3	-	-	-	-	-	-	-	-	ø
Coefficient of rolling friction	μ_r	0	-	-	-	-	-	-	-	-	ø
Coefficient of spinning friction	μ_t	0	-	-	-	-	-	-	-	-	ø
Coefficient of restitution, grain-to-grain	e_{pp}	0	-	-	-	-	-	-	-	-	ø
Coefficient of restitution, grain-to-wall	e_{pw}	0	-	-	-	-	-	-	-	-	ø
Adhesion factor	C	40	-	36	20	20	18	20	20	18	J/m^2
Cohesive force	F_c	10	-	9	10	10	9	10	10	9	N
Particles radius	r	0.5	-	-	-	-	-	-	-	-	m
Wall thickness	t	ø	ø	ø	1	1	1	10	10	10	m
Particle mass	m	1	-	-	-	-	-	-	-	-	kg
Gravity level	g	8	10	11	8	10	11	8	10	11	m/s^{-2}
Time step	Δt	10	-	-	-	-	-	-	-	-	μs
Force model	ø	Hertz	-	-	-	-	-	-	-	-	ø
Cohesion model	ø	Perko	-	-	-	-	-	-	-	-	ø

Table 3.4: DEM parameters for cohesive validation tests. Values from Sunday et al. (2020). Dashes indicate that the value is the same as for Test 1.

haviours are similar for particle-particle interactions and wall-particles interactions, regardless of the wall thickness. For tests 1, 4 and 7 ($mg < F_c$) bodies remain stuck together, and the contact force stabilised at $F = F_n - F_c = mg - F_c = -2N$, the difference between the weight of the particle (as a repulsive force) and the cohesive force. For tests 2, 3, 5, 8, 6 and 9, ($mg \geq F_c$), we can see that there is no contact after the body separating from the other reach a certain accumulated acceleration. The tests are thus successful.

3.3.2 Moving particles with box objects

After confirming that interactions between fixed box objects and particles behave as expected, we want to verify that box objects set in motion move particles correctly. As highlighted earlier (Sect. 3.3.1), box objects are largely used, also to set particles in motion. In this section, material parameters are those of Table 3.2.

Moving particles vertically with box objects

The first test we conduct is an elevator test i.e., particles in contact with a box object moving vertically. One way to put an object in motion in *Chrono*, is to update its position at each time step, we refer to this method as teleportation. With this method, moved box objects remain "fixed". For this first test, we wanted to verify that particles reach the expected velocity, i.e. the velocity of the ground/elevator. To do so, we revisited simulations we made to test the normal forces (Figure 3.3) but when the system is at equilibrium, the ground is set in motion upward, with a speed of 20 mm/s. The test has 3 steps, first the settling of the particles on the ground, then, when equilibrium is reached, the ground is set in motion

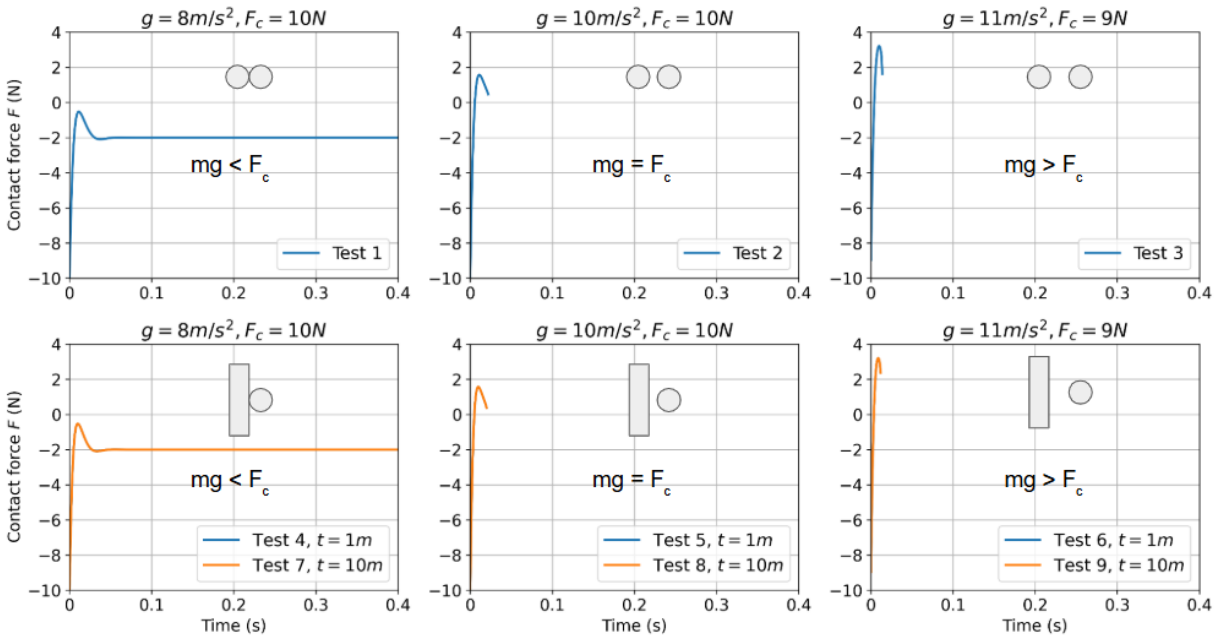

Figure 3.6: Contact force during the cohesive force tests with schematics representing the corresponding test. Similar tests with different wall thicknesses are overlapping (Tests 4 and 7, 5 and 8, 6 and 9) and shown on the same plots. Gravity is "activated" at the beginning of the test, trying to separate the bodies. Bodies in tests 1, 4 and 7 remain in contact while bodies in tests 2, 3, 5, 8, 6 and 9 separate.

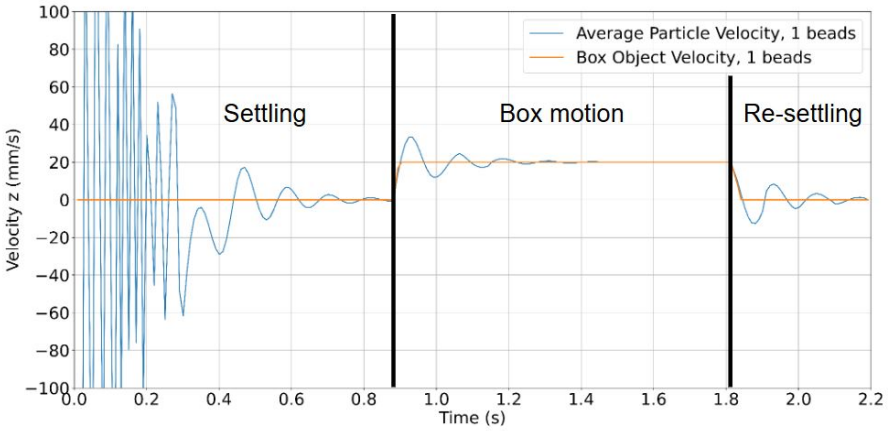

Figure 3.7: Average velocity of the particles and velocity of the ground during the elevator test. The settling step is from 0 to 0.9 s, the motion of the ground is from 0.9 to $\approx$ 1.8 s and the re-settling is from $\approx$ 1.8 to 2.2 s. The average results of the tests are the same for 1, 8 and 75 particles.

and finally, the motion of the ground is stopped and we let the particles re-settled.

The test has been conducted with 1, 8 and 75 particles on the ground (see Figure 3.7), with no difference between them as the initial conditions are identical for all tests and all particles. First, during the settling phase (from 0 to $\approx$ 0.9 s) we can see the particles bouncing on the floor, giving an oscillating average particle velocity. The velocity is really high because the particles are given a 100 mm/s velocity towards the ground. At the end of the settling, the particles reached the intended velocity of nearly zero. Then, the box object is set in motion and as its desired velocity is instantaneously reached, the particles first bounce and then after a few moments reach equilibrium with the ground, with the expected velocity of 20 m/s. When the motion of the box object stops at 1.8 s, the particles quickly decelerate and then bounce again before settling. While physically correct because of the instantaneous motion of the ground, the "bouncing" behaviour of the particles appears somewhat unrealistic but quickly resolves itself over time. If we want to suppress this behaviour, we should add acceleration to the box object by updating its position progressively before reaching the intended velocity i.e., before linearly updating its position.

Moving particles horizontally with box objects

Teleporting box objects After this test, we wanted to verify that we can also laterally move particles using box objects. To do so, we filled a box of $50 \times 50 \times 25$ mm open on the top with 5 mm radius particles, then we place a plate on top of the particles before updating

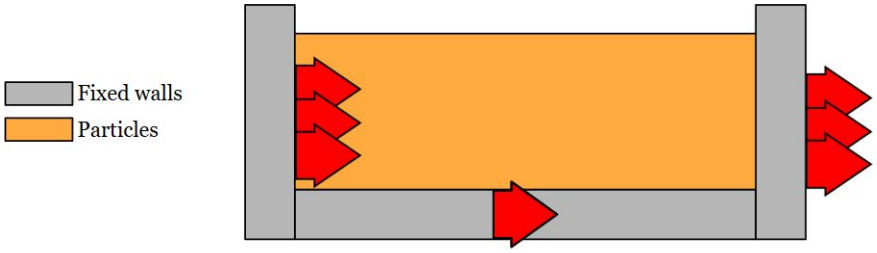

Figure 3.8: Schematic of the horizontal particle displacement test. Red arrows show the direction of the movement.

the box objects' positions (or teleporting the box objects) at each time step. First step of the simulation is the filling of the box: particles are generated as a particle cloud and are given a 1 m/s speed in random directions to ensure a random arrangement of the particles, then we let settle. Finally, when equilibrium is reached, the "fixed" box objects forming the container are set in motion with a speed of 20 mm/s. Similarly to the previous test, the particles quickly reach the desired velocity. This time we can see more oscillations (see Figure 3.9) but it is most likely due to the fact that with this test, all the sample is displaced and particles may collide going back and forth during the movement of the box.

With an increased number of particles (i.e a larger box, of $120 \times 60 \times 60$ mm) in the same setup, we observe that the particles nearest to the side walls of the container in the direction of the movement, are the most likely to move, while those at the center of the box exhibit less displacement at the end of the simulation (see Figure 3.10). This behaviour suggests that the friction between the particles and the ground may not be effective and only the particles pushed by the wall are correctly displaced (as in the elevator test), and the particles near the wall of the other side move as they fall forward because of gravity.

To test the hypothesis that the friction between the ground and the particles is not acting with this simulation method, we conducted a simple simulation: particles are placed on top of a box object of 50×50 mm, that is set in lateral motion at 20 mm/s, repeating the setup of the normal force test and vertical motion of particles.

We can see on Figure 3.11 that the particles are not moving with respect to the ground, except for the furthest one in the negative x-axis, which falls when reaching the edge of the ground (see Figure 3.12).

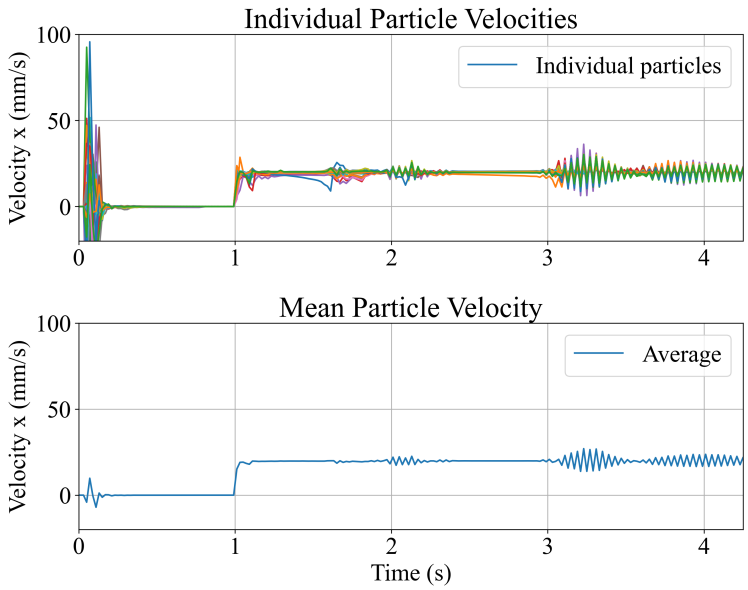

Figure 3.9: Velocity of the individual particles (top) and average velocity of the particles (bottom) in the box during the horizontal displacement test. The filling of the box is from 0 to 1 s, then the "fixed walls" are moved laterally at a 20 mm/s speed.

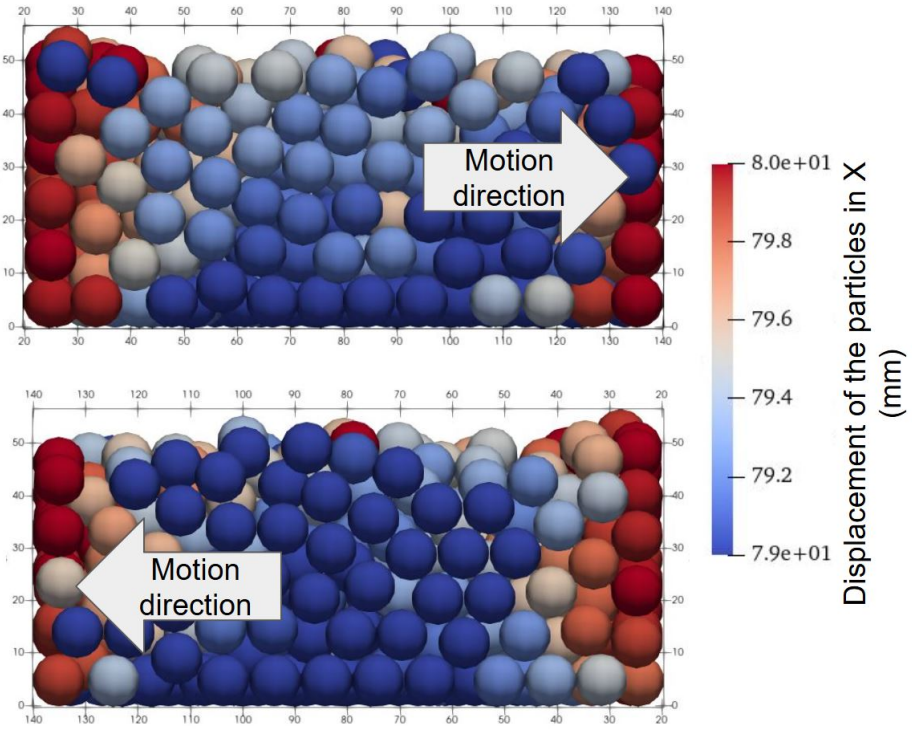

Figure 3.10: Visualisation of the displacement of particles inside of a container made of box objects after a 80 mm displacement of all the box objects constituting the container with teleportation. The particles are coloured according to their X-axis displacement from their original position before the box started moving. The visualisation has been rendered with ParaView (Ahrens et al., 2005; Ayachit, 2015).

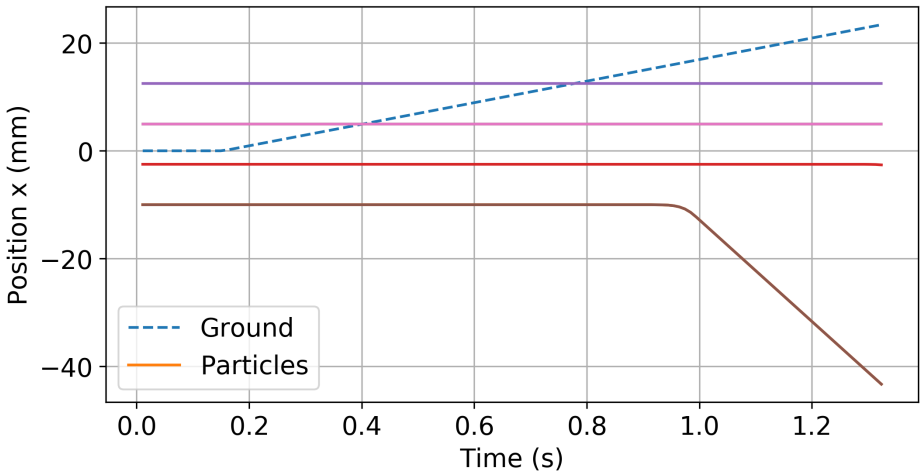

Figure 3.11: Position in x of the particles and the ground during the friction test. Particles settle down on the ground before 0.2 s and then the ground moves towards positive x. There are 6 particles in the simulation, 2 pairs share the same x position. The blue dashed line is the evolution of the position of the box object on which the particles rest. When the box object is moving forward, the particles do not move, expect for the particle represented by the brown line, that reaches the side of the box object (see Figure 3.12).

This simulation shows that this method of moving box objects cannot take in account friction between walls of the container and particles when moving the walls. Indeed, with this method, friction may not be effective because the actual velocity of the box object is zero, and the tangential forces caused by friction in *Chrono* are calculated with the differential velocities of the objects in contact.

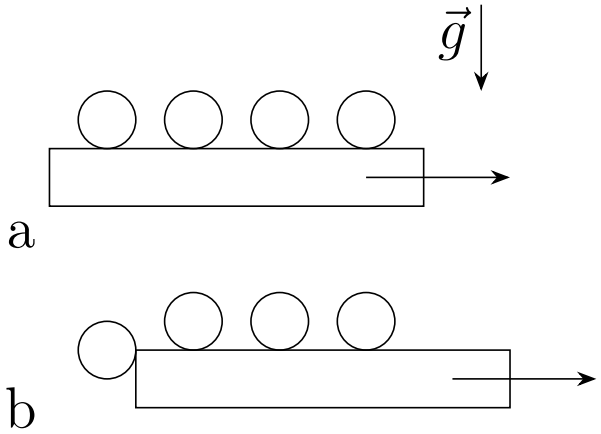

Figure 3.12: Schematic of the sliding test. $\vec{g}$ is the gravitational acceleration. a) The simulation before moving the box object. b) The simulation after moving the box object: particles remained at their original position, expect for the falling particle.

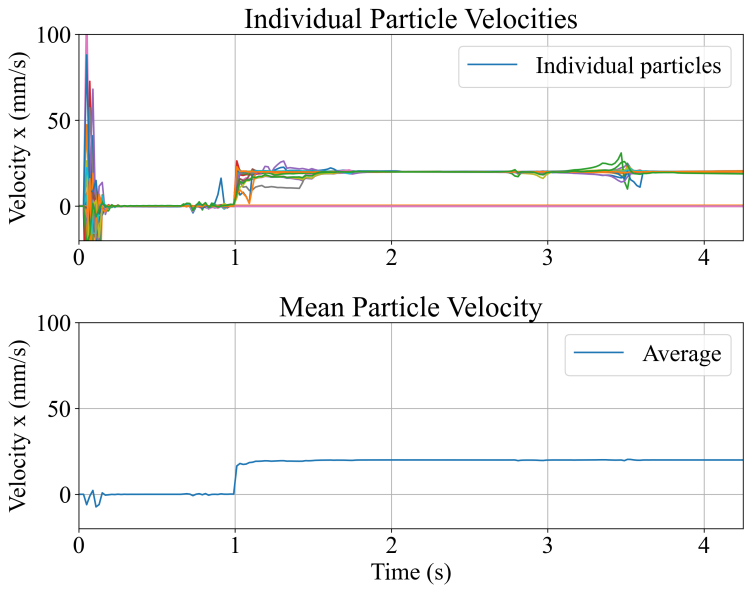

Figure 3.13: Velocity of the individual particles (top) and average velocity of the particles (bottom) in the box during the horizontal displacement test with teleported fixed particles. The filling of the box is from 0 to 1 s, then the "fixed" box objects and the "fixed" particles are moved laterally at a 20 mm/s speed. The plot lines at 0 velocity are the stuck particles: even if they are in movement, their "fixed" status means they have no output velocity. For this reason, their velocity is not taken into account in the average velocity.

Other methods to put objects in motion We tested two simulation methods to make the friction efficient between laterally moving box shaped objects and particles.

A first approach, has been to fix a layer of particles, just on top of the ground. The idea is that, thanks to the irregularities created by the shape of the particles, it would mimic friction and particles on top of the fixed particles would be correctly dragged by the box. This layer of fixed particles is "teleported" laterally with the same speed as the rest of the box. The same test as in Figure 3.8 as been conducted, with the first layer of particles stuck to the ground at the end of the loading step.

Similarly, we ran the same test as in Figure 3.8 and attached motors to the walls of the container (not to the loading plate). In *Project Chrono*, motors are objects that can be used to impose a motion, here at a linear constant speed. A motor must be attached to the "motorised" body (in the "slave frame") and to another object in order to produce motion relative to that object (in the "master frame"). The "motorised" bodies are not fixed: they do output a velocity, and in our case, the object in the master frame is a fixed wall.

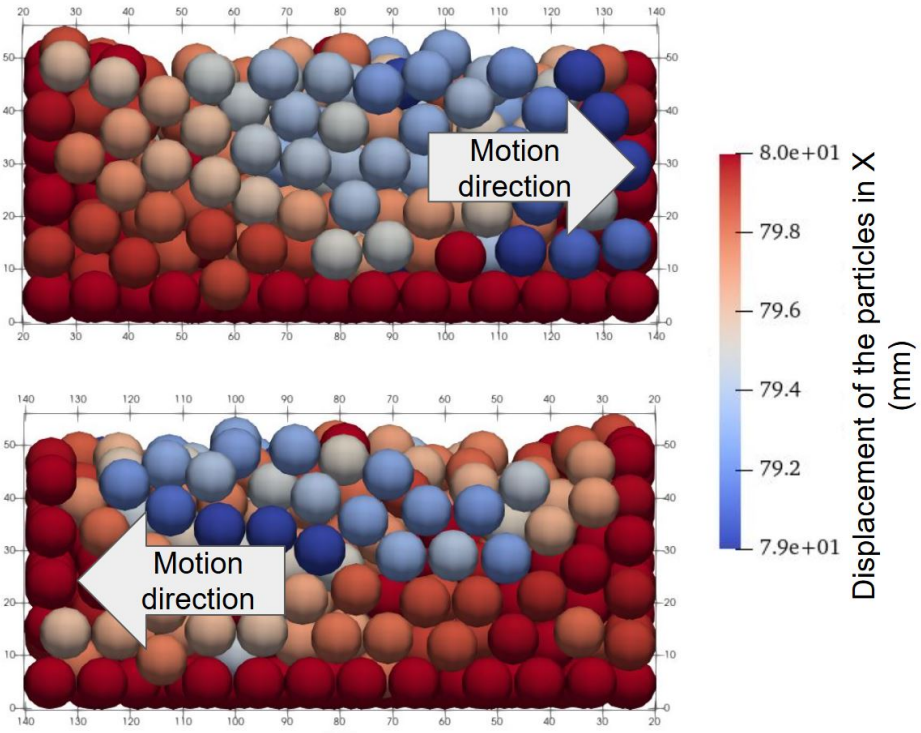

Figure 3.14: Visualisation of the displacement of particles inside of a container made of box objects after a 80 mm displacement of all the box objects constituting the container and the fixed particles (first layer of particle) with teleportation. The particles are coloured according to their X-axis displacement from their original position before the box started moving. The visualisation has been rendered with ParaView (Ahrens et al., 2005; Ayachit, 2015).

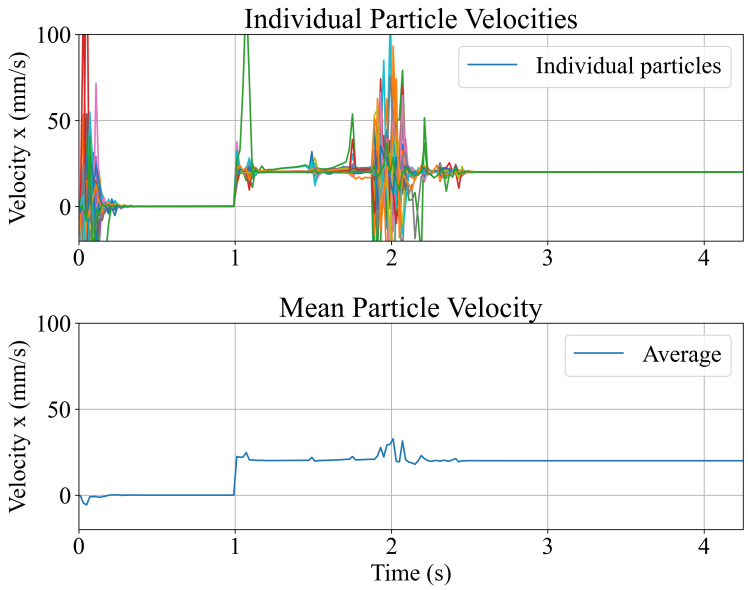

Figure 3.15: Velocity of the individual particles (top) and average velocity of the particles (bottom) in the box during the motorised horizontal displacement test. The filling of the box is from 0 to 1 s, then the motorised box objects are moved laterally at a 20 mm/s speed.

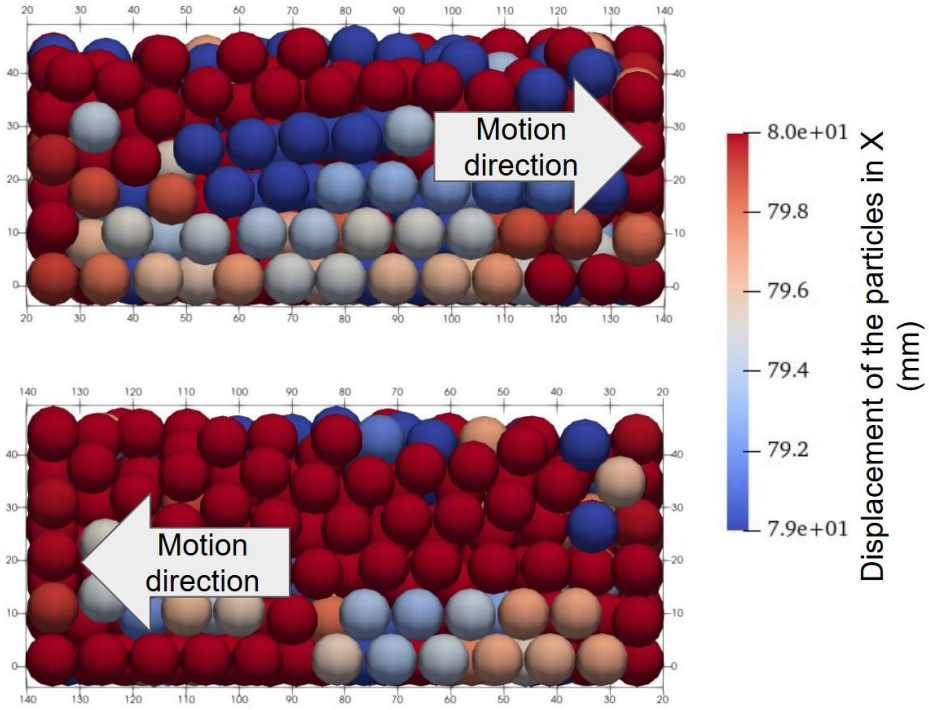

Figure 3.16: Visualisation of the displacement of particles inside of a container made of box objects after a 80 mm displacement of all the box objects constituting the container with motors. The particles are coloured according to their X-axis displacement from their original position before the box started moving. The visualisation has been rendered with ParaView (Ahrens et al., 2005; Ayachit, 2015).

The results for the fixed layer of particle and the motorised tests are respectively in Figures 3.13 and 3.15, and the ParaView visualisations in Figures 3.14 and 3.16. We can see that both methods successfully achieve the desired speed. Both methods also display irregularities and asymmetries for individual particles that can be due to rearrangement of the particles in the granular material however no oscillation similar to the first case are observed (Figure 3.9). Also note that the colour bar is very narrow: blue particles moved 0.1 mm less than the red particles, for a desired displacement of 80 mm.

First, we can see small velocity irregularities for the method with teleported particles (Figure 3.13). Looking more closely at the visualisation, we can see as expected that the first layer has been displaced of 80 mm as the position of each particles in the layer is updated at each time step (Figure 3.14). However, it seems that the further away from the edges of the box in X, the less the particles move. In particular, this behaviour is observable here because friction is not effective with the side walls in the Y direction of the container as they are teleported, similarly to the method presented in the previous subsection.

For the motorised method, even if the velocity irregularities are larger, once stabilised, the particles displaced by motorised walls all achieve a speed very near to 20 mm/s (Figure 3.15). On the visualisation, we can't see any pattern in the displacements of the particles with regards to their position. With this method, the friction with walls is effective, as particles near walls are correctly dragged by them.

Both methods could work correctly for the sole purpose of moving particles with other objects, however, the method of fixing and teleporting a layer (or layers) of particles to mimic the friction with walls should be improved to be more realistic, notably for the friction to be efficient with the side walls in the Y direction. All particles in contact with the walls of the containers should be fixed and these particular particles should have a coefficient of static friction grain-to-grain $\mu_{s,pp}$ equal to the coefficient of static friction grain-to-wall $\mu_{s,pw}$. Also, even if the irregularities formed by the void between the fixed particles help to drag the particles, the behaviour of such geometry is not similar to the friction between a flat wall and a spherical particle. For all these reasons, for physical realism and also for simplicity, it is not recommended to update the positions of bodies in *Chrono* for non-normal contacts. The use of motors is thus recommended, especially in the case of using walls as sensors as contacts will all occurs on a limited amount of objects: with fixed particles all around the inside of the box, such contacts would be much harder to track. These arguments are summarized in Table 3.5. Now that we verified and validated that we can use *Chrono*, and particularly box

Method	Benefits	Disadvantages
Teleporting box objects	Easy to implement	Friction between moved box objects and particles is invisible to the particles
Teleporting particles	No real benefits compared to the other methods	More difficult to implement, the friction between the teleported particles and the regular particles is sphere-sphere friction and not sphere to flat surface friction and tracking for on the pushing wall is also more difficult
Motorised box objects	Easy to implement accurate physics and easy to track force on the pushing wall	No disadvantages compared to the other methods

Table 3.5: The different methods studied to move particles with box objects, with their advantages and disadvantages deduced from the tests conducted in this section.

objects to move particles and record the forces that these particles exert on box objects we can start building a shear test experiment.

3.4 Laboratory Geotechnical Tests: which is most suitable for simulations?

In soil mechanics, two well known methods exist to perform the shear test of a material: the direct shear test and the triaxial shear test. Both these tests allow to measure the strength of the material with the Mohr-coulomb failure criterion (see Equation 1.5). The resulting strength measured with both methods is always comparable (Rahman et al., 1991; Maccarini, 1993; Castellanos and Brandon, 2013), however other parameters may vary, therefore, in order to choose the most suitable test for *Project Chrono*'s simulated granular material, we propose a quick comparative review of both methods.

3.4.1 Direct Shear Test

The direct shear test simply consists of a box, the shear box, in which the tested material is placed (see Figure 3.17). The shear box is made of two parts, the upper frame and the lower frame, with a normal load applied to the top of the sample in the box, typically applying a pressure from a few kPa to a few MPa, but some tests can be done with loads smaller than 1 kPa (Schellart, 2000). The bottom and the top of the box bear a rough surface or teeth depending on the material tested to ensure tangential friction between the box and the material (Taylor, 1948). The lower frame is then displaced at constant speed (not higher than 1 mm/s following International Organization for Standardization (2018)) and the sample is subjected to shear forcing at the separation between the lower and the upper frame. While the normal force is constant, the shearing force, pushing the lower

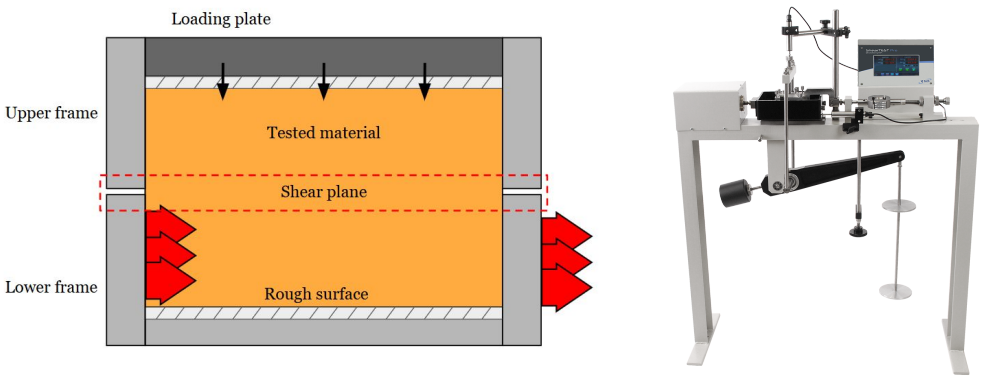

Figure 3.17: (Left) Simplified experimental configuration of a shear box. Displacement occurs in the direction of the red arrows and normal force is applied along the black arrows. (Right) The VJ Tech's shearing machine ShearTEST Pro, similar to the one at ISAE-SUPAERO. The tested sample is placed in the black box and the normal stress is applied by a leaver loading arm with a hanger that can apply up to 10kN of load on the sample. (VJ Tech)

frame, increases with the displacement (Taylor, 1948; Skempton and Bishop, 1950; Saada and Townsend, 1981; Head, 1982; Suits et al., 2008). In the direct shear test, the stress-strain is non-uniform (Rahman et al., 1991); as a constant normal force is applied to the top, an increasing horizontal displacement is applied parallel to the shear plan on the lower frame. Therefore, the magnitudes of the intermediate and minor principal stresses are unknown and governed by the maximum principal stress, i.e. the normal stress applied and the strength of the tested material (Castellanos and Brandon, 2013). This behaviour can be a disadvantage as it does not allow to measure stress-strain properties of the material with this method (Maccarini, 1993) i.e. the plastic and elastic properties of a material. However, this method is well suited and well known for measuring the strength parameters (Taylor, 1948; Skempton and Bishop, 1950; Saada and Townsend, 1981; Head, 1982), which are the parameters we want to infer from the shear test experiment.

3.4.2 Triaxial Test

In the triaxial shear test, the material is confined between two parallel plates that apply a constant normal force, inside a cylindrical chamber that maintains a uniform confining pressure on the material. This confining pressure is applied using a pressurized fluid, like water (applying pressures from dozens of kPa to dozens of MPa) (Taylor, 1948; Bardet, 1997; Head, 1998; Holtz and Kovacs, 1981). During a test, the normal stress is kept constant, similarly to the direct shear test, and the shear stress is increased by increasing the fluid pressure around the chamber. These tests can be performed "consolidated" or "uncon-

solidated" and "drained" or "undrained". In a consolidated-drained (CD) triaxial shear test, the tested material is first saturated with water, then, is slowly loaded, allowing the material to consolidate. During the shear, the rate of axial deformation is kept constant and the pore water is allowed to escape through the porous discs, giving insights on the behaviours of the tested material under slow and sustained loading and allowing to measure the strength of the drained material. In an consolidated-undrained (CU) triaxial shear test, the material is also saturated and slowly loaded but then, the shear speed is kept constant and water in the pores is not allowed to escape, giving insights on the behaviour of the material under slow loading conditions and allowing to measure the strength of the undrained material. Finally, the most suited for our study would be the unconsolidated-undrained (UU) triaxial shear test. The tested material does not have to be saturated, and the tested material may be intact or compacted as needed. The sample is then relatively rapidly sheared (up to 1% displacement per minute) immediately after application of the confining pressure (Bardet, 1997; Head, 1982; Holtz and Kovacs, 1981). This test allows to understand the behaviour of undrained materials under rapid loading conditions, with regards to the behaviour of natural saturated slopes for example (Iverson, 2000). In the triaxial shear test, the location of the shear plane is not constrained by the setup.

While triaxial shear test is more versatile and is able to provide more information than the direct shear test such as the stress-strain properties of the material, the latter is much easier to implement in *Project Chrono*, and as an initial characterization approach, we are mostly interested in the shear strength parameters of the simulated particles. The direct shear test is also appropriate for dry particles in the laboratory, which suits the type of particles we simulate with *Project Chrono*.

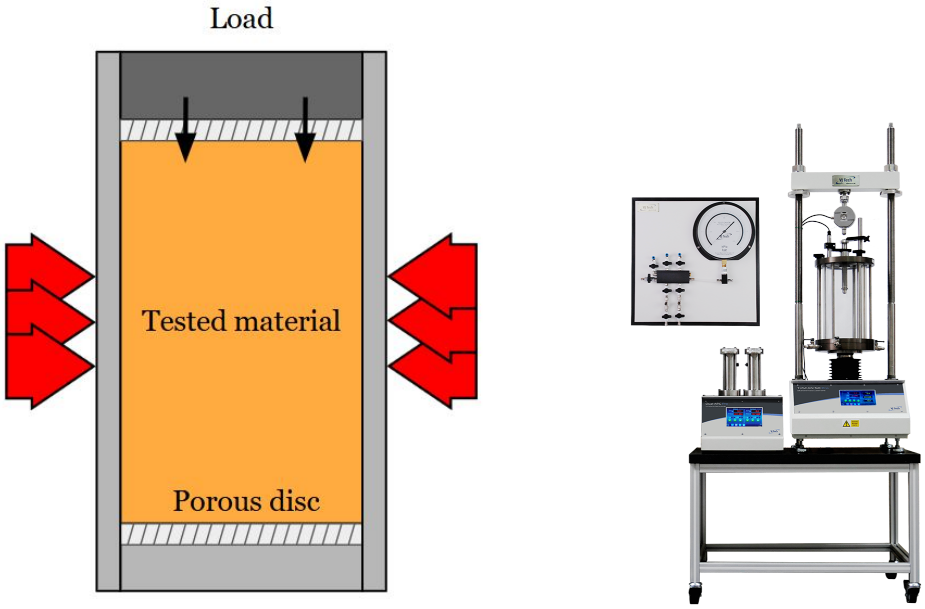

Figure 3.18: (Left) Simplified experimental configuration of a triaxial shear test. Red arrows show the confining pressure applied on the tested material and black arrows show the normal force. (Right) The VJ Tech Pro Automatic Triaxial Testing System. This triaxial test system can Consolidated Drained (CD), Consolidated Undrained (CU) or Unconsolidated Undrained (UU) tests thanks to pump and a pressure controller and apply loads on the sample up to 250 kN. (VJ Tech)

3.5 Digital direct shear tests in the literature

Direct shear tests have been simulated numerous times in order to study the shear behaviour of granular materials. Liu (2006) simulated a 2D direct shear test with 3259 discs and showed that the angle of internal friction in granular materials is not directly related to the inter-particle friction angle. Instead, it relates to the average inter-particle contact angle on the shear plane and the ratio between the slope of the average inter-particle contact forces against the inter-particle contact angle and the average inter-particle contact force. This ratio represents the degree of the probability distribution of the inter-particle contact forces that is directed towards the shear direction. Fleischmann et al. (2015) used the direct shear test with 5000 spheres in *Project Chrono* to show the importance of contact history in DEM codes to yield similar simulated and laboratory shear test results in 3D. Ucgul et al. (2015) used the direct shear test to validate the hysteretic spring contact model (HSCM) with thousands of 3D particles using EDEM 2.4 software, developed by DEM Solutions Ltd. in Edinburgh (United Kingdom). Zhang and Thornton (2015) showed with 2D direct shear tests with 5000 particles that the dilatation inside the shear zone (i.e. around the shear plane) is greater than that deduced from the boundary measurements and that more reliable data in laboratory would be obtained if the shear box aspect ratio was below 1:2. Wang et al. (2018) studied the influence of the presence of rubber particles in the shear behaviour of sand, with 6000 sand particles and 1000 rubber particles in 3D. Snapshots of these simulations are available in Figure 3.19.

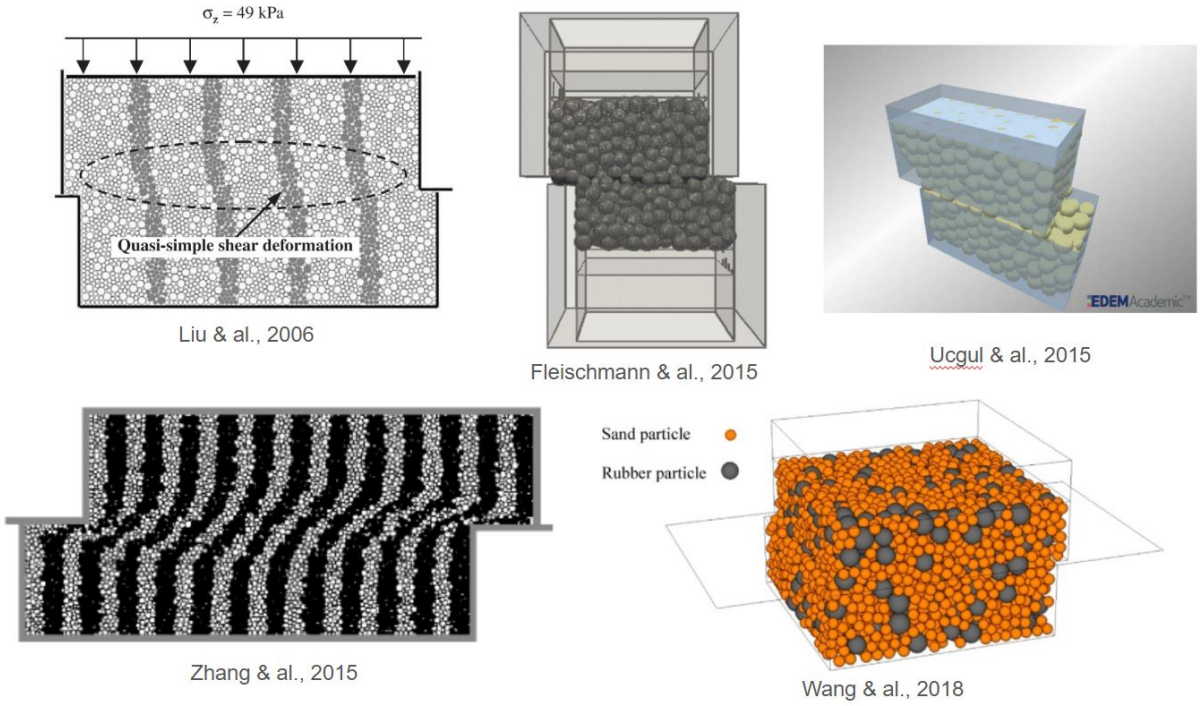

Figure 3.19: Snapshots of the numerical direct shear tests presented in Sect. 3.5. Simulations from Liu (2006) and Zhang and Thornton (2015) are 2D and the others (Fleischmann et al., 2015; Ucgul et al., 2015; Wang et al., 2018) are 3D.

3.6 Constructing a Digital Shear Box

The shear box has been created in *Project Chrono* similarly to a laboratory shear box (see Figures 3.17). Each shear test simulation we conducted has been divided in 2 simulations: a "set box" simulation and a "shear" simulation. The "set box" simulation is the filling part of the procedure and the "shear" simulation is the loading and shearing of the material.

The "set box" simulation consists of "exploding" a particle cloud of a desired height. Particles are generated inside a box with the same size as the shear box in x, y and with a higher height than the particle cloud in z, the latter also being higher than the shear box itself. The particles are given a 1 m/s velocity in a random direction and then left to settle, similarly to what has been done in Sunday (2022) to fill containers with particles in *Chrono*.

The shear box consists of 5 walls in the lower frame, that are linked to 5 different motors, one for each wall. Each motor is attached to a fixed wall placed behind the lower frame. The upper frame is composed of 4 fixed walls of the same size as the bottom walls, i.e. 40 mm tall. The loading plate in the laboratory is held in place in the horizontal directions thanks

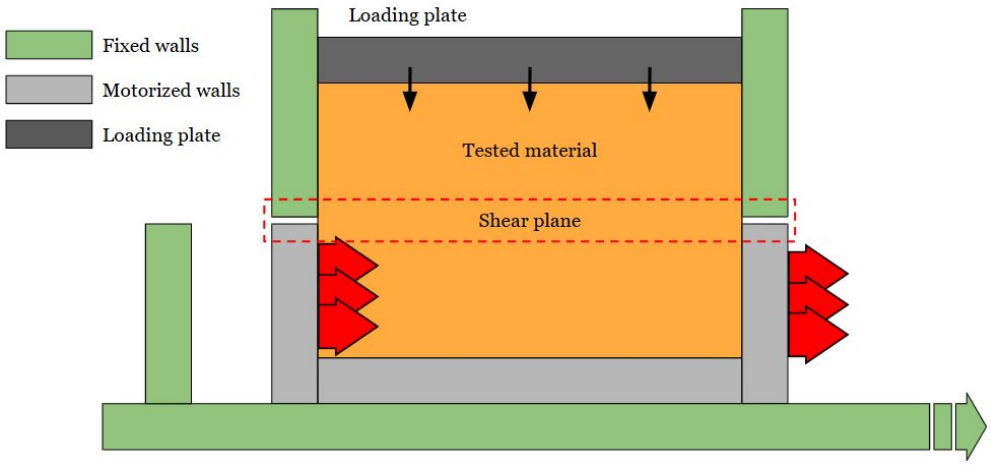

Figure 3.20: Schematic of the shear box setup in *Project Chrono*. Displacement occurs in the direction of the red arrows, towards positive X and normal force is gravitationally applied by the loading plate towards negative Z. Fixed walls are in green and unfixed walls are in gray. Walls of the lower frame are linked to motors that are attached to the fixed wall on the left. The whole shear box is placed on a fixed ground.

to a mechanical arm and is loaded by applying weight to it. In *Chrono*, we can vary the weight of the loading plate and keep it's horizontal position to the center of the shear box while allowing to rotate or tilt if necessary, as in the laboratory. A schematic of the shear box setup is displayed in Figure 3.20.

The shear test simulation first retrieves the positions and radii of the last time step of the set box simulation, without the particles above 80 mm i.e. the size of the shear box. The particles are then left to re-settle because the forces between the particles are not registered between two simulations. After the re-resettle, the loading plate is placed slightly above the granular sample and is allowed to fall and apply normal pressure on the sample until it stabilizes.

The granular sample is sheared at a 1 mm/s rate (1 mm/mn), by putting in motion the lower frame thanks to the motors. This shear rate is fast compared to shear rate in the laboratory (shearing at a maximum rate of 1 mm/mn). However, this shear rate has already been used to perform direct shear test in *Project Chrono* (Fleischmann et al., 2015) and the relative displacement between the lower frame and the particles in contact with the wall pushing is only 10 μm per integration step at a simulation time step of 10 μs. It is very small compared to the size of a 6 mm particle, as the recommended limit for an overlap is 5 % of a particle (Itasca Consulting Group, 2007). Moreover, for each test, we verify that the

shear rate combined with the compression ensure negligible inertial effects to remain in the quasi-static regime (Vu et al., 2025). To do so, we calculate the inertia number I expressed as (GDR MiDi, 2004):

$$I = \dot{\epsilon} d \sqrt{\frac{\rho}{\sigma_n}} \tag{3.18}$$

With $\dot{\epsilon}$ the strain rate, (for us $\dot{\epsilon} = \frac{1}{200} = 0.005$ corresponding to a 1 mm/s displacement over a 200 mm large box), d the mean particle diameter, ρ the particle density and σ_n the the normal stress applied on the sample. The system is in a quasi-static if $I \lesssim 10^{-3}$ (Forterre and Pouliquen, 2008; Radjai and Dubois, 2011; Vu et al., 2025). In our case, with the material tested presented in the next section, the values of I are between 1.5×10^{-5} and 3.0×10^{-5}.

A 1 mm/s shear rate also allows a reasonable computational time to reach a displacement of 20 mm, as each of these simulations have a large RTF (≈ 14000) and have to run for about 120 hours.

3.7 A direct shear test simulation

First, to test our direct shear test simulation, we perform the shearing of a simulated glass bead sample with around 12000 particles. Glass beads represent a low frictional material, with no cohesion, and the inter-particle parameters used are in Table 3.6.

First, Figure 3.21 shows the visualisation of the shear test simulation at the beginning of the shear and after a displacement of 20 mm i.e. 10% of the box length: the shear stress measured from each test at a given normal stress is the maximum stress reached or the stress after a displacement of 10% of the box length i.e. 20 mm (International Organization for Standardization, 2018), whichever occurs first during shearing. In comparison with Figure 3.22, we can see similar patterns forming with the particles with an above average stress. However, the contact networks have not been studied in detail in this thesis. Thus, the patterns observed in Figure 3.22 can not precisely be identified on Figure 3.21.

On the other hand, Figure 3.23 shows the average stress in the system sampled in 5 mm slices. We can see that the maximum stress in the granular sample during the shear test is located around the shear plane, and that the stress is increasing with time/displacement.

Finally, we can see on Figure 3.24 the shear stress as a function of the displacement during the shear test. We can see fluctuations that are due to rearrangement of particles during the

Parameter	Units	Value
d	mm	6 ± 0.5
ρ_g	g cm^{-3}	2.48
F_c	mN	0
E	MPa	70
ν	-	0.24
e_{pp}	-	0.9
e_{pw}	-	0.5
$\mu_{s,pp}$	-	0.16
$\mu_{s,pw}$	-	0.45
μ_r	-	0.09
μ_t	-	0.01

Table 3.6: Simulation parameters for glass beads: the grain diameter d, the grain density ρ_g, the Young's modulus E, the Poisson ratio ν, the particle-particle coefficient of restitution e_{pp}, the particle-wall coefficient of restitution e_{pw}, the particle-particle sliding friction coefficient $\mu_{s,pp}$, the particle-wall sliding friction coefficient $\mu_{s,pw}$, the rolling friction coefficient μ_r and twisting friction coefficient μ_t.

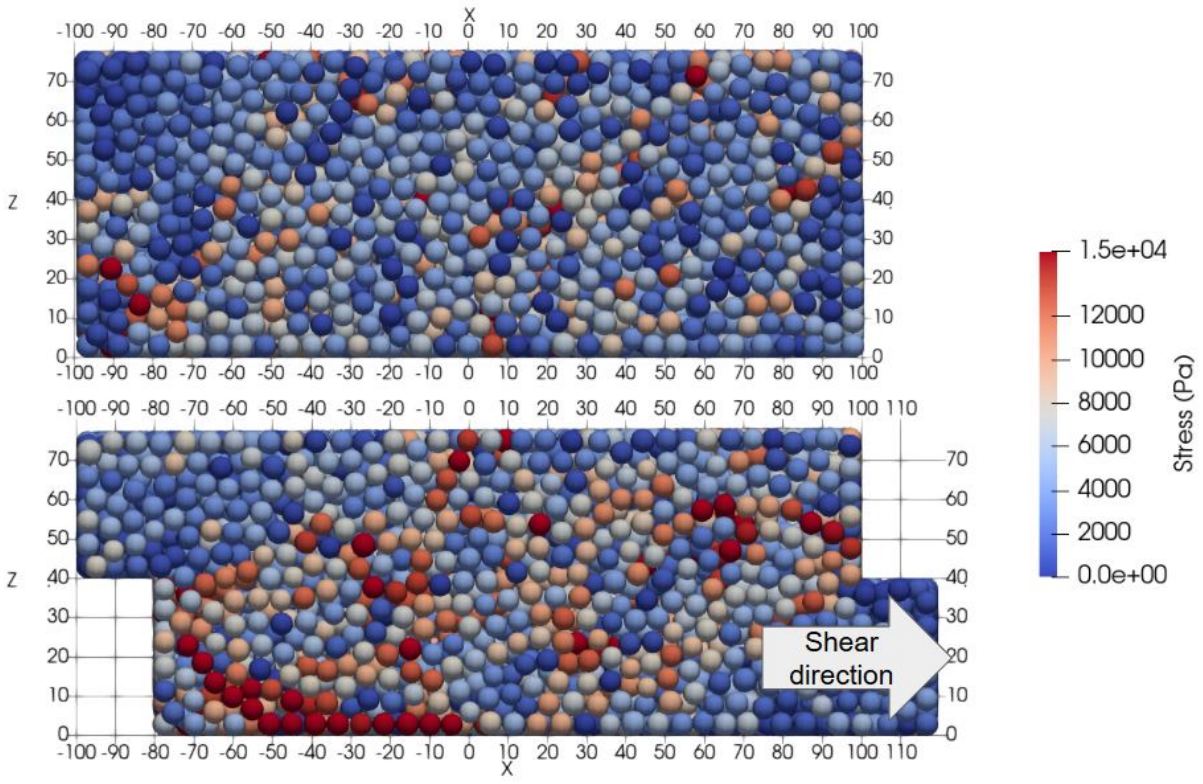

Figure 3.21: ParaView visualisation of a sample of ≈ 12000 glass beads before and after a 20 mm displacement of the lower frame of the shear box. The colour corresponds to the stress experienced by the particle in Pa.

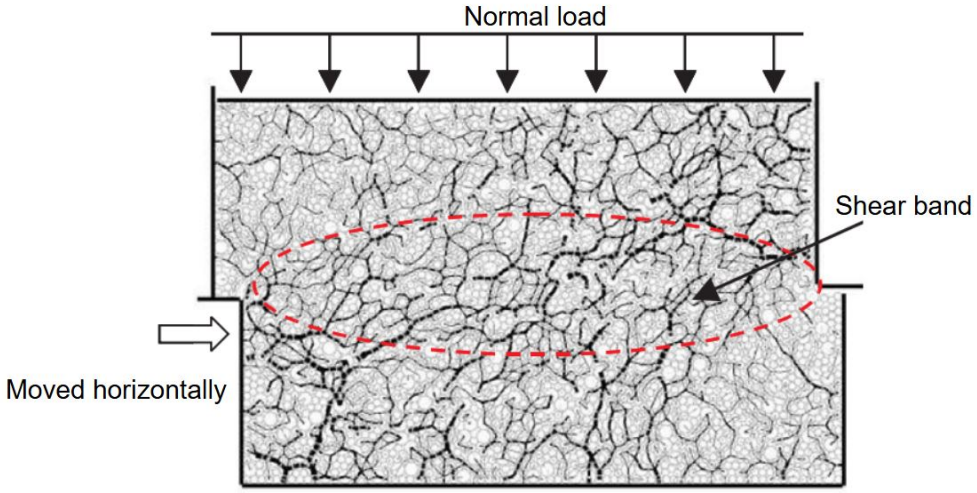

Figure 3.22: Inter-particle contact forces network in a simulated direct shear box test. Adapted from Liu (2006).

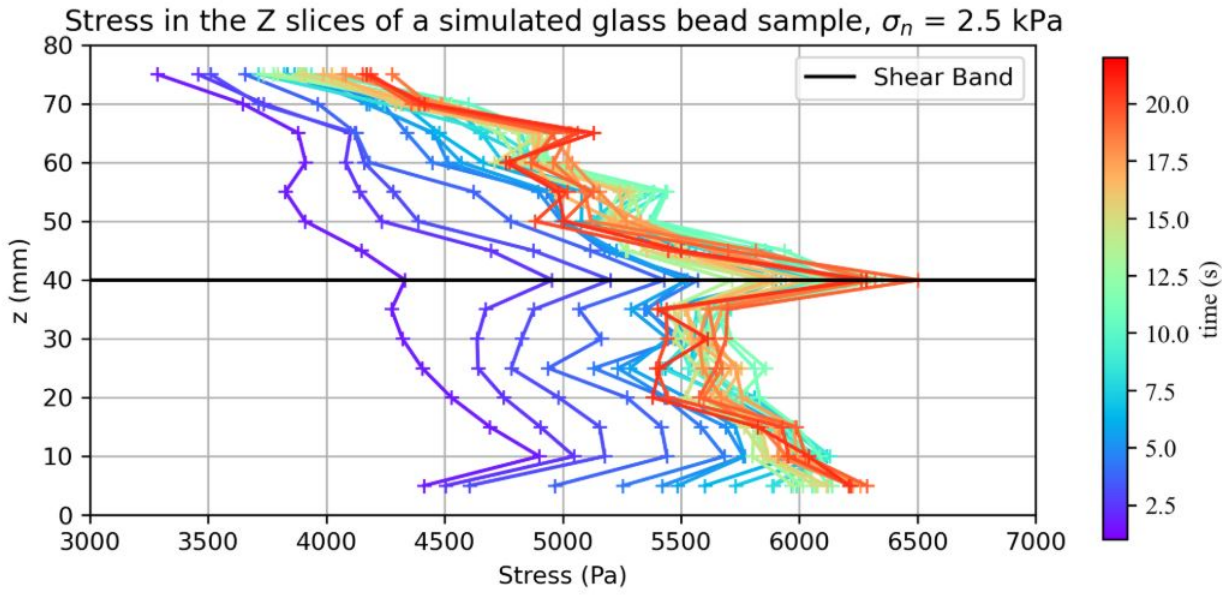

Figure 3.23: Average stress in the slices of the shear box during the shear test. The colour bar corresponds to the time during the shear test.

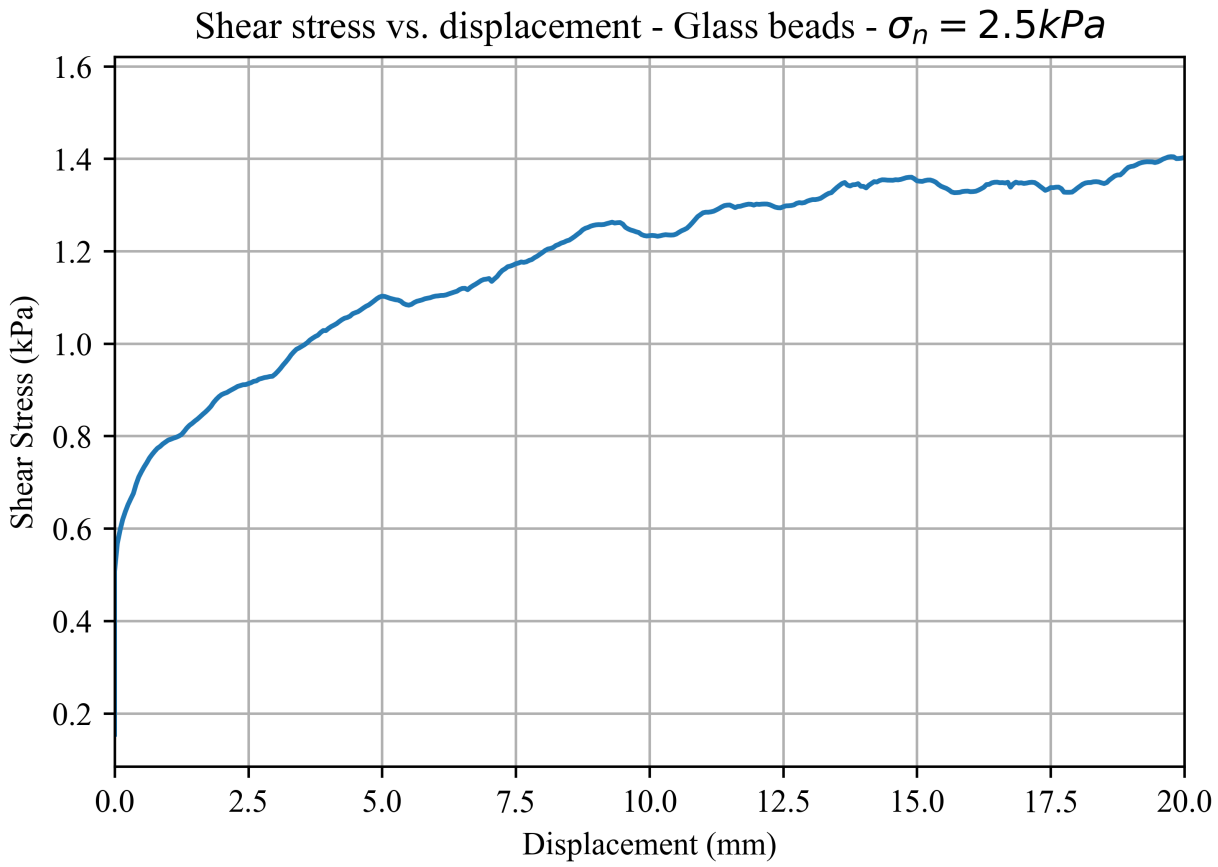

Figure 3.24: Shear stress as a function of the displacement of the lower walls of the shear box. The tested material is a sample of ≈ 12000 glass beads particles, under a normal stress of 2.5 kPa

displacement of the shear box. The shear stress values obtained here are similar to values obtained for simulations of shear tests of glass beads under similar normal stresses: Fleischmann et al. (2015) obtain a shear stress plateau around 2 kPa for a normal stress of 3.1 kPa, here we are around 1.3 kPa for a 2.5 kPa normal stress.

Consequently, the simulated direct shear test simulation described in the end of this chapter is able to recreate the conditions necessary to infer the bulk strength properties of simulated granular materials thanks to the Mohr-Coulomb failure criterion by performing at least three of these tests at three different normal stresses. These tests will be will be presented in the next chapter in which the parameters of the tested samples will be presented and the influence of various inter-particle parameters on the bulk properties of the material will be explored.

3.8 Conclusion

To conclude, in this chapter, I first introduced numerical techniques than can be used to simulate granular materials. These numerical techniques adopt either a Lagrangian, Eulerian or hybrid point-of-view depending on what is studied. In order to study granular media in detail, we focused on a DEM code, adopting an Eulerian point-of-view: *Project Chrono*. *Chrono* is the DEM code used in this thesis and it was presented along with the contact model used: the Hertz model.

This model has been verified for particle-particle interactions in (Sunday et al., 2020), however normal contacts between particle and box objects have not, notably in order to use box objects as sensors and tools. Different tests have been run to verify that contact forces behave as expected as well as different methods. Notably, we noticed that displacing objects without giving them velocity does not allow to calculate friction between a thereby displaced object and another object, as the tangential forces caused by friction are calculated with differential velocities in *Chrono*. We therefore chose to put in motion box-objects in *Chrono* thanks to motors, in order to perform a digital shear test in the same way as in the laboratory.

The purpose of performing these tests is to infer the bulk properties of simulated granular materials, notably those that have been used by C. Sunday to study the behaviour of granular materials in low-gravity in the context of the MMX mission (Sunday, 2022). I have therefore proposed in this chapter a quick review on the direct shear tests and the triaxial tests, the most common techniques to perform shear tests. The most suitable test identified for this study has been the direct shear test. it allows to measure the strength properties of a material thanks to the Mohr-Coulomb failure criterion with a simple shear box consisting of an upper and a lower frame in which the studied granular sample is placed under pressure with a loading plate.

Finally, I presented how the digital shear box has been set-up in *Chrono* as well as the different parameters of the test, before presenting a first shear test of a simulated glass beads sample of $\approx$ 12,000 particles. The maximum stress in the shear box is located around the shear band as expected and the results are qualitatively similar to other digital shear tests performed in other studies.

In the next chapter, we will focus on the results of the shear tests performed on the granular material used in C. Sunday's thesis and the implications of these results. We will notably

try to understand the role of normal load and gravity on the bulk properties of granular material and the link with terramechanics parameters, in the scope of driving in granular materials in a low-gravity environment.

Chapter 4

Digital Shear Box Simulations for Macroscopic Characterization

In this chapter, we will focus on the results of the different shear tests simulations that have been run in order to characterize the bulk properties such as internal friction and bulk cohesion of the materials that have been used in C. Sunday's thesis (Sunday, 2022). To this end, I will first present the tested materials and the different parameters of the direct shear tests performed in this chapter. Then, I will discuss the influence of inter-particle properties, the normal stress and gravity on the bulk properties of granular materials. Finally, the resulting bulk properties will be discussed, in comparison with laboratory and in-situ data, and on the other hand, regarding their implications in terramechanics.

4.1 C. Sunday's thesis results and tested materials.

During her thesis, C. Sunday performed sinkage and roving simulations with *Project Chrono*. She was notably able to show that, in a quasi-static regime for materials without cohesion, sinkage is independent of gravity, however it is not the case when cohesion is added between the grains. C. Sunday was also able to show that the particle flow beneath a wheel, and the driving performances are the same when the Froude Numbers Fr are similar. The Froude number for a rotating system is written as:

$$Fr = \frac{\omega^2 D}{2g} = \frac{\omega^2 R}{g} \tag{4.1}$$

with ω, D and R respectively the rotational velocity, diameter and radius of the rotating object (here, the wheel) and g the gravity of the system. In the cases tested by C. Sunday, Fr $= 0.05$, with $g = 9.81\ m.s^{-2}$ and $g = 0.006\ m.s^{-2}$ respectively at Earth and Phobos gravity, and $\omega = 2.65\ rad.s^{-1}$ and $\omega = 0.065\ rad.s^{-1}$ respectively. In both cases, the radius

Parameter	Units	Case 1	Case 2	Case 3
d	mm	6 ± 0.5	6 ± 0.5	6 ± 0.5
ρ_g	g cm^{-3}	2.48	2.48	2.48
$\rho_{s,E}$	g cm^{-3}	1.41	1.40	1.32
$\rho_{s,P}$	g cm^{-3}	1.42	1.40	1.28
$F_{c,E}$	mN	0	0	68.9
$F_{c,P}$	mN	0	0	0.04
E	MPa	70	70	70
ν	-	0.24	0.24	0.24
e_{pp}	-	0.9	0.9	0.9
e_{pw}	-	0.5	0.5	0.5
$\mu_{s,pp}$	-	0.16	0.40	0.40
$\mu_{s,pw}$	-	0.45	0.45	0.45
μ_r	-	0.09	0.09	0.09
μ_t	-	0.01	0.01	0.01

Table 4.1: Simulation parameters for cases 1-3. The grain diameter d, the grain density ρ_g, the bulk density under Earth gravity $\rho_{s,E}$, the bulk density under Phobos gravity $\rho_{s,P}$, the cohesive force under Earth gravity $F_{c,E}$, the cohesive force under Phobos gravity $F_{c,P}$, the Young's modulus E, the Poisson ratio ν, the particle-particle coefficient of restitution e_{pp}, the particle-wall coefficient of restitution e_{pw}, the particle-particle sliding friction coefficient $\mu_{s,pp}$, the particle-wall sliding friction coefficient $\mu_{s,pw}$, the rolling friction coefficient μ_r and the twisting friction coefficient μ_t. Case 1 corresponds to the glass bead case, case 2 is an estimated rough glass bead case and case 3 is an estimated rough glass bead case, with cohesion. Adapted from Sunday (2022).

R of the wheel is 77 mm (without the grousers), corresponding to the design of the MMX rover Idefix wheel, provided by DLR.

The parameters of the simulation materials used to performed these sinking and driving tests are displayed in Table 4.1. These different materials named as cases 1, 2 and 3 respectively correspond to a glass bead case, a rough glass bead case and a rough glass bead case with cohesion. For the last case, the cohesive forces have been selected to represent a similar Bond number (Eq. 1.4) between Earth and Phobos gravities. However, as explained in the precedent chapter, only the inter-particle parameters are known. We are thus performing shear tests of these 3 materials, in order to know their bulk properties.

First, to assess the order of magnitude of the bulk properties of various materials, let's take a look at laboratory results. Table 4.2 shows the strength properties of both granular and solid materials. For the granular materials, direct shear testing has been used to obtain these results. We note that the cohesion of granular materials is smaller by several order of

Material (grain size)	Material Type	μ	θ (°)	C (MPa)	ρ (g/cm^3)	**Reference**
Granite (-)	Solid	0.64	32.6	31	2.65-2.75	[1]
Gabbro (-)	Solid	0.66	33.4	38	2.7-3.5	[1]
Serpentinized olivine (-)	Solid	0.65	33.0	90	≈ 2.6	[2]
Sandstone (-)	Solid	0.51	26.6	28	1.61 - 2.76	[1]
Berea sandstone (-)	Solid	0.49	26.1	24	1.61 - 2.76	[3]
Weber sandstone (-)	Solid	0.60	31.0	70	1.61 - 2.76	[3]
Tennessee sandstone (-)	Solid	0.84	40.0	50	1.61 - 2.76	[4]
Lueders limestone (-)	Solid	0.53	27.9	15	1.5 - 2.7	[4]
Marble (-)	Solid	0.75	36.9	110	≈ 2.75	[1]
Blair dolomite (-)	Solid	1.00	45.0	45	2.84	[4]
Dry sand ($< 400\mu m$)	Granular	0.89	41.7	2.45×10^{-4}	1.73	[5]
Dry sand ($80 - 180\mu m$)	Granular	0.88	41.3	2.30×10^{-4}	1.67	[5]
Glass beads ($400 - 600\mu m$)	Granular	0.87	41.0	1.37×10^{-4}	1.91	[5]
Glass beads ($90 - 180\mu m$)	Granular	0.65	33.0	1.60×10^{-4}	1.61	[5]
Caster sugar ($< 355\mu m$)	Granular	1.14	48.8	2.47×10^{-4}	1.04	[5]
Glass beads ($1 - 1.3mm$)	Granular	0.62	31.77	2.22×10^{-4}	1.80	[6]
Glass beads ($0.5mm$)	Granular	0.57	29.56	1.46×10^{-4}	1.58	[6]

Table 4.2: Adapted from Schellart (2000). Coefficient of internal friction (μ), friction angle (θ) cohesion (c) and bulk density (ρ) for various non-granular and granular materials measured from shear tests. The bulk density values of the solid materials are typical values for these rocks. References: [1] Jaeger (1979), [2] Raleigh and Paterson (1965), [3] Twiss and Moores (1992), [4] Handin (1969), [5] Schellart (2000). [6] Tests performed by Jeanne Bigot at ISAE-SUPAERO in the context of the Surface Investigation in Low gravity Environment (SILOE) experiment (Duchêne et al., 2025).

magnitude compared to igneous or sedimentary rocks.

4.2 Parameters influencing the material bulk density

Before performing a shear test, in the laboratory, the procedure for filling the shear box and conducting the experiment must ensure reproducibility to allow for accurate comparison of results and proper linear fitting of the Mohr-Coulomb criterion to the data (Suits et al., 2008). While these procedures can be challenging to follow in the laboratory, replicating similar conditions across different tests is significantly easier in simulations. For each tested material, the same "set box" (see Sect. 3.6) simulation output is used, ensuring identical densities for each material before loading. Indeed, the density before loading is a key parameter as studying the same granular material in a loose state or a compacted state yields different strength results (Taylor, 1948). More specifically, the higher the density is, the more the sample resists to shear and the higher the resulting angle of internal friction is (see

review by Yin et al., 2021) . The desired density for each tested material are the densities indicated for Earth gravity in Table 4.1.

The desired densities obtained in Sunday (2022) have been calculated from samples in 800×250 mm containers, generated from a column with a height of 300 mm.

In order to understand how different parameters influence the density of the sample before loading, we ran several "set box" simulations and varied parameters that could influence the bulk densities compared to the simulations from Sunday (2022). We thus performed tests by varying the drop height of the particle cloud with the same numbers of particles, the number of particles with the drop height, and finally the Young's modulus of the particles to better understand these different parameters influence the bulk density. The sample bulk density ρ_s is computed in post-process such as:

$$\rho_s = \frac{m_s}{V_s} = \frac{\sum \frac{4}{3}\pi r_i^3 \rho_g}{\sum V_{x,y}} \tag{4.2}$$

with m_s the mass of the sample, V_s the volume of the sample, r_i the radius of particle i, ρ_g the density of a particle and $V_{x,y}$ the volume of an x by y sub-section of the sample. Indeed, the top surface area of the sample is not flat before loading, so to compute the volume of the sample, the bin is subdivided into a 10 x 10 mm grid in x and y. The top-most point in the z direction is then retrieved for each bin in order to obtain the volume of the section for the density calculation. The volume of the column $V_{x,y}$ is thus $V_{x,y} = 10 \times 10 \times (z_{max} + r_{z_{max}})\ mm^3$. The values from Sunday (2022) have been calculated from the volume formed by the minimal positions to the maximum positions of the particles in x, y and z minus the last layer of particle in z. Our new method to compute the bulk density is more accurate and still comparable to the values from Sunday (2022).

A summary of the influence of the tested parameters on the bulk density of granular materials is available in Table 4.3.

First, we tested if the height at which the sample is dropped would influence the density of the granular material (see Figure 4.1). At the end of the test, after stabilisation of the samples, the densities of the tests dropped from 300 mm and from 900 mm are respectively 1.49 g/cm^3 and 1.46 g/cm^3. The higher density of the sample dropped from a higher height can be explained by the fact that the particles are more accelerated by gravity when falling, allowing them to better overcome friction than slower particles and thus settle into denser

Parameter	Effect on bulk density	Figure
Drop height	Density decreases slightly with as drop height increases	4.1
Number of particles	Density increases with the number of particles	4.2
Young's Modulus E	Density increases as E decreases	4.4
Inter-particle friction	Density decreases as friction increases	4.6
Cohesion	Density decreases as cohesion increases	4.6

Table 4.3: Summary of the influence of the tested parameters on the bulk density of granular materials. Note that inter-particle friction and cohesion are parameters defined by the tested material.

configurations.

We then tested the influence of the number of particles in the sample (Figure 4.2). The more particles there are in the initial column (and thus the higher the column), the denser the sample is: the densities of the tests with 8485 particles from a 150 mm column and with 2980 particles from a 450 mm column are respectively 1.59 g/cm^3 and 1.46 g/cm^3. We can see that these parameters (number of particles and column height) clearly influence the density of the granular sample: with more particles, pressure is increasing with the depth in the sample, therefore density is increasing (see Figure 4.3), following the hydrostatic pressure equation $P = \rho g z$ with P the pressure, ρ the density of the material, g the gravity and z the depth. In this test, the number of particles and the drop height of the particle cloud have not been tested independently, however, we can see with the test Figure 4.1 that the drop height alone has less influence on the density than the number of particles and the drop height together.

Finally, we tested the influence of the Young's modulus: as seen in the precedent chapter, the Young's modulus is a key parameter in contact physics and thus controls the final positions of the particles in this simulation i.e. controls the density (see Figure 4.4). The densities of the tests with a Young's modulus of 0.7 MPa and 70 MPa are respectively 1.59 g/cm^3 and 1.45 g/cm^3. Decreasing the Young's modulus increases the density of the granular sample. Indeed, the smaller the modulus the smaller the stiffness (see Eq. 3.5) resulting in higher forces at impact thanks to less deformation resistance, allowing the particles to overcome friction and settle into denser configurations.

Understanding these parameters, the number of particles is the most dominant parameter on density. In the simulation, the number of particle is determined by the height of the column and the size of the container. Consequently, we chose a column height of 360 mm,

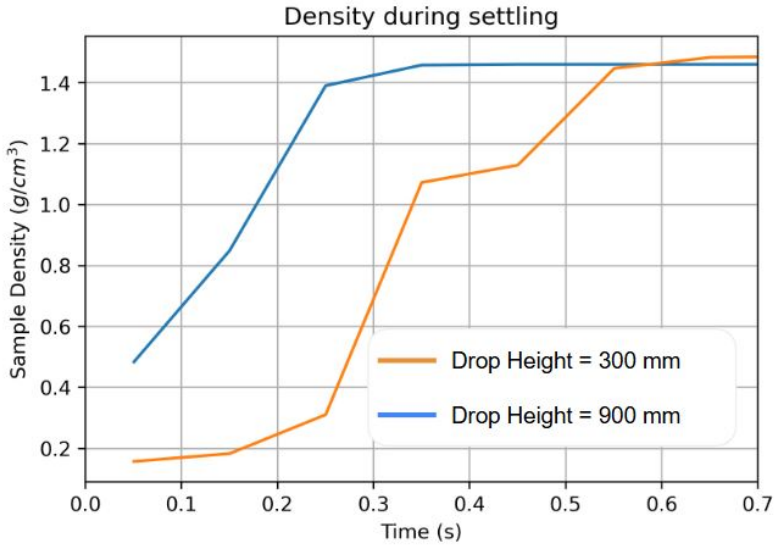

Figure 4.1: Density of a granular sample (case 1) during the settling of the "set box" simulation. The orange line is the density of the material with dropped with the top of the sample dropped from a 300 mm height and the blue line is the density of the material with the top of the sample dropped from a 900 mm height both with 2980 particles.

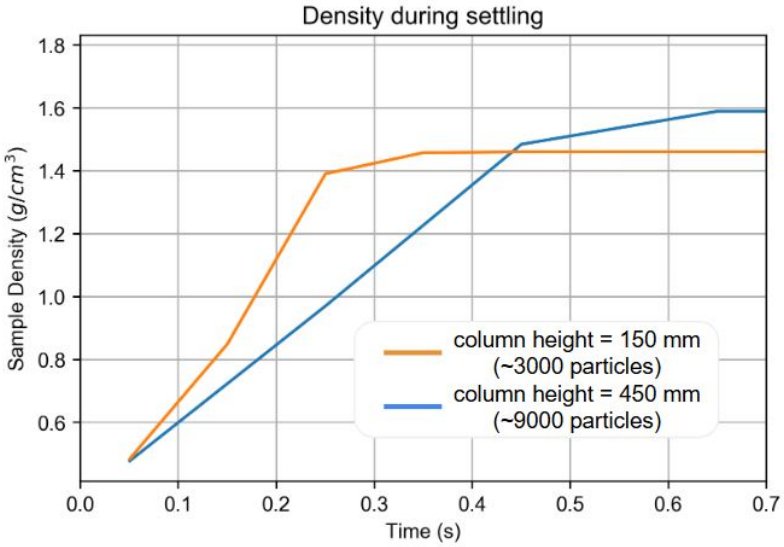

Figure 4.2: Density of a granular sample (case 1) during the settling of the "set box" simulation. The orange line is the density of the material generated from a 150 mm column (2980 particles) and the blue line is the density of the material generated from a 450 mm column (8485 particles).

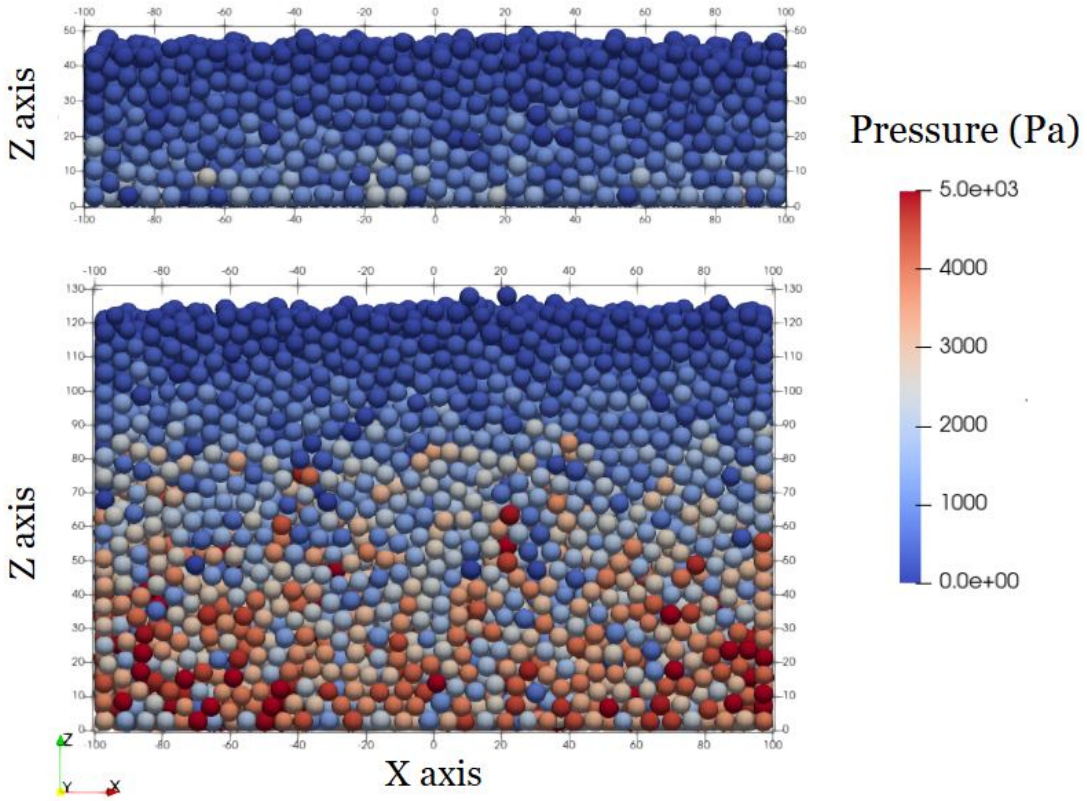

Figure 4.3: Visualisation of the pressure on each particles of the system after a set box simulation. The top figure corresponds to the orange line (Figure 4.2), with 2980 particles, and the bottom figure corresponds to the blue line, with approximately 8485 particles, both in a 200×60 mm container.

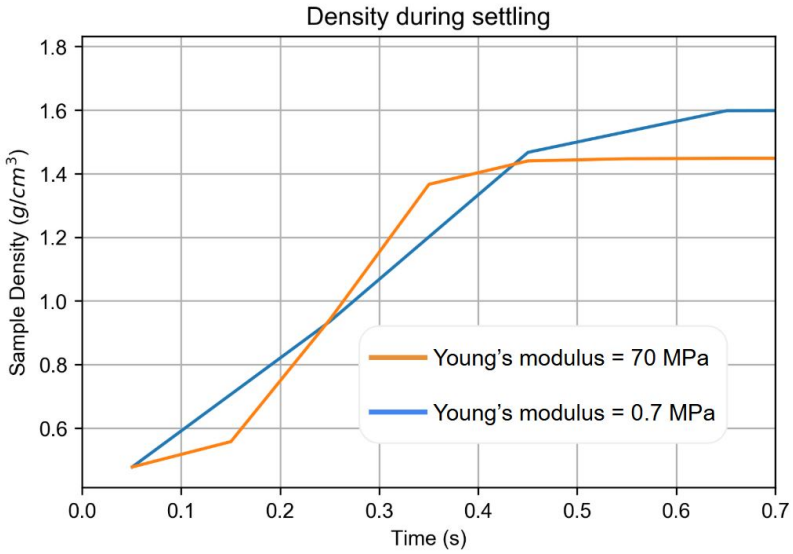

Figure 4.4: Density of the granular sample (case 1) during the settling of the "set box" simulation. The orange line is the density of the material with a Young's modulus of 70 MPa and the blue line is the density of the material with a Young's modulus of 0.7 MPa both with 8485 particles.

corresponding to 9 times the height of half the shear box (40 mm) and extended the (x,y) size of the container to 200×150 mm to ensure both a large shearing area as well as a fairly large number of particles ($\approx$ 12000 particles in the set box simulation).

Figure 4.6 shows the densities obtained with these parameters. Here, cases 1, 2 and 3 have densities of respectively 1.44, 1.40 and 1.31 g/cm^3 and 1.41, 1.40 and 1.32 g/cm^3 in Sunday (2022). In order to estimate if these differences are significant, we used the work of Yin et al. (2021) that used data from O'Rourke et al. (1990), who have tested the influence of sand density on the resulting shear stresses of direct shear tests. Yin et al. (2021) pointed that for sands looser than 15.7 kN/m^3 equivalent to a density of 1.6 g/cm^3 at Earth gravity, the resulting coefficient of frictions is almost constant, while increasing at an accelerating rate above (see Figure 4.5). Consequently, we considered the differences in densities of 0.03 g/cm^3 for case 1 and 0.01 g/cm^3 for case 3 between this study and the work of Sunday (2022) insignificant for the results of our shear tests. To conclude, this column size allow both reproducibility as well as consistent densities between this study and the study of the same granular materials in Sunday (2022). Similar densities between both works ensure that the bulk properties measured with our shear tests and the results of C. Sunday are comparable.

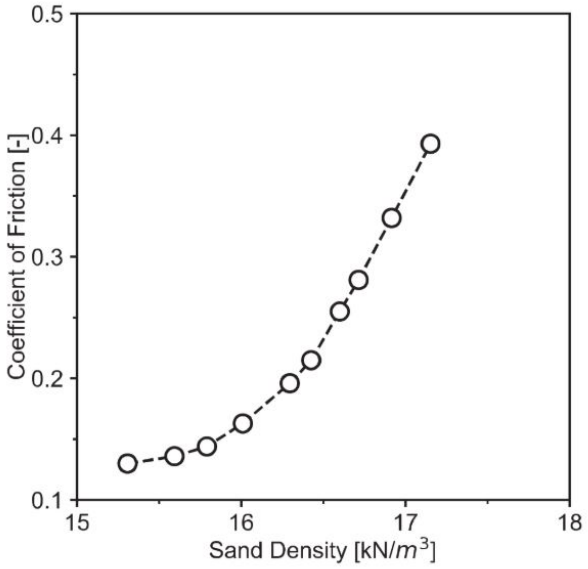

Figure 4.5: Coefficient of friction as a function of sand density. Figure from Yin et al. (2021), with data from O'Rourke et al. (1990).

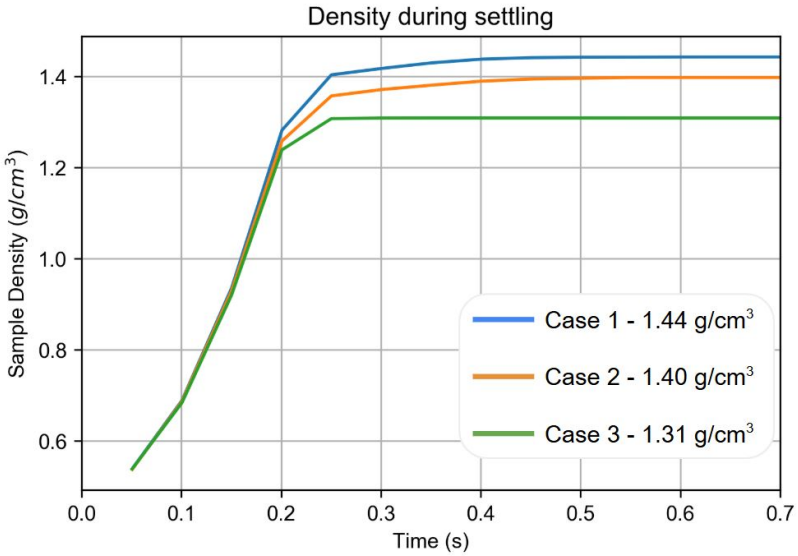

Figure 4.6: Bulk densities obtained for simulated cases 1, 2 and 3 during the settling of the particle samples.

4.3 Loading parameters

After the settling of the granular sample, a confining pressure is applied along the z axis. For each shear test, we chose 3 different normal pressures σ_n of 2.5, 5 and 10 kPa. These pressures are relatively low compared to normal stresses applied on granular samples in the laboratory (usually in the range of a few dozen of kPa to hundreds of kPa), but high enough to yield satisfactory results (Schellart, 2000). These normal pressures corresponds to loading plates with respective weights m of 7.6 kg, 15.3 kg and 30.6 kg, obtained for a 200×150 mm shear box ($m = \sigma_n \times \frac{A}{g}$, with m the mass of the loading plate, σ_n the normal stress applied on the granular sample, A, the area of the shear plane and g the gravitational acceleration). Applying higher loads on the simulated granular samples would require smaller time steps, meaning longer simulations. Indeed, each of these shear test simulations took 5 to 6 days to run with an RTF of ≈ 14000.

To verify that this range of normal pressures combine with the chosen shear speed allow a low enough inertia of the granular system to remain in a quasi-static regime, we used Eq. 3.18. The results are in Table 4.4. Thus, we verified that the inertia numbers are low enough ($< 10^{-3}$), indicating that the system is in quasi-static regime and not shear-rate-dependant (GDR MiDi, 2004).

Now that we have chosen the parameters and verified that these are correct in order to perform the shear tests of simulated granular materials, I will present how we estimated the bulk properties of these materials in the next section. These parameters are summarised in Table 4.5.

σ_n (kPa)	Inertia number ($kg.m^2$)
2.5	3.0×10^{-5}
5.0	2.1×10^{-5}
10.0	1.5×10^{-5}

Table 4.4: Inertia numbers of the granular system under different loading pressures. Values of inertia numbers are calculated from Eq. 3.18, and the other parameters besides σ_n are $\dot{\epsilon} = 0.005\ s^{-1}$, $d = 6.0 \times 10^{-3}\ m$ and $\rho = 2480\ kg.m^{-3}$.

Parameters	Values	Units
Box size	$200 \times 150 \times 80$	$mm \times mm \times mm$
Shear Speed	1	mm/s
Shear Rate	0.005	s^{-1}
Number of Particles	≈ 12000	-
Drop Height	360	mm
Normal Loads	2.5, 5, 10	kPa
Loading Weights	7.6, 15.3, 30.6	kg

Table 4.5: Summary of the parameters chosen to perform the shear tests of numerical cases 1, 2 and 3.

4.4 Results of the Direct Shear Test

4.4.1 From Direct Shear Test to maximum shear stresses

From the example with case 1, presented at the end of the precedent chapter (see Sect. 3.7), I will present how we were able to estimate the bulk properties of simulated granular materials, namely their angle of internal friction and their bulk cohesion.

First, we need to perform the shear test at the three different normal stresses chosen earlier: 2.5 kPa, 5 kPa and 10 kPa. The resulting shear stresses as a function of the displacement of the lower frame of the shear box strain is displayed in Figure 4.7. Then as stated in Sect. 3.7, we measure the shear stress at each normal stress either after a displacement of 10% of the shear box i.e. 20 mm here, or the maximum stress measured, whichever occurs first during shearing (International Organization for Standardization, 2018).

4.4.2 Estimation of the measurement variability

Before showing the results, in order to estimate the variability of the measured shear stress, we performed the same shear test at the same normal stress with three different set box simulations. The resulting plot is in Figure 4.8. We thus measured three different shear stresses τ: 4542.4 Pa, 4479.1 Pa and 4431.4 Pa. From these results, we calculated a standard deviation of the shear stress for this test of 45.4 Pa and an average shear stress of 4484.3 Pa. From these values, we estimate a relative standard deviation (RSD) of the measured shear stress such as :

$$RSD = \frac{\sigma}{\bar{\tau}} * 100 \tag{4.3}$$

with σ the standard deviation and $\bar{\tau}$ the average shear stress. If we want a 95% confidence

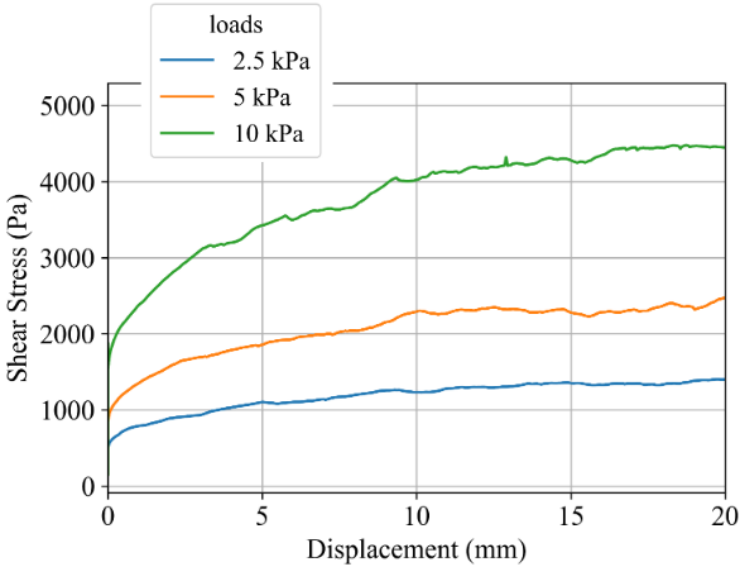

Figure 4.7: Shear stress as a function of the displacement of the lower frame of the shear box during the shearing of a sample of ≈ 12000 low frictional glass particles under normal stresses of 2.5 kPa, 5 kPa and 10 kPa.

interval, the measured shear stress error is $\frac{1.96\times\sigma}{\bar{\tau}} * 100$, so in our case 2%. The RSD calculated with Eq. 4.3 is 1%, indicating that our shear stress results are in the 95% confidence interval.

4.4.3 From maximum shear stresses to bulk properties

Finally, we plot the three different shear stresses as a function of the three normal stresses at which these have been measured. Then we fit a linear regression on those points and the resulting linear equation in the form $y = ax + b$ is the Mohr-Coulomb criterion (Eq. 1.5) with $y = \tau$ the shear stress, $a = tan\theta = \mu$ the coefficient of friction and θ the angle of internal friction of the material, $x = \sigma$ the normal stress and $b = c$ the bulk cohesion of the material.

In order to take into account the variability of the measurements on the shear stress, we used the numpy polyfit function (Harris et al., 2020), allowing us to find the coefficient a and b of the linear fit while taking in account the error on the measure. Then, thanks to the covariance matrix also provided by the polyfit function, we are able to know the error on the coefficient of the fitted linear function. The resulting error on the shear stress combining the measurement variability and the fit error is $\sqrt{\delta_\tau^2 + \delta_{fit}^2}$ with δ_τ the variability of the measure and δ_{fit} the error of the fit obtained from the covariance matrix. The results thus obtained for case 1, a low frictional glass beads sample are displayed in Figure 4.9.

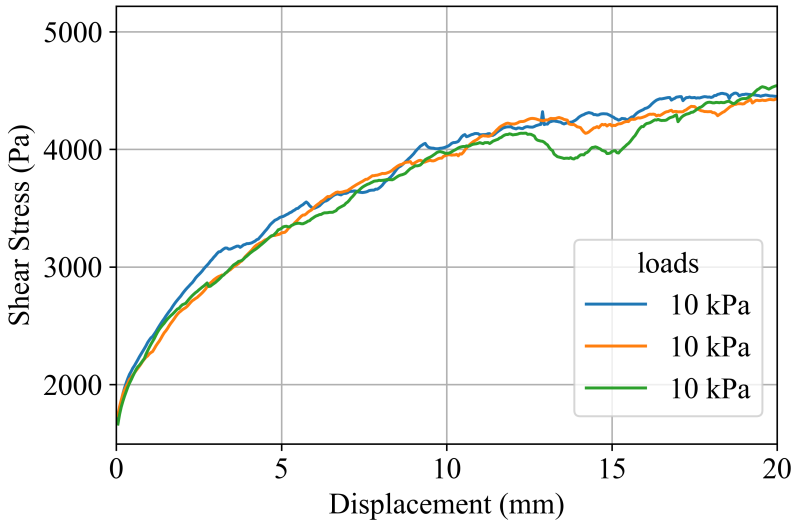

Figure 4.8: Shear stress as a function of the displacement of the lower frame of the shear box during the direct shear test of a sample of simulated low frictional glass beads. Here, the test has been performed with three different set box simulations to estimate the variability of the results of the direct shear test. The measured shear stress here are 4542.4 Pa, 4479.1 Pa and 4431.4 Pa.

Thus, we were able to measure the bulk properties of a simulated granular material. In comparison with the friction of glass beads measured from laboratory direct shear tests (see Table 4.2), the simulated ones have low friction. However, the simulated particles are larger in size and the sample is also looser, which may explain the difference in friction between our simulations and real glass beads: $\mu = 0.57$ for 0.6 mm glass beads in the laboratory and $\mu = 0.41$ for 12 mm simulated glass beads respectively corresponding to angles of internal friction of 29.56° and 22.4°. Indeed, particle size (Podczeck and Mia, 1996; Islam et al., 2017), inter-particle friction, as well as bulk density of the sample before loading (O'Rourke et al., 1990) influence the angle of internal friction of the granular sample: the increase of particle size and the decrease of density both result in a decrease of the angle of internal friction.

However, from tri-axial shear tests of 4 mm glass beads with a bulk density of 1.39 g/cm^3, Wu et al. (2017) measured angle of internal frictions as low as 22.5°, similar to what we measured with the direct shear test simulation. On the other hand, the bulk cohesions are in the same order of magnitude even if both materials apparently do not present inter-particle cohesion.

The results obtained for the other simulated cases 2 and 3, the frictional glass beads without

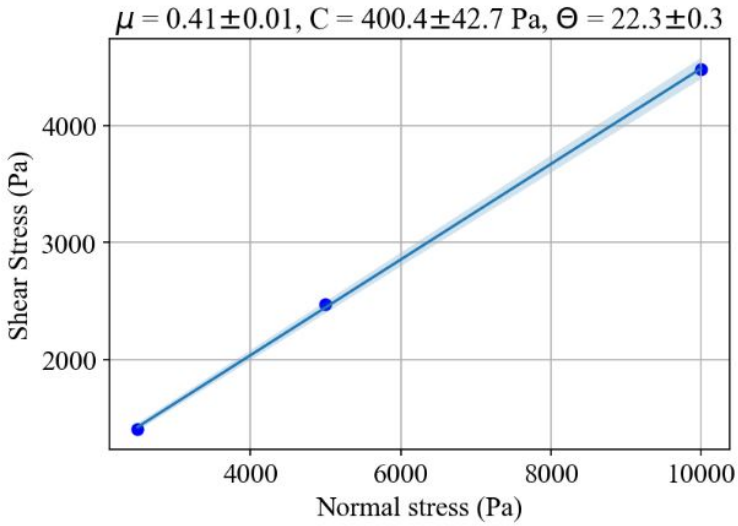

Figure 4.9: Shear stress as a function of normal stress for case 1, corresponding to simulated low frictional glass beads. The blue line is the linear regression of the three points obtained from the shear tests (Figure 4.7). The shaded area corresponds to the error zone of the fit, resulting in the errors displayed for the bulk parameters above the plot.

Case	Coefficient of friction μ (-)	Angle of internal friction θ (°)	Bulk cohesion C (Pa)
1	0.41 ± 0.01	22.4 ± 0.3	400.4 ± 42.7
2	0.41 ± 0.01	22.3 ± 0.4	469.0 ± 46.0
3	0.38 ± 0.01	20.8 ± 0.4	559.8 ± 46.2

Table 4.6: Bulk strength properties of the simulated granular material measured with the shear test

cohesion and the frictional glass beads with cohesion are displayed in Figure 4.10 and in Table 4.6 along with the results of case 1.

4.4.4 Influence of inter-particle properties on bulk properties of granular material

First, when the inter-particle friction is increasing from 0.16 to 0.4 between case 1 and 2 (see Table 4.1), the angle of internal friction is decreasing of 0.1°, while it is expected to increase (see Table 4.6). It seems that changing inter-particle friction does not influence the internal friction angle measured by the shear tests. This is a behaviour that could be expected, knowing that the angle of internal friction first increases with the inter-particle friction but then reaches a plateau (Skinner, 1969; Gong et al., 2019).

However, with the same increase of inter-particle friction (0.16 to 0.4), the bulk cohesion of

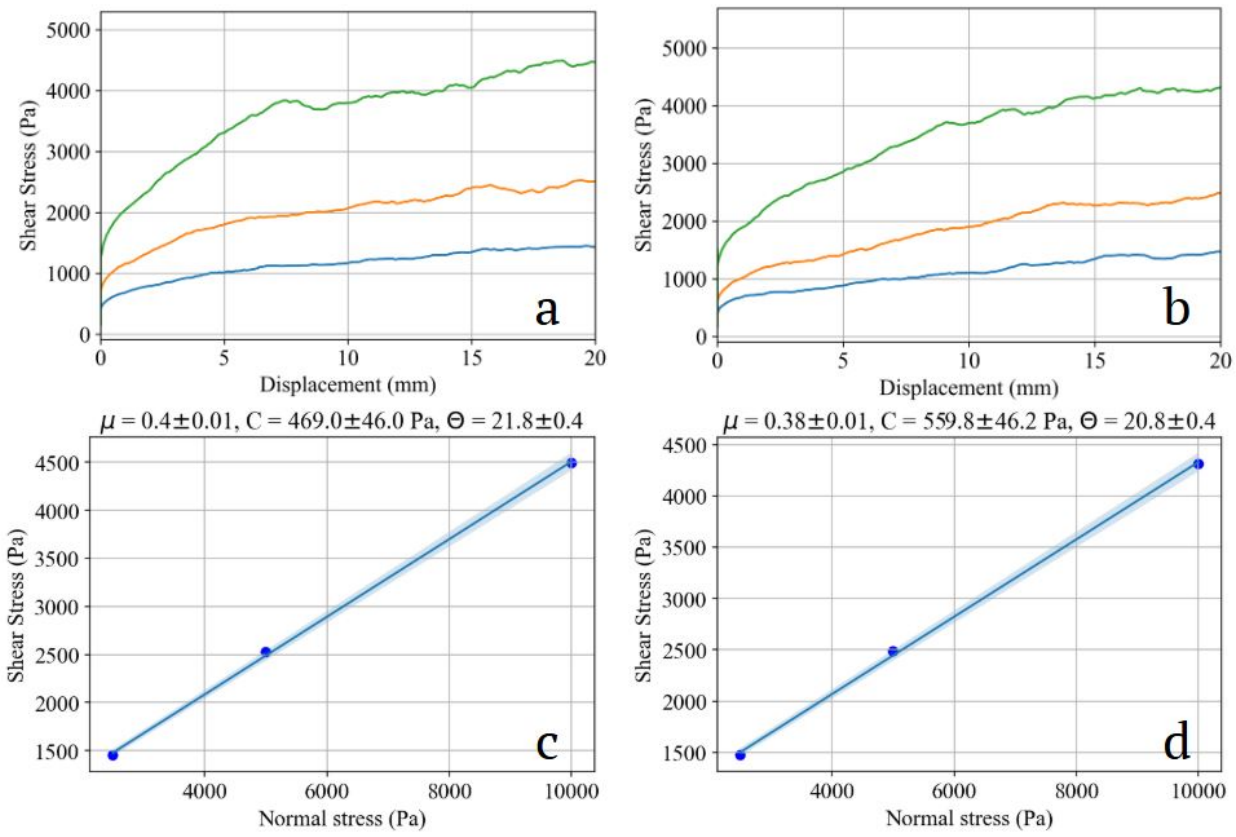

Figure 4.10: (Top) Shear stress as a function of displacement of the lower frame of the shear box for simulated cases 2 (a) and 3 (b), respectively corresponding to frictional glass beads without cohesion and frictional glass beads with cohesion. (Bottom) Shear stress as a function of normal stress for simulated cases 2 (c) and 3 (d). The blue line is the linear regression of the three points obtained from the shear tests above. The shaded area corresponds to the error zone of the fit, resulting in the errors displayed for the bulk parameters above the plot.

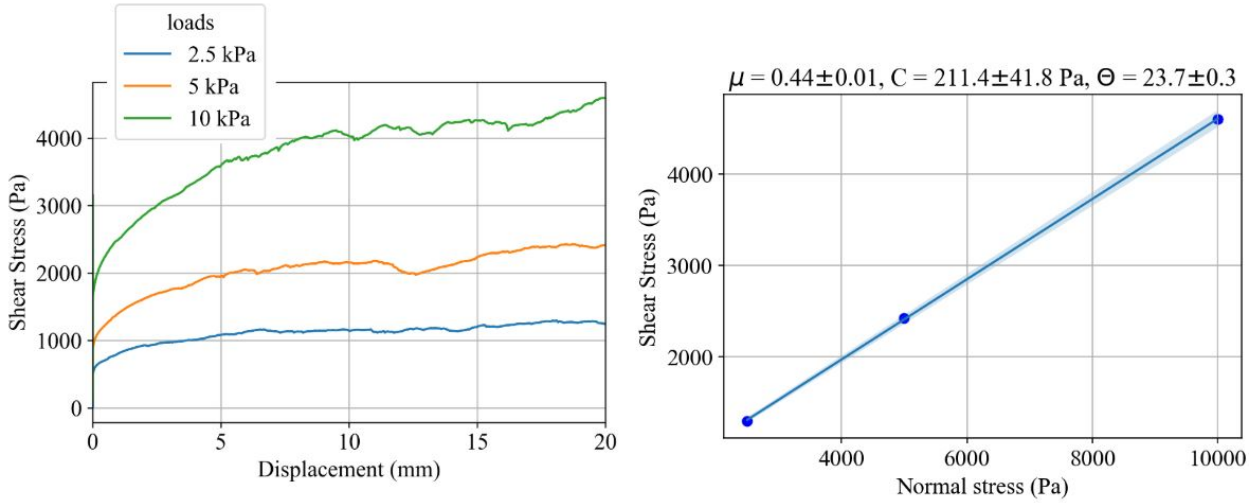

Figure 4.11: (Left) Shear stress as a function of displacement of the lower frame of the shear box for a simulated sample of a low frictional material without twisting or rolling friction. (Right) Shear stress as a function of normal stress. The blue line is the linear regression of the three points obtained from the shear tests on the left. The shaded area corresponds to the error zone of the fit, resulting in the errors displayed for the bulk parameters above the plot.

the material is also increasing, from 400.4 ± 42.7 Pa to 469.0 ± 46.0 Pa, for cases 1 and 2 respectively. Most notably, we measure non-zero bulk cohesions for these materials without inter-particle cohesion. We hypothesise that this is actually geometric cohesion, a well known parameter for granular material (Franklin, 2012; Aponte et al., 2024; Barés et al., 2026), mimicked in *Project Chrono* by the different friction coefficients (inter-particle friction, twisting friction and rolling friction).

In order to verify this hypothesis, we performed the direct shear test of a low frictional material without twisting and rolling friction (case 1 in Table 4.1 with $\mu_r = \mu_t = 0$). If our hypothesis is correct, we should measure less cohesion with the shear test (see Figure 4.11). As expected, bulk cohesion is decreasing, from 400.4 ± 42.7 Pa to $211.4.0 \pm 41.8$ Pa between case 1 and the case with rolling and twisting friction set to zero.

To summarise, we observe from our direct shear tests simulation that increasing the inter-particle frictions (tangential, rolling and twisting frictions) increase the bulk cohesion of the material, due to simulated geometrical cohesion but does not affect the internal friction angle as we would expect. In the next section, we will focus on the role of normal stress in the results of our direct shear tests results.

4.4.5 Influence of normal stress on bulk properties of granular materials

In planetary environments and especially on Phobos, gravity is significantly reduced (on Earth $g = 9.81\ m/^2$ and $g = 0.006\ m/s^2$ on Phobos). Notably, the normal stress applied or acting on regolith will be very different from those that we tested in our direct shear tests. Indeed, for a rover of 25 kg, a quarter of its mass is $m = 6.25$ kg (Sunday, 2022). For a wheel with a radius R of 77 mm, a thickness t of 53 mm, and assuming a penetration depth h of 40 mm of the wheel in the regolith, the cross section in contact has a surface $S = 2\sqrt{R^2 - (R-h)^2} \times t = 2\sqrt{77^2 - (77-40)^2} \times 53 = 7157,97\ mm^2$. Finally, at Phobos gravity, the normal stress σ_n applied by the wheel on the regolith is $\sigma_n = \frac{mg}{S} = \frac{6.25 \times 0.006}{7.158 \times 10^{-3}} = 5.24$ Pa. A wheel of the MMX rover Idefix on a flat terrain would thus apply a 5.24 Pa normal stress on Phobos' regolith, which is three orders of magnitude under the normal stresses of 2.5, 5 and 10 kPa that we applied in our shear tests.

Thus, in order to investigate the role of normal stress, we will perform the shear test of case 1 (see Table 4.1) with low normal stresses. This has notably been inspired by the work of Schellart (2000) who performed direct shear tests with normal stresses under 400 Pa. Below this threshold, W.P. Schellart observed that the Mohr-Coulomb curves tends towards zero bulk cohesion (See Figure 4.12), also meaning higher coefficients of friction. In addition to low normal stresses, we will perform these direct shear tests in Phobos gravity. We chose normal stresses of 5 and 10 Pa, corresponding to a quarter and half the weight of the rover applied on a wheel of the MMX rover Idefix and a near zero normal pressure of 0.6 mPa. The results are displayed in Figure 4.13. First, we can see that the measured shear stress is more unstable by a factor 10 compared to the stresses under a few kPa. Indeed, for example, on Figure 4.8, these variations are in the order of 50 Pa, corresponding to 1% variations of the measured shear stress. In the low gravity shear tests, these variations are on average of 1 Pa for the 10 Pa normal stress corresponding to variations of 15% of the measured shear stress. These observations have been taken in account in the estimations of the error on the coefficient of friction and the bulk cohesion of this material. Thus, in Phobos gravity, under low normal stresses, the measured coefficient of friction of case 1 is 0.63 ± 0.2, its bulk cohesion is 0.3 ± 1.4 Pa, and its angle of internal friction is $32.2 \pm 11.5°$. In agreement with Schellart (2000), the measured bulk cohesion under low normal stresses is near zero. Similarly, the angle of internal friction has increased from $22.3° \pm 0.3°$ to $32.2° \pm 11.5°$ for the same glass beads, between high normal stresses in Earth gravity and low normal stresses in Phobos gravity. This test confirms and highlights the fact that the confining pressure and

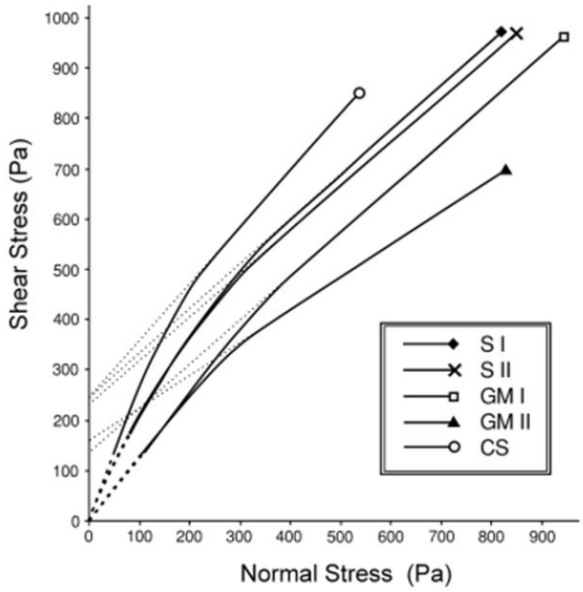

Figure 4.12: Mohr-Coulomb curves obtained from direct shear test experiments. S I is sand with a grain size smaller than 400 μm, S II is sand with a grain size in the 90-180 μm size range, GM I are glass microsphere in the 400-600 μm size range, GM II are glass microspheres in the 90-180 size range and CS is caster sugar with a grain size smaller than 355 μm. The values of strength parameters measured from these plots are in Table 4.2. Figure from Schellart (2000).

the normal stress applied on a granular material will affect its bulk cohesion and its angle of internal friction under very low confining stress.

In order to verify this result with other data, we compared our results with other results of the bibliography. First, Gasteiner et al. (2026) made a database of the properties of different lunar materials and simulant, tested both in-situ or on Earth. In this database, the only material tested with available angle of internal friction and bulk cohesion are the Apollo 12 data, measured in-situ from Extra-Vehicular Activities observations (Manned Spacecraft Center, 1970) and from a core tube experiment (Collinson, 1992). On Earth, the samples returned from the Apollo 12 mission have been tested with direct shear test, triaxial shear test and vacuum direct shear test in Collinson (1992) and with direct shear test in Jaffe (1973). As different methods are used, I compared the average angle of internal friction and bulk cohesion measured on the Moon for the Apollo 12 experiments with the average angle of internal friction and bulk cohesion measured on Earth for the Apollo 12 samples. In-situ, the Apollo 12 experiments measured an average internal friction angle of 39° and an average bulk cohesion of 593 Pa. On Earth, the Apollo 12 samples have been measured with an

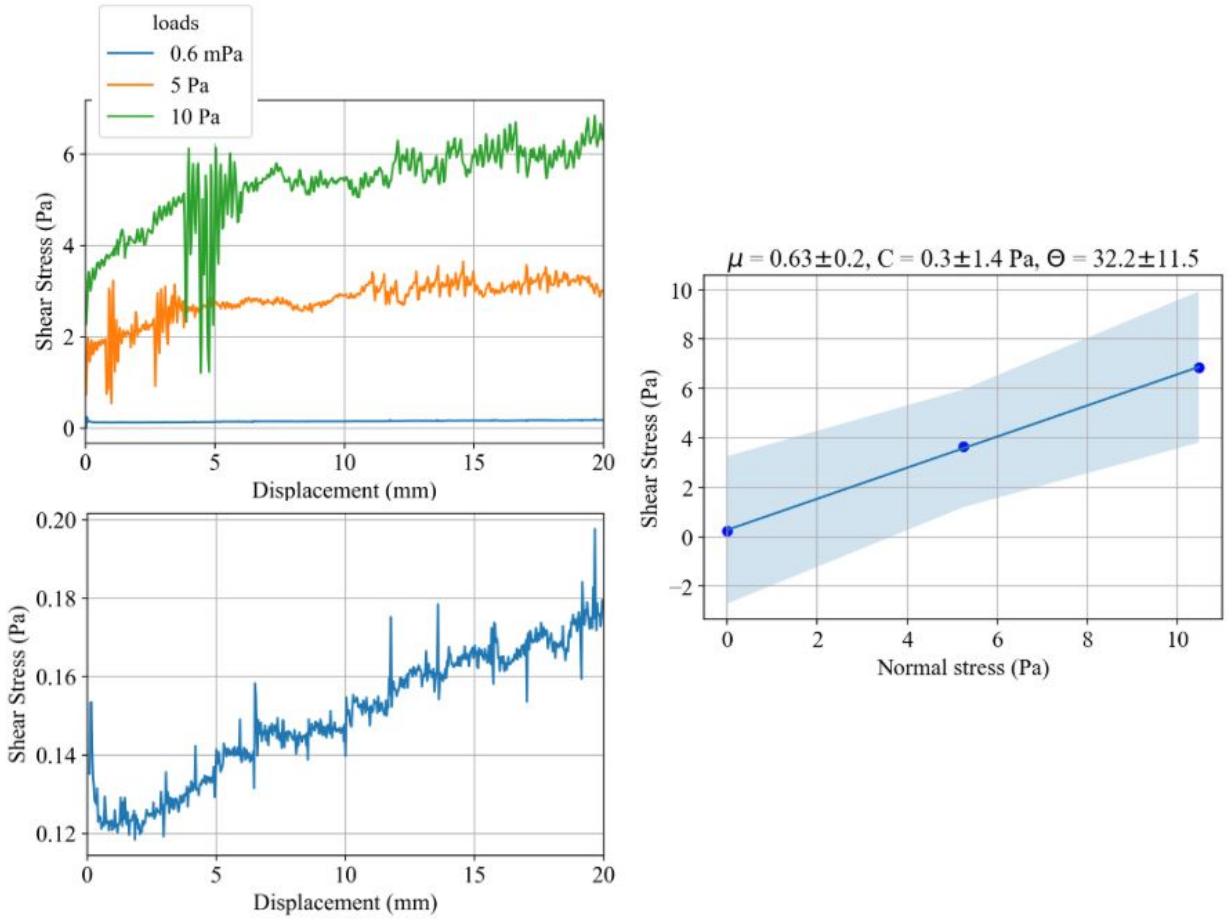

Figure 4.13: (Left) Shear stress as a function of displacement of the lower frame of the shear box for a simulated sample of a low frictional glass beads (case 1) under Phobos gravity. The bottom figure is a close-up of the shear test with a normal stress of 0.6 mPa. (Right) Shear stress as a function of normal stress for a simulated sample of a low frictional glass beads (case 1) under Phobos gravity. The blue line is the linear regression of the three points obtained from the shear tests on the left. The shaded area corresponds to the error zone of the fit, resulting in the errors displayed for the bulk parameters above the plot.

average internal friction angle of 30° and an average bulk cohesion of 1156 Pa. Here, we can see that the internal friction angle and bulk cohesion are different for a similar material, and respectively higher and lower in a low gravity environment, similarly to our observations and those of Schellart (2000). However, we cannot say with certainty that this result is only due the low gravity environment as different methods have been used. In addition, we compared this results with the results of our digital study, the results of Schellart (2000) obtained under high normal stresses, as well as the results of angle of internal frictions obtained from our morphological study of Dimorphos, Ryugu and Bennu and the estimations of their bulk cohesion, respectively by Raducan et al. (2024), Jutzi et al. (2022) and Walsh et al. (2022), in Figure 4.14. We can notably see that the results we obtained with our direct shear tests in low gravity fall within the values estimated for Dimorphos, Ryugu and Bennu.

As stated earlier, it seems that the cohesion of materials is linked with gravity and confining stress, however, the disparity of methods used to measure or compute these different parameters makes it difficult to affirm this hypothesis with certitude. Also, it is possible that Earth gravity and Moon gravity are not different enough to observe significant changes in internal friction angles and bulk cohesion of materials. Indeed, we can see that the cohesion of materials tested on the Moon are on average higher than the materials tested in Schellart (2000) (see Figure 4.14) and the internal friction angle is in the same range, around 40 °.

To conclude, the influence of normal stress on the bulk properties of materials also highlights the importance of performing macroscopic, bulk characterisation tests in-situ to ensure the tests are performed under appropriate confining stress levels. Indeed, in the laboratory, maintaining a constant low confining pressure is almost impossible (Marti, 2024), and the hydrostatic pressure gradient, which is linear in g, will be significantly reduced in low-g leading to much lower confining stresses. It is notably relevant regarding sample return missions, as the strength properties of such returned materials would be different under different gravity conditions. Similarly, this result is also of particular importance in the terramechanics field, which will be discussed in the next section.

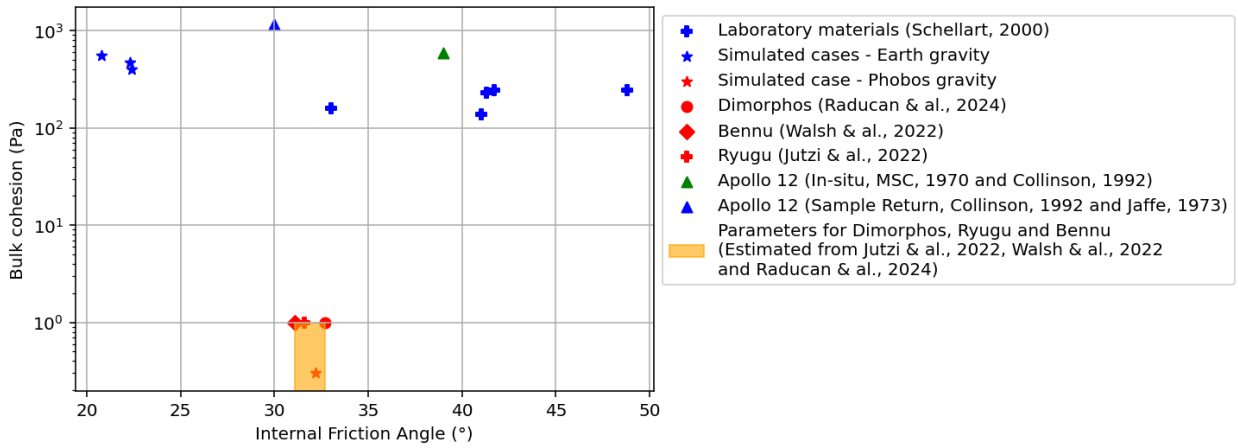

Figure 4.14: Bulk cohesion as a function of angle of internal friction of different granular materials measured at different at different gravity levels. Blue corresponds to Earth gravity, green corresponds to Moon gravity and red corresponds to microgravity. For Dimorphos, Bennu and Ryugu, the value of 1 Pa for the cohesion is an upper limit. The orange area thus represents the possible values of bulk cohesion and internal friction for these rubble-pile asteroids, estimated from the red data points from Jutzi et al. (2022); Walsh et al. (2022) and Raducan et al. (2024).

4.5 Implication of the results of the shear tests for terramechanics

Terramechanics models use empirical terrain parameters in order to interpret or predict vehicles behaviour when roving or sinking. However, if these terrain parameters are incorrect, the model will also be incorrect. As stated at the beginning of this chapter, C. Sunday performed sinking and driving simulations during her thesis, and to do so, she used models from the field of terramechanics. In the following section, I will first introduce the terramechanics models and equation used by C. Sunday in her thesis, along with the empirical soil parameters studied and then we will verify and discuss if our previous conclusions hold for the results of C. Sunday's thesis, notably regarding the strength of materials with respect to terramechanics equations under low gravity conditions.

4.5.1 An introduction to terramechanics

Terramechanics is the study of wheeled vehicles in interaction with deformable terrains such as soils, sand or more generally granular terrains. In our case, it is the study of the regolith of Phobos in interaction with the wheels of the MMX rover Idefix.

Terramechanics mainly study the driving performances of vehicles in relation with the properties of the soil on which they drive thanks to analytic, empirical or semi-empirical equations.

The parameters most commonly used to asses driving performance include the sinkage of the wheel, its slippage, defined as the difference between the circumference velocity of the wheel ωr and its lateral velocity v, and can be considered as a ratio ranging from -1 to 1, such as:

$$s = 1 - \frac{v}{r_s \omega} \tag{4.4}$$

with s the slip ratio, ω the rotational velocity of the wheel, and r_s the shearing radius of the wheel, defined in Ding et al. (2011) as the radius beneath the wheel where mobilized grains shear against the remained static material. For smooth wheels, without grousers, $r_s = r$, with r the radius of the wheel. For lugged wheels, Ding et al. (2009) propose an estimation of the shear radius r_s, adopted in Sunday (2022), such as:

$$r_s = r + \frac{h}{2} \tag{4.5}$$

with r the radius of the wheel without grousers and h the height of the grousers. Finally, the slipping ratio enables a qualitative representation of slippage as the wheel is slipping when $s > 0$ and skidding when $s > 0$.

Other parameters studied in terramechanics are the travel distance, which is simply the the lateral displacement of the wheel and the traction and drawbar pull: traction is defined as the force a vehicle can develop against the ground to advance itself in a desired direction, then, the drawbar pull is the remaining force after removing the motion resistance of the ground on the wheels of the vehicle. Meirion-Griffith and Spenko (2011) emphasise that compaction resistance - the force used to compress and displace the surface material when driving - is the largest contributor to motion resistance.

The most famous theory and the base of terramechanics is the Bekker theory, which is a semi-empirical model considering the soil as significantly softer than the wheel i.e. that the soil is deformable and the wheel is not (Bekker, 1956). This model notably allows to compute the pressure acting under the wheel thanks to a set of empirical soil parameters, determined thanks to plate-sinkage experiments or bevameter testing, a penetration test. In the Bekker model, the wheel sinkage is described as the pressure p applied on a flat plate as it is penetrating a granular material using the Bernstein-Goriatchkin equation:

$$p(z) = kz^n \tag{4.6}$$

with z the plate depth and n the sinkage exponent, an empirical parameter. k is a coefficient

function of the plate width b and two other empirical constants k_c and k_ϕ, such as:

$$k = \frac{k_c}{b} + k_\phi \tag{4.7}$$

k_c is the cohesive modulus of sinkage and k_ϕ is the frictional modulus of sinkage. Then the normal stress on the wheel is determined by integrating Eq. 4.6 on the depth of the wheel, resulting in:

$$z_0 = \left[\frac{3W}{b(3-n)\left(\frac{k_c}{b} + k_\phi\right)} \right]^{\frac{2}{2n+1}} \tag{4.8}$$

with z_0 the static sinkage of the wheel, W the normal load on the wheel and D the diameter of the wheel. However, this model does not take in account the influence of the rotation of the wheel. Since the 1950's, the model has been revised and improved several times or modified to be used in more particular setups. Notably, the Bekker theory is only valid for large and heavy vehicles, and its model has thus been adapt by Meirion-Griffith and Spenko (2011) for small and light-weight vehicles. Irani et al. (2011) modified the model to take in account for rigid wheels with grousers of rovers operating in loose sandy soil. Kovács et al. (2019) also adapted the model to take in account for deformable wheels as well as gravity.

In all these cases, the Bekker models for wheel sinkage and compaction resistance rely on the three empirical parameters presented above: k_c, k_ϕ and n, respectively the cohesive modulus of sinkage, the frictional modulus of sinkage and the sinkage exponent.

4.5.2 Linking the shear tests results with terramechanics parameters

Following the procedure in Wong (1980), C. Sunday determined these three empirical parameters (k_c, k_ϕ and n) for the different cases 1, 2 and 3 (see Table 4.1) numerically studied in her thesis and in this thesis. Following the theory of Wong (1980), by performing sinkage tests with two different plates sizes we can calculate k_c and k_ϕ such as:

$$k_c = \frac{b_1 b_2 (a_1 - a_2)}{b_2 - b_1} \tag{4.9}$$

$$k_\phi = \frac{a_2 b_2 - a_1 b_1}{b_2 - b_1} \tag{4.10}$$

with b_1 and b_2 the widths of the two different plates and a_1 and a_2 the pressures on these plates at a given depth z. C. Sunday thus performed two different pressure-sinkage tests with $b_1 = 150$ mm and $b_2 = 200$ mm for each materials. The test simply consist in placing

Material	g (m/s^2)	v_b (mm/s)	Fr_b	n	k (kN/m^{2n})	z_0 (mm)
case 1	9.81	10	0.01	0.62	72	71
	9.81	100	0.1	0.74	171	48
	0.006	2.5	0.1	0.72	0.12	40
case 2	9.81	10	0.01	0.52	77	49
	9.81	100	0.1	0.57	161	29
	0.006	2.5	0.1	0.65	0.15	26
case 3	9.81	10	0.01	0.36	76	27
	9.81	100	0.1	0.28	92	14
	0.006	2.5	0.1	0.75	0.31	20

Table 4.7: Bekker soil parameters and rover wheel sinkage estimates for material cases 1, 2 and 3 described in Table 4.1. The soil parameters have been estimated using plate-sinkage simulations with a penetration speed v_b and Froude number Fr_b. The sinkage exponent n and the sinkage modulus k have been calculated with a least-squares regression using Eq. 4.6. z_0 has been calculated using Eq. 4.8, with $W = 6.25 \times g$ N, $D = 0.154$ m, and $b = 0.053$ m. Adapted from (Sunday et al., 2022).

a plate on the surface of a material and pushing the plate into the granular material at a constant velocity v_b. The pressure p on the plate is recorded while it sinks, until it reaches a final depth of 40 mm. However, the aspect ratios of the plates used were not different enough to identify distinct trends in the pressure-sinkage plots and calculate k_c and k_ϕ using equations 4.9 and 4.10. Nevertheless, it was still possible to calculate n and k from the slopes of the pressure-sinkage curves when the data is plotted on a logarithmic scale by performing a least-squares regression with Eq. 4.6 and 4.8 (Sunday, 2022). The results of these tests are available in Table 4.7. We then compared those values with other data from the literature, notably from Ding et al. (2022). This study focuses on China's Mars rover Zhurong that touched down on Mars in 2021 (Mallapaty, 2021). Thanks to terramechanics and observations of wheel-terrains interactions, they were able to estimate the soil parameters of the Mars terrains on which the rover drove. These estimations along with other various data are displayed in Figures 4.15 and 4.16.

We earlier hypothesised that with lower gravity and lower confining stress, granular material seems to be less strong, with a lower bulk cohesion. This is a behaviour that we can also witness in Figure 4.15: for the numerically tested materials, we can see that for similar Froude Numbers but at different gravity levels, the sinkage moduli indicate that the materials are also much less strong under microgravity. We can also see that at a lower Froude number under the same gravity level, i.e. when less pressure is applied on the sample as the plate is sinking slower, that the sinkage modulus is also smaller, which supports the link between

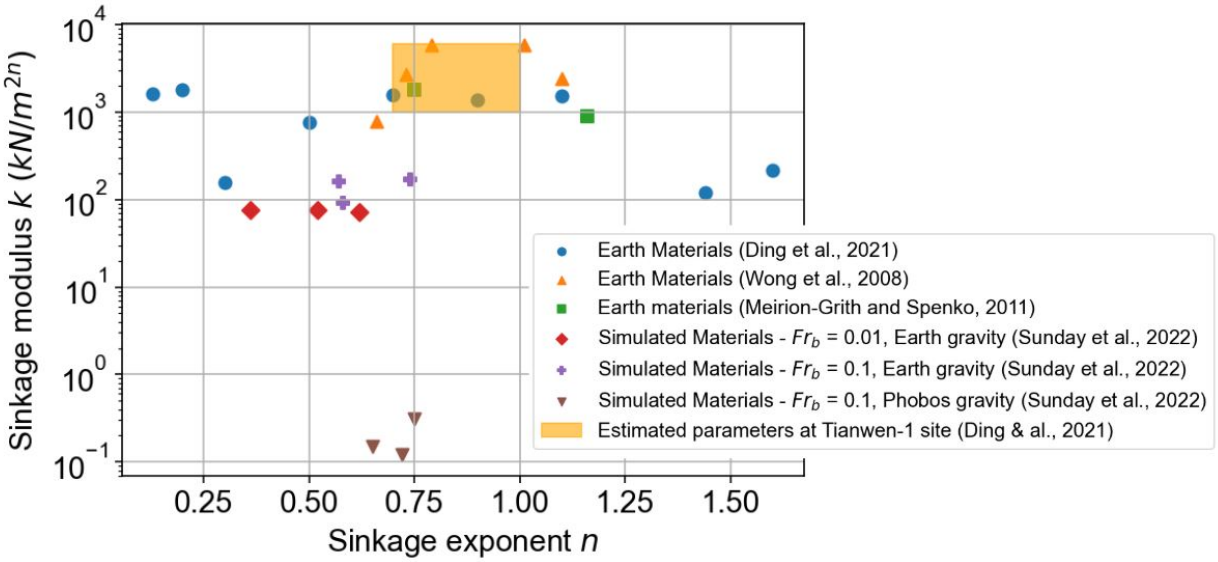

Figure 4.15: Sinkage modulus as a function of sinkage exponent estimated from different studies. The blue dots corresponds to typical soil samples on Earth such as sands, clays and loams (mix of sand, silt and clay) studied by Ding et al. (2022) with their own terramechanics model. Orange triangles corresponds to other Earth materials such as sands and loams studied by Wong (2008). Green squares corresponds to materials studied by Meirion-Griffith and Spenko (2011), namely quartz sand and moist earth. Red diamonds and purple crosses corresponds to cases 1, 2 and 3 with different penetration speeds and Froude numbers under Earth gravity studied by Sunday (2022). Brown triangles corresponds to cases 1, 2 and 3 under Phobos gravity studied by Sunday (2022). The orange area corresponds to the estimated parameters of the soil samples at the Tianwen-1 site (Ding et al., 2022).

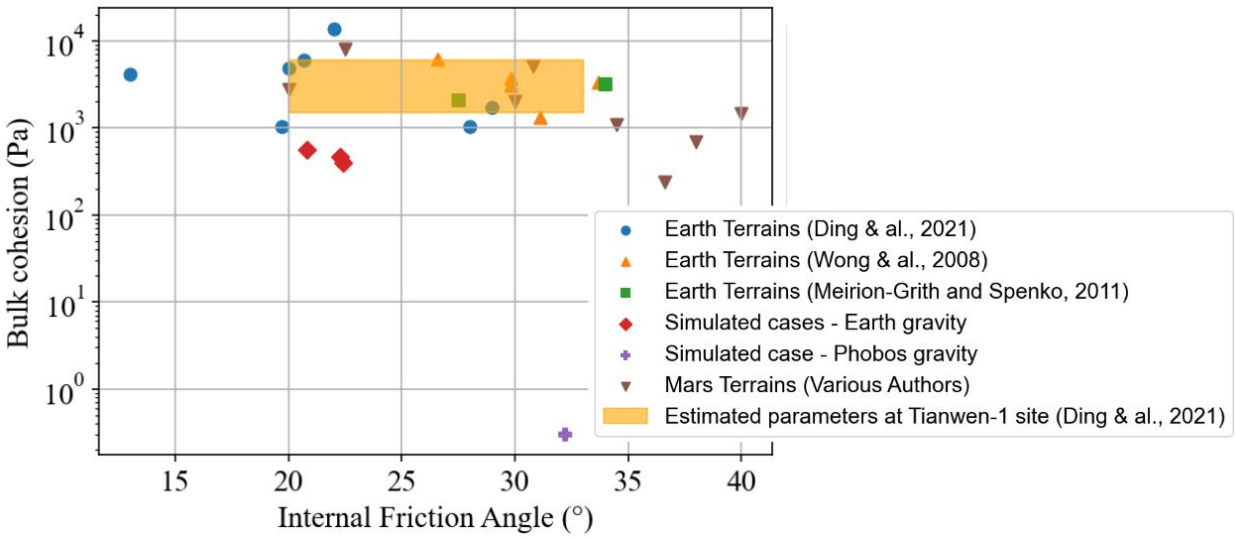

Figure 4.16: Bulk cohesion as a function on angle of internal friction of different materials. The blue dots corresponds to the properties of typical soil samples on Earth such as sands, clays and loams studied by Ding et al. (2022). Orange triangles corresponds to the properties other Earth materials such as sands and loams studied by Wong (2008). Green squares corresponds to the properties of materials studied by Meirion-Griffith and Spenko (2011), namely quartz sand and moist earth. Red diamonds corresponds to the properties of cases 1, 2 and 3 under Earth gravity. Purple crosses corresponds to the properties of case 1 under Phobos gravity. The brown triangles corresponds to the properties of the Mars terrains for various missions (Viking 1 and 2 (Moore and Jakosky, 1989), Mars Pathfinder (Matijevic et al., 1997), MER-Spirit (Arvidson et al., 2004a), MER-Opportunity (Arvidson et al., 2004b), Curiosity (Arvidson et al., 2014), Phoenix (Any et al., 2009) and InSight (Golombek et al., 2020)). The orange area corresponds to the estimated bulk properties of the soil samples at the Tianwen-1 site (Ding et al., 2022).

the confining pressure applied on a granular sample and its bulk strength. These different behaviours have also been observed in a low gravity simulation device: Zou et al. (2015) performed sinkage tests in an inclined bin and also observed that lower gravity makes n, k_{phi} and the cohesion of the material decrease and has little effect on k_c and the angle of internal friction.

Similarly to what we observe for the Moon in Figure 4.14, we do not see a significant difference between the estimated soil properties of the Mars terrains with the Earth terrains. In this case, the gravity difference is even smaller than between Earth and Moon. However, we can estimate the load each wheel is applying on Mars' surface. The load on each wheel of the Zhurong's rover are estimated to 148.8 N under Martian gravity and the wheel area is estimated between 150 and 210 cm^2 (Ding et al., 2022). This would result in a loading between approximately between 7000 and 10000 Pa, which are similar to the loads that we have used to perform the direct shear tests in Earth gravity.

4.6 Conclusions, future works and implications for the MMX rover Idefix and other small-body missions

In this chapter, we performed the direct shear tests of numerical granular samples that were studied in Sunday (2022). We were able to show that geometric cohesion may appear and be measured as bulk cohesion with simulated granular material, even when there is no inter-particle cohesion in the system, due to friction. We were also able to show that gravity seems to be a key parameter in the bulk strength properties of granular materials, in accordance with other observations and studies. Notably, those results also hold for the sinkage-pressure tests that C. Sunday ran during her thesis, using the terramechanics equations.

To go further, we should perform the direct shear tests on the two other cases that were used in C. Sunday thesis under low confining pressure in Phobos gravity. Notably, we could be able to better understand the role of inter-particle cohesion on bulk cohesion with the direct shear test of case 3. As we also saw that geometric cohesion seems to play an important role on bulk cohesion, it would be interesting going further to perform DEM simulations with complex shapes. Indeed, complex shapes of particles allow to better capture the behaviours of granular materials, notably shear banding (Kawamoto et al., 2018). Simulations could be for example run with the Chrono DEM-Engine allowing both GPU computation and complex shapes, for faster and powerful simulations (Zhang et al., 2024).

Finally, regarding the MMX rover Idefix and the other small-body missions or the sample return missions, we should be really careful on the strength properties measured, especially regarding cohesion. For example, it is very likely that if we measure the strength properties of a granular sample returned from a small-body, its cohesion will be higher on Earth than in-situ. More precisely, the derived bulk cohesion of a granular material such as regolith is drastically reduced in low gravity conditions. Future works regarding exploration missions should also aim at defining a unified methodology to measure bulk properties of regolith in-situ, in order to improve interpretations regarding any objects-regolith interactions and allow systematic comparison of these results.

Conclusion and perspectives

This thesis studied granular material in the context of the growing popularity of space exploration missions to small bodies of the solar system. As these missions often involve direct interactions with the surfaces of these small-bodies, with landing, impact experiments or sample returns (see Sect. 1.1.3), understanding the behaviour of their surface covered by regolith in low gravity is crucial. However, we saw through past laboratory experiments, numerical simulations and in-situ observations presented in Sect. 1.2.3 that the behaviour of granular materials in low gravity is complex and often unexpected, notably in the context of space missions.

In the context of the JAXA MMX mission to Phobos, this thesis investigated granular materials in low gravity environments. More precisely, the aim was to contribute to the scientific objectives of the WheelCams onboard the MMX rover Idefix, which will provide exclusive observations of wheel-regolith interactions in low gravity conditions at the surface of Phobos. Notably, this study focused on the scientific objectives 1 and 2 of the Wheelcams as defined in Murdoch et al. (2025). These objectives are determining the physical properties of the regolith particles and determining the bulk mechanical properties of the regolith at the surface of Phobos. To address this challenge, two methods were adopted: an image-based morphological analysis of particles and numerical simulations using the soft-sphere discrete element method.

A first contribution of this thesis, in chapter 2, was the development and validation of an image analysis pipeline. This pipeline is dedicated to the quantitative characterisation of the shape of particles constituting granular materials. This pipeline will notably be helpful to make a first estimation of the angle of internal friction of Phobos' regolith from images of the WheelCams. Its application to images acquired from the WheelCams test bed and from different observations of rubble-pile asteroids, demonstrated its versatility and scientific interest. In particular, the morphological analysis of boulders at the surface of asteroids Itokawa, Ryugu, Bennu and Dimorphos allowed us to contribute in the understanding of the

formation of Dimorphos as part of the DART mission (Robin et al., 2024). It also allowed us to show similarities between the boulders of these different rubble-pile asteroids. The similarities in shapes indicate a shared history, and in particular a common origin of the boulders, which would be the result of the catastrophic disruptions of parent bodies. This study was notably the first analysis of some morphological parameters such as roundness of the boulders at the surface of asteroids. Finally, the results obtained for the boulders of Dimorphos with the pipeline have also been used in other studies, including DART impact simulations showing that Dimorphos has a very low cohesive strength (Raducan et al., 2024) and an analysis of the shape model of Dimorphos, used to estimate the age of Dimorphos' surface and its origins Barnouin et al. (2023).

The second contribution of this thesis was the numerical investigation of the bulk mechanical properties of granular materials, in Earth gravity and in low gravity. The aim was measure the bulk properties of the numerical materials that were used in C. Sunday's thesis (Sunday, 2022) who performed pressure-sinkage and wheel-regolith interactions simulations in Earth and Phobos gravity to investigate the sinkage and driving performances of the MMX rover at the surface of Phobos. However, in DEM codes, the properties of granular materials are inter-particle properties and the bulk properties of the materials are unknown. Consequently, a digital shear box has been developed using the soft-sphere DEM code of *Project Chrono*, allowing us to reproduce laboratory direct shear tests in a numerical environment and retrieve the angle of internal friction and bulk cohesion of simulated granular materials with the Mohr-coulomb failure criterion. In chapter 3, I therefore presented *Project Chrono*, and validated the physics of box objects in interactions with particles. In the thesis of C. Sunday, *Chrono* has been heavily modified, however the physics of box objects have been partially verified and in this thesis, I tested and validated the ability of these box objects to be used as sensors to perform direct shear tests. These tests include normal force tests, cohesion tests and the ability to displace particles with box objects. Finally, I presented how the digital shear box has been built.

Making use of this validated set-up, in chapter 4, we were able to compute the angle of internal friction and the bulk cohesion of numerical materials that were used by C. Sunday in sinkage-pressure tests and wheel-granular material interactions. The results of the shear tests highlighted the influence of inter-particle properties, confining pressure and gravity level on the granular bulk properties. Notably, the simulations showed that increasing the inter-particle friction leads to an increase of the bulk cohesion of granular materials, even when there is no inter-particle cohesion between the grains. We interpreted this behaviour

as geometrical cohesion between the grains, a well known behaviour of granular materials, mimicked in *Chrono* by the different inter-particle frictions. However, in the context of the MMX mission, we performed the direct shear test of a granular material under low normal stresses in Phobos gravity. Indeed, the normal loads applied by the wheel of the MMX rover will be as low as 5 Pa per wheel i.e. three order of magnitudes lower than the shear tests we performed before. This idea was motivated by the observation of Schellart (2000), that under 400 Pa normal stresses, the derived bulk cohesion of the tested material is drastically reduced, leading to a more drastic drop-off of the shear strength than predicted by Mohr-coulomb equation. Our results of this test in low gravity, showed the same behaviour: for the same numerical material, its bulk cohesion is 400.4 ± 42.7 Pa in Earth gravity under normal stresses in the $2.5 - 10$ kPa range and 0.3 ± 1.4 Pa in Phobos gravity under normal stresses in the $6.0 \times 10^{-4} - 10$ Pa range. We were thus able to confirm the observation of Schellart (2000) who performed direct shear stress in the laboratory with normal stresses from 50 to 900 Pa, by performing direct shear tests at even lower normal stresses, in Phobos gravity. In the context of space missions and interactions with regolith, our results highlight the importance of performing macroscopic, bulk characterisation tests in-situ in order to ensure that the material is tested under the correct confining stress.

Finally, in the context of terramechanics, these results have direct implications for rover mobility and surface interactions on small body surfaces. Indeed our direct shear tests results hold for the sinkage-pressure tests performed by C. Sunday, indicating that materials are weaker under low gravity, influencing the terramechanics parameters. However, the exact interrelationship between gravity, normal stress acting on the granular material, its bulk cohesion and especially inter-particle cohesion of the material is still incomplete and further investigations are needed.

In the future, we first plan to use the morphological analysis pipeline on the WheelCams images when the MMX rover Idefix will be deployed and operational at the surface of Phobos. We could also be able to estimate their 3D properties from the 2D images thanks to the methodology proposed by Duchêne et al. (2026), in order to make further interpretations from the images. We also plan to perform the digital shear tests of the other materials that were used by C. Sunday in Phobos gravity. This will help us to have a better understanding of the interrelationship between the bulk properties of the material and its inter-particle properties or with gravity and normal stress. Numerical shear tests should also be performed under other different gravity levels to perform a parametric study from micro-gravity to Earth gravity, to try to quantify the influence of gravity on the bulk properties of granular

materials. Future works should also include the use of non-spherical particles as geometrical cohesion plays an important role in the bulk cohesion of granular material (Kawamoto et al., 2018). Geometrical cohesion may enhance the link between confining external forces and bulk cohesion. This may notably be possible with the use of the *Chrono* DEM-engine, enabling the use of complex shapes and GPU computation. In the future, we could also imagine adding the shaped identified with the morphological analysis pipeline, into a DEM framework. Finally, with the idea that normal load influences the properties of granular material, new wheel simulations should be carried out with varying wheel weights as the MMX rover will most likely apply different loads on each of its wheels if the terrain is uneven. This would notably allow us to try to tests scaling relations such as those presented in Zhang et al. (2020), for cohesive granular materials, in order to better understand the role of cohesion in low gravity.

In conclusion, this thesis contributed to the understanding of granular material behaviours and characterisations in low gravity thanks to image analysis and numerical simulations. While this thesis focused on Phobos and the MMX rover, we believe and showed that the image analysis pipeline can be useful for any granular material observed with a sufficient resolution. Finally, our interpretations of the shear tests results could be of interest for any interactions between any objects with regolith and even for laboratory experiments on granular materials.

Conclusion et perspectives

Cette thèse a étudié les matériaux granulaires dans le contexte de la popularité croissante des missions d'exploration spatiale vers les petits corps du Système solaire. Ces missions impliquant souvent des interactions directes avec les surfaces de ces petits corps, telles que des atterrissages, des expériences d'impact ou des retours d'échantillons (voir Sect. 1.1.3), il est crucial de comprendre le comportement de leurs surfaces en faible gravité, qui sont couvertes de régolithe. Cependant, comme nous l'avons présenté à travers une bibliographie des expériences de laboratoire, des simulations numériques et des observations in situ dans la Sect. 1.2.3, le comportement des matériaux granulaires en faible gravité est complexe et souvent inattendu, notamment dans le contexte des missions spatiales.

Dans le cadre de la mission MMX de la JAXA vers Phobos, cette thèse s'est intéressée aux matériaux granulaires en faible gravité. Plus précisément, l'objectif était de contribuer aux objectifs scientifiques des WheelCams embarquées sur le rover MMX Idefix, qui fourniront des observations inédites des interactions roue–régolithe en conditions de faible gravité à la surface de Phobos. Cette étude s'est notamment concentrée sur les objectifs scientifiques 1 et 2 des WheelCams tels que définis dans Murdoch et al. (2025). Ces objectifs sont respectivement la détermination des propriétés physiques des particules du régolithe et la détermination des propriétés mécaniques macroscopiques du régolithe à la surface de Phobos. Pour relever ce défi, deux méthodes ont été adoptées : une analyse morphologique des particules basée sur l'imagerie et des simulations numériques utilisant la méthode des éléments discrets à sphères molles.

Une première contribution de cette thèse, présentée au chapitre 2, a été le développement et la validation d'un "pipeline" de traitement d'images. Ce pipeline est dédié à la caractérisation quantitative de la forme des particules constituant les matériaux granulaires. Elle sera notamment utile pour effectuer une première estimation de l'angle de frottement interne du régolithe de Phobos à partir des images des WheelCams. Son application à des images acquises sur le banc d'essai des WheelCams ainsi qu'à différentes observations d'astéroïdes

de type « rubble-pile » a démontré sa polyvalence et son intérêt scientifique. En particulier, l'analyse morphologique des blocs rocheux à la surface des astéroïdes Itokawa, Ryugu, Bennu et Dimorphos nous a permis de contribuer à la compréhension de la formation de Dimorphos dans le cadre de la mission DART (Robin et al., 2024). Le pipeline a également permis de mettre en évidence des similarités entre les blocs rocheux de ces différents astéroïdes de type rubble-pile. Ces similarités de forme indiquent une histoire commune, et en particulier une origine commune des blocs rocheux, résultant de disruptions catastrophiques de corps parents. Cette étude constitue notamment la première analyse de certains paramètres morphologiques, tels que l'angularité des blocs rocheux à la surface d'astéroïdes. Enfin, les résultats du pipeline obtenus pour les blocs de Dimorphos ont également été utilisés dans d'autres études, notamment des simulations d'impact de la mission DART montrant que Dimorphos possède une très faible cohésion macroscopique (Raducan et al., 2024), ainsi qu'une analyse du modèle de forme de Dimorphos, utilisé pour estimer l'âge de sa surface et ses origines Barnouin et al. (2023).

La seconde contribution de cette thèse a porté sur l'étude numérique des propriétés mécaniques globales des matériaux granulaires, en gravité terrestre et en faible gravité. L'objectif était de mesurer les propriétés macroscopiques des matériaux numériques utilisés dans la thèse de C. Sunday (Sunday, 2022), qui a réalisée des simulations de tests pression–enfoncement et d'interactions roue–régolithe en gravité terrestre et en gravité de Phobos afin d'étudier l'enfoncement et les performances de roulage du rover MMX à la surface de Phobos. Cependant, dans les codes DEM, les propriétés des matériaux granulaires sont définies à l'échelle inter-particulaire, et les propriétés macroscopiques des matériaux sont inconnues. En conséquence, une boîte de cisaillement numérique a été développée à l'aide du code DEM à sphères molles de *Project Chrono*, permettant de reproduire des essais de cisaillement direct de laboratoire dans un environnement numérique et d'en déduire l'angle de frottement interne et la cohésion macroscopiques des matériaux granulaires simulés selon le critère de rupture de Mohr–Coulomb. Ainsi, dans le chapitre 3, j'ai présenté Project Chrono et validé la physique des objets de type « boîte » dans leurs interactions avec les particules sphériques. Dans la thèse de C. Sunday, *Chrono* a été largement modifié, mais la physique des objets de type boîte n'avait été que partiellement vérifiée. Dans cette thèse, j'ai testé et validé la capacité de ces objets à être utilisés comme capteurs pour réaliser des essais de cisaillement direct. Ces essais incluent des tests de force normale, des tests de cohésion et la capacité à déplacer des particules à l'aide d'objets de type boîte. Enfin, j'ai présenté la construction de la boîte de cisaillement numérique.

En utilisant ce dispositif validé, nous avons pu, dans le chapitre 4, calculer l'angle de frottement interne et la cohésion macroscopiques des matériaux numériques utilisés par C. Sunday dans les tests d'enfoncement–pression et les interactions roue–matériau granulaire. Les résultats des essais de cisaillement ont mis en évidence l'influence des propriétés inter-particulaires, de la pression de confinement et du niveau de gravité sur les propriétés macroscopiques des matériaux granulaires. En particulier, les simulations ont montré que l'augmentation du frottement inter-particulaire conduit à une augmentation de la cohésion globale des matériaux granulaires, même en l'absence de cohésion inter-particulaire entre les grains. Nous avons interprété ce comportement comme une cohésion géométrique entre les grains, un phénomène bien connu dans les matériaux granulaires, reproduit dans *Chrono* par les différentes valeurs de frottement inter-particulaire. Toutefois, dans le contexte de la mission MMX, nous avons réalisé des essais de cisaillement direct d'un matériau granulaire sous de très faibles contraintes normales en gravité de Phobos. En effet, les charges normales appliquées par les roues du rover MMX seront aussi faibles que 5 Pa par roue, soit trois ordres de grandeur en dessous que les essais de cisaillement réalisés précédemment. Cette approche a été motivée par les travaux de Schellart (2000), qui a observé que sous des contraintes normales inférieures à 400 Pa, la cohésion globale déduite du matériau testé est fortement réduite, conduisant à une chute plus marquée de la résistance au cisaillement que celle prédite par l'équation de Mohr–Coulomb. Nos résultats en faible gravité ont montré le même comportement: pour un même matériau numérique, sa cohésion macroscopique est de 400.4 ± 42.7 Pa en gravité terrestre sous des contraintes normales comprises entre 2.5 et 10 kPa, et de 0.3 ± 1.4 Pa en gravité de Phobos sous des contraintes normales comprises entre 6.0×10^{-4} et 10 Pa. Nous avons ainsi confirmé l'observation de Schellart (2000), qui avait réalisé des essais de cisaillement direct en laboratoire sous des contraintes normales comprises entre 50 et 900 Pa, en réalisant des essais de cisaillement direct sous des contraintes encore plus faibles, en gravité de Phobos. Dans le contexte des missions spatiales et des interactions avec le régolithe, ces résultats soulignent l'importance de réaliser des tests de caractérisation macroscopiques in situ afin de garantir que le matériau est testé sous les contraintes de confinement appropriées.

Enfin, dans le domaine de la terramécanique, ces résultats ont des implications directes pour la mobilité des rovers et les interactions avec la surface des petits corps. En effet, les résultats de nos essais de cisaillement direct sont cohérents avec les tests pression–enfoncement réalisés par C. Sunday, indiquant que les matériaux sont plus faibles mécaniquement en faible gravité, ce qui influence les paramètres de terramécanique. Cependant, les relations exactes entre la gravité, les contraintes normales agissant sur le matériau granulaire, sa cohésion globale

et en particulier la cohésion inter-particulaire restent encore incomplètes et nécessitent des investigations supplémentaires.

À l'avenir, nous prévoyons tout d'abord d'utiliser le pipeline d'analyse morphologique sur les images des WheelCams lorsque le rover MMX Idefix sera déployé et opérationnel à la surface de Phobos. Nous pourrions également estimer leurs propriétés 3D à partir des images 2D grâce à la méthodologie proposée par Duchêne et al. (2026), afin de pousser plus loin l'interprétation des images. Nous prévoyons également de réaliser des essais de cisaillement numérique des autres matériaux utilisés par C. Sunday en gravité de Phobos. Cela nous permettra de mieux comprendre les relations entre les propriétés globales du matériau, ses propriétés inter-particulaires, la gravité et la contrainte normale. Les travaux futurs de simulations devraient également inclure l'utilisation de particules non sphériques, la cohésion géométrique jouant un rôle important dans la cohésion globale des matériaux granulaires (Kawamoto et al., 2018). La cohésion géométrique pourrait renforcer le lien entre les forces de confinement externes et la cohésion globale. Cela pourrait notamment être rendu possible par l'utilisation du moteur DEM-engine de *Chrono*, permettant l'utilisation de formes complexes et le calcul sur GPU. À terme, on pourrait également envisager d'intégrer les formes identifiées par le pipeline d'analyse morphologique dans une simulation DEM. Enfin, étant donné l'influence de la charge normale sur les propriétés des matériaux granulaires, de nouvelles simulations de roues devraient être réalisées avec des charges variables, le rover MMX étant susceptible d'appliquer des charges différentes sur chacune de ses roues en cas de terrain irrégulier. Cela permettrait notamment de tester des lois d'échelle telles que celles présentées dans Zhang et al. (2020) pour les matériaux granulaires cohésifs, afin de mieux comprendre le rôle de la cohésion en faible gravité.

En conclusion, cette thèse a contribué à la compréhension du comportement et de la caractérisation des matériaux granulaires en faible gravité grâce à l'analyse d'images et aux simulations numériques. Bien que cette thèse se soit concentrée sur Phobos et le rover MMX, nous pensons, et avons montré avec différentes études, que la chaîne d'analyse d'images peut être utile pour tout matériau granulaire observé avec une résolution suffisante. Enfin, nos interprétations des résultats des essais de cisaillement pourraient être pertinentes pour toute interaction entre des objets et du régolithe, ainsi que pour des expériences de laboratoire sur les matériaux granulaires.

Bibliography

Abe, S., Mukai, T., Hirata, N., Barnouin-Jha, O. S., Cheng, A. F., Demura, H., Gaskell, R. W., Hashimoto, T., Hiraoka, K., Honda, T., Kubota, T., Matsuoka, M., Mizuno, T., Nakamura, R., Scheeres, D. J., and Yoshikawa, M. (2006). Mass and local topography measurements of Itokawa by Hayabusa. *Science (New York, N.Y.)*, 312(5778):1344–1347.

Ahrens, J., Geveci, B., and Law, C. (2005). ParaView: An End-User Tool for Large-Data Visualization. pages 717–731. Elsevier. Book Title: Visualization Handbook.

Ajmal, M., Roessler, T., Richter, C., and Katterfeld, A. (2020). Calibration of cohesive DEM parameters under rapid flow conditions and low consolidation stresses. *Powder Technology*, 374:22–32.

Albee, A. L., Palluconi, F. D., and Arvidson, R. E. (1998). Mars global surveyor mission: overview and status. *Science (New York, N.Y.)*, 279(5357):1671–1672.

André, D., Charles, J.-L., and Iordanoff, I. (2015). *3D Discrete Element Workbench for Highly Dynamic Thermo-Mechanical Analysis: GranOO*. Pages: 183.

Any, S. et al. (2009). Phoenix soil physical properties investigation. *Journal of Geophysical Research*, 114:E00E0.

Aponte, D., Estrada, N., Barés, J., Renouf, M., and Azéma, E. (2024). Geometric cohesion in two-dimensional systems composed of star-shaped particles. *Physical Review E*, 109(4):044908. Publisher: American Physical Society.

Arakawa, M., Saiki, T., Wada, K., Ogawa, K., Kadono, T., Shirai, K., Sawada, H., Ishibashi, K., Honda, R., Sakatani, N., Iijima, Y., Okamoto, C., Yano, H., Takagi, Y., Hayakawa, M., Michel, P., Jutzi, M., Shimaki, Y., Kimura, S., Mimasu, Y., Toda, T., Imamura, H., Nakazawa, S., Hayakawa, H., Sugita, S., Morota, T., Kameda, S., Tatsumi, E., Cho, Y., Yoshioka, K., Yokota, Y., Matsuoka, M., Yamada, M., Kouyama, T., Honda, C., Tsuda, Y., Watanabe, S., Yoshikawa, M., Tanaka, S., Terui, F., Kikuchi, S., Yamaguchi, T., Ogawa, N., Ono, G., Yoshikawa, K., Takahashi, T., Takei, Y., Fujii, A., Takeuchi, H., Yamamoto, Y., Okada, T., Hirose, C., Hosoda, S., Mori, O., Shimada, T., Soldini, S., Tsukizaki, R., Iwata, T., Ozaki, M., Abe, M., Namiki, N.,

Kitazato, K., Tachibana, S., Ikeda, H., Hirata, N., Hirata, N., Noguchi, R., and Miura, A. (2020). An artificial impact on the asteroid (162173) Ryugu formed a crater in the gravity-dominated regime. *Science*, 368(6486):67–71. Publisher: American Association for the Advancement of Science.

Arvidson, R., Bellutta, P., Calef, F., Fraeman, A., Garvin, J., Gasnault, O., Grant, J., Grotzinger, J., Hamilton, V., Heverly, M., Iagnemma, K., Johnson, J., Lanza, N., Mouélic, S., Mangold, N., Ming, D., Mehta, M., Morris, R., Newsom, H., and Wiens, R. (2014). Terrain Physical Properties Derived From Orbital Data and the First 360 Sols of Mars Science Laboratory Curiosity Rover Observations in Gale Crater. *Journal of Geophysical Research: Planets*, 119.

Arvidson, R. E., Anderson, R. C., Bartlett, P., Bell, J. F., Blaney, D., Christensen, P. R., Chu, P., Crumpler, L., Davis, K., Ehlmann, B. L., Fergason, R., Golombek, M. P., Gorevan, S., Grant, J. A., Greeley, R., Guinness, E. A., Haldemann, A. F. C., Herkenhoff, K., Johnson, J., Landis, G., Li, R., Lindemann, R., McSween, H., Ming, D. W., Myrick, T., Richter, L., Seelos, F. P., Squyres, S. W., Sullivan, R. J., Wang, A., and Wilson, J. (2004a). Localization and Physical Properties Experiments Conducted by Spirit at Gusev Crater. *Science*, 305:821–824. ADS Bibcode: 2004Sci...305..821A.

Arvidson, R. E., Anderson, R. C., Bartlett, P., Bell, J. F., Christensen, P. R., Chu, P., Davis, K., Ehlmann, B. L., Golombek, M. P., Gorevan, S., Guinness, E. A., Haldemann, A. F. C., Herkenhoff, K. E., Landis, G., Li, R., Lindemann, R., Ming, D. W., Myrick, T., Parker, T., Richter, L., Seelos, F. P., Soderblom, L. A., Squyres, S. W., Sullivan, R. J., and Wilson, J. (2004b). Localization and physical property experiments conducted by Opportunity at Meridiani Planum. *Science (New York, N.Y.)*, 306(5702):1730–1733.

Attree, N., Groussin, O., Jorda, L., Rodionov, S., Auger, A.-T., Thomas, N., Brouet, Y., Poch, O., Kührt, E., Knapmeyer, M., Preusker, F., Scholten, F., Knollenberg, J., Hviid, S., and Hartogh, P. (2018). Thermal fracturing on comets - Applications to 67P/Churyumov-Gerasimenko. *Astronomy & Astrophysics*, 610:A76. Publisher: EDP Sciences.

Ayachit, U. (2015). *The ParaView Guide: A Parallel Visualization Application*. Kitware, Inc., Clifton Park, NY, USA.

Bagheri, A., Khan, A., Efroimsky, M., Kruglyakov, M., and Giardini, D. (2021). Dynamical evidence for Phobos and Deimos as remnants of a disrupted common progenitor. *Nature Astronomy*, 5(6):539–543. Publisher: Nature Publishing Group.

Ballouz, R. L., Walsh, K. J., Barnouin, O. S., DellaGiustina, D. N., Asad, M. A., Jawin, E. R., Daly, M. G., Bottke, W. F., Michel, P., Avdellidou, C., Delbo, M., Daly, R. T., Asphaug, E., Bennett, C. A., Bierhaus, E. B., Connolly, H. C., Golish, D. R., Molaro, J. L., Nolan, M. C.,

Pajola, M., Rizk, B., Schwartz, S. R., Trang, D., Wolner, C. W. V., and Lauretta, D. S. (2020). Bennu's near-Earth lifetime of 1.75 million years inferred from craters on its boulders. *Nature*, 587:205–209. ADS Bibcode: 2020Natur.587..205B.

Ballouz, R.-L., Walsh, K. J., Sánchez, P., Holsapple, K. A., Michel, P., Scheeres, D. J., Zhang, Y., Richardson, D. C., Barnouin, O. S., Nolan, M. C., Bierhaus, E. B., Connolly, Jr., H. C., Schwartz, S. R., Çelik, O., Baba, M., and Lauretta, D. S. (2021). Modified granular impact force laws for the OSIRIS-REx touchdown on the surface of asteroid (101955) Bennu. *Monthly Notices of the Royal Astronomical Society*, 507(4):5087–5105.

Bardet, J.-P. (1997). *Experimental soil mechanics*. Prentice Hall, Upper Saddle River, NJ.

Bareither, C. A., Edil, T. B., Benson, C. H., and Mickelson, D. M. (2008). Geological and Physical Factors Affecting the Friction Angle of Compacted Sands. *Journal of Geotechnical and Geoenvironmental Engineering*, 134(10):1476–1489. Publisher: American Society of Civil Engineers.

Barnouin, O., Ballouz, R., Marchi, S., Vincent, J.-B., Agrusa, H., Zhang, Y., Ernst, C., Pajola, M., Tusberti, F., Lucchetti, A., Daly, R., Palmer, E., Walsh, K., Michel, P., Sunshine, J., Farnham, T., Richardson, D., Parro, L., Murdoch, N., and Rivkin, A. (2023). *The geology and evolution of a the Near-Earth binary asteroid system (65803) Didymos.*

Barnouin, O. S., Daly, M. G., Palmer, E. E., Gaskell, R. W., Weirich, J. R., Johnson, C. L., Asad, M. M. A., Roberts, J. H., Perry, M. E., Susorney, H. C. M., Daly, R. T., Bierhaus, E. B., Seabrook, J. A., Espiritu, R. C., Nair, A. H., Nguyen, L., Neumann, G. A., Ernst, C. M., Boynton, W. V., Nolan, M. C., Adam, C. D., Moreau, M. C., Risk, B., D'Aubigny, C. D., Jawin, E. R., Walsh, K. J., Michel, P., Schwartz, S. R., Ballouz, R.-L., Mazarico, E. M., Scheeres, D. J., McMahon, J., Bottke, W., Sugita, S., Hirata, N., Hirata, N., Watanabe, S., Burke, K. N., DellaGuistina, D. N., Bennett, C. A., Lauretta, D. S., and OSIRIS-REx Team. (2019). Shape of (101955) Bennu indicative of a rubble pile with internal stiffness. *Nature Geoscience*, 12(4):247–252.

Barucci, M. A., Bernardi, P., Reess, J.-M., Fornasier, S., Merlin, F., Doressoundiram, A., Gautier, T., Iwata, T., Nakagawa, H., Nakamura, T., Donny, C., Abbaki, S., Aoki, S., Arai, T., Beck, P., Bonafous, M., Boutelier, M., Bouquier, J.-C., Brucato, J. R., Bruno, M., Buey, J.-T., Castelnau, M., Charnoz, S., Chaussidon, M., Chapron, F., Coustenis, A., D'anna, W., David, G., Delbo, M., Dubois, B., Etcheverry, S., Garat, C., Gauffre, S., Genda, H., Glize, F., Hassen-Khodja, R., Hazard, V., Hervet, G., Hyodo, R., Imamura, T., Imbert, C., Jacquinod, S., Jorda, L., Kameda, S., Kouach, D., Kouyama, T., Kuroda, T., Kurokawa, H., Lapauw, L., Lasue, J., Le Deit, L., Le Du, M., Leyrat, C., Mathé, C., Matsuoka, M., Millan, M., Miyamoto, H., Moynier, F., Tuong, N. N., Ogohara, K., Osawa, T., Parisot, J., Pilleri, P., Piou, V., Poggiali, G., Pons, N., Quertier-Dagorn, B., Rasamoela, A., Raymond, S., Rocard, F., Rouvié, A., Sakanoi, T., Sato, T. M., Soulie, H., Sawyer, E., Spiga, A., Sultana, R., Theret, N., Trémolières, S., Truchelut, P.,

Tsuchiya, F., Vernazza, P., Wargnier, A., Yumoto, K., and Zeganadin, D. (2025). The MMX InfraRed Spectrometer (MIRS) for the spectral characterization of the Martian system. *Progress in Earth and Planetary Science*, 12(1):69.

Barucci, M. A., Reess, J.-M., Bernardi, P., Doressoundiram, A., Fornasier, S., Le Du, M., Iwata, T., Nakagawa, H., Nakamura, T., André, Y., Aoki, S., Arai, T., Baldit, E., Beck, P., Buey, J.-T., Canalias, E., Castelnau, M., Charnoz, S., Chaussidon, M., Chapron, F., Ciarletti, V., Delbo, M., Dubois, B., Gauffre, S., Gautier, T., Genda, H., Hassen-Khodja, R., Hervet, G., Hyodo, R., Imbert, C., Imamura, T., Jorda, L., Kameda, S., Kouach, D., Kouyama, T., Kuroda, T., Kurokawa, H., Lapaw, L., Lasue, J., Le Deit, L., Ledot, A., Leyrat, C., Le Ruyet, B., Matsuoka, M., Merlin, F., Miyamoto, H., Moynier, F., Nguyen Tuong, N., Ogohara, K., Osawa, T., Parisot, J., Pistre, L., Quertier, B., Raymond, S. N., Rocard, F., Sakanoi, T., Sato, T. M., Sawyer, E., Tache, F., Trémolières, S., Tsuchiya, F., Vernazza, P., and Zeganadin, D. (2021). MIRS: an imaging spectrometer for the MMX mission. *Earth, Planets and Space*, 73(1):211.

Barés, J., Regazzi, A., Aponte, D., Buonomo, S., Renouf, M., Estrada, N., and Azéma, E. (2026). Origin of geometric cohesion in non-convex granular materials: interplay between interdigitation and rotational constraints enhancing frictional stability. arXiv:2601.00262 [cond-mat].

Basilevsky, A. T., Lorenz, C. A., Shingareva, T. V., Head, J. W., Ramsley, K. R., and Zubarev, A. E. (2014). The surface geology and geomorphology of Phobos. *Planetary and Space Science*, 102:95–118.

Bekker, M. G. (1956). Theory of Land Locomotion (1955).

Biele, J., Ulamec, S., Maibaum, M., Roll, R., Witte, L., Jurado, E., Muñoz, P., Arnold, W., Auster, H.-U., Casas, C., Faber, C., Fantinati, C., Finke, F., Fischer, H.-H., Geurts, K., Güttler, C., Heinisch, P., Herique, A., Hviid, S., Kargl, G., Knapmeyer, M., Knollenberg, J., Kofman, W., Kömle, N., Kührt, E., Lommatsch, V., Mottola, S., Pardo de Santayana, R., Remetean, E., Scholten, F., Seidensticker, K. J., Sierks, H., and Spohn, T. (2015). The landing(s) of Philae and inferences about comet surface mechanical properties. *Science*, 349(6247):aaa9816. Publisher: American Association for the Advancement of Science.

Bierhaus, E. B., Songer, J. T., Clark, B. C., Dubisher, R. D., Deden, S. L., Payne, K. S., Wurts, D., McMahon, J. W., Rozitis, B., and Lauretta, D. S. (2021). Bennu regolith mobilized by TAGSAM: Expectations for the OSIRIS-REx sample collection event and application to understanding naturally ejected particles. *Icarus*, 355:114142.

Blume, W. H. (2005). Deep Impact Mission Design. *Space Science Reviews*, 117(1):23–42.

Bocquet, L., Charlaix, , and Restagno, F. (2002). Physics of humid granular media. *Comptes Rendus Physique*, 3(2):207–215.

Brisset, J., Cox, C., Anderson, S., Hatchitt, J., Madison, A., Mendonca, M., Partida, A., and Remie, D. (2020). Regolith behavior under asteroid-level gravity conditions: low-velocity impacts into mm- and cm-sized grain targets. *Astronomy & Astrophysics*, 642:A198. Publisher: EDP Sciences.

Broughton, R. P. (1979). The Visibility of Halley's Comet. *Journal of the Royal Astronomical Society of Canada*, 73:24.

Burke, K. N., DellaGiustina, D. N., Bennett, C. A., Walsh, K. J., Pajola, M., Bierhaus, E. B., Nolan, M. C., Boynton, W. V., Brodbeck, J. I., Connolly, H. C., Prasanna Deshapriya, J. D., Dworkin, J. P., Elder, C. M., Golish, D. R., Hoover, R. H., Jawin, E. R., McCoy, T. J., Michel, P., Molaro, J. L., Nolau, J. O., Padilla, J., Rizk, B., Robbins, S. J., Sahr, E. M., Smith, P. H., Stewart, S. J., Susorney, H. C. M., Enos, H. L., and Lauretta, D. S. (2021). Particle Size-Frequency Distributions of the OSIRIS-REx Candidate Sample Sites on Asteroid (101955) Bennu. *Remote Sensing*, 13(7):1315. Number: 7 Publisher: Multidisciplinary Digital Publishing Institute.

Burns, J. A. (1992). Contradictory clues as to the origin of the Martian moons. In *Mars*, pages 1283–1301. ADS Bibcode: 1992mars.book.1283B.

Cambianica, P., Cremonese, G., Naletto, G., Lucchetti, A., Pajola, M., Penasa, L., Simioni, E., Massironi, M., Ferrari, S., Bodewits, D., La Forgia, F., Sierks, H., Lamy, P. L., Rodrigo, R., Koschny, D., Davidsson, B., Barucci, M. A., Bertaux, J. L., Bertini, I., Da Deppo, V., Debei, S., De Cecco, M., Deller, J., Fornasier, S., Fulle, M., Gutiérrez, P. J., Güttler, C., Ip, W. H., Keller, H. U., Lara, L. M., Lazzarin, M., Lin, Z. Y., López-Moreno, J. J., Marzari, F., Mottola, S., Shi, X., Scholten, F., Toth, I., Tubiana, C., and Vincent, J. B. (2019). Quantitative analysis of isolated boulder fields on comet 67P/Churyumov-Gerasimenko. *Astronomy and Astrophysics*, 630:A15. ADS Bibcode: 2019A&A...630A..15C.

Carr, M. H., Baum, W. A., Blasius, K. R., Briggs, G. A., Cutts, J. A., Duxbury, T. C., Greeley, R., Guest, J., Masursky, H., and Smith, B. A. (1980). Viking orbiter views of Mars. NTRS Author Affiliations: NASA Headquarters NTRS Report/Patent Number: NASA-SP-441 NTRS Document ID: 19810003458 NTRS Research Center: Legacy CDMS (CDMS).

Carr, M. J., Roessler, T., Robinson, P. W., Otto, H., Richter, C., Katterfeld, A., and Wheeler, C. A. (2023). Calibration procedure of Discrete Element Method (DEM) parameters for wet and sticky bulk materials. *Powder Technology*, 429:118919.

Carrier, III, W. D., Olhoeft, G. R., and Mendell, W. (1991). Physical Properties of the Lunar Surface. In *Lunar Sourcebook, A User's Guide to the Moon*, pages 475–594. ADS Bibcode: 1991lsug.book..475C.

Castellanos, A. (2005). The relationship between attractive interparticle forces and bulk behaviour in dry and uncharged fine powders. *Advances in Physics*, 54(4):263–376. Publisher: Taylor & Francis _eprint: https://doi.org/10.1080/17461390500402657.

Castellanos, B. and Brandon, T. (2013). A Comparison between the Shear Strength Measured with Direct Shear and Triaxial Devices on Undisturbed and Remolded Soils.

Cellino, A., Bus, S., Doressoundiram, A., and Lazzaro, D. (2002). Spectroscopic Properties of Asteroid Families. *Asteroids III*, pages 633–643.

Chan, Q. H. S., Stephant, A., Franchi, I. A., Zhao, X., Brunetto, R., Kebukawa, Y., Noguchi, T., Johnson, D., Price, M. C., Harriss, K. H., Zolensky, M. E., and Grady, M. M. (2021). Organic matter and water from asteroid Itokawa. *Scientific Reports*, 11(1):5125. Publisher: Nature Publishing Group.

Chapman, C. R. (1975). The Nature of Asteroids. *Scientific American*, 232(1):24–33. Publisher: Scientific American, a division of Nature America, Inc.

Chapman, C. R. (1978). Asteroid collisions, craters, regoliths, and lifetimes. *In Asteroids: An Exploration Assessment (Eds. D. Morrison & W.C. Wells, NASA Conf. Publ. 2053)*, pages 145–160.

Chapman, C. R., Morrison, D., and Zellner, B. (1975). Surface properties of asteroids: A synthesis of polarimetry, radiometry, and spectrophotometry. *Icarus*, 25(1):104–130.

Chen, H., Chen, Y. X., Wei, Q. S., and Shi, Y. S. (2019). Effect of Gravity on Repose Angle and Contact Forces of Particulate Pile Composed of Non-monodispersed Particles. *International Journal of Aerospace Engineering*, 2019(1):8513149. _eprint: https://onlinelibrary.wiley.com/doi/pdf/10.1155/2019/8513149.

Chen, P. Y., Chantharayukhonthorn, M., Yue, Y., Grinspun, E., and Kamrin, K. (2021). Hybrid discrete-continuum modeling of shear localization in granular media. *Journal of the Mechanics and Physics of Solids*, 153:104404. Publisher: Elsevier BV.

Chen, X., Wang, J., and Li, J. (2015). Multiscale modeling of rapid granular flow with a hybrid discrete-continuum method. arXiv:1512.07354 [physics].

Chen, Y.-C. (2017). A Tutorial on Kernel Density Estimation and Recent Advances. arXiv:1704.03924 [stat].

Cheng, A. (2002). Near Earth Asteroid Rendezvous: Mission Summary.

Cheng, A. F. (1997). Near Earth Asteroid Rendezvous: Mission Overview. In Russell, C. T., editor, *The Near Earth Asteroid Rendezvous Mission*, pages 3–29. Springer Netherlands, Dordrecht.

Cheng, A. F., Agrusa, H. F., Barbee, B. W., Meyer, A. J., Farnham, T. L., Raducan, S. D., Richardson, D. C., Dotto, E., Zinzi, A., Della Corte, V., Statler, T. S., Chesley, S., Naidu, S. P., Hirabayashi, M., Li, J.-Y., Eggl, S., Barnouin, O. S., Chabot, N. L., Chocron, S., Collins, G. S.,

Daly, R. T., Davison, T. M., DeCoster, M. E., Ernst, C. M., Ferrari, F., Graninger, D. M., Jacobson, S. A., Jutzi, M., Kumamoto, K. M., Luther, R., Lyzhoft, J. R., Michel, P., Murdoch, N., Nakano, R., Palmer, E., Rivkin, A. S., Scheeres, D. J., Stickle, A. M., Sunshine, J. M., Trigo-Rodriguez, J. M., Vincent, J.-B., Walker, J. D., Wünnemann, K., Zhang, Y., Amoroso, M., Bertini, I., Brucato, J. R., Capannolo, A., Cremonese, G., Dall'Ora, M., Deshapriya, P. J. D., Gai, I., Hasselmann, P. H., Ieva, S., Impresario, G., Ivanovski, S. L., Lavagna, M., Lucchetti, A., Epifani, E. M., Modenini, D., Pajola, M., Palumbo, P., Perna, D., Pirrotta, S., Poggiali, G., Rossi, A., Tortora, P., Zannoni, M., and Zanotti, G. (2023). Momentum transfer from the DART mission kinetic impact on asteroid Dimorphos. *Nature*, 616(7957):457–460. Number: 7957 Publisher: Nature Publishing Group.

Cheng, A. F., Rivkin, A. S., Michel, P., Atchison, J., Barnouin, O., Benner, L., Chabot, N. L., Ernst, C., Fahnestock, E. G., Kueppers, M., Pravec, P., Rainey, E., Richardson, D. C., Stickle, A. M., and Thomas, C. (2018). AIDA DART asteroid deflection test: Planetary defense and science objectives. *Planetary and Space Science*, 157:104–115.

Cho, G.-C., Dodds, J., and Santamarina, J. (2006). Particle Shape Effects on Packing Density, Stiffness, and Strength: Natural and Crushed Sands. *Journal of Geotechnical and Geoenvironmental Engineering*, 132:591–602.

Cho, Y., Böttger, U., Rull, F., Hübers, H.-W., Belenguer, T., Börner, A., Buder, M., Bunduki, Y., Dietz, E., Hagelschuer, T., Kameda, S., Kopp, E., Lieder, M., Lopez-Reyes, G., Moral Inza, A. G., Mori, S., Ogura, J. A., Paproth, C., Perez Canora, C., Pertenais, M., Peter, G., Prieto-Ballesteros, O., Rockstein, S., Rodd-Routley, S., Rodriguez Perez, P., Ryan, C., Santamaria, P., Säuberlich, T., Schrandt, F., Schröder, S., Stangarone, C., Ulamec, S., Usui, T., Weber, I., Westerdorff, K., and Yumoto, K. (2021). In situ science on Phobos with the Raman spectrometer for MMX (RAX): preliminary design and feasibility of Raman measurements. *Earth, Planets and Space*, 73(1):232.

Cleveland, W. S. and Devlin, S. J. (1988). Locally Weighted Regression: An Approach to Regression Analysis by Local Fitting. *Journal of the American Statistical Association*, 83(403):596–610. Publisher: Taylor & Francis _eprint: https://www.tandfonline.com/doi/pdf/10.1080/01621459.1988.10478639.

Collins, G. S., Melosh, H. J., and Marcus, R. A. (2005). Earth Impact Effects Program: A Web-based computer program for calculating the regional environmental consequences of a meteoroid impact on Earth. *Meteoritics & Planetary Science*, 40(6):817–840. _eprint: https://onlinelibrary.wiley.com/doi/pdf/10.1111/j.1945-5100.2005.tb00157.x.

Collinson, D. W. (1992). Lunar sourcebook—A user's guide to the moon: G.H. Heiken, D.T. Vaniman and B.M. French (Editors), Cambridge University Press, Cambridge, 1991, 693 pp.,

hardback, £50 (US$59.50), ISBN: 0-521-33444-6. *Physics of the Earth and Planetary Interiors*, 72(1):132–133.

Colwell, J., Brisset, J., Dove, A., Whizin, A., Nagler, H., Brown, N., Rascon, A., Brightwell, N., and Seward, L. (2017). Low-Velocity Impacts into Regolith under Microgravity Conditions. pages 81–93. Publisher: American Society of Civil Engineers.

Colwell, J. E., Sture, S., Cintala, M., Durda, D., Hendrix, A., Goudie, T., Curtis, D., Ashcom, D. J., Kanter, M., Keohane, T., Lemos, A., Lupton, M., and Route, M. (2008). Ejecta from impacts at 0.2–2.3 m/s in low gravity. *Icarus*, 195(2):908–917.

Colwell, J. E. and Taylor, M. (1999). Low-Velocity Microgravity Impact Experiments into Simulated Regolith. *Icarus*, 138(2):241–248.

Coulomb, C.-A. (1776). Essai sur une application des règles de maximis et minimis à quelques problèmes de statique, relatifs à l'architecture. *Mémoires de Mathématique de l'Académie Royale des Sciences*, 7.

Coulomb, C.-A. d. (1773). Essai sur une application des règles des maximis et minimis à quelques problèmes de statique relatifs à l'architecture. Mémoires de Mathématique et de Physique, présentés à l'Académie Royale des Sciences, Vol. 7. Also known as Coulomb's essay on the theory of friction and the stability of materials.

Council, N. R. (2010). *Defending Planet Earth: Near-Earth Object Surveys and Hazard Mitigation Strategies*. National Academies Press, Washington, D.C.

Cox, E. (1927). A method of assigning numerical and percentage values to the degree of roundness of sand grains. *Journal of Paleontology*.

Craddock, R. A. (2011). Are Phobos and Deimos the result of a giant impact? *Icarus*, 211(2):1150–1161.

Cundall, P. A. and Strack, O. D. L. (1979). A discrete numerical model for granular assemblies. *Geotechnique*, 29:47–65. ADS Bibcode: 1979Getq...29...47C.

da Cruz, F., Emam, S., Prochnow, M., Roux, J.-N., and Chevoir, F. (2005). Rheophysics of dense granular materials: Discrete simulation of plane shear flows. *Physical Review E*, 72(2):021309. Publisher: American Physical Society.

Dadvand, P., Rossi, R., and Oñate, E. (2010). An Object-oriented Environment for Developing Finite Element Codes for Multi-disciplinary Applications. *Archives of Computational Methods in Engineering*, 17(3):253–297.

Daly, R. T., Ernst, C. M., Barnouin, O. S., Chabot, N. L., Rivkin, A. S., Cheng, A. F., Adams, E. Y., Agrusa, H. F., Abel, E. D., Alford, A. L., Asphaug, E. I., Atchison, J. A., Badger, A. R., Baki, P., Ballouz, R.-L., Bekker, D. L., Bellerose, J., Bhaskaran, S., Buratti, B. J., Cambioni, S., Chen, M. H., Chesley, S. R., Chiu, G., Collins, G. S., Cox, M. W., DeCoster, M. E., Ericksen, P. S., Espiritu, R. C., Faber, A. S., Farnham, T. L., Ferrari, F., Fletcher, Z. J., Gaskell, R. W., Graninger, D. M., Haque, M. A., Harrington-Duff, P. A., Hefter, S., Herreros, I., Hirabayashi, M., Huang, P. M., Hsieh, S.-Y. W., Jacobson, S. A., Jenkins, S. N., Jensenius, M. A., John, J. W., Jutzi, M., Kohout, T., Krueger, T. O., Laipert, F. E., Lopez, N. R., Luther, R., Lucchetti, A., Mages, D. M., Marchi, S., Martin, A. C., McQuaide, M. E., Michel, P., Moskovitz, N. A., Murphy, I. W., Murdoch, N., Naidu, S. P., Nair, H., Nolan, M. C., Ormö, J., Pajola, M., Palmer, E. E., Peachey, J. M., Pravec, P., Raducan, S. D., Ramesh, K. T., Ramirez, J. R., Reynolds, E. L., Richman, J. E., Robin, C. Q., Rodriguez, L. M., Roufberg, L. M., Rush, B. P., Sawyer, C. A., Scheeres, D. J., Scheirich, P., Schwartz, S. R., Shannon, M. P., Shapiro, B. N., Shearer, C. E., Smith, E. J., Steele, R. J., Steckloff, J. K., Stickle, A. M., Sunshine, J. M., Superfin, E. A., Tarzi, Z. B., Thomas, C. A., Thomas, J. R., Trigo-Rodríguez, J. M., Tropf, B. T., Vaughan, A. T., Velez, D., Waller, C. D., Wilson, D. S., Wortman, K. A., and Zhang, Y. (2023). Successful kinetic impact into an asteroid for planetary defence. *Nature*, 616(7957):443–447. Number: 7957 Publisher: Nature Publishing Group.

D'Amario, L. A., Bright, L. E., and Wolf, A. A. (1992). Galileo trajectory design. *Space Science Reviews*, 60(1):23–78.

de Pater, I. and Lissauer, J. J. (2015). *Planetary Sciences*. Cambridge University Press, Cambridge, 2 edition.

Delbo, M., Libourel, G., Wilkerson, J., Murdoch, N., Michel, P., Ramesh, K. T., Ganino, C., Verati, C., and Marchi, S. (2014). Thermal fatigue as the origin of regolith on small asteroids. *Nature*, 508(7495):233–236. Number: 7495 Publisher: Nature Publishing Group.

Delbo, M., Walsh, K. J., Matonti, C., Wilkerson, J., Pajola, M., Al Asad, M. M., Avdellidou, C., Ballouz, R.-L., Bennett, C. A., Connolly, H. C., DellaGiustina, D. N., Golish, D. R., Molaro, J. L., Rizk, B., Schwartz, S. R., and Lauretta, D. S. (2022). Alignment of fractures on Bennu's boulders indicative of rapid asteroid surface evolution. *Nature Geoscience*, 15(6):453–457. Number: 6 Publisher: Nature Publishing Group.

DellaGiustina, D. N., Emery, J. P., Golish, D. R., Rozitis, B., Bennett, C. A., Burke, K. N., Ballouz, R.-L., Becker, K. J., Christensen, P. R., Drouet d'Aubigny, C. Y., Hamilton, V. E., Reuter, D. C., Rizk, B., Simon, A. A., Asphaug, E., Bandfield, J. L., Barnouin, O. S., Barucci, M. A., Bierhaus, E. B., Binzel, R. P., Bottke, W. F., Bowles, N. E., Campins, H., Clark, B. C., Clark, B. E., Connolly, H. C., Daly, M. G., Leon, J. d., Delbo', M., Deshapriya, J. D. P., Elder, C. M., Fornasier, S., Hergenrother, C. W., Howell, E. S., Jawin, E. R., Kaplan, H. H., Kareta,

T. R., Le Corre, L., Li, J.-Y., Licandro, J., Lim, L. F., Michel, P., Molaro, J., Nolan, M. C., Pajola, M., Popescu, M., Garcia, J. L. R., Ryan, A., Schwartz, S. R., Shultz, N., Siegler, M. A., Smith, P. H., Tatsumi, E., Thomas, C. A., Walsh, K. J., Wolner, C. W. V., Zou, X.-D., and Lauretta, D. S. (2019). Properties of rubble-pile asteroid (101955) Bennu from OSIRIS-REx imaging and thermal analysis. *Nature Astronomy*, 3(4):341–351. Publisher: Nature Publishing Group.

DeMeo, F. E., Binzel, R. P., Slivan, S. M., and Bus, S. J. (2009). An extension of the Bus asteroid taxonomy into the near-infrared. *Icarus*, 202(1):160–180.

Diener, J. (2025). 2D Minimal Bounding Box. https://www.mathworks.com/matlabcentral/fileexchange/31126-2d-minimal-bounding-box. MATLAB Central File Exchange. Retrieved July 17, 2025.

Ding, L., Deng, Z., Gao, H., Guo, J., Zhang, D., and Iagnemma, K. D. (2013). Experimental study and analysis of the wheels' steering mechanics for planetary exploration wheeled mobile robots moving on deformable terrain. *The International Journal of Robotics Research*, 32(6):712–743. Publisher: SAGE Publications Ltd STM.

Ding, L., Deng, Z., Gao, H., Nagatani, K., and Yoshida, K. (2011). Planetary rovers' wheel–soil interaction mechanics: new challenges and applications for wheeled mobile robots. *Intelligent Service Robotics*, 4(1):17–38.

Ding, L., Gao, H., Deng, Z., Yoshida, K., and Nagatani, K. (2009). Slip ratio for lugged wheel of planetary rover in deformable soil: definition and estimation. In *2009 IEEE/RSJ International Conference on Intelligent Robots and Systems*, pages 3343–3348, St. Louis, MO, USA. IEEE.

Ding, L., Zhou, R., Yu, T., Gao, H., Yang, H., Li, J., Yuan, Y., Liu, C., Wang, J., Zhao, Y.-Y. S., Wang, Z., Wang, X., Bao, G., Deng, Z., Huang, L., Li, N., Cui, X., He, X., Jia, Y., Yuan, B., Liu, G., Zhang, H., Zhao, R., Zhang, Z., Cheng, Z., Wu, F., Xu, Q., Lu, H., Richter, L., Liu, Z., Niu, F., Qi, H., Li, S., Feng, W., Yang, C., Chen, B., Dang, Z., Zhang, M., Li, L., Wang, X., Huang, Z., Zhang, J., Xing, H., Wang, G., Niu, L., Xu, P., Wan, W., and Di, K. (2022). Surface characteristics of the Zhurong Mars rover traverse at Utopia Planitia. *Nature Geoscience*, 15(3):171–176. Publisher: Nature Publishing Group.

Dippel, S. and Wolf, D. E. (1999). Molecular dynamics simulations of granular chute flow. *Computer Physics Communications*, 121-122:284–289.

Dombard, A. J., Barnouin, O. S., Prockter, L. M., and Thomas, P. C. (2010). Boulders and ponds on the asteroid 433 eros. *Icarus*, 210(2):713–721.

Domokos, G., Jerolmack, D. J., Sipos, A. , and Török, (2014). How river rocks round: resolving the shape-size paradox. *PLoS ONE*, 9(2):e88657. arXiv:1311.6574 [physics].

Dosta, M., Andre, D., Angelidakis, V., Caulk, R. A., Celigueta, M. A., Chareyre, B., Dietiker, J. F., Girardot, J., Govender, N., Hubert, C., Kobyłka, R., Moura, A. F., Skorych, V., Weatherley, D. K., and Weinhart, T. (2024). Comparing open-source DEM frameworks for simulations of common bulk processes. *Computer Physics Communications*, 296:109066.

Dosta, M. and Skorych, V. (2020). MUSEN: An open-source framework for GPU-accelerated DEM simulations. *SoftwareX*, 12:100618.

Duchêne, A., Bigot, J., Stankiewicz, M., Dghais, S., Robin, C., Wilhelm, A., Kollmer, J. E., and Murdoch, N. (2025). Sinking or bouncing in low gravity environments? In *EPSC-DPS Joint Meeting 2025*, pages EPSC–DPS2025–113, Helsinki, Finland.

Duchêne, A., Murdoch, N., Robin, C. Q., Barnouin, O. S., Ballouz, R.-L., Mimoun, D., Jerves, A. X., and D. Mikesell, T. (2026). Guidelines for estimating the 3D size and shape of boulders from planetary surface images. Manuscript under review.

Duchêne, A., Murdoch, N., Robin, C. Q., Barnouin, O. S., Ballouz, R. L., Mimoun, D., Jerves, A. X., and Mikesell, T. D. (2025). Guidelines for estimating the 3d size and shape of boulders from planetary surface images. *Submitted manuscript*. Manuscript submitted for publication.

Dunatunga, S. and Kamrin, K. (2015). Continuum modelling and simulation of granular flows through their many phases. *Journal of Fluid Mechanics*, 779:483–513. arXiv:1411.5447 [cond-mat].

Dunatunga, S. and Kamrin, K. (2017). Continuum modeling of projectile impact and penetration in dry granular media. *Journal of the Mechanics and Physics of Solids*, 100:45–60.

Edil, T. B., Krizek, R. J., and Zelasko, J. S. (1975). EFFECT OF GRAIN CHARACTERISTICS ON PACKING OF SANDS. *[No source information available]*, 1:46–54.

Ehlmann, B. L., Viles, H. A., and Bourke, M. C. (2008). Quantitative morphologic analysis of boulder shape and surface texture to infer environmental history: A case study of rock breakdown at the Ephrata Fan, Channeled Scabland, Washington. *Journal of Geophysical Research (Earth Surface)*, 113:F02012. ADS Bibcode: 2008JGRF..113.2012E.

Ernst, C. M., Daly, R. T., Gaskell, R. W., Barnouin, O. S., Nair, H., Hyatt, B. A., Al Asad, M. M., and Hoch, K. K. W. (2023). High-resolution shape models of Phobos and Deimos from stereophotoclinometry. *Earth, Planets and Space*, 75(1):103.

Farquhar, R., Dunham, D., Hsu, S., Uesugi, K., and Kawaguchi, J. (1988). Trajectories for the Sakigake extended-mission phase. 1:663–669. Conference Name: 16th International Symposium on Space Technology and Science, Vol. 1 ADS Bibcode: 1988spte....1..663F.

Fimmel, R. O., Allen, J. A. V., and Burgess, E. (1980). *Pioneer, First to Jupiter, Saturn, and Beyond*. Scientific and Technical Information Office, National Aeronautics and Space Administration.

Fleischmann, J., Serban, R., Negrut, D., and Jayakumar, P. (2015). On the Importance of Displacement History in Soft-Body Contact Models. *Journal of Computational and Nonlinear Dynamics*, 11(044502).

Fletcher, Z. J., Ryan, K. J., Ernst, C. M., Maas, B., Dickman, J., Greenberg, J., Nelson, T., Lewis, D., Mize, J., Cheng, A., Bekker, D., Rodriguez, L., Daly, R. T., Smith, R., and Tran, M. Q. (2022). Didymos Reconnaissance and Asteroid Camera for OpNav (DRACO): design, fabrication, test, and operation. In *Space Telescopes and Instrumentation 2022: Optical, Infrared, and Millimeter Wave*, volume 12180, pages 113–138. SPIE.

Flores, P., Machado, M., Silva, M. T., and Martins, J. M. (2011). On the continuous contact force models for soft materials in multibody dynamics. *Multibody System Dynamics*, 25(3):357–375.

Folk, R. L. (1980). *Petrology of Sedimentary Rocks*. Hemphill Publishing Company. Accepted: 2014-01-23T15:52:58Z.

Forterre, Y. and Pouliquen, O. (2008). Flows of Dense Granular Media. *Annual Review of Fluid Mechanics*, 40:1 – 24. Publisher: Annual Reviews.

Fraeman, A. A., Arvidson, R. E., Murchie, S. L., Rivkin, A., Bibring, J.-P., Choo, T. H., Gondet, B., Humm, D., Kuzmin, R. O., Manaud, N., and Zabalueva, E. V. (2012). Analysis of disk-resolved OMEGA and CRISM spectral observations of Phobos and Deimos. *Journal of Geophysical Research: Planets*, 117(E11). _eprint: https://agupubs.onlinelibrary.wiley.com/doi/pdf/10.1029/2012JE004137.

Franklin, S. (2012). Geometric cohesion in granular materials. *Physics Today*, 65:70.

Fujiwara, A., Kawaguchi, J., Yeomans, D. K., Abe, M., Mukai, T., Okada, T., Saito, J., Yano, H., Yoshikawa, M., Scheeres, D. J., Barnouin-Jha, O., Cheng, A. F., Demura, H., Gaskell, R. W., Hirata, N., Ikeda, H., Kominato, T., Miyamoto, H., Nakamura, A. M., Nakamura, R., Sasaki, S., and Uesugi, K. (2006). The Rubble-Pile Asteroid Itokawa as Observed by Hayabusa. *Science*, 312(5778):1330–1334. Publisher: American Association for the Advancement of Science.

Gasteiner, L., Murdoch, N., and D'Angelo, O. (2026). An Open Database of Lunar Regolith and Simulants Properties. arXiv:2602.03829 [astro-ph.EP].

Gautier, F., Sitepu, E., Le Blay, C., Kersey, G., and Sánchez, J. P. (2020). Drop Your Thesis! 2018 results: 4.74 seconds of microgravity conditions to enable future cubesat landings on asteroids. *Acta Astronautica*, 176:139–155.

GDR MiDi (2004). On dense granular flows. *The European Physical Journal E*, 14(4):341–365.

Gierse, A., Kaczmarczik, U., Greif, A., Selig, H., Kampen, P., Könemann, T., and Lämmerzahl, C. (2017). A Fast and Self-Acting Release-Caging-Mechanism for Actively Driven Drop Tower Systems. *Microgravity Science and Technology*, 29.

Glassmeier, K.-H., Boehnhardt, H., Koschny, D., Kührt, E., and Richter, I. (2007). The Rosetta Mission: Flying Towards the Origin of the Solar System. *Space Science Reviews*, 128(1):1–21.

Glavin, D. P., Dworkin, J. P., Alexander, C. M. O., Aponte, J. C., Baczynski, A. A., Barnes, J. J., Bechtel, H. A., Berger, E. L., Burton, A. S., Caselli, P., Chung, A. H., Clemett, S. J., Cody, G. D., Dominguez, G., Elsila, J. E., Farnsworth, K. K., Foustoukos, D. I., Freeman, K. H., Furukawa, Y., Gainsforth, Z., Graham, H. V., Grassi, T., Giuliano, B. M., Hamilton, V. E., Haenecour, P., Heck, P. R., Hofmann, A. E., House, C. H., Huang, Y., Kaplan, H. H., Keller, L. P., Kim, B., Koga, T., Liss, M., McLain, H. L., Marcus, M. A., Matney, M., McCoy, T. J., McIntosh, O. M., Mojarro, A., Naraoka, H., Nguyen, A. N., Nuevo, M., Nuth, J. A., Oba, Y., Parker, E. T., Peretyazhko, T. S., Sandford, S. A., Santos, E., Schmitt-Kopplin, P., Seguin, F., Simkus, D. N., Shahid, A., Takano, Y., Thomas-Keprta, K. L., Tripathi, H., Weiss, G., Zheng, Y., Lunning, N. G., Righter, K., Connolly, H. C., and Lauretta, D. S. (2025). Abundant ammonia and nitrogen-rich soluble organic matter in samples from asteroid (101955) Bennu. *Nature Astronomy*, 9(2):199–210. Publisher: Nature Publishing Group.

Golombek, M., Warner, N., Grant, J., Hauber, E., Ansan, V., Weitz, C., Williams, N., Charalambous, C., Wilson Purdy, S., DeMott, A., Kopp, M., Lethcoe-Wilson, H., Berger, L., Hausmann, R., Marteau, E., Vrettos, C., Trussell, A., Folkner, W., Le maistre, S., and Banerdt, W. (2020). Geology of the InSight landing site on Mars. *Nature Communications*, 11:1014.

Golombek, M. P., Trussell, A., Williams, N., Charalambous, C., Abarca, H., Warner, N. H., Deahn, M., Trautman, M., Crocco, R., Grant, J. A., Hauber, E., and Deen, R. (2021). Rock Size-Frequency Distributions at the InSight Landing Site, Mars. *Earth and Space Science*, 8(12):e2021EA001959. _eprint: https://agupubs.onlinelibrary.wiley.com/doi/pdf/10.1029/2021EA001959.

Gong, J., Zou, J., Zhao, L., Li, L., and Nie, Z. (2019). New insights into the effect of interparticle friction on the critical state friction angle of granular materials. *Computers and Geotechnics*, 113:103105.

Govender, N., Wilke, D. N., and Kok, S. (2016). Blaze-DEMGPU: Modular high performance DEM framework for the GPU architecture. *SoftwareX*, 5:62–66.

Gundlach, B. and Blum, J. (2013). A new method to determine the grain size of planetary regolith. *Icarus*, 223(1):479–492.

Guo, F., Zhang, H., Yu, Y., Cheng, B., Sun, Q., Zhao, Z., Zou, M., Zhang, X., and Lv, L. (2024). Slow intrusion experiments into granular media under microgravity. *Advances in Space Research*, 73(5):2774–2787.

Handin, J. (1969). On the Coulomb-Mohr failure criterion. *Journal of Geophysical Research (1896-1977)*, 74(22):5343–5348. _eprint: https://agupubs.onlinelibrary.wiley.com/doi/pdf/10.1029/JB074i022p05343.

Harris, C. R., Millman, K. J., van der Walt, S. J., Gommers, R., Virtanen, P., Cournapeau, D., Wieser, E., Taylor, J., Berg, S., Smith, N. J., Kern, R., Picus, M., Hoyer, S., van Kerkwijk, M. H., Brett, M., Haldane, A., del Río, J. F., Wiebe, M., Peterson, P., Gérard-Marchant, P., Sheppard, K., Reddy, T., Weckesser, W., Abbasi, H., Gohlke, C., and Oliphant, T. E. (2020). Array programming with NumPy. *Nature*, 585(7825):357–362. Publisher: Nature Publishing Group.

Hartmann, W. K. and Neukum, G. (2001). Cratering Chronology and the Evolution of Mars. In Kallenbach, R., Geiss, J., and Hartmann, W. K., editors, *Chronology and Evolution of Mars*, pages 165–194, Dordrecht. Springer Netherlands.

Hartzell, C. and Carter, D. (2017). Electrostatic forces on grains near asteroids and comets. *EPJ Web of Conferences*, 140:14009.

Head, K. H. (1982). *MANUAL OF SOIL LABORATORY TESTING. VOLUME 2: PERMEABILITY, SHEAR STRENGTH AND COMPRESSIBILITY TESTS*. Number: Monograph.

Head, K. H. (1998). Manual of soil laboratory testing. 3: Effective stress tests. Pentech Pr, London, 2. ed edition. Num Pages: 428.

Hestroffer, D., Sánchez, P., Staron, L., Bagatin, A. C., Eggl, S., Losert, W., Murdoch, N., Opsomer, E., Radjai, F., Richardson, D. C., Salazar, M., Scheeres, D. J., Schwartz, S., Taberlet, N., and Yano, H. (2019). Small Solar System Bodies as granular media. *The Astronomy and Astrophysics Review*, 27(1):6.

Hills, J. G. and Goda, M. P. (1993). The Fragmentation of Small Asteroids in the Atmosphere. *The Astronomical Journal*, 105:1114. ADS Bibcode: 1993AJ....105.1114H.

Hirao, K. and Itoh, T. (1988). The Sakigake/Suisei missions to Halley's Comet. In Grewing, M., Praderie, F., and Reinhard, R., editors, *Exploration of Halley's Comet*, pages 965–968, Berlin, Heidelberg. Springer.

Ho, T.-M., Baturkin, V., Grimm, C., Grundmann, J. T., Hobbie, C., Ksenik, E., Lange, C., Sasaki, K., Schlotterer, M., Talapina, M., Termtanasombat, N., Wejmo, E., Witte, L., Wrasmann, M., Wübbels, G., Rößler, J., Ziach, C., Findlay, R., Biele, J., Krause, C., Ulamec, S., Lange, M.,

Mierheim, O., Lichtenheldt, R., Maier, M., Reill, J., Sedlmayr, H.-J., Bousquet, P., Bellion, A., Bompis, O., Cenac-Morthe, C., Deleuze, M., Fredon, S., Jurado, E., Canalias, E., Jaumann, R., Bibring, J.-P., Glassmeier, K. H., Hercik, D., Grott, M., Celotti, L., Cordero, F., Hendrikse, J., and Okada, T. (2017). MASCOT—The Mobile Asteroid Surface Scout Onboard the Hayabusa2 Mission. *Space Science Reviews*, 208(1-4):339–374.

Hollingsworth, S. A. and Dror, R. O. (2018). Molecular dynamics simulation for all. *Neuron*, 99(6):1129–1143.

Holsapple, K. A. (2007). Spin limits of Solar System bodies: From the small fast-rotators to 2003 EL61. *Icarus*, 187(2):500–509.

Holsapple, K. A. and Housen, K. R. (2019). The catastrophic disruptions of asteroids: History, features, new constraints and interpretations. *Planetary and Space Science*, 179:104724.

Holtz, R. D. and Kovacs, W. D. (1981). *An introduction to geotechnical engineering*. Prentice-Hall, Englewood Cliffs, N.J.

Hoppa, G., Tufts, B. R., Greenberg, R., and Geissler, P. (1999). Strike–Slip Faults on Europa: Global Shear Patterns Driven by Tidal Stress. *Icarus*, 141(2):287–298.

Housen, K. R., Wilkening, L. L., Chapman, C. R., and Greenberg, R. (1979). Asteroidal regoliths. *Icarus*, 39(3):317–351.

Howett, C. J. A., Spencer, J. R., Pearl, J., and Segura, M. (2010). Thermal inertia and bolometric Bond albedo values for Mimas, Enceladus, Tethys, Dione, Rhea and Iapetus as derived from Cassini/CIRS measurements. *Icarus*, 206(2):573–593.

Hu, W., Li, P., Rogg, A., Schepelmann, A., Chandler, S., Kamrin, K., and Negrut, D. (2025). A Study Demonstrating That Using Gravitational Offset to Prepare Extraterrestrial Mobility Missions Is Misleading. *Journal of Field Robotics*. Publisher: Wiley.

Hu, W., Serban, R., Kamrin, K., and Negrut, D. (2024). *Using physics-based simulation towards eliminating empiricism in extraterrestrial terramechanics applications*.

Hunten, D. M. (1979). Capture of Phobos and Deimos by photoatmospheric drag. *Icarus*, 37(1):113–123.

Huynh, T. Q., Nguyen, T. T., and Indraratna, B. (2025). Evaluating cohesive models in discrete element simulation through drawdown test with new assessment perspectives. *Powder Technology*, 452:120542.

Hörz, F. (1977). Impact cratering and regolith dynamics. *Physics and Chemistry of the Earth*, 10:3–15.

International Organization for Standardization (2018). ISO 17892-10:2018 – Geotechnical investigation and testing – Laboratory testing of soil – Part 10: Direct shear tests. International Standard.

Irani, R. A., Bauer, R. J., and Warkentin, A. (2011). A dynamic terramechanic model for small lightweight vehicles with rigid wheels and grousers operating in sandy soil. *Journal of Terramechanics*, 48(4):307–318.

Islam, A., Badhon, F., and Abedin, M. (2017). *Relation between Effective Particle Size and Angle of Internal Friction of Cohesionless Soil*.

Itasca Consulting Group (2007). *PFC3D Version 4.0 User Manual*. Itasca Consulting Group, Minneapolis, MN, USA.

Iverson, R. M. (2000). Landslide triggering by rain infiltration. *Water Resources Research*, 36(7):1897–1910. _eprint: https://onlinelibrary.wiley.com/doi/pdf/10.1029/2000WR900090.

Jacobson, R. A. (2010). THE ORBITS AND MASSES OF THE MARTIAN SATELLITES AND THE LIBRATION OF PHOBOS. *The Astronomical Journal*, 139(2):668. Publisher: The American Astronomical Society.

Jaeger, C. (1979). *Rock Mechanics and Engineering*. Cambridge University Press, Cambridge.

Jaeger, H. M., Nagel, S. R., and Behringer, R. P. (1996). Granular solids, liquids, and gases. *Reviews of Modern Physics*, 68(4):1259–1273. Publisher: American Physical Society.

Jaffe, L. D. (1973). Shear strength of lunar soil from oceanus procellarum. *The moon*, 8(1):58–72.

Jawin, E. R., Ballouz, R.-L., Ryan, A. J., Kaplan, H. H., McCoy, T. J., Al Asad, M. M., Molaro, J. L., Rozitis, B., and Keller, L. P. (2023). Boulder Diversity in the Nightingale Region of Asteroid (101955) Bennu and Predictions for Physical Properties of the OSIRIS-REx Sample. *Journal of Geophysical Research: Planets*, 128(12):e2023JE008019. _eprint: https://agupubs.onlinelibrary.wiley.com/doi/pdf/10.1029/2023JE008019.

Jean, M. (1999). The non-smooth contact dynamics method. *Computer Methods in Applied Mechanics and Engineering*, 177(3):235–257.

Jewitt, D., Kim, Y., Li, J., and Mutchler, M. (2023). The Dimorphos Boulder Swarm. *The Astrophysical Journal Letters*, 952(1):L12. Publisher: The American Astronomical Society.

Jiang, Y., Ji, J., Huang, J., Marchi, S., Li, Y., and Ip, W.-H. (2015). The distribution and source of boulders on asteroid 4179 Toutatis. *Proceedings of the International Astronomical Union*, 10(S318):153–155.

Johnson, J. B., Kulchitsky, A. V., Duvoy, P., Iagnemma, K., Senatore, C., Arvidson, R. E., and Moore, J. (2015). Discrete element method simulations of Mars Exploration Rover wheel performance. *Journal of Terramechanics*, 62:31–40.

Jop, P., Forterre, Y., and Pouliquen, O. (2006). A constitutive law for dense granular flows. *Nature*, 441:727–730. Publisher: Nature Publishing Group.

Jutzi, M., Raducan, S. D., Zhang, Y., Michel, P., and Arakawa, M. (2022). Constraining surface properties of asteroid (162173) Ryugu from numerical simulations of Hayabusa2 mission impact experiment. *Nature Communications*, 13(1):7134. Publisher: Nature Publishing Group.

Kameda, S., Ozaki, M., Enya, K., Fuse, R., Kouyama, T., Sakatani, N., Suzuki, H., Osada, N., Kato, H., Miyamoto, H., Yamazaki, A., Nakamura, T., Okamoto, T., Ishimaru, T., Hong, P., Ishibashi, K., Takashima, T., Ishigami, R., Kuo, C.-L., Abe, S., Goda, Y., Murao, H., Fujishima, S., Aoyama, T., Hagiwara, K., Mizumoto, S., Tanaka, N., Murakami, K., Matsumoto, M., Tanaka, K., and Sakuta, H. (2021). Design of telescopic nadir imager for geomorphology (TENGOO) and observation of surface reflectance by optical chromatic imager (OROCHI) for the Martian Moons Exploration (MMX). *Earth, Planets and Space*, 73(1):218.

Kameda, S., Suzuki, H., Takamatsu, T., Cho, Y., Yasuda, T., Yamada, M., Sawada, H., Honda, R., Morota, T., Honda, C., Sato, M., Okumura, Y., Shibasaki, K., Ikezawa, S., and Sugita, S. (2017). Preflight Calibration Test Results for Optical Navigation Camera Telescope (ONC-T) Onboard the Hayabusa2 Spacecraft. *Space Science Reviews*, 208(1):17–31.

Karapiperis, K., Marshall, J., and Andrade, J. (2020). Reduced Gravity Effects on the Strength of Granular Matter: DEM Simulations versus Experiments. *Journal of Geotechnical and Geoenvironmental Engineering*, 146:06020005.

Karplus, M. and McCammon, J. A. (2002). Molecular dynamics simulations of biomolecules. *Nature Structural Biology*, 9(9):646–652. Publisher: Nature Publishing Group.

Kawakatsu, Y., Kuramoto, K., Usui, T., Sugahara, H., Ootake, H., Yasumitsu, R., Yoshikawa, K., Mary, S., Grebenstein, M., Sawada, H., Imada, T., Shimada, T., Ogawa, K., Otsuki, M., Baba, M., Fujita, K., Zacny, K., van Dyne, D., Satoh, Y., and Tokaji, A. (2023). Preliminary design of Martian Moons eXploration (MMX). *Acta Astronautica*, 202:715–728.

Kawamoto, R., Andò, E., Viggiani, G., and Andrade, J. E. (2018). All you need is shape: Predicting shear banding in sand with LS-DEM. *Journal of the Mechanics and Physics of Solids*, 111:375–392.

Keaton, J. R. (2017). Angle of Internal Friction. In *Encyclopedia of Engineering Geology*, pages 1–2. Springer, Cham. ISSN: 1871-756X.

Kim, Y., Suh, H. S., and Yun, T. (2019). Reliability and applicability of the Krumbein-Sloss chart for estimating geomechanical properties in sands. *Engineering Geology*, 248:117–123.

Klein, S. P. and White, B. R. (1990). Dynamic shear of granular material under variable gravity conditions. *AIAA Journal*, 28(10):1701–1702. Publisher: American Institute of Aeronautics and Astronautics.

Kleinhans, M. G., Markies, H., de Vet, S. J., in 't Veld, A. C., and Postema, F. N. (2011). Static and dynamic angles of repose in loose granular materials under reduced gravity. *Journal of Geophysical Research: Planets*, 116(E11). _eprint: https://onlinelibrary.wiley.com/doi/pdf/10.1029/2011JE003865.

Kloss, C. and Goniva, C. (2011). LIGGGHTS—open source discrete element simulations of granular materials based on LAMMPS. *TMS Annual Meeting*, 2:781–788.

Kloss, C., Goniva, C., Hager, A., Amberger, S., and Pirker, S. (2012). Models, algorithms and validation for opensource DEM and CFD–DEM. *Progress in Computational Fluid Dynamics, an International Journal*, 12(2-3):140–152. Publisher: Inderscience Publishers.

Knollenberg, J., Grott, M., Hamm, M., Ihring, A., Ziese, R., and Biele, J. (2025). The miniRAD instrument for the MMX IDEFIX rover. *Progress in Earth and Planetary Science*, 12(1):53.

Knuth, M., Johnson, J., Hopkins, M., Sullivan, R., and Moore, J. (2012). Discrete element modeling of a Mars Exploration Rover wheel in granular material. *Journal of Terramechanics - J TERRAMECH*, 49.

Kobayashi, M., Krüger, H., Senshu, H., Wada, K., Okudaira, O., Sasaki, S., and Kimura, H. (2018). In situ observations of dust particles in Martian dust belts using a large-sensitive-area dust sensor. *Planetary and Space Science*, 156:41–46.

Kobayashi, M., Okudaira, O., Sasaki, S., Fujii, M., Tsukuda, M., Hayakawa, Y., Tanaka, N., and Fujishima, S. (2024). Engineering Model of Circum-Martian Dust Monitor to be aboard MMX. *Journal of Evolving Space Activities*, 2.

Kobayashi, T., Fujiwara, Y., Yamakawa, J., Yasufuku, N., and Omine, K. (2010). Mobility performance of a rigid wheel in low gravity environments. *Journal of Terramechanics*, 47(4):261–274.

Kobayashi, T., Ochiai, H., Suyama, Y., Aoki, S., Yasufuku, N., and Omine, K. (2009). Bearing capacity of shallow foundations in a low gravity environment. *Soils and foundations*, 49(1):115–134.

Kosinski, P., Balakin, B. V., and Kosinska, A. (2020). Extension of the hard-sphere model for particle-flow simulations. *Physical Review E*.

Kovács, L., Ghotbi, B., González, F., Niksirat, P., Skonieczny, K., and Kövecses, J. (2019). Effect of gravity in wheel/terrain interaction models. *Journal of Field Robotics*, 37:754–767.

Kozicki, J. and Donzé, F. (2009). YADE-OPEN DEM: an open-source software using a discrete element method to simulate granular material. *Engineering Computations*, 26(7):786–805.

Krumbein, W. C. and Pettijohn, F. J. (1966). *Manual of Sedimentary Petrography*. Appleton-Century-Crofts. Google-Books-ID: 328ZwQEACAAJ.

Krumbein, W. C. and Sloss, L. L. (1963). *Stratigraphy and Sedimentation*. W. H. Freeman, New York.

Krynine, P.-D. (1960). On the antiquity of "sedimentation" and hydrology. *Bulletin of the Geological Society of America*, 71:1721–1726.

Kumamoto, K. M., Owen, J. M., Syal, M. B., Pearl, J., Raskin, C., Caldwell, W. K., Rainey, E., Stickle, A. M., Daly, R. T., and Barnouin, O. (2022). Predicting Asteroid Material Properties from a DART-like Kinetic Impact. *The Planetary Science Journal*, 3(10):237. Publisher: IOP Publishing.

Kumar, S., Khatoon, S., Dubey, P., Yogi, J., and Anand, A. (2024). Shape-dependent radial segregation in rotating drum: Insights from DEM simulations. *Powder Technology*, 432:119134.

Kuramoto, K., Kawakatsu, Y., Fujimoto, M., Araya, A., Barucci, M. A., Genda, H., Hirata, N., Ikeda, H., Imamura, T., Helbert, J., Kameda, S., Kobayashi, M., Kusano, H., Lawrence, D. J., Matsumoto, K., Michel, P., Miyamoto, H., Morota, T., Nakagawa, H., Nakamura, T., Ogawa, K., Otake, H., Ozaki, M., Russell, S., Sasaki, S., Sawada, H., Senshu, H., Tachibana, S., Terada, N., Ulamec, S., Usui, T., Wada, K., Watanabe, S.-i., and Yokota, S. (2022). Martian moons exploration MMX: sample return mission to Phobos elucidating formation processes of habitable planets. *Earth, Planets and Space*, 74(1):12.

Kwarta, M. and Negrut, D. (2017). Technical Report TR-2016-17, Using the Complementarity and Penalty Methods for Solving Frictional Contact Problems in Chrono: Validation for the Standard Triaxial Test. Technical report, University of Wisconsin-Madison.

Könemann, T., Kaczmarczik, U., Gierse, A., Greif, A., Lutz, T., Mawn, S., Siemer, J., Eigenbrod, C., von Kampen, P., and Lämmerzahl, C. (2015). Concept for a next-generation drop tower system. *Advances in Space Research*, 55:1728–1733. Publisher: Elsevier ADS Bibcode: 2015AdSpR..55.1728K.

Lade, P. V. (2016). *Triaxial Testing of Soils*. John Wiley & Sons. Google-Books-ID: bytECwAAQBAJ.

Lange, C., Yoshimitsu, T., Ulamec, S., Düvel, C., and Ho, T.-M. (2020). Micro- and nanolander on the surface of Ryugu – Commonalities, differences and lessons learned for future microgravity exploration. *Planetary and Space Science*, 194:105094.

Lauretta, D. S., Adam, C. D., Allen, A. J., Ballouz, R.-L., Barnouin, O. S., Becker, K. J., Becker, T., Bennett, C. A., Bierhaus, E. B., Bos, B. J., Burns, R. D., Campins, H., Cho, Y., Christensen, P. R., Church, E. C. A., Clark, B. E., Connolly, H. C., Daly, M. G., DellaGiustina, D. N., Drouet d'Aubigny, C. Y., Emery, J. P., Enos, H. L., Kasper, S. F., Garvin, J. B., Getzandanner, K., Golish, D. R., Hamilton, V. E., Hergenrother, C. W., Kaplan, H. H., Keller, L. P., Lessac-Chenen, E. J., Liounis, A. J., Ma, H., McCarthy, L. K., Miller, B. D., Moreau, M. C., Morota, T., Nelson, D. S., Nolau, J. O., Olds, R., Pajola, M., Pelgrift, J. Y., Polit, A. T., Ravine, M. A., Reuter, D. C., Rizk, B., Rozitis, B., Ryan, A. J., Sahr, E. M., Sakatani, N., Seabrook, J. A., Selznick, S. H., Skeen, M. A., Simon, A. A., Sugita, S., Walsh, K. J., Westermann, M. M., Wolner, C. W. V., and Yumoto, K. (2022). Spacecraft sample collection and subsurface excavation of asteroid (101955) Bennu. *Science (New York, N.Y.)*, 377(6603):285–291.

Lauretta, D. S., Balram-Knutson, S. S., Beshore, E., Boynton, W. V., Drouet d'Aubigny, C., DellaGiustina, D. N., Enos, H. L., Golish, D. R., Hergenrother, C. W., Howell, E. S., Bennett, C. A., Morton, E. T., Nolan, M. C., Rizk, B., Roper, H. L., Bartels, A. E., Bos, B. J., Dworkin, J. P., Highsmith, D. E., Lorenz, D. A., Lim, L. F., Mink, R., Moreau, M. C., Nuth, J. A., Reuter, D. C., Simon, A. A., Bierhaus, E. B., Bryan, B. H., Ballouz, R., Barnouin, O. S., Binzel, R. P., Bottke, W. F., Hamilton, V. E., Walsh, K. J., Chesley, S. R., Christensen, P. R., Clark, B. E., Connolly, H. C., Crombie, M. K., Daly, M. G., Emery, J. P., McCoy, T. J., McMahon, J. W., Scheeres, D. J., Messenger, S., Nakamura-Messenger, K., Righter, K., and Sandford, S. A. (2017). OSIRIS-REx: Sample Return from Asteroid (101955) Bennu. *Space Science Reviews*, 212(1):925–984.

Lauretta, D. S., Connolly, H. C., Aebersold, J. E., Alexander, C. M. O. D., Ballouz, R.-L., Barnes, J. J., Bates, H. C., Bennett, C. A., Blanche, L., Blumenfeld, E. H., Clemett, S. J., Cody, G. D., DellaGiustina, D. N., Dworkin, J. P., Eckley, S. A., Foustoukos, D. I., Franchi, I. A., Glavin, D. P., Greenwood, R. C., Haenecour, P., Hamilton, V. E., Hill, D. H., Hiroi, T., Ishimaru, K., Jourdan, F., Kaplan, H. H., Keller, L. P., King, A. J., Koefoed, P., Kontogiannis, M. K., Le, L., Macke, R. J., McCoy, T. J., Milliken, R. E., Najorka, J., Nguyen, A. N., Pajola, M., Polit, A. T., Roper, H. L., Russell, S. S., Ryan, A. J., Sandford, S. A., Schofield, P. F., Schultz, C. D., Tachibana, S., Thomas-Keprta, K. L., Thompson, M. S., Tu, V., Tusberti, F., Wang, K., Zega, T. J., Wolner, C. W. V., and Team, t. O.-R. S. A. (2024). Asteroid (101955) Bennu in the Laboratory: Properties of the Sample Collected by OSIRIS-REx. arXiv:2404.12536 [astro-ph].

Lauretta, D. S., DellaGiustina, D. N., Bennett, C. A., Golish, D. R., Becker, K. J., Balram-Knutson, S. S., Barnouin, O. S., Becker, T. L., Bottke, W. F., Boynton, W. V., Campins, H., Clark, B. E.,

Connolly, H. C., Drouet d'Aubigny, C. Y., Dworkin, J. P., Emery, J. P., Enos, H. L., Hamilton, V. E., Hergenrother, C. W., Howell, E. S., Izawa, M. R. M., Kaplan, H. H., Nolan, M. C., Rizk, B., Roper, H. L., Scheeres, D. J., Smith, P. H., Walsh, K. J., and Wolner, C. W. V. (2019). The unexpected surface of asteroid (101955) Bennu. *Nature*, 568(7750):55–60. Number: 7750 Publisher: Nature Publishing Group.

Lauretta, D. S., Enos, H. L., Polit, A. T., Roper, H. L., and Wolner, C. W. V. (2021). Chapter 8 - OSIRIS-REx at Bennu: Overcoming challenges to collect a sample of the early Solar System. In Longobardo, A., editor, *Sample Return Missions*, pages 163–194. Elsevier.

Lawrence, D. (2025). The Mars-moon Exploration with GAmma rays and NEutrons (MEGANE) Investigation for the Martian Moon eXploration (MMX) Mission: Progress Towards Launch. Technical Report EPSC-DPS2025-1071, Copernicus Meetings. Conference Name: EPSC-DPS2025.

Lawrence, D. J., Peplowski, P. N., Beck, A. W., Burks, M. T., Chabot, N. L., Cully, M. J., Elphic, R. C., Ernst, C. M., Fix, S., Goldsten, J. O., Hoffer, E. M., Kusano, H., Murchie, S. L., Schratz, B. C., Usui, T., and Yokley, Z. W. (2019). Measuring the Elemental Composition of Phobos: The Mars-moon Exploration with GAmma rays and NEutrons (MEGANE) Investigation for the Martian Moons eXploration (MMX) Mission. *Earth and Space Science*, 6(12):e2019EA000811. _eprint: https://agupubs.onlinelibrary.wiley.com/doi/pdf/10.1029/2019EA000811.

Li, B., Ling, Z., Zhang, J., and Chen, J. (2017). Rock size-frequency distributions analysis at lunar landing sites based on remote sensing and in-situ imagery. *Planetary and Space Science*, 146:30–39. ADS Bibcode: 2017P&SS..146...30L.

Li, C., Zhang, T., and Goldman, D. I. (2013). A Terradynamics of Legged Locomotion on Granular Media. *Science*, 339(6126):1408–1412. Publisher: American Association for the Advancement of Science.

Li, H. (2006). IMPACT OF COHESION FORCES ON PARTICLE MIXING AND SEGREGATION. Publisher: University of Pittsburgh.

Li, J.-Y., Hirabayashi, M., Farnham, T. L., Sunshine, J. M., Knight, M. M., Tancredi, G., Moreno, F., Murphy, B., Opitom, C., Chesley, S., Scheeres, D. J., Thomas, C. A., Fahnestock, E. G., Cheng, A. F., Dressel, L., Ernst, C. M., Ferrari, F., Fitzsimmons, A., Ieva, S., Ivanovski, S. L., Kareta, T., Kolokolova, L., Lister, T., Raducan, S. D., Rivkin, A. S., Rossi, A., Soldini, S., Stickle, A. M., Vick, A., Vincent, J.-B., Weaver, H. A., Bagnulo, S., Bannister, M. T., Cambioni, S., Campo Bagatin, A., Chabot, N. L., Cremonese, G., Daly, R. T., Dotto, E., Glenar, D. A., Granvik, M., Hasselmann, P. H., Herreros, I., Jacobson, S., Jutzi, M., Kohout, T., La Forgia, F., Lazzarin, M., Lin, Z.-Y., Lolachi, R., Lucchetti, A., Makadia, R., Mazzotta Epifani, E., Michel, P., Migliorini, A., Moskovitz, N. A., Ormö, J., Pajola, M., Sánchez, P., Schwartz, S. R.,

Snodgrass, C., Steckloff, J., Stubbs, T. J., and Trigo-Rodríguez, J. M. (2023). Ejecta from the DART-produced active asteroid Dimorphos. *Nature*, 616(7957):452–456. Number: 7957 Publisher: Nature Publishing Group.

Liu, S. H. (2006). Simulating a direct shear box test by dem. *Canadian Geotechnical Journal*, 43(2):155–168.

Lucchetti, A., Cambioni, S., Nakano, R., Barnouin, O. S., Pajola, M., Penasa, L., Tusberti, F., Ramesh, K. T., Dotto, E., Ernst, C. M., Daly, R. T., Mazzotta Epifani, E., Hirabayashi, M., Parro, L., Poggiali, G., Campo Bagatin, A., Ballouz, R.-L., Chabot, N. L., Michel, P., Murdoch, N., Vincent, J. B., Karatekin, , Rivkin, A. S., Sunshine, J. M., Kohout, T., Deshapriya, J. D. P., Hasselmann, P. H. A., Ieva, S., Beccarelli, J., Ivanovski, S. L., Rossi, A., Ferrari, F., Rossi, C., Raducan, S. D., Steckloff, J., Schwartz, S., Brucato, J. R., Dall'Ora, M., Zinzi, A., Cheng, A. F., Amoroso, M., Bertini, I., Capannolo, A., Caporali, S., Ceresoli, M., Cremonese, G., Della Corte, V., Gai, I., Gomez Casajus, L., Gramigna, E., Impresario, G., Lasagni Manghi, R., Lavagna, M., Lombardo, M., Modenini, D., Palumbo, P., Perna, D., Pirrotta, S., Tortora, P., Zannoni, M., and Zanotti, G. (2024). Fast boulder fracturing by thermal fatigue detected on stony asteroids. *Nature Communications*, 15(1):6206. Publisher: Nature Publishing Group.

Luding, S. (2004). Molecular Dynamics Simulations of Granular Materials. In *The Physics of Granular Media*, pages 297–324. John Wiley & Sons, Ltd. Section: 13 _eprint: https://onlinelibrary.wiley.com/doi/pdf/10.1002/352760362X.ch13.

Lunine, J. I., Neugebauer, G., and Jakosky, B. M. (1982). Infrared observations of Phobos and Deimos from Viking. *Journal of Geophysical Research: Solid Earth*, 87(B12):10297–10305. _eprint: https://onlinelibrary.wiley.com/doi/pdf/10.1029/JB087iB12p10297.

Maccarini, M. (1993). A comparison of direct shear box tests with triaxial compression tests for a residual soil. *Geotechnical & Geological Engineering*, 11(2):69–80.

Mahlke, M., Carry, B., and Mattei, P.-A. (2022). Asteroid taxonomy from cluster analysis of spectrometry and albedo. *Astronomy & Astrophysics*, 665:A26.

Majmudar, T. S. and Behringer, R. P. (2005). Contact force measurements and stress-induced anisotropy in granular materials. *Nature*, 435(7045):1079–1082. Publisher: Nature Publishing Group.

Maladen, R. D., Ding, Y., Li, C., and Goldman, D. I. (2009). Undulatory swimming in sand: subsurface locomotion of the sandfish lizard. *Science (New York, N.Y.)*, 325(5938):314–318.

Mallapaty, S. (2021). China has landed its first rover on Mars — here's what happens next. *Nature*, 593(7859):323–324. Bandiera_abtest: a Cg_type: News Publisher: Nature Publishing Group Subject_term: Space physics, Astronomy and astrophysics, Planetary science, Technology.

Manned Spacecraft Center (1970). *Apollo 12 Preliminary Science Report*. Number SP-235 in NASA Special Publication. Scientific and Technical Information Division, Office of Technology Utilization, National Aeronautics and Space Administration, Washington, D.C.

Marov, M. Y., Avduevsky, V. S., Akim, E. L., Eneev, T. M., Kremnev, R. S., Kulikov, S. D., Pichkhadze, K. M., Popov, G. A., and Rogovsky, G. N. (2004). Phobos-Grunt: Russian sample return mission. *Advances in Space Research*, 33(12):2276–2280.

Marshall, J., Hurley, R., Arthur, D., Vlahinic, I., Senatore, C., Iagnemma, K., Trease, B., and Andrade, J. (2018). Failures in Sand in Reduced Gravity Environments. *Journal of the Mechanics and Physics of Solids*, 113.

Marti, J. (2024). *Structure des régolithes planétaires: approche sismologique et expérimentale*. thesis, Université de Toulouse (2023-....).

Marty, B. and Yokochi, R. (2006). Water in the Early Earth. *Reviews in Mineralogy and Geochemistry*, 62(1):421–450.

Mathias, D. L., Wheeler, L. F., and Dotson, J. L. (2017). A probabilistic asteroid impact risk model: assessment of sub-300m impacts. *Icarus*, 289:106–119.

Matijevic, J., Crisp, J., Bickler, D., Banes, R., Cooper, B., Eisen, H., Gensler, J., Haldemann, A., Hartman, F., Jewett, K., Matthies, L., Laubach, S., Mishkin, A., Morrison, J., Nguyen, T., Sirota, A., Stone, H., Stride, S., Sword, L., and Wil, D. (1997). Characterization of the Martian Surface Deposits by the Mars Pathfinder Rover, Sojourner. *Science*, 278:1765–1768.

Matsumoto, T., Noguchi, T., Miyake, A., Igami, Y., Matsumoto, M., Yada, T., Uesugi, M., Yasutake, M., Uesugi, K., Takeuchi, A., Yuzawa, H., Ohigashi, T., and Araki, T. (2024). Sodium carbonates on Ryugu as evidence of highly saline water in the outer Solar System. *Nature Astronomy*, 8(12):1536–1543. Publisher: Nature Publishing Group.

Matsumura, S., Richardson, D. C., Michel, P., Schwartz, S. R., and Ballouz, R.-L. (2014). The Brazil nut effect and its application to asteroids. *Monthly Notices of the Royal Astronomical Society*, 443(4):3368–3380. Publisher: Oxford University Press (OUP).

Maurel, C., Gattacceca, J., and Uehara, M. (2024). Hayabusa 2 returned samples reveal a weak to null magnetic field during aqueous alteration of Ryugu's parent body. *Earth and Planetary Science Letters*, 627:118559.

Maurer, C., Qi, R., and Raghavan, V. (2003). A linear time algorithm for computing exact Euclidean distance transforms of binary images in arbitrary dimensions. *IEEE Transactions on Pattern Analysis and Machine Intelligence*, 25(2):265–270.

Mazhar, H., Heyn, T., and Negrut, D. (2011). A scalable parallel method for large collision detection problems. *Multibody System Dynamics*, 26(1):37–55.

Mazhar, H., Heyn, T., Pazouki, A., Melanz, D., Seidl, A., Bartholomew, A., Tasora, A., and Negrut, D. (2013). CHRONO: a parallel multi-physics library for rigid-body, flexible-body, and fluid dynamics. *Mechanical Sciences*, 4(1):49–64. Publisher: Copernicus GmbH.

McFadden, L.-A. and Britt, D. T. (2003). Primitive Solar System Objects: Asteroids and Comets. In Meyers, R. A., editor, *Encyclopedia of Physical Science and Technology (Third Edition)*, pages 73–85. Academic Press, New York.

Meirion-Griffith, G. and Spenko, M. (2011). A modified pressure–sinkage model for small, rigid wheels on deformable terrains. *Journal of Terramechanics*, 48(2):149–155.

Merrill, G. P. (1897). *A treatise on rocks, rock-weathering and soils*. New York Macmillan.

Michel, P., Küppers, M., Bagatin, A. C., Carry, B., Charnoz, S., Leon, J. d., Fitzsimmons, A., Gordo, P., Green, S. F., Hérique, A., Juzi, M., Karatekin, , Kohout, T., Lazzarin, M., Murdoch, N., Okada, T., Palomba, E., Pravec, P., Snodgrass, C., Tortora, P., Tsiganis, K., Ulamec, S., Vincent, J.-B., Wünnemann, K., Zhang, Y., Raducan, S. D., Dotto, E., Chabot, N., Cheng, A. F., Rivkin, A., Barnouin, O., Ernst, C., Stickle, A., Richardson, D. C., Thomas, C., Arakawa, M., Miyamoto, H., Nakamura, A., Sugita, S., Yoshikawa, M., Abell, P., Asphaug, E., Ballouz, R.-L., Bottke, W. F., Lauretta, D. S., Walsh, K. J., Martino, P., and Carnelli, I. (2022a). The ESA Hera Mission: Detailed Characterization of the DART Impact Outcome and of the Binary Asteroid (65803) Didymos. *The Planetary Science Journal*, 3(7):160. Publisher: IOP Publishing.

Michel, P., Küppers, M., Fitzsimmons, A., Green, S., Lazzarin, M., Ulamec, S., Abell, P., Sugita, S., Campo Bagatin, A., Carry, B., Charnoz, S., de León, J., Ferrari, F., Hérique, A., Jutzi, M., Karatekin, , Kohout, T., Murdoch, N., Okada, T., Palomba, E., Pravec, P., Raducan, S., Snodgrass, C., Tortora, P., Vincent, J.-B., and Wünnemann, K. (2025). The Hera Space Mission in the Context of Small Near-Earth Asteroid Missions in the Past, Present and Future. *Space Science Reviews*, 221(5):70.

Michel, P., Ulamec, S., Böttger, U., Grott, M., Murdoch, N., Vernazza, P., Sunday, C., Zhang, Y., Valette, R., Castellani, R., Biele, J., Tardivel, S., Groussin, O., Jorda, L., Knollenberg, J., Grundmann, J. T., Arrat, D., Pont, G., Mary, S., Grebenstein, M., Miyamoto, H., Nakamura, T., Wada, K., Yoshikawa, K., and Kuramoto, K. (2022b). The MMX rover: performing in situ surface investigations on Phobos. *Earth, Planets and Space*, 74(1):2.

Michikami, T. and Hagermann, A. (2021). Boulder sizes and shapes on asteroids: A comparative study of Eros, Itokawa and Ryugu. *Icarus*, 357:114282.

Michikami, T., Hagermann, A., Kadokawa, T., Yoshida, A., Shimada, A., Hasegawa, S., and Tsuchiyama, A. (2016). Fragment shapes in impact experiments ranging from cratering to catastrophic disruption. *Icarus*, 264:316–330.

Michikami, T., Honda, C., Miyamoto, H., Hirabayashi, M., Hagermann, A., Irie, T., Nomura, K., Ernst, C. M., Kawamura, M., Sugimoto, K., Tatsumi, E., Morota, T., Hirata, N., Noguchi, T., Cho, Y., Kameda, S., Kouyama, T., Yokota, Y., Noguchi, R., Hayakawa, M., Hirata, N., Honda, R., Matsuoka, M., Sakatani, N., Suzuki, H., Yamada, M., Yoshioka, K., Sawada, H., Hemmi, R., Kikuchi, H., Ogawa, K., Watanabe, S.-i., Tanaka, S., Yoshikawa, M., Tsuda, Y., and Sugita, S. (2019). Boulder size and shape distributions on asteroid Ryugu. *Icarus*, 331:179–191.

Michikami, T., Nakamura, A. M., and Hirata, N. (2010). The shape distribution of boulders on Asteroid 25143 Itokawa: Comparison with fragments from impact experiments. *Icarus*, 207(1):277–284.

Michikami, T., Nakamura, A. M., Hirata, N., Gaskell, R. W., Nakamura, R., Honda, T., Honda, C., Hiraoka, K., Saito, J., Demura, H., Ishiguro, M., and Miyamoto, H. (2008). Size-frequency statistics of boulders on global surface of asteroid 25143 Itokawa. *Earth, Planets and Space*, 60(1):13–20.

Miyamoto, H., Niihara, T., Wada, K., Ogawa, K., Senshu, H., Michel, P., Kikuchi, H., Hemmi, R., Nakamura, T., Nakamura, A. M., Hirata, N., Sasaki, S., Asphaug, E., Britt, D. T., Abell, P. A., Ballouz, R.-L., Banouin, O. S., Baresi, N., Barucci, M. A., Biele, J., Grott, M., Hino, H., Hong, P. K., Imada, T., Kameda, S., Kobayashi, M., Libourel, G., Mogi, K., Murdoch, N., Nishio, Y., Okamoto, S., Ota, Y., Otsuki, M., Otto, K. A., Sakatani, N., Shimizu, Y., Takemura, T., Terada, N., Tsukamoto, M., Usui, T., and Willner, K. (2021). Surface environment of Phobos and Phobos simulant UTPS. *Earth, Planets and Space*, 73(1):214.

Miyamoto, H., Yano, H., Scheeres, D. J., Abe, S., Barnouin-Jha, O., Cheng, A. F., Demura, H., Gaskell, R. W., Hirata, N., Ishiguro, M., Michikami, T., Nakamura, A. M., Nakamura, R., Saito, J., and Sasaki, S. (2007). Regolith Migration and Sorting on Asteroid Itokawa. *Science*, 316(5827):1011–1014. Publisher: American Association for the Advancement of Science.

Mo, P.-Q., Gao, F., and Zhou, G. (2019). Magneto-gravity simulation of cone penetration test in cohesionless soil under small gravity fields. In *Enhancements in Applied Geomechanics, Mining, and Excavation Simulation and Analysis: Proceedings of the 5th GeoChina International Conference 2018–Civil Infrastructures Confronting Severe Weathers and Climate Changes: From Failure to Sustainability, held on July 23 to 25, 2018 in HangZhou, China*, pages 1–10. Springer.

Molaro, J. L., Walsh, K. J., Jawin, E. R., Ballouz, R.-L., Bennett, C. A., DellaGiustina, D. N., Golish, D. R., Drouet d'Aubigny, C., Rizk, B., Schwartz, S. R., Hanna, R. D., Martel, S. J.,

Pajola, M., Campins, H., Ryan, A. J., Bottke, W. F., and Lauretta, D. S. (2020). In situ evidence of thermally induced rock breakdown widespread on Bennu's surface. *Nature Communications*, 11(1):2913. Number: 1 Publisher: Nature Publishing Group.

Moore, A., Hagermann, A., Kaufmann, E., Granvik, M., Barabash, V., Murdoch, N., Sunday, C., Miyamoto, H., Ogawa, K., and Soria-Salinas, A. (2022). Penetrometry in microgravity-from brie to bennu. In *European Planetary Science Congress*, pages EPSC2022–178.

Moore, H. J. and Jakosky, B. M. (1989). Viking landing sites, remote-sensing observations, and physical properties of Martian surface materials. *Icarus*, 81(1):164–184.

Mora, C. F. and Kwan, A. K. H. (2000). Sphericity, shape factor, and convexity measurement of coarse aggregate for concrete using digital image processing. *Cement and Concrete Research*, 30(3):351–358.

Moreau, J. J. (1988). Unilateral Contact and Dry Friction in Finite Freedom Dynamics. In Moreau, J. J. and Panagiotopoulos, P. D., editors, *Nonsmooth Mechanics and Applications*, pages 1–82. Springer, Vienna.

Moreau, J. J. (1997). Numerical investigation of shear zones in granular materials. In Grassberger, P. and Wolf, D., editors, *Proceedings of the HLRZ-Workshop on Friction, Arching, Contact Dynamics*, Proceedings of the HLRZ-Workshop on Friction, Arching, Contact Dynamics, pages 233–247, Singapour, Singapore.

Moreno, F., Bagatin, A. C., Tancredi, G., Li, J.-Y., Rossi, A., Ferrari, F., Hirabayashi, M., Fahnestock, E., Maury, A., Sandness, R., Rivkin, A. S., Cheng, A., Farnham, T. L., Soldini, S., Giordano, C., Merisio, G., Panicucci, P., Pugliatti, M., Castro-Tirado, A. J., Fernández-García, E., Pérez-García, I., Ivanovski, S., Penttila, A., Kolokolova, L., Licandro, J., Muñoz, O., Gray, Z., Ortiz, J. L., and Lin, Z.-Y. (2023). Characterization of the Ejecta from the NASA/DART Impact on Dimorphos: Observations and Monte Carlo Models. *The Planetary Science Journal*, 4(8):138. Publisher: IOP Publishing.

Murchie, S. L., Thomas, P. C., Rivkin, A. S., and Chabot, N. L. (2015). *Phobos and Deimos*. ADS Bibcode: 2015aste.book..451M.

Murdoch, N. (2018). Methods for modelling the interaction between a wheel and the regolith on a small body. Technical report, Institut Supérieur de l'Aéronautique et de l'Espace and Centre National d'Études Spatiales.

Murdoch, N., Drilleau, M., Sunday, C., Thuillet, F., Wilhelm, A., Nguyen, G., and Gourinat, Y. (2021). Low-velocity impacts into granular material: application to small-body landing. *Monthly Notices of the Royal Astronomical Society*, 503(3):3460–3471.

Murdoch, N., Lalucaa, V., Sunday, C., Tardivel, S., Bertrand, J., Théret, N., Vivet, D., Amsili, A., Robin, C., Delton, P., Duchene, A., Douaglin, Q., Maillard, A., Virmontois, C., Vernazza, P., Jorda, L., Groussin, O., Miyamoto, H., Vincent, J.-B., and Baroukh, J. (2025). The WheelCams on the IDEFIX rover. *Progress in Earth and Planetary Science*, 12.

Murdoch, N., Martinez, I. A., Sunday, C., Zenou, E., Cherrier, O., Cadu, A., and Gourinat, Y. (2017). An experimental study of low-velocity impacts into granular material in reduced gravity. *Monthly Notices of the Royal Astronomical Society*, vol. 468(n° 2):pp. 1259–1272. Publisher: Oxford University Press (OUP): Policy P - Oxford Open Option A.

Murdoch, N., Rozitis, B., Green, S. F., Michel, P., de Lophem, T.-L., and Losert, W. (2013). Simulating regoliths in microgravity. *Monthly Notices of the Royal Astronomical Society*, 433(1):506–514.

Murdoch, N., Sánchez, P., Schwartz, S. R., and Miyamoto, H. (2015). Asteroid Surface Geophysics. In Michel, P., DeMeo, F. E., and Bottke, W. F., editors, *Asteroids IV*. University of Arizona Press.

Mühlhaus, H. B., Sakaguchi, H., Moresi, L., and Fahey, M. (2001). Discrete and continuum modelling of granular materials. In Vermeer, P. A., Herrmann, H. J., Luding, S., Ehlers, W., Diebels, S., and Ramm, E., editors, *Continuous and Discontinuous Modelling of Cohesive-Frictional Materials*, pages 185–204. Springer, Berlin, Heidelberg.

Nagaashi, Y., Aoki, T., and Nakamura, A. M. (2021). Cohesion of regolith: Measurements of meteorite powders. *Icarus*, 360:114357. arXiv:2101.11837 [astro-ph].

Nakamura, T., Matsumoto, M., Amano, K., Enokido, Y., Zolensky, M. E., Mikouchi, T., Genda, H., Tanaka, S., Zolotov, M. Y., Kurosawa, K., Wakita, S., Hyodo, R., Nagano, H., Nakashima, D., Takahashi, Y., Fujioka, Y., Kikuiri, M., Kagawa, E., Matsuoka, M., Brearley, A. J., Tsuchiyama, A., Uesugi, M., Matsuno, J., Kimura, Y., Sato, M., Milliken, R. E., Tatsumi, E., Sugita, S., Hiroi, T., Kitazato, K., Brownlee, D., Joswiak, D. J., Takahashi, M., Ninomiya, K., Takahashi, T., Osawa, T., Terada, K., Brenker, F. E., Tkalcec, B. J., Vincze, L., Brunetto, R., Aléon-Toppani, A., Chan, Q. H. S., Roskosz, M., Viennet, J.-C., Beck, P., Alp, E. E., Michikami, T., Nagaashi, Y., Tsuji, T., Ino, Y., Martinez, J., Han, J., Dolocan, A., Bodnar, R. J., Tanaka, M., Yoshida, H., Sugiyama, K., King, A. J., Fukushi, K., Suga, H., Yamashita, S., Kawai, T., Inoue, K., Nakato, A., Noguchi, T., Vilas, F., Hendrix, A. R., Jaramillo-Correa, C., Domingue, D. L., Dominguez, G., Gainsforth, Z., Engrand, C., Duprat, J., Russell, S. S., Bonato, E., Ma, C., Kawamoto, T., Wada, T., Watanabe, S., Endo, R., Enju, S., Riu, L., Rubino, S., Tack, P., Takeshita, S., Takeichi, Y., Takeuchi, A., Takigawa, A., Takir, D., Tanigaki, T., Taniguchi, A., Tsukamoto, K., Yagi, T., Yamada, S., Yamamoto, K., Yamashita, Y., Yasutake, M., Uesugi, K., Umegaki, I., Chiu, I., Ishizaki, T., Okumura, S., Palomba, E., Pilorget, C., Potin, S. M., Alasli,

A., Anada, S., Araki, Y., Sakatani, N., Schultz, C., Sekizawa, O., Sitzman, S. D., Sugiura, K., Sun, M., Dartois, E., De Pauw, E., Dionnet, Z., Djouadi, Z., Falkenberg, G., Fujita, R., Fukuma, T., Gearba, I. R., Hagiya, K., Hu, M. Y., Kato, T., Kawamura, T., Kimura, M., Kubo, M. K., Langenhorst, F., Lantz, C., Lavina, B., Lindner, M., Zhao, J., Vekemans, B., Baklouti, D., Bazi, B., Borondics, F., Nagasawa, S., Nishiyama, G., Nitta, K., Mathurin, J., Matsumoto, T., Mitsukawa, I., Miura, H., Miyake, A., Miyake, Y., Yurimoto, H., Okazaki, R., Yabuta, H., Naraoka, H., Sakamoto, K., Tachibana, S., Connolly, H. C., Lauretta, D. S., Yoshitake, M., Yoshikawa, M., Yoshikawa, K., Yoshihara, K., Yokota, Y., Yogata, K., Yano, H., Yamamoto, Y., Yamamoto, D., Yamada, M., Yamada, T., Yada, T., Wada, K., Usui, T., Tsukizaki, R., Terui, F., Takeuchi, H., Takei, Y., Iwamae, A., Soejima, H., Shirai, K., Shimaki, Y., Senshu, H., Sawada, H., Saiki, T., Ozaki, M., Ono, G., Okada, T., Ogawa, N., Ogawa, K., Noguchi, R., Noda, H., Nishimura, M., Namiki, N., Nakazawa, S., Morota, T., Miyazaki, A., Miura, A., Mimasu, Y., Matsumoto, K., Kumagai, K., Kouyama, T., Kikuchi, S., Kawahara, K., Kameda, S., Iwata, T., Ishihara, Y., Ishiguro, M., Ikeda, H., Hosoda, S., Honda, R., Honda, C., Hitomi, Y., Hirata, N., Hirata, N., Hayashi, T., Hayakawa, M., Hatakeda, K., Furuya, S., Fukai, R., Fujii, A., Cho, Y., Arakawa, M., Abe, M., Watanabe, S., and Tsuda, Y. (2022). Formation and evolution of carbonaceous asteroid Ryugu: Direct evidence from returned samples. *Science*, 379(6634):eabn8671. Publisher: American Association for the Advancement of Science.

Nakamura, T., Nakamura, A. M., Saito, J., Sasaki, S., Nakamura, R., Demura, H., Akiyama, H., Tholen, D., and AMICA team (2001). Multi-band imaging camera and its sciences for the Japanese near-earth asteroid mission MUSES-C. *Earth, Planets and Space*, 53(11):1047–1063.

Nakashima, H., Fujii, H., Oida, A., Momozu, M., Kanamori, H., Aoki, S., Yokoyama, T., Shimizu, H., Miyasaka, J., and Ohdoi, K. (2010). Discrete element method analysis of single wheel performance for a small lunar rover on sloped terrain. *Journal of Terramechanics*, 47(5):307–321.

Nakato, A., Yada, T., Nishimura, M., Yogata, K., Miyazaki, A., Nagashima, K., Hatakeda, K., Kumagai, K., Hitomi, Y., Soejima, H., Bibring, J.-P., Pilorget, C., Hamm, V., Brunetto, R., Riu, L., Lourit, L., Loizeau, D., Le Pivert-Jolivet, T., Lequertier, G., Moussi-Soffys, A., Abe, M., Okada, T., Usui, T., Nakazawa, S., Saiki, T., Tanaka, S., Terui, F., Yoshikawa, M., Watanabe, S.-i., and Tsuda, Y. (2023). Variations of the surface characteristics of Ryugu returned samples. *Earth, Planets and Space*, 75(1):45.

Nase, S. T., Vargas, W. L., Abatan, A. A., and McCarthy, J. J. (2001). Discrete characterization tools for cohesive granular material. *Powder Technology*, 116(2):214–223.

Neukum, G., Ivanov, B. A., and Hartmann, W. K. (2001). Cratering Records in the Inner Solar System in Relation to the Lunar Reference System. In Kallenbach, R., Geiss, J., and Hartmann, W. K., editors, *Chronology and Evolution of Mars*, pages 55–86, Dordrecht. Springer Netherlands.

Oba, Y., Takano, Y., Dworkin, J. P., and Naraoka, H. (2023). Ryugu asteroid sample return provides a natural laboratory for primordial chemical evolution. *Nature Communications*, 14(1):3107. Publisher: Nature Publishing Group.

Oberst, J., Matz, K. D., Roatsch, T., Giese, B., Hoffmann, H., Duxbury, T., and Neukum, G. (2006). Astrometric observations of Phobos and Deimos with the SRC on Mars Express. *Astronomy & Astrophysics*, 447(3):1145–1151.

Onodera, K., Ino, Y., Tanaka, S., Kawamura, T., Ishizaki, T., Kanemaru, R., Fukai, R., Tsuji, T., Nakamura, T., Nakashima, D., Uesugi, M., Tachibana, S., Sugita, S., Yurimoto, H., Noguchi, T., Okazaki, R., Yabuta, H., Naraoka, H., Sakamoto, K., Yada, T., Nishimura, M., Nakato, A., Miyazaki, A., Yogata, K., Abe, M., Okada, T., Usui, T., Yoshikawa, M., Saiki, T., Terui, F., Nakazawa, S., Watanabe, S. i., and Tsuda, Y. (2025). Elastic Properties of Returned Samples From Asteroid (162173) Ryugu. *Journal of Geophysical Research (Planets)*, 130:e2025JE008944. Publisher: Wiley ADS Bibcode: 2025JGRE..13008944O.

O'Rourke, T. D., Druschel, S. J., and Netravali, A. N. (1990). Shear Strength Characteristics of Sand-Polymer Interfaces. *Journal of Geotechnical Engineering*, 116(3):451–469. Publisher: American Society of Civil Engineers.

Ozaki, S., Ishigami, G., Otsuki, M., Miyamoto, H., Wada, K., Watanabe, Y., Nishino, T., Kojima, H., Soda, K., Nakao, Y., Sutoh, M., Maeda, T., and Kobayashi, T. (2023). Granular flow experiment using artificial gravity generator at International Space Station. *npj Microgravity*, 9(1):1–13. Publisher: Nature Publishing Group.

Pajola, M., Lazzarin, M., Bertini, I., Marzari, F., Turrini, D., Magrin, S., La Forgia, F., Thomas, N., Küppers, M., Moissl, R., Ferri, F., Barbieri, C., Rickman, H., Sierks, H., and the OSIRIS Team (2012). Spectrophotometric investigation of Phobos with the Rosetta OSIRIS-NAC camera and implications for its collisional capture. *Monthly Notices of the Royal Astronomical Society*, 427(4):3230–3243.

Pajola, M., Tusberti, F., Lucchetti, A., Barnouin, O., Cambioni, S., Ernst, C. M., Dotto, E., Daly, R. T., Poggiali, G., Hirabayashi, M., Nakano, R., Epifani, E. M., Chabot, N. L., Della Corte, V., Rivkin, A., Agrusa, H., Zhang, Y., Penasa, L., Ballouz, R.-L., Ivanovski, S., Murdoch, N., Rossi, A., Robin, C., Ieva, S., Vincent, J. B., Ferrari, F., Raducan, S. D., Campo-Bagatin, A., Parro, L., Benavidez, P., Tancredi, G., Karatekin, , Trigo-Rodriguez, J. M., Sunshine, J., Farnham, T., Asphaug, E., Deshapriya, J. D. P., Hasselmann, P. H. A., Beccarelli, J., Schwartz, S. R., Abell, P., Michel, P., Cheng, A., Brucato, J. R., Zinzi, A., Amoroso, M., Pirrotta, S., Impresario, G., Bertini, I., Capannolo, A., Caporali, S., Ceresoli, M., Cremonese, G., Dall'Ora, M., Gai, I., Casajus, L. G., Gramigna, E., Manghi, R. L., Lavagna, M., Lombardo, M., Modenini, D.,

Palumbo, P., Perna, D., Tortora, P., Zannoni, M., and Zanotti, G. (2024). Evidence for multi-fragmentation and mass shedding of boulders on rubble-pile binary asteroid system (65803) Didymos. *Nature Communications*, 15(1):6205.

Pajola, M., Vincent, J.-B., Güttler, C., Lee, J.-C., Bertini, I., Massironi, M., Simioni, E., Marzari, F., Giacomini, L., Lucchetti, A., Barbieri, C., Cremonese, G., Naletto, G., Pommerol, A., El-Maarry, M. R., Besse, S., Küppers, M., Forgia, F. L., Lazzarin, M., Thomas, N., Auger, A.-T., Sierks, H., Lamy, P., Rodrigo, R., Koschny, D., Rickman, H., Keller, H. U., Agarwal, J., A'Hearn, M. F., Barucci, M. A., Bertaux, J.-L., Deppo, V. D., Davidsson, B., Cecco, M. D., Debei, S., Ferri, F., Fornasier, S., Fulle, M., Groussin, O., Gutierrez, P. J., Hviid, S. F., Ip, W.-H., Jorda, L., Knollenberg, J., Kramm, J.-R., Kürt, E., Lara, L. M., Lin, Z.-Y., Moreno, J. J. L., Magrin, S., Marchi, S., Michalik, H., Moissl, R., Mottola, S., Oklay, N., Preusker, F., Scholten, F., and Tubiana, C. (2015). Size-frequency distribution of boulders 7 m on comet 67P/Churyumov-Gerasimenko. *Astronomy & Astrophysics*, 583:A37. Publisher: EDP Sciences.

Pang, K. D., Pollack, J. B., Veverka, J., Lane, A. L., and Ajello, J. M. (1978). The Composition of Phobos: Evidence for Carbonaceous Chondrite Surface from Spectral Analysis. *Science*, 199(4324):64–66. Publisher: American Association for the Advancement of Science.

Parzen, E. (1962). On Estimation of a Probability Density Function and Mode. *The Annals of Mathematical Statistics*, 33(3):1065–1076. Publisher: Institute of Mathematical Statistics.

Pazouki, A., Kwarta, M., Williams, K., Likos, W., Serban, R., Jayakumar, P., and Negrut, D. (2017). Compliant contact versus rigid contact: A comparison in the context of granular dynamics. *Physical Review E*, 96(4):042905. Publisher: American Physical Society.

Perko, H. A., Nelson, J. D., and Sadeh, W. Z. (2001). Surface Cleanliness Effect on Lunar Soil Shear Strength. *Journal of Geotechnical and Geoenvironmental Engineering*, 127(4):371–383. Publisher: American Society of Civil Engineers.

Peters, J. F., Muthuswamy, M., Wibowo, J., and Tordesillas, A. (2005). Characterization of force chains in granular material. *Physical Review E*, 72(4):041307.

Pettijohn, F. J. (1975). *Sedimentary Rocks*. HarperCollins, New York.

Pignatale, F. C., Charnoz, S., Rosenblatt, P., Hyodo, R., Nakamura, T., and Genda, H. (2018). On the impact origin of Phobos and Deimos III: resulting composition from different impactors. *The Astrophysical Journal*, 853(2):118. arXiv:1712.05154 [astro-ph].

Podczeck, F. and Mia, Y. (1996). The influence of particle size and shape on the angle of internal friction and the flow factor of unlubricated and lubricated powders. *International Journal of Pharmaceutics*, 144(2):187–194.

Poeschel, T. and Buchholtz, V. (2002). Molecular dynamics of arbitrarily shaped granular particles. arXiv:cond-mat/0203587.

Pollack, J. B., Veverka, J., Pang, K., Colburn, D., Lane, A. L., and Ajello, J. M. (1978). Multicolor observations of phobos with the viking lander cameras: evidence for a carbonaceous chondritic composition. *Science (New York, N.Y.)*, 199(4324):66–69.

Powers, M. C. (1953). A new roundness scale for sedimentary particles. *Journal of Sedimentary Research*, 23(2):117–119. Publisher: GeoScienceWorld.

Radau, R. (1896). Tisserand (F.). — Traité de Mécanique céleste, t. IV. In-40. Paris, Gauthier-Villars et fils ; 1896. Publisher: Persée - Portail des revues scientifiques en SHS.

Radjai, F. and Dubois, F. (2011). *Discrete-element modeling of granular materials*. Wiley-Iste.

Radjai, F., Roux, S., and Moreau, J. J. (1999). Contact forces in a granular packing. *Chaos: An Interdisciplinary Journal of Nonlinear Science*, 9(544). Publisher: American Institute of Physics.

Radjai, F. and Vincent, R. (2009). Contact dynamics as a nonsmooth discrete element method. *Mechanics of Materials*, 41:715–728. Publisher: Elsevier.

Raducan, S. D., Jutzi, M., Cheng, A. F., Zhang, Y., Barnouin, O., Collins, G. S., Daly, R. T., Davison, T. M., Ernst, C. M., and Farnham, T. L. (2024). Physical properties of asteroid Dimorphos as derived from the DART impact. *Nature Astronomy*, 8(4):445–455. Publisher: Nature Publishing Group UK London.

Rahman, J., Nelson, J. D., Siller, T. J., and Mielke, P. W. (1991). Comparison of direct shear and triaxial tests for measurement of shear strength of sand. Publisher: Colorado State University. Libraries.

Raleigh, C. B. and Paterson, M. S. (1965). Experimental deformation of serpentinite and its tectonic implications. *Journal of Geophysical Research (1896-1977)*, 70(16):3965–3985. _eprint: https://agupubs.onlinelibrary.wiley.com/doi/pdf/10.1029/JZ070i016p03965.

Ramsley, K. R. and Head, J. W. (2013). Mars impact ejecta in the regolith of Phobos: Bulk concentration and distribution. *Planetary and Space Science*, 87:115–129.

Richard, P. and Taberlet, N. (2008). Recent advances in DEM simulations of grains in a rotating drum. *Soft Matter*, 4(7):1345–1348. Publisher: The Royal Society of Chemistry.

Richardson, J. E. and Jay Melosh, H. (2013). An examination of the Deep Impact collision site on Comet Tempel 1 via Stardust-NExT: Placing further constraints on cometary surface properties. *Icarus*, 222(2):492–501.

Riley, N. A. (1941). Projection sphericity. *Journal of Sedimentary Research*, 11(2):94–95.

Rivkin, A. S., Brown, R. H., Trilling, D. E., Bell, J. F., and Plassmann, J. H. (2002). Near-Infrared Spectrophotometry of Phobos and Deimos. *Icarus*, 156(1):64–75.

Rivkin, A. S., Chabot, N. L., Stickle, A. M., Thomas, C. A., Richardson, D. C., Barnouin, O., Fahnestock, E. G., Ernst, C. M., Cheng, A. F., Chesley, S., Naidu, S., Statler, T. S., Barbee, B., Agrusa, H., Moskovitz, N., Daly, R. T., Pravec, P., Scheirich, P., Dotto, E., Corte, V. D., Michel, P., Küppers, M., Atchison, J., and Hirabayashi, M. (2021). The Double Asteroid Redirection Test (DART): Planetary Defense Investigations and Requirements. *The Planetary Science Journal*, 2(5):173. Publisher: IOP Publishing.

Rizk, B., Drouet d'Aubigny, C., Golish, D., Fellows, C., Merrill, C., Smith, P., Walker, M. S., Hendershot, J. E., Hancock, J., Bailey, S. H., DellaGiustina, D. N., Lauretta, D. S., Tanner, R., Williams, M., Harshman, K., Fitzgibbon, M., Verts, W., Chen, J., Connors, T., Hamara, D., Dowd, A., Lowman, A., Dubin, M., Burt, R., Whiteley, M., Watson, M., McMahon, T., Ward, M., Booher, D., Read, M., Williams, B., Hunten, M., Little, E., Saltzman, T., Alfred, D., O'Dougherty, S., Walthall, M., Kenagy, K., Peterson, S., Crowther, B., Perry, M. L., See, C., Selznick, S., Sauve, C., Beiser, M., Black, W., Pfisterer, R. N., Lancaster, A., Oliver, S., Oquest, C., Crowley, D., Morgan, C., Castle, C., Dominguez, R., and Sullivan, M. (2018). OCAMS: The OSIRIS-REx Camera Suite. *Space Science Reviews*, 214(1):26.

Robin, C. Q., Duchene, A., Murdoch, N., Vincent, J.-B., Lucchetti, A., Pajola, M., Ernst, C. M., Daly, R. T., Barnouin, O. S., Raducan, S. D., Michel, P., Hirabayashi, M., Stott, A., Cuervo, G., Jawin, E. R., Trigo-Rodriguez, J. M., Parro, L. M., Sunday, C., Vivet, D., Mimoun, D., Rivkin, A. S., and Chabot, N. L. (2024). Mechanical properties of rubble pile asteroids (Dimorphos, Itokawa, Ryugu, and Bennu) through surface boulder morphological analysis. *Nature Communications*, 15(1):6203. Publisher: Nature Publishing Group.

Robinson, M. S., Thomas, P. C., Veverka, J., Murchie, S. L., and Wilcox, B. B. (2002). The geology of 433 Eros. *Meteoritics & Planetary Science*, 37(12):1651–1684. _eprint: https://onlinelibrary.wiley.com/doi/pdf/10.1111/j.1945-5100.2002.tb01157.x.

Rognon, P., Roux, J.-N., Naaim, M., and Chevoir, F. (2008). Dense flows of cohesive granular materials. *Journal of Fluid Mechanics*, 596:21–47. Publisher: Cambridge University Press (CUP).

Rosenblatt, M. (1956). Remarks on Some Nonparametric Estimates of a Density Function. *The Annals of Mathematical Statistics*, 27(3):832–837. Publisher: Institute of Mathematical Statistics.

Rosenblatt, P. (2011). The origin of the Martian moons revisited. *The Astronomy and Astrophysics Review*, 19(1):44.

Rumpf, C. M., Mathias, D. L., Wheeler, L. F., Dotson, J. L., Barbee, B., Roa, J., Chodas, P., and Farnocchia, D. (2020). Deflection driven evolution of asteroid impact risk under large uncertainties. *Acta Astronautica*, 176:276–286.

Saada, A. and Townsend, F. (1981). State of the Art: Laboratory Strength Testing of Soils. In *Laboratory Shear Strength of Soil*, pages 7–77. ASTM International100 Barr Harbor Drive, PO Box C700, West Conshohocken, PA 19428-2959.

Santamarina, J. and Cho, G. (2004). Soil behaviour: The role of particle shape. In *Advances in geotechnical engineering: The Skempton conference*, Conference Proceedings, pages 604–617. Thomas Telford Publishing.

Sawyer Hogg, H. (1948). Out of Old Books (The Titius-Bode Law and the Discovery of Ceres). *Journal of the Royal Astronomical Society of Canada*, 42:241. ADS Bibcode: 1948JRASC..42..241S.

Scheeres, D. J., Hartzell, C. M., Sanchez, P., and Swift, M. (2010). Scaling forces to asteroid surfaces: The role of cohesion. *Icarus*, 210(2):968–984. arXiv:1002.2478 [astro-ph].

Schellart, W. P. (2000). Shear test results for cohesion and friction coefficients for different granular materials: scaling implications for their usage in analogue modelling. *Tectonophysics*, 324(1):1–16.

Scholten, F., Preusker, F., Elgner, S., Matz, K.-D., Jaumann, R., Biele, J., Hercik, D., Auster, H.-U., Hamm, M., Grott, M., Grimm, C., Ho, T.-M., Koncz, A., Schmitz, N., Trauthan, F., Kameda, S., Sugita, S., Honda, R., Morota, T., Tatsumi, E., Cho, Y., Yoshioka, K., Sawada, H., Yokota, Y., Sakatani, N., Hayakawa, M., Matsuoka, M., Yamada, M., Kouyama, T., Suzuki, H., Honda, C., and Ogawa, K. (2019). The descent and bouncing path of the Hayabusa2 lander MASCOT at asteroid (162173) Ryugu. *Astronomy & Astrophysics*, 632:L3. Publisher: EDP Sciences.

Schwartz, S. R., Richardson, D. C., and Michel, P. (2012). An implementation of the soft-sphere discrete element method in a high-performance parallel gravity tree-code. *Granular Matter*, 14(3):363–380.

Schäfer, B., , Andreas, G., , Rainer, K., , and Rebele, B. (2010). Planetary rover mobility simulation on soft and uneven terrain. *Vehicle System Dynamics*, 48(1):149–169. Publisher: Taylor & Francis _eprint: https://doi.org/10.1080/00423110903243224.

Senshu, H., Mizuno, T., Umetani, K., Nakura, T., Konishi, A., Ogawa, A., Ikeda, H., Matsumoto, K., Noda, H., Ishihara, Y., Sasaki, S., Tateno, N., Ikuse, Y., Mayuzumi, K., Kase, T., and Kashine, H. (2021). Light detection and ranging (LIDAR) laser altimeter for the Martian Moons Exploration (MMX) spacecraft. *Earth, Planets and Space*, 73(1):219.

Shimizu, Y., Miyamoto, H., and Michel, P. (2025). Diverse evolutionary pathways of spheroidal asteroids driven by rotation rate. *Scientific Reports*, 15(1):10284. Publisher: Nature Publishing Group.

Shoemaker, E. M., Batson, R. M., Holt, H. E., Morris, E. C., Rennilson, J. J., and Whitaker, E. A. (1967). Surveyor V: Television Pictures. *Science*, 158(3801):642–652. Publisher: American Association for the Advancement of Science.

Simonelli, D. P., Wisz, M., Switala, A., Adinolfi, D., Veverka, J., Thomas, P. C., and Helfenstein, P. (1998). Photometric Properties of PHOBOS Surface Materials From Viking Images. *Icarus*, 131:52–77. ADS Bibcode: 1998Icar..131...52S.

Skempton, A. W. and Bishop, A. W. (1950). The measurement of the shear strength of soils. *Geotechnique*, 2:90–108.

Skinner, A. E. (1969). A Note on the Influence of Interparticle Friction on the Shearing Strength of a Random Assembly of Spherical Particles. *Géotechnique*, 19(1):150–157.

Smilauer, V., Angelidakis, V., Catalano, E., Caulk, R., Chareyre, B., Chèvremont, W., Dorofeenko, S., Duriez, J., Dyck, N., Elias, J., Er, B., Eulitz, A., Gladky, A., Guo, N., Jakob, C., Kneib, F., Kozicki, J., Marzougui, D., Maurin, R., Modenese, C., Pekmezi, G., Scholtès, L., Sibille, L., Stransky, J., Sweijen, T., Thoeni, K., and Yuan, C. (2021). *Yade documentation*. The Yade Project. Version Number: 3rd.

Sneed, E. D. and Folk, R. L. (1958). Pebbles in the Lower Colorado River, Texas a Study in Particle Morphogenesis. *Journal of Geology*, 66:114–150. ADS Bibcode: 1958JG.....66..114S.

Spencer, J. R. and Denk, T. (2010). Formation of Iapetus' extreme albedo dichotomy by exogenically triggered thermal ice migration. *Science (New York, N.Y.)*, 327(5964):432–435.

Steinpilz, T., Musiolik, G., Kruss, M., Jungmann, F., Demirci, T., Aderholz, M., Kollmer, J. E., Teiser, J., Bila, T., Guay, E., and Wurm, G. (2019). ARISE: A granular matter experiment on the International Space Station. *Review of Scientific Instruments*, 90(10):104503. arXiv:1911.05429 [astro-ph].

Stickle, A. M., DeCoster, M. E., Burger, C., Caldwell, W. K., Graninger, D., Kumamoto, K. M., Luther, R., Ormö, J., Raducan, S., Rainey, E., Schäfer, C. M., Walker, J. D., Zhang, Y., Michel, P., Owen, J. M., Barnouin, O., Cheng, A. F., Cochron, S., Collins, G. S., Davison, T. M., Dotto, E., Ferrari, F., Herreros, M. I., Ivanovski, S. L., Jutzi, M., Lucchetti, A., Martellato, E., Pajola, M., Plesko, C. S., Syal, M. B., Schwartz, S. R., Sunshine, J. M., and Wünnemann, K. (2022). Effects of impact and target parameters on the results of a kinetic impactor: predictions for the Double Asteroid Redirection Test (DART) mission. arXiv:2209.06659 [astro-ph].

Stratton, R. E. and Wensrich, C. M. (2010). Modelling of multiple intra-time step collisions in the hard-sphere discrete element method. *Powder Technology*, 199(2):120–130.

Suh, H. S., Kim, K. Y., Lee, J., and Yun, T. S. (2017). Quantification of bulk form and angularity of particle with correlation of shear strength and packing density in sands. *Engineering Geology*, 220:256–265.

Suits, L., Sheahan, T., Bareither, C., Benson, C., and Edil, T. (2008). Reproducibility of Direct Shear Tests Conducted on Granular Backfill Materials. *Geotechnical Testing Journal - GEOTECH TESTING J*, 31.

Sunday, C. (2022). *Landing, sinking, and rolling on small body surfaces*. These de doctorat, Toulouse, ISAE.

Sunday, C., Murdoch, N., Tardivel, S., Schwartz, S. R., and Michel, P. (2020). Validating N-body code Chrono for granular DEM simulations in reduced-gravity environments. *Monthly Notices of the Royal Astronomical Society*, 498(1):1062–1079. arXiv:2009.10448 [astro-ph].

Sunday, C., Murdoch, N., Wilhelm, A., Drilleau, M., Zhang, Y., Tardivel, S., and Michel, P. (2022). The influence of gravity on granular impacts. II. A gravity-scaled collision model for slow interactions. *Astronomy and Astrophysics*, 658:A118. ADS Bibcode: 2022A&A...658A.118S.

Sunday, C., Zhang, Y., Thuillet, F., Tardivel, S., Michel, P., and Murdoch, N. (2021). The influence of gravity on granular impacts - I. A DEM code performance comparison. *Astronomy & Astrophysics*, 656:A97. Publisher: EDP Sciences.

Sylvester, Z. (2024). segmenteverygrain (version 0.0.4). https://github.com/zsylvester/segmenteverygrain. Accessed 2025-07-17.

Sánchez, P., Azema, E., Jardine, K., Hoover, C., Biele, J., Ryan, A., Ballouz, R.-L., Macke, R., Pajola, M., Harold Connolly, J., and Lauretta, D. (2025). A Universal Scaling Framework for Granular Asteroid Strength and its Application to Bennu's Surface. ISSN: 2693-5015.

Sánchez, P. and Scheeres, D. J. (2020). Cohesive regolith on fast rotating asteroids. *Icarus*, 338:113443.

Taheri, S., Sandu, C., Taheri, S., Pinto, E., and Gorsich, D. (2015). A technical survey on Terramechanics models for tire–terrain interaction used in modeling and simulation of wheeled vehicles. *Journal of Terramechanics*, 57:1–22.

Takehana, K., Kizaki, S., Tanaka, T., Uno, K., and Yoshida, K. (2025). Comparison of lunar rover wheel performance in soils with different cohesive properties. *Journal of Terramechanics*, 117:101011.

Tanbakouei, S., Trigo-Rodríguez, J. M., Sort, J., Michel, P., Blum, J., Nakamura, T., and Williams, I. (2019). Mechanical properties of particles from the surface of asteroid 25143 Itokawa. *Astronomy & Astrophysics*, 629:A119. Publisher: EDP Sciences.

Tancredi, G., Maciel, A., Heredia, L., Richeri, P., and Nesmachnow, S. (2012). Granular physics in low-gravity environments using discrete element method. *Monthly Notices of the Royal Astronomical Society*, 420(4):3368–3380.

Tancredi, G., Roland, S., and Bruzzone, S. (2015). Distribution of boulders and the gravity potential on asteroid Itokawa. *Icarus*, 247:279–290.

Tasora, A., Serban, R., Mazhar, H., Pazouki, A., Melanz, D., Fleischmann, J., Taylor, M., Sugiyama, H., and Negrut, D. (2016). Chrono: An Open Source Multi-physics Dynamics Engine. In Kozubek, T., Blaheta, R., Šístek, J., Rozložník, M., and Čermák, M., editors, *High Performance Computing in Science and Engineering*, pages 19–49, Cham. Springer International Publishing.

Tasora, A., Serban, R., and Negrut, D. (1998). Project chrono. https://github.com/projectchrono/chrono. Accessed: 2025-07-21.

Tasora, A., Serban, R., and Negrut, D. (2018). Project chrono. https://projectchrono.org/. Accessed: 2025-07-21.

Taylor, D. W. (1948). *Fundamentals of Soil Mechanics*. JOHN WILEY SONS.

Terzaghi, K. and Peck, R. B. (1954). *Soil Mechanics in Engineering Practice*. Wiley, New York.

Tholen, D. J. (1984). *Asteroid Taxonomy from Cluster Analysis of Photometry*. Ph.D. thesis. ADS Bibcode: 1984PhDT.....3T.

Thomas, C. A., Naidu, S. P., Scheirich, P., Moskovitz, N. A., Pravec, P., Chesley, S. R., Rivkin, A. S., Osip, D. J., Lister, T. A., Benner, L. A. M., Brozović, M., Contreras, C., Morrell, N., Rożek, A., Kušnirák, P., Hornoch, K., Mages, D., Taylor, P. A., Seymour, A. D., Snodgrass, C., Jørgensen, U. G., Dominik, M., Skiff, B., Polakis, T., Knight, M. M., Farnham, T. L., Giorgini, J. D., Rush, B., Bellerose, J., Salas, P., Armentrout, W. P., Watts, G., Busch, M. W., Chatelain, J., Gomez, E., Greenstreet, S., Phillips, L., Bonavita, M., Burgdorf, M. J., Khalouei, E., Longa-Peña, P., Rabus, M., Sajadian, S., Chabot, N. L., Cheng, A. F., Ryan, W. H., Ryan, E. V., Holt, C. E., and Agrusa, H. F. (2023). Orbital period change of Dimorphos due to the DART kinetic impact. *Nature*, 616(7957):448–451. Publisher: Nature Publishing Group.

Thomas, N., Stelter, R., Ivanov, A., Bridges, N. T., Herkenhoff, K. E., and McEwen, A. S. (2011). Spectral heterogeneity on Phobos and Deimos: HiRISE observations and comparisons to Mars Pathfinder results. *Planetary and Space Science*, 59(13):1281–1292.

Thomas, P. and Veverka, J. (1979). Grooves on asteroids: A prediction. *Icarus*, 40(3):394–405.

Thomas, P. C. (1993). Gravity, Tides, and Topography on Small Satellites and Asteroids: Application to Surface Features of the Martian Satellites. *Icarus*, 105:326–344. ADS Bibcode: 1993Icar..105..326T.

Thomas, P. C., Adinolfi, D., Helfenstein, P., Simonelli, D., and Veverka, J. (1996). The Surface of Deimos: Contribution of Materials and Processes to Its Unique Appearance. *Icarus*, 123:536–556. ADS Bibcode: 1996Icar..123..536T.

Thomas, P. C., Parker, J. W., McFadden, L. A., Russell, C. T., Stern, S. A., Sykes, M. V., and Young, E. F. (2005). Differentiation of the asteroid Ceres as revealed by its shape. *Nature*, 437:224–226. ADS Bibcode: 2005Natur.437..224T.

Thomas, P. C., Veverka, J., Robinson, M. S., and Murchie, S. (2001). Shoemaker crater as the source of most ejecta blocks on the asteroid 433 Eros. *Nature*, 413(6854):394–396.

Thuillet, F., Michel, P., Maurel, C., Ballouz, R.-L., Zhang, Y., Richardson, D. C., Biele, J., Tatsumi, E., and Sugita, S. (2018). Numerical modeling of lander interaction with a low-gravity asteroid regolith surface - Application to MASCOT on board Hayabusa2. *Astronomy & Astrophysics*, 615:A41. Publisher: EDP Sciences.

Tolson, R. H., Duxbury, T. C., Born, G. H., Christensen, E. J., Diehl, R. E., Farless, D., Hildebrand, C. E., Mitchell, R. T., Molko, P. M., Morabito, L. A., Palluconi, F. D., Reichert, R. J., Taraji, H., Veverka, J., Neugebauer, G., and Findlay, J. T. (1978). Viking First Encounter of Phobos: Preliminary Results. *Science*, 199(4324):61–64. Publisher: American Association for the Advancement of Science.

Travers, T., Ammi, M., Bideau, D., Gervois, A., Messager, J. C., and Troadec, J. P. (1987). Uniaxial Compression of 2d Packings of Cylinders. Effects of Weak Disorder. *Europhysics Letters*, 4(3):329.

Tsu, W. S. (1934). The observations of Halley's comet in Chinese history. pages 191–201.

Tsuda, Y., Saiki, T., Terui, F., Nakazawa, S., Yoshikawa, M., and Watanabe, S.-i. (2020). Hayabusa2 mission status: Landing, roving and cratering on asteroid Ryugu. *Acta Astronautica*, 171:42–54.

Tsuji, Y., Tanaka, T., and Ishida, T. (1992). Lagrangian numerical simulation of plug flow of cohesionless particles in a horizontal pipe. *Powder Technology*, 71(3):239–250.

Tusberti, F., Pajola, M., Penasa, L., Lucchetti, A., Massironi, M., Munaretto, G., Beccarelli, J., Pozzobon, R., Rossi, C., Poggiali, G., Murdoch, N., Robin, C. Q., Duchene, A., Amoroso, M., Bertini, I., Brucato, J. R., Capannolo, A., Caporali, S., Ceresoli, M., Cremonese, G., Dall'Ora,

M., Corte, V. D., Deshapriya, J. D. P., Dotto, E., Epifani, E. M., Gai, I., Gramigna, E., Hasselmann, P. H. A., Ieva, S., Impresario, G., Ivanovski, S., Manghi, R. L., Lavagna, M., Lombardo, M., Modenini, D., Palumbo, P., Perna, D., Pirrotta, S., Rossi, A., Tortora, P., Zannoni, M., Zanotti, G., Zinzi, A., Buratti, B., Trigo-Rodrigez, J. M., and Casajus, L. G. (2025). Lithologies of Dimorphos revealed by boulder morphological classes. *Icarus*, 442:116744. Publisher: Elsevier ADS Bibcode: 2025Icar..44216744T.

Twiss, R. J. and Moores, E. M. (1992). *Structural geology*. W. H. Freeman, New York.

Ucgul, M., Fielke, J. M., and Saunders, C. (2015). Three-dimensional discrete element modelling (DEM) of tillage: Accounting for soil cohesion and adhesion. *Biosystems Engineering*, 129:298–306.

Ulamec, S., Michel, P., Murdoch, N., Vernazza, P., Grott, M., Knollenberg, J., Schröder, S., Hübers, H.-W., Cho, Y., Prieto-Ballesteros, O., Biele, J., Tardivel, S., Buse, F., Miyamoto, H., Krause, C., May, D., Delmas, C., Baroukh, J., Mary, S., and Grebenstein, M. (2025). Science operations of IDEFIX, the MMX Phobos rover. *Progress in Earth and Planetary Science*, 12(1):97.

Unjhawala, H., Bakke, L., Zhang, H., Taylor, M., Arivoli, G., Serban, R., and Negrut, D. (2025). A Physics-Based Continuum Model for Versatile, Scalable, and Fast Terramechanics Simulation. arXiv:2507.05643 [cs].

Usui, T., Bajo, K. i., Fujiya, W., Furukawa, Y., Koike, M., Miura, Y. N., Sugahara, H., Tachibana, S., Takano, Y., and Kuramoto, K. (2020). The Importance of Phobos Sample Return for Understanding the Mars-Moon System. *Space Science Reviews*, 216(4):49. Publisher: Springer Netherlands.

Verbiscer, A. J., Skrutskie, M. F., and Hamilton, D. P. (2009). Saturn's largest ring. *Nature*, 461(7267):1098–1100.

Verdier, N., Ansan, V., Delage, P., Ali, K. S., Beucler, E., Charalambous, C., Constant, E., Spiga, A., Golombek, M., Marteau, E., Lapeyre, R., Gaudin, E., Yana, C., Hurst, K., Lognonné, P., and Banerdt, B. W. (2023). Using Wind Dispersion Effects During the InSight Tether Burial Activities to Better Constrain the Regolith Grain Size Distribution. *Journal of Geophysical Research: Planets*, 128(5):e2022JE007707. _eprint: https://agupubs.onlinelibrary.wiley.com/doi/pdf/10.1029/2022JE007707.

Vernazza, P., Jorda, L., Tardivel, S., Baroukh, J., Groussin, O., Pimorin, C., Poulain, A., Chabaud, P.-Y., Robert, E., Bertrand, J., Lalucaa, V., Remetean, E., Théret, N., Virmontois, C., Murdoch, N., Le Mouélic, S., Beck, P., Rüsch, O., Flahaut, J., Charnoz, S., Lasue, J., Barucci, M.-A., Doressoundiram, A., Michel, P., and Ulamec, S. (2025). Surface science on Phobos with

the navigation cameras of the MMX IDEFIX rover. *Progress in Earth and Planetary Science*, 12(1):46.

Viles, H. A. (2001). Scale issues in weathering studies. *Geomorphology*, 41:63–72. ADS Bibcode: 2001Geomo..41...63V.

Vu, D. C., Amarsid, L., Richefeu, V., Delenne, J.-Y., and Radjai, F. (2025). Quasistatic rheology of granular materials composed of dodecahedra. *The European Physical Journal Special Topics*.

W. C. Krumbein (1941). Measurement and Geological Significance of Shape and Roundness of Sedimentary Particles. *SEPM Journal of Sedimentary Research*, Vol. 11.

Wada, K., Senshu, H., and Matsui, T. (2006). Numerical simulation of impact cratering on granular material. *Icarus*, 180:528–545. ADS Bibcode: 2006Icar..180..528W.

Wadell, H. (1932). Volume, Shape, and Roundness of Rock Particles. *The Journal of Geology*, 40(5):443–451.

Wadell, H. (1933). Sphericity and Roundness of Rock Particles. *Journal of Geology*, 41:310–331. ADS Bibcode: 1933JG.....41..310W.

Wadell, H. (1935). Volume, Shape, and Roundness of Quartz Particles. *The Journal of Geology*, 43(3):250–280. Publisher: The University of Chicago Press.

Walsh, K. J., Ballouz, R.-L., Jawin, E. R., Avdellidou, C., Barnouin, O. S., Bennett, C. A., Bierhaus, E. B., Bos, B. J., Cambioni, S., Connolly, H. C., Delbo, M., DellaGiustina, D. N., DeMartini, J., Emery, J. P., Golish, D. R., Haas, P. C., Hergenrother, C. W., Ma, H., Michel, P., Nolan, M. C., Olds, R., Rozitis, B., Richardson, D. C., Rizk, B., Ryan, A. J., Sánchez, P., Scheeres, D. J., Schwartz, S. R., Selznick, S. H., Zhang, Y., and Lauretta, D. S. (2022). Near-zero cohesion and loose packing of Bennu's near subsurface revealed by spacecraft contact. *Science Advances*, 8(27):eabm6229. Publisher: American Association for the Advancement of Science.

Wang, C., Deng, A., and Taheri, A. (2018). Three-dimensional discrete element modeling of direct shear test for granular rubber–sand. *Computers and Geotechnics*, 97:204–216.

Wang, X., Schwan, J., Hsu, H.-W., Grün, E., and Horányi, M. (2016). Dust charging and transport on airless planetary bodies. *Geophysical Research Letters*, 43(12):6103–6110. _eprint: https://onlinelibrary.wiley.com/doi/pdf/10.1002/2016GL069491.

Wargnier, A., Poggiali, G., Yumoto, K., Fornasier, S., Mahlke, M., Gautier, T., and Doressoundiram, A. (2025). Insights into the origins of Phobos and Deimos based on a spectral comparison with small bodies and Martian materials. *Astronomy & Astrophysics*, 694:A304. Publisher: EDP Sciences.

Waskom, M. L. (2021). seaborn: statistical data visualization. *Journal of Open Source Software*, 6(60):3021.

Watanabe, S., Hirabayashi, M., Hirata, N., Hirata, N., Noguchi, R., Shimaki, Y., Ikeda, H., Tatsumi, E., Yoshikawa, M., Kikuchi, S., Yabuta, H., Nakamura, T., Tachibana, S., Ishihara, Y., Morota, T., Kitazato, K., Sakatani, N., Matsumoto, K., Wada, K., Senshu, H., Honda, C., Michikami, T., Takeuchi, H., Kouyama, T., Honda, R., Kameda, S., Fuse, T., Miyamoto, H., Komatsu, G., Sugita, S., Okada, T., Namiki, N., Arakawa, M., Ishiguro, M., Abe, M., Gaskell, R., Palmer, E., Barnouin, O. S., Michel, P., French, A. S., McMahon, J. W., Scheeres, D. J., Abell, P. A., Yamamoto, Y., Tanaka, S., Shirai, K., Matsuoka, M., Yamada, M., Yokota, Y., Suzuki, H., Yoshioka, K., Cho, Y., Tanaka, S., Nishikawa, N., Sugiyama, T., Kikuchi, H., Hemmi, R., Yamaguchi, T., Ogawa, N., Ono, G., Mimasu, Y., Yoshikawa, K., Takahashi, T., Takei, Y., Fujii, A., Hirose, C., Iwata, T., Hayakawa, M., Hosoda, S., Mori, O., Sawada, H., Shimada, T., Soldini, S., Yano, H., Tsukizaki, R., Ozaki, M., Iijima, Y., Ogawa, K., Fujimoto, M., Ho, T.-M., Moussi, A., Jaumann, R., Bibring, J.-P., Krause, C., Terui, F., Saiki, T., Nakazawa, S., and Tsuda, Y. (2019). Hayabusa2 arrives at the carbonaceous asteroid 162173 Ryugu—A spinning top–shaped rubble pile. *Science*, 364(6437):268–272.

Watanabe, S.-i., Tsuda, Y., Yoshikawa, M., Tanaka, S., Saiki, T., and Nakazawa, S. (2017). Hayabusa2 Mission Overview. *Space Science Reviews*, 208(1):3–16.

Weinhart, T., Orefice, L., Post, M., van Schrojenstein Lantman, M. P., Denissen, I. F. C., Tunuguntla, D. R., Tsang, J. M. F., Cheng, H., Shaheen, M. Y., Shi, H., Rapino, P., Grannonio, E., Losacco, N., Barbosa, J., Jing, L., Alvarez Naranjo, J. E., Roy, S., den Otter, W. K., and Thornton, A. R. (2020). Fast, flexible particle simulations — An introduction to MercuryDPM. *Computer Physics Communications*, 249:107129.

Willner, K., Shi, X., and Oberst, J. (2014). Phobos' shape and topography models. *Planetary and Space Science*, 102:51–59.

Wong, J. Y. (1980). Data processing methodology in the characterization of the mechanical properties of terrain. *Journal of Terramechanics*, 17(1):13–41.

Wong, J. Y. (2008). *Theory of Ground Vehicles*. John Wiley & Sons, Hoboken, NJ, 4 edition.

Wu, K., Abriak, N., Becquart, F., Pizette, P., Remond, S., and Liu, S. (2017). Shear mechanical behavior of model materials samples by experimental triaxial tests: case study of 4 mm diameter glass beads. *GRANULAR MATTER*, 19(4).

Yada, T., Abe, M., Okada, T., Nakato, A., Yogata, K., Miyazaki, A., Hatakeda, K., Kumagai, K., Nishimura, M., Hitomi, Y., Soejima, H., Yoshitake, M., Iwamae, A., Furuya, S., Uesugi, M., Karouji, Y., Usui, T., Hayashi, T., Yamamoto, D., Fukai, R., Sugita, S., Cho, Y., Yumoto, K.,

Yabe, Y., Bibring, J.-P., Pilorget, C., Hamm, V., Brunetto, R., Riu, L., Lourit, L., Loizeau, D., Lequertier, G., Moussi-Soffys, A., Tachibana, S., Sawada, H., Okazaki, R., Takano, Y., Sakamoto, K., Miura, Y. N., Yano, H., Ireland, T. R., Yamada, T., Fujimoto, M., Kitazato, K., Namiki, N., Arakawa, M., Hirata, N., Yurimoto, H., Nakamura, T., Noguchi, T., Yabuta, H., Naraoka, H., Ito, M., Nakamura, E., Uesugi, K., Kobayashi, K., Michikami, T., Kikuchi, H., Hirata, N., Ishihara, Y., Matsumoto, K., Noda, H., Noguchi, R., Shimaki, Y., Shirai, K., Ogawa, K., Wada, K., Senshu, H., Yamamoto, Y., Morota, T., Honda, R., Honda, C., Yokota, Y., Matsuoka, M., Sakatani, N., Tatsumi, E., Miura, A., Yamada, M., Fujii, A., Hirose, C., Hosoda, S., Ikeda, H., Iwata, T., Kikuchi, S., Mimasu, Y., Mori, O., Ogawa, N., Ono, G., Shimada, T., Soldini, S., Takahashi, T., Takei, Y., Takeuchi, H., Tsukizaki, R., Yoshikawa, K., Terui, F., Nakazawa, S., Tanaka, S., Saiki, T., Yoshikawa, M., Watanabe, S.-i., and Tsuda, Y. (2022). Preliminary analysis of the Hayabusa2 samples returned from C-type asteroid Ryugu. *Nature Astronomy*, 6(2):214–220. Publisher: Nature Publishing Group.

Yang, J. and Luo, X. (2015). Exploring the relationship between critical state and particle shape for granular materials. *Journal of the Mechanics and Physics of Solids*, 84:196–213.

Yang, J. and Wei, L. (2012). Collapse of loose sand with the addition of fines: the role of particle shape. *Géotechnique*, 62(12):1111–1125.

Yin, K., Fauchille, A.-L., Di Filippo, E., Kotronis, P., and Sciarra, G. (2021). A Review of Sand–Clay Mixture and Soil–Structure Interface Direct Shear Test. *Geotechnics*, 1(2):260–306. Publisher: Multidisciplinary Digital Publishing Institute.

Yingst, R. A., Haldemann, A. F. C., Biedermann, K. L., and Monhead, A. M. (2007). Quantitative morphology of rocks at the Mars Pathfinder landing site. *Journal of Geophysical Research: Planets*, 112(E6). _eprint: https://onlinelibrary.wiley.com/doi/pdf/10.1029/2005JE002582.

Yokota, S., Matsuoka, A., Murata, N., Saito, Y., Asamura, K., Kasahara, S., Delcourt, D., Hadid, L. Z., Terada, N., Keika, K., Harada, Y., Nakagawa, H., Masunaga, K., Sakai, S., Futaana, Y., Imajo, S., Seki, K., Nishino, M. N., and Kitamura, Y. (2025). Pre-flight performance of the ion energy mass spectrum analyzer for the Martian Moons eXploration (MMX) mission. *Progress in Earth and Planetary Science*, 12(1):51.

Yokota, S., Terada, N., Matsuoka, A., Murata, N., Saito, Y., Delcourt, D., Futaana, Y., Seki, K., Schaible, M. J., Asamura, K., Kasahara, S., Nakagawa, H., Nishino, M. N., Nomura, R., Keika, K., Harada, Y., and Imajo, S. (2021). In situ observations of ions and magnetic field around Phobos: the mass spectrum analyzer (MSA) for the Martian Moons eXploration (MMX) mission. *Earth, Planets and Space*, 73(1):216.

Yokoyama, T., Nagashima, K., Nakai, I., Young, E. D., Abe, Y., Aléon, J., Alexander, C. M. O., Amari, S., Amelin, Y., Bajo, K.-i., Bizzarro, M., Bouvier, A., Carlson, R. W., Chaussidon,

M., Choi, B.-G., Dauphas, N., Davis, A. M., Di Rocco, T., Fujiya, W., Fukai, R., Gautam, I., Haba, M. K., Hibiya, Y., Hidaka, H., Homma, H., Hoppe, P., Huss, G. R., Ichida, K., Iizuka, T., Ireland, T. R., Ishikawa, A., Ito, M., Itoh, S., Kawasaki, N., Kita, N. T., Kitajima, K., Kleine, T., Komatani, S., Krot, A. N., Liu, M.-C., Masuda, Y., McKeegan, K. D., Morita, M., Motomura, K., Moynier, F., Nguyen, A., Nittler, L., Onose, M., Pack, A., Park, C., Piani, L., Qin, L., Russell, S. S., Sakamoto, N., Schönbächler, M., Tafla, L., Tang, H., Terada, K., Terada, Y., Usui, T., Wada, S., Wadhwa, M., Walker, R. J., Yamashita, K., Yin, Q.-Z., Yoneda, S., Yui, H., Zhang, A.-C., Connolly, H. C., Lauretta, D. S., Nakamura, T., Naraoka, H., Noguchi, T., Okazaki, R., Sakamoto, K., Yabuta, H., Abe, M., Arakawa, M., Fujii, A., Hayakawa, M., Hirata, N., Hirata, N., Honda, R., Honda, C., Hosoda, S., Iijima, Y.-i., Ikeda, H., Ishiguro, M., Ishihara, Y., Iwata, T., Kawahara, K., Kikuchi, S., Kitazato, K., Matsumoto, K., Matsuoka, M., Michikami, T., Mimasu, Y., Miura, A., Morota, T., Nakazawa, S., Namiki, N., Noda, H., Noguchi, R., Ogawa, N., Ogawa, K., Okada, T., Okamoto, C., Ono, G., Ozaki, M., Saiki, T., Sakatani, N., Sawada, H., Senshu, H., Shimaki, Y., Shirai, K., Sugita, S., Takei, Y., Takeuchi, H., Tanaka, S., Tatsumi, E., Terui, F., Tsuda, Y., Tsukizaki, R., Wada, K., Watanabe, S.-i., Yamada, M., Yamada, T., Yamamoto, Y., Yano, H., Yokota, Y., Yoshihara, K., Yoshikawa, M., Yoshikawa, K., Furuya, S., Hatakeda, K., Hayashi, T., Hitomi, Y., Kumagai, K., Miyazaki, A., Nakato, A., Nishimura, M., Soejima, H., Suzuki, A., Yada, T., Yamamoto, D., Yogata, K., Yoshitake, M., Tachibana, S., and Yurimoto, H. (2022). Samples returned from the asteroid Ryugu are similar to Ivuna-type carbonaceous meteorites. *Science*, 379(6634):eabn7850. Publisher: American Association for the Advancement of Science.

Yoshikawa, K., Van Wal, S., Mimasu, Y., Ogawa, N., Ono, G., Terui, F., Saiki, T., and Tsuda, Y. (2022). Chapter 11 - MINERVA-II-1A/B Asteroid Rovers Deployment and Landing. In Hirabayashi, M. and Tsuda, Y., editors, *Hayabusa2 Asteroid Sample Return Mission*, pages 209–228. Elsevier.

Yoshikawa, M., Kawaguchi, J., Fujiwara, A., and Tsuchiyama, A. (2021). Chapter 6 - The Hayabusa mission. In Longobardo, A., editor, *Sample Return Missions*, pages 123–146. Elsevier.

Zega, T. J., McCoy, T. J., Russell, S. S., Keller, L. P., Gainsforth, Z., Singerling, S. A., Manga, V. R., Harrison, C., Libourel, G., Prince, B. S., Thomas-Keprta, K., King, A., Portail, M., Guigoz, V., Tu, V., Le, L., Thompson, M., Benner, M. C., Kerrison, N. A., Barnes, J. J., Ong, I., Haenecour, P., Chaves, L., Smith, L., Kontogiannis, M., Vega Santiago, N., Hill, D., Zeszut, Z., Domanik, K., Chang, Y.-J., Corrigan, C. M., Ray, S., Wardell, L. R., Gooding, T., Rose, T. R., Bates, H. C., Schofield, P. F., Almeida, N. V., Salge, T., Najorka, J., Seifert, L. B., Lunning, N., Righter, K., Nguyen, A. N., Brenker, F. E., Eckley, S. A., Dworkin, J. P., Jones, R. H., Sandford, S. A., Marcus, M. A., Bechtel, H. A., Dominguez, G., Yurimoto, H., Kawasaki, N., Bajo, K., Sakamoto, N., Zanetta, P.-M., Tachibana, S., Busemann, H., Hamilton, V. E., Franchi, I. A., Grady, M., Greenwood, R. C., Tait, K., Timms, N., Bland, P., Jourdan,

F., Reddy, S. M., Rickard, W., Saxey, D., Vincze, L., Connolly, H. C., and Lauretta, D. S. (2025). Mineralogical evidence for hydrothermal alteration of Bennu samples. *Nature Geoscience*, 18(9):832–839. Publisher: Nature Publishing Group.

Zhang, L. and Thornton, C. (2015). A numerical examination of the direct shear test. *Géotechnique*. Publisher: Thomas Telford Ltd.

Zhang, Q., Townsend, S., and Kamrin, K. (2020). Expanded scaling relations for locomotion in sloped or cohesive granular beds. *Physical Review Fluids*, 5(11):114301. Publisher: American Physical Society.

Zhang, R., Tagliafierro, B., Vanden Heuvel, C., Sabarwal, S., Bakke, L., Yue, Y., Wei, X., Serban, R., and Negruţ, D. (2024). Chrono DEM-Engine: A Discrete Element Method dual-GPU simulator with customizable contact forces and element shape. *Computer Physics Communications*, 300:109196.

Zhang, Y., Dai, J., Hu, W., and Negrut, D. (2025). Using high fidelity discrete element simulation to calibrate an expeditious terramechanics model in a multibody dynamics framework. *Multibody System Dynamics*, pages 1–40.

Zhang, Y., Michel, P., Barnouin, O. S., Roberts, J. H., Daly, M. G., Ballouz, R.-L., Walsh, K. J., Richardson, D. C., Hartzell, C. M., and Lauretta, D. S. (2022). Inferring interiors and structural history of top-shaped asteroids from external properties of asteroid (101955) Bennu. *Nature Communications*, 13(1):4589. Number: 1 Publisher: Nature Publishing Group.

Zhang, Y., Richardson, D. C., Barnouin, O. S., Michel, P., Schwartz, S. R., and Ballouz, R.-L. (2018). Rotational Failure of Rubble-pile Bodies: Influences of Shear and Cohesive Strengths. *The Astrophysical Journal*, 857:15. Publisher: IOP ADS Bibcode: 2018ApJ...857...15Z.

Zheng, J. and Hryciw, R. D. (2015). Traditional soil particle sphericity, roundness and surface roughness by computational geometry. *Géotechnique*, 65(6):494–506.

Zheng, J. and Hryciw, R. D. (2016). Roundness and Sphericity of Soil Particles in Assemblies by Computational Geometry. *Journal of Computing in Civil Engineering*, 30(6):04016021. Publisher: American Society of Civil Engineers.

Zhu, X., Xie, L., Xu, S., and Zhang, W. (2023). DEM Simulation of a Rotary Drum with Inclined Flights Using the Response Surface Methodology. *Processes*, 11(5):1363. Publisher: Multidisciplinary Digital Publishing Institute.

Zingg, T. (1935). *Beitrag zur Schotteranalyse*. Doctoral Thesis, ETH Zurich. Accepted: 2017-06-12T22:43:06Z.

Zou, M., Fan, S., Shi, R., Yang, Y., and Li, J. (2015). Effect of gravity on the mechanical properties of lunar regolith tested using a low gravity simulation device. *Journal of Terramechanics*, 60:11–22.

Zuiderveld, K. (1994). *Graphic Gems IV*, chapter Contrast Limited Adaptive Histograph Equalization. San Diego: Academic Press Professional.

Zuriguel, I., Mullin, T., and Rotter, J. M. (2007). Effect of Particle Shape on the Stress Dip Under a Sandpile. *Physical Review Letters*, 98(2):028001. Publisher: American Physical Society.

Çelik, O., Ballouz, R.-L., Scheeres, D. J., and Kawakatsu, Y. (2022). A numerical simulation approach to the crater-scaling relationships in low-speed impacts under microgravity. *Icarus*, 377:114882.

RÉPUBLIQUE FRANÇAISE
Liberté
Égalité
Fraternité

Université de Toulouse

Titre : Investigation des propriétés globales des matériaux granulaires dans le contexte de l'instrument WheelCams à bord du rover MMX.

Mots clés : Faible gravité, Surface, Phobos, propriétés macroscopiques, Matériaux granulaires

Résumé : Les petits corps, vestiges des blocs à l'origine du Système solaire, contiennent des informations clés sur la formation et l'évolution de ses planètes. Ils sont récemment devenus les cibles d'un nombre croissant de missions d'exploration spatiale, impliquant souvent des interactions directes avec leur surface. Ainsi, comprendre le comportement mécanique de la surface de ces corps est essentiel au succès de ces missions. Les surfaces des astéroïdes visités par ces missions sont couvertes de régolithe, un matériau granulaire meuble dont les propriétés sont gouvernées par les interactions entre ses particules, leurs morphologies, ainsi que par les conditions externes telles que la faible gravité. Cependant, il n'est pas évident de déterminer dans quelles mesures les hypothèses de la mécanique des milieux granulaires sur Terre restent valables en faible gravité. Nous souhaitons donc étudier les propriétés mécaniques des matériaux granulaires en faible gravité, avec un intérêt pour les lunes martiennes Phobos et Deimos, dans le contexte de la mission Martian Moons eXploration (MMX) de l'agence spatiale japonaise. En particulier, ce travail se concentre sur le rover Idefix de la mission MMX, développé par l'agence spatiale allemande (DLR) en collaboration avec l'agence spatiale française (CNES). Cette thèse vise à contribuer à l'atteinte des objectifs scientifiques des WheelCams, des caméras installées sous le rover et orientées vers ses roues. Pour ce faire, différentes techniques d'analyse ont été utilisées, incluant l'analyse morphologique de particules à partir d'images et des simulations numériques basées sur la méthode des éléments discrets (DEM) à sphères déformables, afin d'étudier les propriétés mécaniques macroscopiques des matériaux granulaires en faible gravité.
Dans un premier temps, une étude d'analyse morphologique de matériaux granulaires est proposée. Une chaîne de traitement d'images a été développée et validée afin d'extraire des descripteurs morphologiques quantitatifs à partir des images des WheelCams. Cette chaîne a été appliquée à des images issues du banc d'essai des WheelCams ainsi qu'à une étude approfondie de blocs rocheux présents à la surface de différents astéroïdes de type « rubble-pile ». Les morphologies observées ont pu être mises en relation avec les propriétés mécaniques de ces blocs et montrer qu'ils proviendraient de la disruption d'un corps parent.
Dans un second temps, cette thèse s'intéresse aux propriétés mécaniques macroscopiques de matériaux granulaires simulés, qui ont été utilisés dans la thèse de Cecily Sunday, publiée en 2022. À l'aide du logiciel Project Chrono et de son code DEM à sphères déformables, une boîte de cisaillement direct a été conçue afin de reproduire numériquement des essais géotechniques de laboratoire. Cet outil permet d'extraire les propriétés macroscopiques de ces matériaux, telles que l'angle de frottement interne et la cohésion macroscopique. Les résultats de ces tests ont permis d'étudier l'influence des propriétés inter-particulaires, de la pression de confinement et de la gravité sur les propriétés macroscopiques de ces matériaux. Ces résultats mettent en évidence un lien entre la diminution de la gravité, de la pression de confinement ou de la charge normale sous un certain seuil avec une baisse importante de la cohésion apparente du matériau. Ils ont ensuite été interprétés dans le cadre de la terramécanique afin d'en tirer des informations pour la mobilité des rovers et les interactions avec le régolithe en faible gravité.
Dans l'ensemble, cette thèse propose de nouveaux outils ainsi que des éléments de compréhension supplémentaires afin de caractériser les matériaux granulaires et leur comportement à la surface des petits corps. Ces résultats sont particulièrement pertinents pour l'interprétation scientifique et les opérations de la mission MMX, et d'autres missions dédiées aux petits corps.

Title: Investigating the bulk properties of granular materials in the context of the MMX rover WheelCams

Key words: Low-gravity, Surface, Phobos, Bulk properties, Granular materials

Abstract: Small bodies, as the leftovers of the building blocks of the Solar System contain key informations on the formation and evolution of the planets of the Solar System. These small-bodies have thus become the targets of a increasing number of space exploration missions, often involving direct interactions with their surface. Understanding the mechanical behaviours of the surfaces of these bodies is thus essential for the success of these missions. The surfaces of the asteroids that have been visited by space missions to date are covered by regolith, a loose granular material whose properties are governed by complex inter-particle interactions, grain morphology, and environmental conditions such as low gravity. Predicting regolith behaviour in such conditions is a challenge as it is not clear how terrestrial assumptions on granular material scale in low gravity. This thesis aims to investigates the mechanical properties of granular materials in low gravity, with a focus on the Martian moon Phobos in the context of the future Japanese space agency's Martian Moon eXploration mission. Notably, this study focuses on the MMX Rover Idefix provided by the German space agency, and the French space agency. More specifically, this thesis aims to contribute to the scientific objectives of the WheelCams, cameras placed under the rover pointing towards its wheels. To do so, we combined different analysis techniques such as morphological analysis of particles from images and numerical simulations using a soft-sphere Discrete Element Method (DEM) code, in order to investigate the bulk mechanical properties of granular material in low gravity.
First, we propose a morphological analysis study of granular material. An image analysis pipeline has been developed and validated, with the aim to extract quantitative morphological descriptors from the WheelCams images. We used this pipeline on images from the WheelCams testbed and in a comprehensive study of boulders at the surfaces of different rubble-pile asteroids, including the last image captured of Dimorphos by the DART spacecraft that aimed to change its orbit in the context of planetary defence. We were notably able to link the observed morphologies with bulk properties of the boulders at the surface of these asteroids and make further interpretations regarding their formations, showing that these boulders originated from the disruption of a parent body.
Then, this thesis focuses on the bulk mechanical properties of simulated granular materials that were studied in a precedent thesis published by Cecily Sunday in 2022. Using Project Chrono and its soft-sphere DEM framework, a digital direct shear box has been designed to reproduce laboratory geotechnical tests in a numerical environment. This digital shear box aims to extract the mechanical bulk properties of simulated granular materials, as these materials are defined by their inter-particle properties. Finally, using the results of the direct shear tests, we investigated the influence of inter-particle properties, confining pressure and gravity on the macroscopic properties of granular materials. Most notably our results highlight the fact that decreasing gravity, confining pressure or normal load under a certain threshold will drastically decrease the bulk cohesion of granular materials. These results have been then interpreted in the framework of terramechanics, to draw further interpretations relevant to rover mobility and surface interactions in low gravity.
Overall, this thesis aims to provides new tools as well as further insights to characterize granular materials and granular behaviours at the surface of small bodies. These results are notably of importance for the interpretation and operations of MMX and other current or future small body exploration missions.